Understanding geological evolution of chalk cliffs and coastal processes using InSAR

A thesis submitted to Imperial College London in partial fulfilment of the requirements for the degree of Master of Philosophy

By

Malgorzata Mider

Department of Civil and Environmental Engineering

Imperial College London

London SW7 2AZ

December 2021

Declaration

The work presented in this thesis was undertaken in the Department of Civil and Environmental Engineering at Imperial College London. This thesis is result of my own work and any quotation from, or description of, the work of others has been appropriately referenced, whether published or unpublished. This thesis is not the same as any that I have submitted for any degree, diploma or other qualification at any other university. No part of this thesis has been or being concurrently submitted for any such degree, diploma or other classification.

Malgorzata Mider

London, December 2021

Abstract

A tenth of the world's population lives in coastal zones (Evans, 2004), where human activity and rising global sea levels intensify the erosion and flooding. To enable the coastal area to remain viable for human use, reliable and repeatable methods of monitoring are necessary, along with better understanding of geological processes that can be encountered in such areas. Current monitoring methods are often expensive, requiring specialist equipment, which can prove problematic when trying to gain access to the coast, work can be weather and/or tide dependant.

Space-borne Synthetic Aperture Radar Interferometry (InSAR) is increasingly used to monitor ground motions related to natural and anthropogenic geohazards with up to millimetre accuracy. The European Space Agency (ESA) satellites, Sentinel-1A and 1B, provide freely available detailed data with repeat time of 6 days.

The aim of this research was to investigate and understand use of InSAR data for monitoring and analysis of geological processes affecting coastal zones. The focus of the research is downwearing and erosion of the shoreline, cliff collapse and rotational landslides. Permanent Scatterer Interferometry (PSI) technique was used on Sentinel-1 data to measure surface deformation and relate to these coastal processes and mechanisms.

The UK chalk coast was selected for the research sites, the results show that identifying evidence of vertical cliff collapses was very challenging and the results were inconclusive, mainly due to the vegetation present, leading to a loss of coherence. Platform downwearing can be successfully monitored both at a local and regional scale, and large scale coastal, rotational landslides can also be successfully monitored. This has been performed to sub-millimetre accuracy and allowed for the natural processes to be interpreted.

The effectiveness of the PSI methodology as a monitoring tool for coastal environments has been shown, especially when coupled with conventional monitoring methods.

Table of Contents

List of Figures

List of Tables

List of Symbols

Roman Alphabet

$B_n^{(k)}$	Phase component with normal baseline
BW	Range bandwidth
D	Antenna's width
$d^{(k)}$	Displacement
D_r	Antenna's length
e*	Voids ratio
G_s	Specific gravity
I_{d2}	Slake durability index
I_p	Plasticity index
$I_{s(50)}$	Point load index
L	Antenna's length
m_{sat}	Saturated moisture content
n	Noise
n*	Porosity
q_u	Unconfined compressive strength
r	Distance between source and target
R_a	Azimuth resolution
S	Slant range
V	Velocity
V_E	Horizontal velocity
V_{LoS}	Velocity in Line-of-Sight
V_U	Vertical velocity
w_L	Liquid limit

Greek Alphabet

α	Atmospheric contribution
$\alpha_{(k)}$	Atmospheric phase screen
α	Orbit azimuth angle
γd	Dry density
$\lvert\bar{\gamma}\rvert$	Coherence
$\lvert\gamma\rvert_{temp}$	Temporal decorrelation

Δr_{disp}	Displacement in line of sight
ε	Elevation error in DEM
θ	Incidence angle
λ	Radar wavelength
ν	Noise source
τ	Pulse duration
ϕ	Phase

Abbreviations and Acronyms

AOI	Area of Investigation
APS	Atmospheric Phase Screen
BODC	British Oceanographic Data Centre
DEM	Digital Elevation Model
DInSAR	Differential Interferometric Synthetic Aperture Radar
DS	Distributed Scatterers
EO	Earth Observation
ESA	European Space Agency
EW	Extra wide swath mode
GCP	Ground Control Points
GIS	Geographic Information System
GPS	Global Positioning System
IDW	Inverse Distance Weighted average
InSAR	Interferometric Synthetic Aperture Radar
IW	Interferometric wide swath mode
LiDAR	Light Detection and Ranging
LoS	Line-Of-Sight
LS	Laser Scanning
LSM	Landslide Susceptibility Maps
MEM	Micro-Erosion Metre
ML	Machine Learning
OD	Ordnance Datum
PSI	Persistent Scatterer Interferometry
PSI	Persistent (or Permanent) Scatterer
SAR	Synthetic Aperture Radar

SLC	Single Look Complex
SNR	Signal-To-Noise-Ratio
SPT	Standard Penetration Test
SW	Strip map mode
TLS	Terrestrial Laser Scanning
UAV	Unmanned Aerial Vehicle
WV	Wave mode

1 Introduction

Approximately one tenth of the world's population lives in coastal zones (Evans, 2004) where human activity and rising global sea levels are intensifying natural processes such as erosion and flooding. Coastal cliff environments are also constantly under siege from littoral zone processes and the predicted impact of climate change will only increase these risks. An Environment Agency climate report by Howard et al. (2019) suggests the global sea levels might rise between 0.29 and 0.67 m by year 2100 and as much as 1.7 m by year 2300. To enable these areas to remain viable for human use, it is crucial to identify reliable and repeatable methods for monitoring of the coastal zones and understanding the processes that can be encountered within them. Coastal cliff areas are considered to be one of the key features of the shorelines, with numerous purposes, including providing habitat to flora and fauna as well as providing sediment for the nearby beaches. However they can almost be considered a major geohazard since they are prone to collapse, can cause accidents, and they erode and retreat, thus creating threats to the urban environment and infrastructure, and to natural protected areas (Young and Carilli, 2019).

The coastal zone in East Sussex, UK is almost entirely composed of Chalk formations, creating a variety of geomorphological features, including littoral platforms, cliffs, and landslides. Chalk, being a very weak to weak rock in engineering terms (compressive strength between 1 and 25 MPa), is especially prone to erosion and collapse, and its downwearing can be observed within a relatively short period of time. These properties make chalk a useful analogue, that can provide a proxy for other, more resistant, rock formations that are much slower to erode.

Chalk cliffs and adjacent platforms in East Sussex have been the subject of multiple studies and assessments of coastal zone erosion. This area, as with many others globally, experiences a variety of geological processes that threaten the coast, such as platform erosion, cliff collapse and landslides. A wide variety of methods are available for monitoring the erosion experienced within coastal zones, including laser scanning surveys, micro-erosion meters (MEM), walkover surveys and laboratory testing. All these require specialist equipment that can be costly, and the areas may not be easily accessible on foot. Coastal zones are also continuously affected by storms and high tides, which can lead to equipment damage, and may interrupt access to measurement sites. Additionally, it would be impractical and prohibitively costly to set up multiple equipment sites at frequent intervals along the entire coastal zone.

Platform downwearing is currently mainly monitored with methods including Micro-Erosion Metre (MEM) and terrestrial laser scanners (TLS); both of these require a trained professional to be on the site to record information. Remote measurements from airborne LiDAR instruments are also available, but they often need to be calibrated with multiple flights needed prior to the surveys which makes them expensive and requires trained operators.

Cliff collapses are generally catastrophic in nature, often leading to many tens or even tens of thousands of cubic metres of material failing almost instantaneously, with little or no warning, and so they represent a major natural geohazard. They can remove large sections of cliff top land (up to several metres wide) in a single event, and the moment of their occurrence is very difficult to predict. Often, it is multiple coupled processes that ultimately lead to cliff failures, for instance, wave cut notch development with prolonged and heavy rainfall. These processes impact in different ways, and over differing spatial and temporal extents, but eventually leading to the rock structure weakening and finally failure. Even when these processes are well advanced, it is still difficult to pinpoint the moment when such a collapse will happen, and which combination of natural processes will finally trigger it.

Landslides are naturally occurring, gravity-driven movements of rock mass, debris or earth down a slope (Cruden, 1991). Coastal landslides are considered as complex erosional systems, since they are caused by multiple factors, including erosion caused by wave action, and they are dependent on local stratigraphy, structure, and hydrogeology (Bromhead, 1978). In the case of landslides within chalk strata, they most commonly occur where Gault Clay crops out at the base, creating a slip surface along which landslide movement can develop. Such landslides have been observed and monitored for many years, heavily relying on manual mapping during field surveys in the past, with increasing focus on aerial imagery mapping in recent days. Such monitoring and measuring techniques, as well as equipment needed at the sites are dependent on the weather and tides, can induce safety risks and can be prone to errors.

The use of Interferometric Synthetic Aperture Radar (InSAR) for monitoring geological processes is now well established and has been documented for more than 30 years (e.g. (Massonnet et al., 1993); (Gabriel et al., 1989)) but, due to the initial cost of data, limited spatial resolution and temporal sampling, and the east-west viewing geometry, InSAR technology has not been considered for monitoring coastal areas until very recently. This dramatically changed in when the European Space Agency's (ESA) launched Sentinel satellites -1A (2014) and -1B (2016), which provide near global observations with a repeat time of 6 days and all Sentinel data are freely available to the public under the Copernicus programme. These SAR sensors operate independently of sun and weather, giving information about Earth processes without disturbance from rain or lack of sunlight; importantly these data allow ground monitoring without need for any in situ instrumentation. Thanks to recent advances in data processing, these data can deliver ground movement information accurate to within the millimetre scale (Scoular et al., 2020a), and now provide 4+ years of potential monitoring and analysis of the coastal processes, within which time several chalk cliff failures have occurred. Their data also provide information for monitoring platform downwearing, a key factor in coastal landslides.

When considering coastal cliff failures and landslides, the application of InSAR has the potential to become a highly beneficial tool that is complementary to existing data and current coastal monitoring methods. It can aid coastal engineers in better understanding coastal processes and can provide useful information on erosion rates, as well as expand knowledge of cliff instability in more detail than was previously achievable.

This study is focused mainly on areas within the UK that have chalk strata, including the cliffs of East Sussex, Folkestone Warren in Kent, and Ventnor town on Isle of Wight. Coastal chalk areas have been chosen as a study material because the erosional and weathering results can be seen within a MPhil timeframe (3-5 years). Chalk that crops out in the East Sussex area between Brighton to the West and Eastbourne to the East, outcrops in both urban and rural areas, making it an excellent and varied environment for this study. These areas are also known for the active rotational slope failures which occur there.

1.1 Research aims and objectives

The aim of this research is to investigate and understand how InSAR can be used to monitor and analyse changes in the coastal zones caused by natural processes, and to consider the impact this has on cliff instability, large landslides and more generally on the littoral zone. This requires careful interpretation of InSAR results and linking them to natural processes and geohazards. The Persistent Scatterer Interferometry (PSI) methodology is used, with data from Sentinel-1 satellites and applied to coastal areas to provide better understanding of the spatiotemporal characteristics of coastal processes. The methodology is used with goal of helping to monitor, analyse and interpret ground deformation rates and mechanisms that lead to the coastal erosion. InSAR data from the Sentinel1 satellites provide regularly acquired images with a short revisit period and coverage of large areas of interest; this has rarely, if at all, been achieved for the majority of coastal events examined in the past.

The specific objectives include:

- Collection and processing of the 4+ years of available data for coastal areas, including:
    - The chalk coast between Brighton and Eastbourne, which covers both urban and rural environments with landslides, platform downwearing and cliff collapses;
    - Isle of Wight, Ventnor Undercliff landslide. This is an urban area of an active landslide with chalk strata, underlying Gault Clay; and
    - Folkestone Warren in Kent. Another urban area with an active landslide, with railway tracks running through the middle, also with chalk strata being the main component.
- Analysis of the processed data, with main focus on:
    - Platform downwearing monitoring and analysis of speed of platform erosion in both urban and rural areas;
    - Cliff failure monitoring and assessment whether it is possible to predict the failure with use of the InSAR data;
    - Landslide monitoring and analysis of the landslide movement with PSI data; and

- Investigate how InSAR can be used to better understand and interpret coastal processes, leading to understanding the past, current, and potentially future rates and mechanisms leading to coastal erosion and cliff collapse.

1.2 Thesis structure

This thesis is organised into eight chapters, the first one being the current **Chapter 1**, providing introduction and setting out the scope for research.

Chapters 2 and 3 form a background review of the literature focusing on chalk in coastal environments and Earth Observation (EO) technology with particular emphasis on InSAR.

Chapter 2 provides an overview of the coastal chalk environments and processes observed in coastal areas. It discusses chalk deposition and lithostratigraphy, as well as its mechanical properties. The geomorphology of coastal areas is described, including cliff shorelines and littoral platforms. The morphology and processes associated with coastal areas is also discussed. Understanding the rock formations of coastal environments and natural processes present is crucial for the interpretation of InSAR data which is the key element of this thesis.

Chapter 3 focuses on the theory associated with InSAR and the Persistent Scatterer Interferometry (PSI) methodology that has been applied in this research. It reviews PSI, explaining the procedures that have been developed for the purpose of this research. It also explains the approach to data processing for each of the coastal processes discussed in next chapter.

Chapters 4, 5 and 6 present the results of data processing and interpretation.

Chapter 4 focuses on coastal cliff collapses that have been analysed during this project. It discusses the attempt at monitoring cliff collapses near Birling Gap (TV 55384 96110) in East Sussex, UK. It reviews monitoring techniques that are currently used for cliff collapses as well as the methodology used for analysing the case studies within this research. Each study region is described in detail, specifying where and when the collapses have occurred, followed by presentation of the processed results and their interpretation. It also presents a discussion of the meaning of the results in each case.

Chapter 5 describes three active coastal landslide case studies withing the United Kingdom. It includes landslides in rural and urban environments: Cow Gap (TV 5959 9581), which is a rural landslide, and two active landslides that impact civil infrastructure: Folkestone Warren (TR 24988 38114) and Ventnor Undercliff (SZ 55944 77388). Conventional coastal landslide monitoring techniques are discussed and use of InSAR in monitoring landslides is reviewed. Each case study includes detailed description of the location and processes that occur in the area. Details of methodology used are described and results are discussed for each of the case studies.

Chapter 6 discusses platform downwearing processes and their monitoring using InSAR for the area between Brighton (TQ 31272 0418) and Eastbourne (TV 60749 98791) in East Sussex, UK. It starts by discussing current and past methods for measuring coastal platform erosion. The chapter then describes three case studies chosen and explains the intricacies of the PSI methodology used in each case. The results are divided by scale, into a regional overview with maps showing average movements of the south coast, and more detailed ground level changes for the research sites. It also presents the overall results of the platform downwearing monitoring and considers how this approach can be better used to interpret natural processes and their impact on coastal engineering.

Chapter 7 includes a discussion of the research outcomes, presenting the main results achieved. It also details specific results for each of the case studies within this MPhil project. It provides information on the accessibility and ease of use of the results for civilians and local councils, as well as discussing the next steps required to make certain elements of the approaches used more robust.

Chapter 8 summarises the main conclusions from the project and discusses recommendations for future research.

2 Coastal chalk environments and processes

Chapter 2 discusses the coastal environments and processes that are observed in coastal areas. It focusses on coastal chalk environments and discusses geomorphology of the coastal areas, cliff shorelines. It also presents hazards like collapses and landslides. The morphology and processes associated with shore platforms are also discussed.

Understanding the rock formations of the coastal environments and processes that are present within the areas of interest are crucial for the meaningful interpretation of the InSAR data that are a key element of this thesis. It would be very difficult to distinguish what the ground movement represents based on PSI methodology without the knowledge of rock formation properties, as well, as characteristics of coastal processes occurring within them.

2.1 Introduction

Coastal cliffs cover about 50% of the world's coastline. They are considered to be one of the key features of shorelines, with numerous purposes, including providing habitat to flora and fauna and providing sediment for nearby beaches, but they are also prone to collapse which can cause accidents and they are thus hazardous to people and infrastructure. Coastal cliffs can erode very rapidly, creating threats to the towns' infrastructure, as well as to natural protected areas (Young and Carilli, 2019). Evans (2004) estimates that about 10% of the world's population live in coastal zones, and human activity, combined with global sea level rise, can intensify the erosion of the coastal areas significantly. Current climate change reports suggests that by the year 2100, sea levels might be up to 0.63 m higher (Kendon et al. (2019), Howard et al. (2019)), which is only going to increase the risks to rural and urban areas.

Coastal chalk cliffs areas are especially prone to collapse and erosion because they comprise a very weak to weak rock; in that sense they make a useful target for this research in that their erosion can be observed within the short frame of a MPhil project (4 years). Such rapid erosion is especially dangerous to houses that are located nearby the coasts, but also to other infrastructure assets adjacent to the chalk, such as roads, water pipes lines, electricity lines, etc. Chalk cliffs and adjacent platforms in the UK have undergone multiple studies over the years to assess the erosion of the coastal zone. These areas, in common with many others all over the world, experience a variety of geological processes that endanger the coast such as platform erosion, cliff collapses and landslides. In addition, the chalk coast in southern Britain is an ideal short-term analogue for other rock types, which take a much longer time to erode or fail and would be much more difficult to study within the 4 years of the project life.

This chapter focuses on the character of chalk in a lithostratigraphic sense, its stratigraphy and location, as well as cliff collapse hazards that it is prone to. It also deals with processes that lead to cliff collapse, and the different collapse types that can be observed on chalk cliffs. Included in the chapter is also a description of landslides and their most common types. It also discusses shore platforms and their morphology, in addition to processes that occur on the platforms.

2.2 Chalk

2.2.1 Chalk deposition

Chalk distribution across Europe is highly influenced by the biogeographical provinces that existed during the Upper Cretaceous Period, called the Boreal Realm and the Tethyan Realm (Figure 2.1). In addition, the Atlantic Ocean opening up in the west, caused changes that led to the deposition of the Black Shale Formation at the end of Cretaceous Period. The Boreal Realm covered most of the North Sea and northern part of Europe – it was an area of cold water with good conditions for belemnites, however when the waters became shallower, they migrated towards the area now covering the British Isles. The Tethyan Realm left ammonites and planktonic foraminifera as the most common fossils of the area, which distinguishes the two biostratigraphies within Cretaceous deposits (Mortimore et al., 2001).

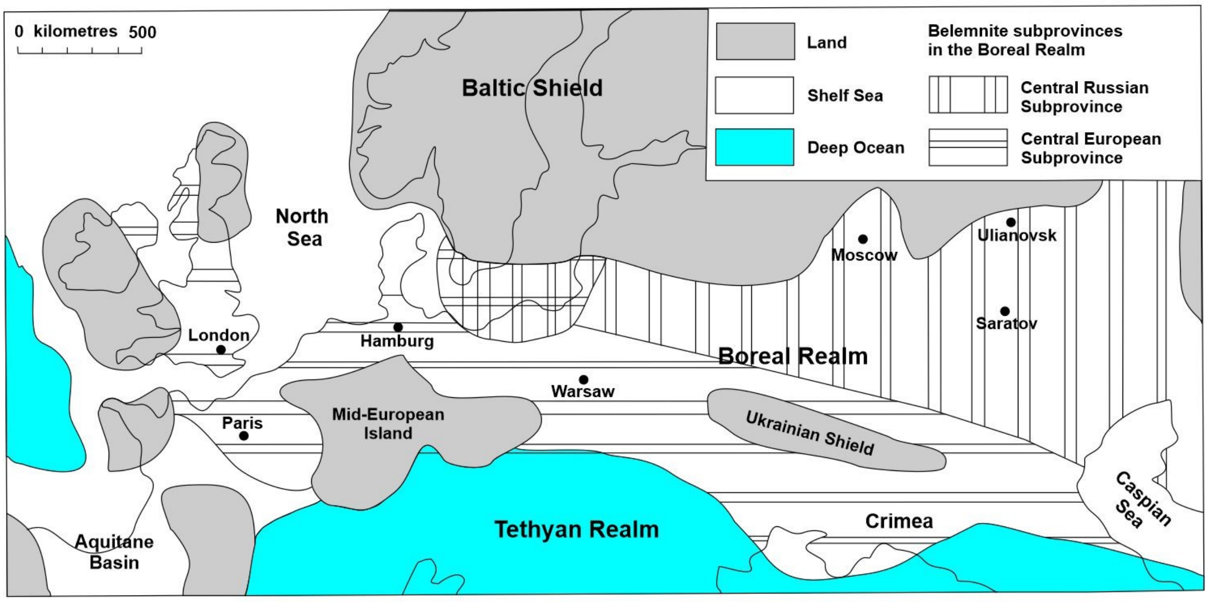

Figure 2.1. Late Cretaceous biogeographical provinces in Europe, adapted from Mortimore et al. (2001)

Because of those biostratigraphical differences, the British Isles can be divided into depositional provinces that are based on litho-and biostratigraphic variations. This has helped to distinguish two main chalk Provinces: Northern and Southern (Figure 2.2). The Southern Province connecting south-eastwards through the Paris Basin to the Tethyan Realm covers the area of South and North Downs, as well as Wessex; and the Northern Province being related to the northern Boreal Realm (including Lincolnshire and Yorkshire Wolds). Between them a region that shows characteristics of both provinces, and is recognised as a Transitional Province (covering Chilterns and East Anglia) (Mortimore et al., 2001).

Major tectonic changes occurred during the Late Cretaceous, accompanied by very high global sea levels. The African plate began to shear laterally and under-ride the southern edge of Europe, changing the tensional tectonics to a compressional stress field, which translated as strike-slip movements across the European Platform on Variscan structures. These tectonic stresses can explain the geometry of the chalk bodies like shelf marginal onlap and some of the anomalous stratigraphy that can be found in every province, as well as erosional channels and slumping (Mortimore et al., 2001).

Even though the sedimentation rates for the carbonates are considered to be slow, they still provide abundant evidence of tectonism, climate change and changes in the sea level. These global processes created solid foundations for local geological settings, such as isolated carbonate platforms and basins, as well as growth of fault controlled periclines that divide the European platform into active zones of deformation, while high sea-levels provided accommodation space required for sediment deposition (Mortimore, 2011).

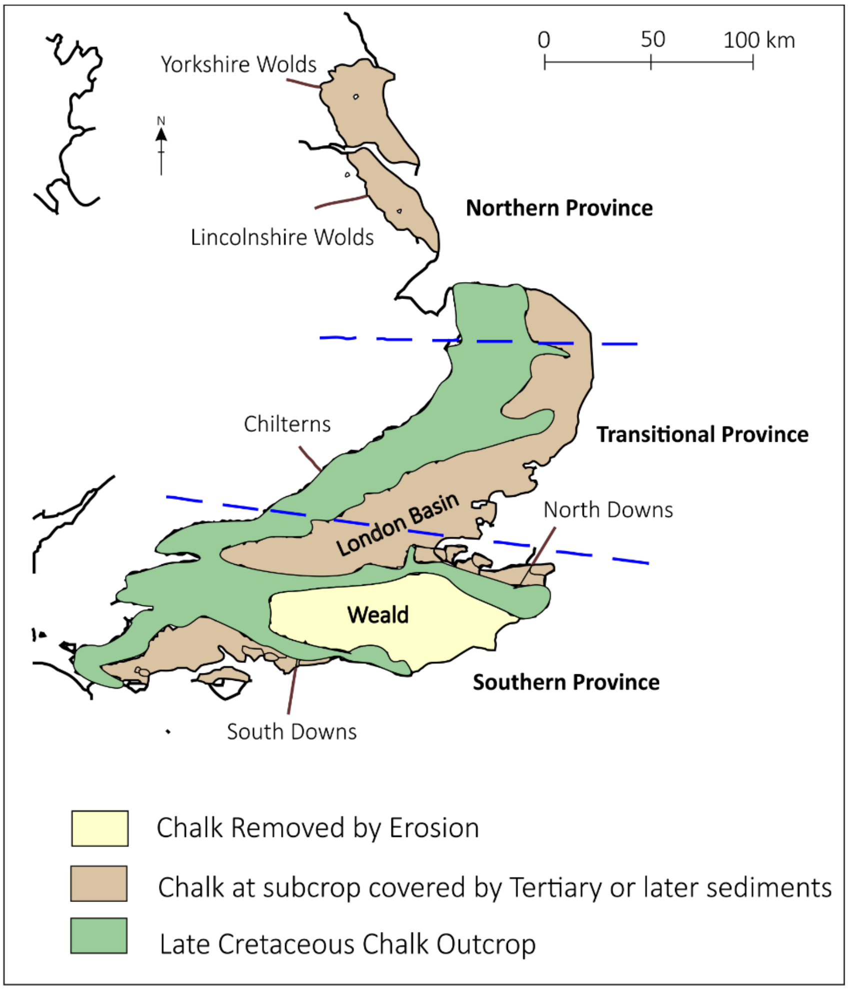

Figure 2.2. Chalk provinces in England, after Lord et al. (2002) simplified

2.2.2 Lithostratigraphy

Prior to the 1980s, every chalk province had its own lithostratigraphic definitions, depending on the characteristics of the rock and on the lateral changes within it, often made on the assumption it was not possible to correlate layers or marl seams between different geographical areas. However some pioneering work was completed in the early 1900s: Rowe (1900) discussed using marker beds like Bedwell's Columnar Flint that could be localised to East Kent only; Brydone (1912) proposed that the marl seams in the chalk cliffs of Newhaven and Brighton could be correlated with seams in Hampshire and also recognised changes in thickness of marker zones in Southern England (Brydone (1914) and Brydone (1915)); but then Gaster (1932) stated that there is almost no variation in the thickness of the Chalk zones in the South Downs. These views continued until Drummond (1967) publicised lateral variations within the Upper Greensand and the Grey Chalk Subgroup. At this time, White Chalk stratigraphy was still too rudimentary, especially since it was at the time considered to be a fully homogenous rock. Hancock (1975) identified that sea level change appeared to be a primary driving force for chalk sedimentation during the Upper Cretaceous and it was clear that more work was needed to be able to create reliable ground models of the Chalk distribution (Mortimore, 2011).

Mortimore (1986) in his "Stratigraphy of Upper Cretaceous White Chalk of Sussex" suggested a new approach to the lithostratigraphic scheme to simplify the differences between the many naming conventions. There are now two accepted lithostratigraphies for the Chalk Group in England, with the South Downs convention proposed by Mortimore et al. (2001), developed for Geological Survey mapping (Bristow et al., 1997) in the Southern Province and in the Northern Province, the lithostratigraphic scheme developed by Wood and Smith (1978).

In Southern England, the Chalk Group has since then been divided into two subgroups (Figure 2.3): the Grey Chalk Subgroup (formerly called Lower Chalk) and the White Chalk Subgroup (which now consists of former Middle and Upper Chalk Subgroups) (Mortimore, 2014).

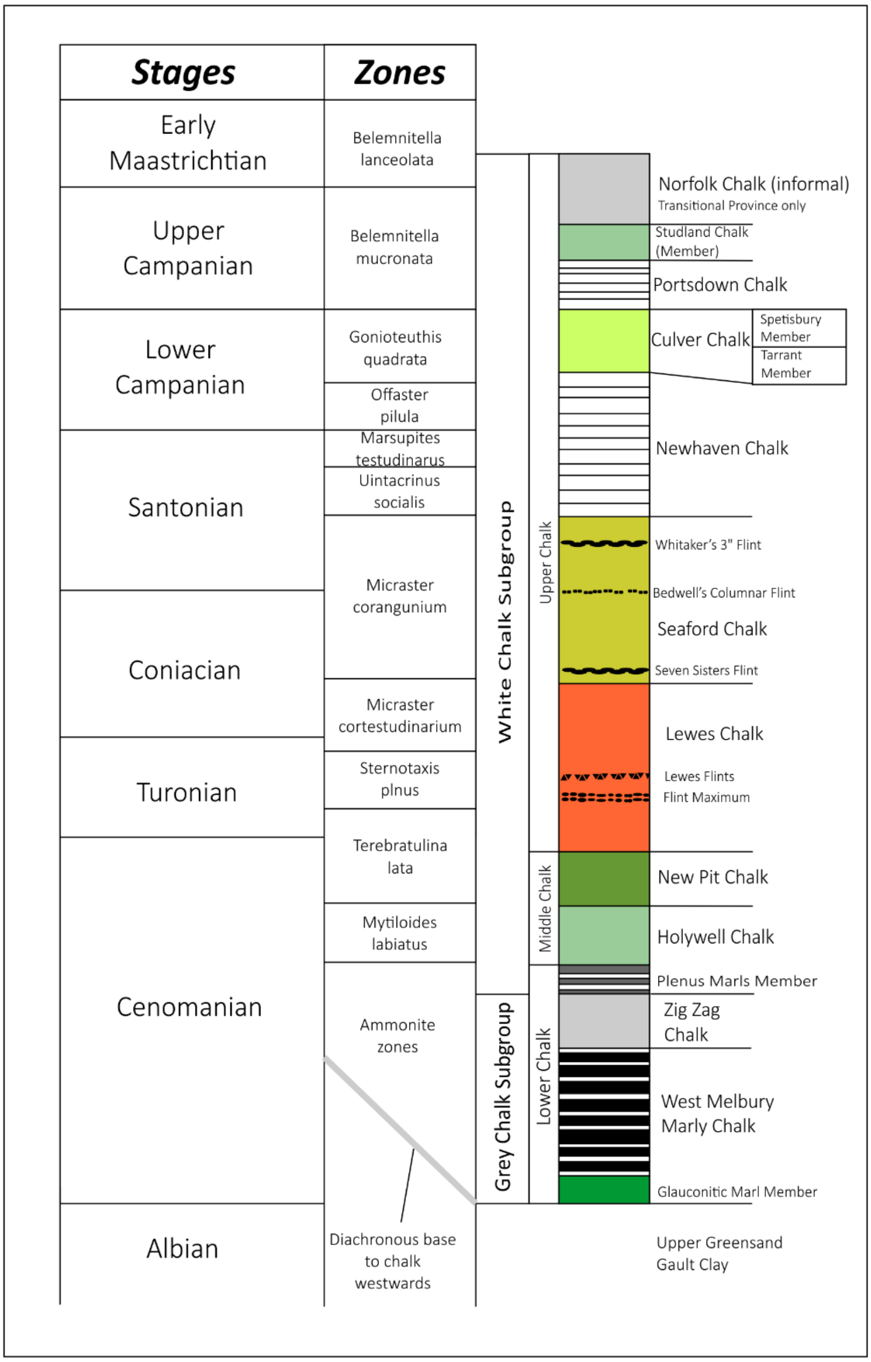

Figure 2.3. Lithostratigraphic column of the Chalk Group from Southern Province (after Mortimore (2014), simplified)

2.2.3 Lithology

Chalk consists of biogenic calcite, formed from the coccolithosphores (a pelagic nanoplankton that forms in the photic zone, where temperatures are favourable). Upon decomposition, the coccoliths settle from the water column to form a calcareous ooze on the ocean floor. Chalk deposition primarily occurred during the Cretaceous period, when the sea levels were covering a majority of Northern Europe (Hancock, 1975). The water depth most likely did not exceed 500 m (Clayton (1983), Bell et al. (1999)). British Chalk has a highly variable thickness, that sometimes represents the original depositional thickness but often erosion has removed a significant fraction (Bell et al., 1999). While some chalk strata contains only small amount of limestone (i.e. marly chalk, with only 20-30% of carbonate), the majority of chalk comprises almost pure calcium carbonate (between 95 – 98%), in a form of a low magnesium calcite (Lord et al., 2002).

During deposition, it is understood that chalk was mainly a granular substance, with some connected (bonded) parts as the coccolithic structures. When the coccoliths are intact within the rock, they form a high porosity deposit, with porosity up to 80% (Scholle, 1977), however it is unusual for them to survive intact during burial (Clayton and Matthews, 1987). In the British Isles, chalk porosity is usually close 30%, due to the consolidation of the calcific structures.

During the Cretaceous period, rising sea levels, warm temperatures, and high nutrient levels created favourable settings for the calcareous algae to evolve near the sea surface. Skeletal remains of those are the main components of Chalk deposits, as mostly sub-microscopic algae, but also consisting of some foraminifera with occasional macro-fossils including echinoids and bivalves (Buckley, 2018). Climate fluctuations mean the Chalk usually has rhythmic laminations that vary in colour and thickness, depending on the amount of clastic material (Hart, 1987). Chalks in Europe also often include layers of flint horizontal to bedding (very hard and brittle siliceous rock), on occasion they fill in fractures (Mortimore (2014), Lord et al. (2002)).

2.2.4 Chalk composition

Chalk is a visually homogenous biomicrite (Clayton, 1983), mainly composed of coccolithic skeletons (nannofossils) with small fraction of plankton like foraminifera (Scholle, 1977). White, pure chalk is usually made mainly of calcium carbonate (95 – 98%), while marly chalks will include only about 20 – 30% of carbonate (Lord et al., 2002). The existence of nannofossils within the chalk is what makes it fine – grained, as well as making it retain moisture, mainly by capillary attraction (Lord et al., 2002).

Within the British Chalk, clay minerals are present in small amounts (Hancock, 1975), and are represented by illite and sometimes montmorillonite (Lord et al., 2002). The texture of chalk mainly depends on the presence of coccoliths, as well as their species. Two different chalk formations can appear visually similar, with similar porosity, but a very different texture, in terms of the shape and size of calcite grains and their cementation (Lord et al., 2002). Flints are common, especially in the Chalk of Great Britain, either in tabular (flint sheets) or nodular forms. Flint is a hard rock made of silica, believed to form in chalk shortly after deposition. There needs to be an acid generated to start dissolving chalk (since it’s an alkaline rock) to allow the silica to precipitate (Lord et al., 2002). Dissolution can take place by the process of reduction of the bacterial sulphates in organic–rich sediments. The activity of the bacteria creates hydrogen sulphide, which migrates towards the interface between the seabed and seawater and there it meets previously dissolved oxygen. Once the oxygen and hydrogen sulphide meet, acidic conditions are created and silica can precipitate into a space where carbonate has dissolved, creating a flint (Clayton, 1986).

2.2.5 Mechanical properties of chalk

As it has been mentioned before, while chalk is sometimes considered as a homogenous material, every formation shows different properties and these are commonly used to classify chalk (Mortimore R. N, 2004). The geotechnical industry often uses a range of tests, resulting in so called index properties for chalk description and classification. Lord et al. (2002) claims that majority of the correlations between chalk's behaviour during engineering construction and its index properties are made based on the intact dry density measurements. The index properties and their ranges for the Chalk are listed in Table 2.1 (after Lord et al. (2002)). The strength and density is mainly dependent on the stratigraphic level and not depth of deposition as previously thought (Bowden et al., 2002). For engineering purposes, it is vital for descriptive schemes to be simple, consistent, and easy to repeat, as well as confirmed with laboratory tests. Intact dry density (IDD) is a simple and repeatable test that can be used as the groundwork for the descriptive scheme (Lamont-Black and Mortimore (1996)).

Table 2.1. The usual ranges for Index Properties of the Chalk, from Lord et al. (2002)

Property	*Symbol*	*Units*	*Range*
Dry Density	γ_d	Mg/m^3	1.29 – 2.46
Porosity	n*	%	9 – 52
Voids Ratio	e*	-	0.10 – 1.10
Saturated Moisture Content	m_{sat}	%	4 – 40
Calcium Carbonate Content		%	55 – 99
Specific Gravity	G_s	-	2.69 – 2.71
Liquid Limit	w_L	%	18 – 53
Plasticity Index	I_p	%	4 – 30
Liquidity Index		-	-2.25 – +2.50
Point Load Index	$I_{s(50)}$	MPa	0.01 – 1.15
Unconfined Compressive Strength	q_u	MPa	0.7 – 40
Slake Durability Index	I_{d2}	%	13 – 96

In Southern England, the Chalk is a dual porosity aquifer with porosity in the matrix and in the fracture network, which can increase the fluid flow within the rock and also can be linked to the deposit's solution and chemical replacement (Price, 1987). As chalk is mainly formed of coccoliths, it often has a high porosity but because of the small pore throats between coccoliths, fluid flow can be restricted and most of the flow occurs through fracture network and larger pores (Allen et al., 1997). Generally, the permeability of chalk reduces with depth, which commonly causes water aquifers to be confined to around 50 m below the water table (Lord et al., 2002). Conversely, fissures and fractures can highly increase the flow of fluids within the rock.

To assess the scale and type of chalk cliff instability, the density scale of Mortimore et al. (2004b) is adopted, which is much more detailed than the standard CIRIA scale (Lord et al., 2002) (Figure 2.4). Mortimore et al. (2004b) noticed that because of the sedimentary structure of chalk, there is an unavoidable cyclic variation in density and porosity caused by alternating Milankovitch Cycle couplets. Softer chalk formations, with lower density, show greater deviation from the line of Saturation Moisture Content (SMC) – IDD relationship. This can be explained by the ability of these softer chalk formations to lose or retain fluids more easily than other chalk formations.

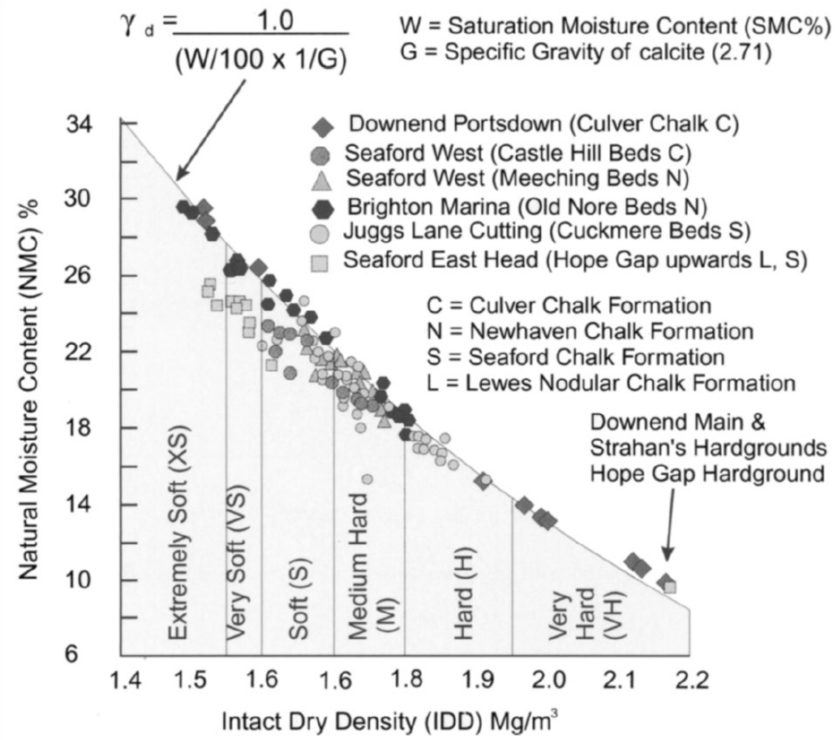

Figure 2.4. Saturation Moisture Content (y-axis) plotted against Intact Dry Density (x-axis) for chalk formations collected from cliffs and quarry faces, from Mortimore et al. (2004b)

2.2.6 Chalk classification

Geotechnical engineering works have long struggled to perform in situ testing of chalk materials and questioned whether such weak rock is suitable for shallow foundations. Then Burland and Lord (1970) presented results of plate loading tests from Munford (Norfolk, UK) showing that different elastic moduli can be correlated with the chalk quality seen in situ. This publication, along with Ward et al. (1968) and Wakeling (1970), was the beginning of what would be known as the Munford classification of chalk (Table 2.2).

This classification scheme depends on a correlation between SPT blowcount and chalk grade but in practice this has proven very unreliable due to its unpredictable relationship between the visual grade of chalk and blowcount. The Munford grades were devised by their authors to relate the structure of the chalk (hardness and jointing) to its deformation properties, for the specific requirements of the Munford site. Even though this caveat has been quoted multiple times, the Munford grades have come into common use since their publication.

Table 2.2. Classification of Munford site's chalk, from Lord et al. (2002) (after Burland and Lord (1970), Ward et al. (1968) and Wakeling (1970))

Grade	*Brief description*
*VI**	Extremely soft, structureless chalk containing small lumps of intact chalk
V	Structureless remoulded chalk containing small lumps of intact chalk
IV	Rubbly, partly weathered chalk with bedding and jointing. Joints 10 – 60 mm apart, open to 20 mm, and often infilled with soft, remoulded chalk and fragments
III	Rubbly to blocky unweathered chalk. Joints 60 – 200 mm apart, open to 3 mm, and sometimes infilled with fragments
II	Blocky medium – hard chalk. Joints more than 200 mm apart and closed
I	As for Grade II, but hard and brittle

**added by Wakeling (1970)*

Lord et al. (1994) acknowledged that a revised approach was needed for chalk classification to recognise its complex engineering properties. CIRIA PR11 identifies that a grade descriptor should be consistent between various disciplines, as well as simple and easy to identify and the CIRIA Grading Scheme (Table 2.3 and Table 2.4) has been created for this purpose. It recognises four main factors that affect chalk mass behaviour: intact chalk hardness, bedding and discontinuity spacing and pattern; and discontinuity aperture.

Table 2.3. CIRIA Chalk Grades, Lord et al. (2002)

CIRIA Chalk Grade	*Typical discontinuity aperture*	*Subdivision*
Grade D	structureless remoulded melange	Dm – comminuted matrix > 35% Dc – comminuted matric <35%
Grade C	> 3 mm	Suffix 1 – 5
Grade B	< 3 mm	Suffix 1 – 5
Grade A	Closed	Suffix 1 – 5

Table 2.4. Subdivision for CIRIA Chalk Grades A - C, Lord et al. (2002)

Suffix	*Typical discontinuity spacing*
1	t > 600 mm
2	t between 200 – 600 mm
3	t between 60 – 200 mm
4	t between 20 – 60 mm
5	t < 20 mm

2.2.7 Chalk weathering

Chalk weathering can be described as the degradation of intact chalk rock in response to mechanical and chemical processes at the near surface, with chemical processes causing weakening of chalk and mechanical processes creating more fractures within the rock (Mortimore, 2014). The chemical alterations usually reduce the rock density, but also soften its consistency to that of a putty, especially near the ground surface, around dissolution pipes, and at depth in weathered valleys, often causing problems in earthworks and embankments. Lawrence et al. (2013) also discusses the impact of sea saltwater weakening causing chalk cliff failures. Two main types of the salt weakening are recognised: haloclasty, which is a result of crystallisation of salt; and chemical weathering. Chalk also undergoes weakening due to the impact of rainwater, river erosion, glacial and periglacial conditions and plant growth (Lord et al., 2002). During winters, chalk is often exposed to freeze-thaw action and rapidly breaks down into angular blocks within a matrix of fine grained material (Lord et al., 2002). Conversely, there are instances when weathering can cause the chalk to strengthen, such as when groundwater dissolves calcite from one horizon and reprecipitates it as an overgrowth cement that fills the pore space elsewhere (Mortimore, 2014).

2.3 Coastal processes observed in chalk formations

2.3.1 Cliff definition

While cliffs aren't always located at the coast, this section will focus on coastal cliffs and their classification. Coastal cliffs can be described as steep slopes (>40º), normally characterised as an uncovered escarpment on a coast (Emery and Kuhn, 1982). Cliffed shorelines also present steep slopes that usually rise abruptly from the water or from the back of a platform, and are sufficiently narrow for the slope toe to be disturbed by storm wave action (Davidson-Arnott et al., 2019). They can be formed from softer rocks, like chalk or till, through sandstone to harder cliffs deposited as limestone or even granite or basalts (Davidson-Arnott et al., 2019), which form the strongest and most resistant cliffs. In hard rocks, like basalts or granites, the recession of cliffs occurs very slowly, at millimetres per century. Soft rocks, like glacial tills, weak sandstones or chalk can rapidly recede under wave action eroding the toe and removing eroded debris from the platform. Recession in very weak to weak cliffs can be on the order of centimetres or even metres per year (Davidson-Arnott et al. (2019)). The speed of recession in very weak to weak rocks, like chalk, offers the opportunity to study the erosional patterns and cliff evolution, providing a short-term analogue for other hard-rock slowly eroding rock cliffs.

Emery and Kuhn (1982) discuss three main stages for coastal cliffs erosion: active, inactive and former. The active stage is when the cliff face is continuously exposed to marine and subaerial processes. During the inactive stage the front of the cliff is commonly covered with a sloped talus (of 25-30º), often vegetated with small bushes or even trees. The former stage for a cliff is defined by marine processes no longer working on the cliff to erode it, and when the deposition of material in front of the cliff face is caused by subaerial erosion.

2.3.1.1 Cliff morphology

Davidson-Arnott et al. (2019) describes the major morphological components of cliffs as follows (Figure 2.5):

- Tableland, an area on the top of the cliff that extends inland;
- Cliff top (or crest), the part of the cliff that shows the slope change (from tableland to the cliff face);
- Cliff face, the area of the cliff that spreads from the cliff top to the toe and is the area that's controlled by erosion. In the case of plunging cliffs, the cliff face goes below the water level;
- Cliff toe, the part of the cliff which creates the transition from the cliff face to the shore platform and beach. It is considered that the upper limit of the cliff toe to be marked by the height that can be reached by the wave action and its lower limit to be the connection with gently sloping shore platform;
- Shore platform, an area extending from the cliff base to the point that is at the level (or just below) the spring low tide; and

- Nearshore slope is formed below the water level and is an addition for the intertidal platform. This is also the area where the waves are breaking.

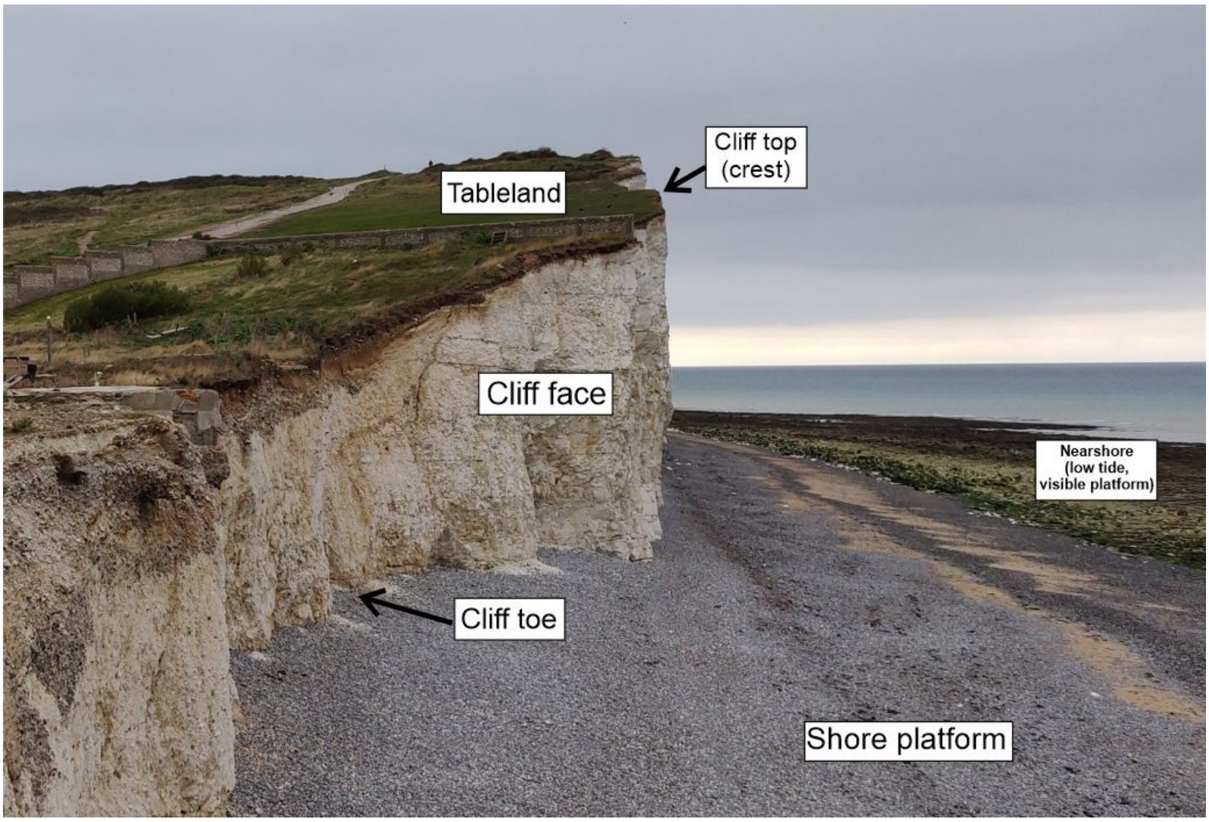

Figure 2.5. Main morphological components of a cliff

It is worth noting that not all cliff components are present in all coastal cliffs. Usually the cliff height will be more than the maximum height of the wave run-up and overtopping (Davidson-Arnott et al., 2019).

Three major types of cliff profile can be distinguished; plunging cliffs, cliffs with sloping shore platform and cliffs with horizontal shore platform (Davidson-Arnott et al., 2019). Plunging cliffs have the platform and nearshore under water, with waves breaking directly onto the cliff face. They are usually present in strong, resistant rocks and erode very slowly. Cliffs with sloping shore platforms have their toe above the intertidal zone or just within it. In this case, erosion of the cliff toe can occur and lead to cliff recession, creating a shore platform as the cliff face recedes.

Masselink et al. (2014) defines cliff morphology with a morphodynamic model (Figure 2.6). Two main cliff formation processes can be distinguished: subaerial and marine. Cliff evolution is mainly related to the erosional processes that remove rock material from the cliff face or platform, by either marine or subaerial processes (Davidson-Arnott et al., 2019). Cliff recession is a measure of the retreat of a point on the cliff face, usually horizontally and in the direction of the land, and is expressed as a rate (i.e., m a^{-1}).

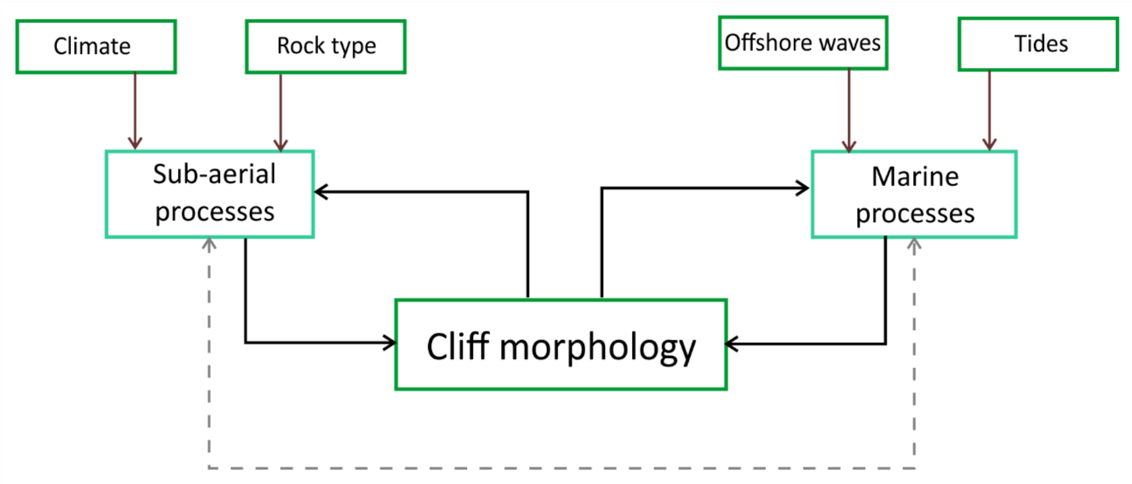

Figure 2.6. Coastal morphodynamic system with main coastal processes. Adapted from Masselink et al. (2014)

Figure 2.7 shows a schematic profile of a cliff system where the marine and sub-aerial processes are marked on (from Castedo et al. (2012)).

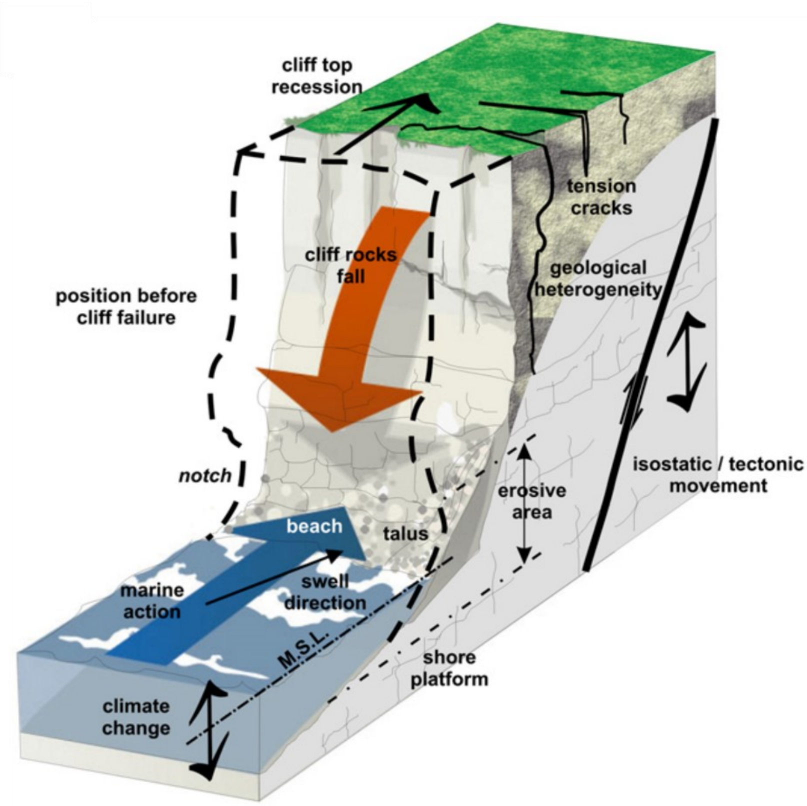

Figure 2.7. Schematic profile of a cliff system with coastal processes affecting it. From Castedo et al. (2012)

Marine processes work predominantly at the base of the cliff and lead to both erosion and the transport of eroded material away from the cliff. Its principal effect is to erode a wave-cut notch at the base of the cliff, removing support for the material above the notch and ultimately causing collapse of the cliff above; followed by erosion of the debris from the shore (Lim, 2014). The extent of cliff erosion is controlled by the nearshore platform profile gradient and the beach sediment thickness (Trenhaile (2005)), due to the vicinity of the waves breaking on the cliff face. Protection for the cliff can be created by the presence of a shore platform under a thin layer of sand (Trenhaile, 2016). Sediment allocation is an important erosion factor, since the longshore sediment transport can contribute to the width of the beach in front of the cliffs (Sunamura (1976), Sunamura (1992), Carpenter et al. (2014)). Sea level changes are one of the most important elements in the long term stability of coastal cliffs: there has been approximately 130 km of coastal retreat in the last 18 000 years and a sea level rise of 130 m (Lim, 2014) – i.e. 1 m erosion for every millimetre of the sea level rise. It is expected that with sea-level rising more rapidly every year, and with increasing storminess, erosion rates will accelerate (Walkden and Hall, 2005). Marine processes are usually cited as the major cause of coastal erosion, but subaerial processes also have a very significant impact.

Subaerial weathering and gravity act on the cliff face leading to small-scale collapse. The exposed surface of a cliff face is subjected to subaerial weathering, principally by rainfall. Rain drops wear down the exposed surfaces and cause many cliff failures (Lim, 2014). The continuous wetting and drying of the rocks, causing expansion and contraction of minerals within the rock, gradually weaken the cement of the rock and widen the fractures and discontinuities (Trenhaile (1987), Coombes (2014)). However, geology should always be considered (Mortimore et al., 2004b) because water flowing through the rock can dissolve or remove the material within the cliff, which then causes weakening of the strata, often focused along pre-existing planes of weakness. Another process that can affect the strength of cliffs is saltwater weakening. It can affect the rock physically by the growth of salt crystals, and through chemical weathering by salts, as well as by dissolution (Lawrence et al., 2013). Thermoclasty, the action of warming and cooling of the rock, can also initiate rock breakdown through the contraction and expansion of minerals due to the change in temperature (Hall and Thorn, 2014). There appears to be a positive correlation between the swelling and shrinking of the coastal zone rocks and temperature changes, especially when there is no rainfall (Hemmingsen et al., 2007). Other subaerial processes that act on the cliff face include mass movements like slides, flows or creep; and transport processes that are caused by water on the slopes, be it from wave or rain splash and overland flow or gullies. The eroded cliff face material is then transported down slope and deposited at the cliff toe for a short period of time. That sediment can provide short term protection for the cliff base from the waves , and if enough debris has accumulated, erosion of the toe might stop (Davidson-Arnott et al., 2019).

Pethick (1984) discusses several different approaches to describe the processes that cause cliff erosion, starting with factors described in Shepard and Grant (1947) that include:

- Hardness of the rock;
- Structural weakness;
- Configuration of the coastline;
- Solubility of the rock;
- Height of the cliff; and
- Nature of the wave attack.

King (1972) describes the factors in a more qualitative way, including:

- Corrosion, in terms of chemical weathering by salt;
- Corrosion, with mechanical weathering (abrasion);
- Attrition, which is a breakdown of debris created by erosion; and
- Hydraulic action, where variations of pressure caused by waves create removal of blocks.

Davies and Clayton (1980) and Clark (1979) discuss six processes that can amplify the processes described by King (1972):

- Quarrying by wave action, which removes loose rock;
- Abrasion, where currents induced by wave action move sand and other debris against the face of the cliff;
- Water-layer weathering, mostly relevant to the erosion of the shore platform;
- Solution of calcareous rock;
- Rock weathering; and
- Bio-erosion.

Walkden and Hall (2005) discuss how soft rock shores can be engineered to protect them from erosion, or how the erosion in these areas can be reduced. Protections like seawalls or groynes can be implemented to reduce the implications of a subaerial cliff recession which can in turn reduce platform downwearing. On the other hand, cliffs that are protected will create less sediment, potentially lowering beach levels the down-drift.

2.3.1.2 Hard cliffs

Hard cliffs are those created within hard bedrock that is highly resistant to erosion. When rock strength exceeds the forces of wave erosion, the cliffs will wear down very slowly, often just few millimetres per a century. The most resistant rocks to create cliffs are often made of limestone, basalt or granite. The erosion forces primarily destroy the bonds that provide the material strength needed to create coastal cliffs (Davidson-Arnott et al., 2019).

2.3.1.3 Soft cliffs

Cliffs created in soft, or weak rocks, like till, chalk or shales are eroded very easily. Wave energy is strong enough to erode the cliff toe quickly and then remove the debris. These cliffs recede very rapidly, sometimes on the order of decimetres per year (Davidson-Arnott et al., 2019).

2.3.2 Soft cliffs of the United Kingdom

The cliffs in the United Kingdom vary in height range, from scarp slopes just above the spring high-water level to rock cliffs that reach hundreds of metres above the sea level (Lim, 2014). This research focusses on chalk cliffs in three major locations:

- Chalk cliffs along the coast in East Sussex, from Brighton in the West to Eastbourne in the East;
- Area surrounding Folkestone Warren in Kent; and
- Several areas on Isle of Wight, including the town of Ventnor, the Needles in the West part of the island and small areas along the Military Road on the Western side of the Isle of Wight.

2.3.2.1 Cliff collapse hazards

The scale of the geohazards like cliff collapses will vary (Mortimore et al. (2001)) , depending on the chalk type, as well as on the lithology (overlying deposits), the height of the cliff and the rock structure (like faults, joints or folds). The cliff collapses in chalk are commonly controlled by fracture networks, since these in turn control the weathering, marine erosion, scale, and type of cliff failure. Coastal protection typically appears to slow the rate of the cliff failure but does not eliminate it completely.

Cliff collapses can be initialised much further inland than might be expected. Considering chalk cliffs have high porosity and are highly fractured, it is anticipated that the fracture network will extend away from the cliff face. The fractures can be filled with meteoric water with the rain precipitating through the network towards the cliff face, causing the cliffs to fail. This may explain the lag of several months between cliff collapse and increased rainfall. Busby et al. (2004) shows how a zone of influence above the cliff face affected by the collapse can extend inland (Figure 2.8). Measurements with azimuthal resistivity show that control sites located about 20 metres away from the cliff face, in Mesnil-Val (France) and in Birling Gap (UK), still present variations in coefficient of anisotropy. Control sites show almost as much variation as those very close to the cliff face (site A, 5 metres from the cliff face). There is also some seasonal variability. To properly identify and predict cliff collapse with remote sensing data, the chalk properties and collapse types. The collapse might not start at the cliff face but much further inland than expected because of the extensive fracture network in chalk.

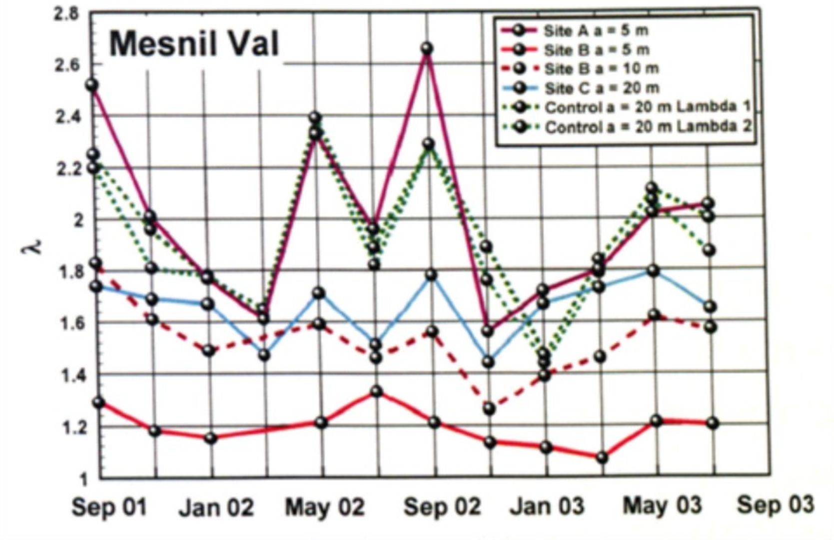

Figure 2.8. Variation of the coefficient of anisotropy (λ on y-axis) with time (on x-axis) at site of Mesnil-Val in France. From Busby et al. (2004)

Hutchinson and De Graff (2002) discuss the major coastal cliff sections in the United Kingdom, mainly of Upper Cretaceous sediments in Yorkshire, Devon, Dorset, Sussex, Kent, and Isle of Wight, although they recognise that the chalk cliffs of Yorkshire and Norfolk are very hard and not susceptible to collapse or chalk flow. the chalk cliffs of the Isle of Wight, Dorset, and Devon, are also hard to very hard and often reach a height of more than 100 m. The chalk cliffs in Sussex and in Kent are either medium or soft and can present some chalk flows along the cliff collapses. In Kent, Folkestone Warren is known for its deep-seated rotational landslide and numerous chalk falls.

Examples of major hazard classes are discussed in the section below, based on the analysis of the coastal line in Sussex by Mortimore et al. (2001), who classified 8 collapse hazard classes (see Table 2.5).

Table 2.5. Chalk collapse hazards classification. From Mortimore et al. (2004a)

Hazard	Description
1. Cliffs with single strata	
1a Simple vertical collapses	Vertical fracture sets control style of failure and height of cliff controls magnitude. Has limited run-out base of cliff
1b Plane and wedge collapses	Loose rock collapses controlled by complex system of conjugate joint sets: sometimes within part of the cliff, others involve entire cliff
1c Large rock falls involving entire cliff (partial flow slides)	Cliff collapse leads to long run-outs in which stratigraphic integrity of blocks is retained
2. Cliffs with more than one type of chalk formations	
2a Staged failure	Failure at top of cliff partly toppling, partly sliding
2b Staged failure	Failure of central mass mainly by complex multiple plane and wedge failures
2c Staged failure	Failure at the base of cliff by plane, wedge and complex rock interactions on fault zones
3. Spalling of chalk and flint	Volume of debris related to weathered state of chalk
4. Rotational slides	Weak mudstone strata at base of cliff beneath the Upper Greensand and Chalk
5. Mudslides from top of cliff	Mudstone formations capping the cliffs
6. Toppling of sandstone from cliff top	
7. Washouts of karst fills	
8. Slope failures in dry valley – fills or related rocks	Related to weathered state of the rock and material

2.3.2.1.1 Simple vertical collapses

Simple vertical collapses are most common in the Seaford Chalk because this formation is very pure and homogenous and has two distinctive near-vertical joint sets throughout the rock mass; this occurs when joints parallel to the cliff face start opening. Eventually the joint opens sufficiently that the unsupported rock column on the cliff face exceeds the tensile strength of the rock and a topple failure occurs. An abundance of powdered chalk is produced during this type of failure, since the rock fails very rapidly (Mortimore et al., 2004a), but the debris often retains some stratigraphy of the cliff face (Figure 2.9).

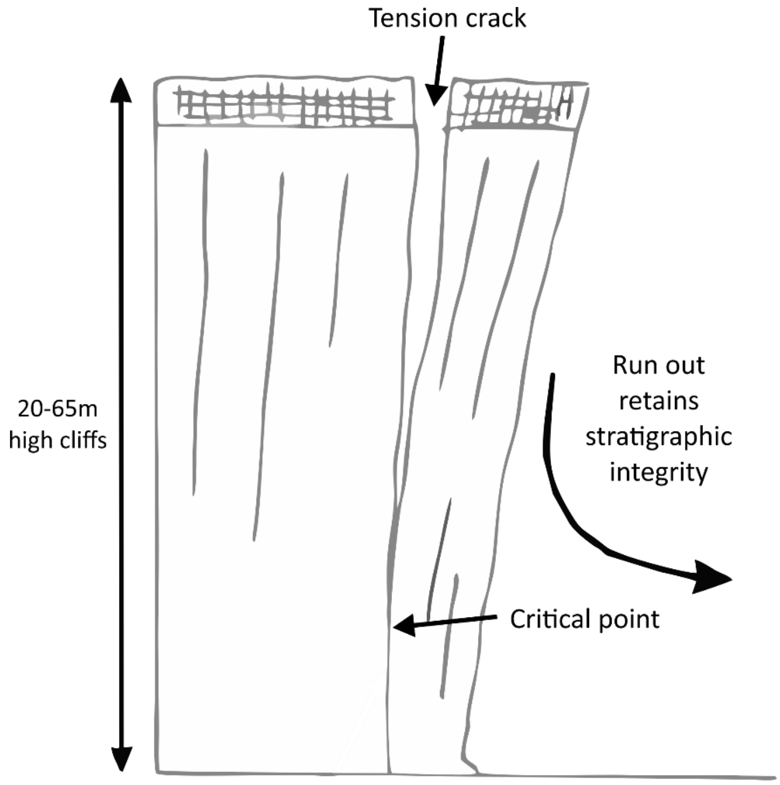

Figure 2.9. Simple vertical collapse failure, adapted from Mortimore et al. (2004a)

2.3.2.1.2 Plane and wedge collapses

Plane and wedge collapses are a type of collapse in which only one formation is usually involved, which has steeply inclined conjugate fracture sets that are prone to wedge failures. These types of failure commonly occur in Holywell Nodular Chalk, New Pit, Lewes Nodular Chalk and Newhaven Chalk formations. Failure starts on daylighting conjugate shear planes that exceed the critical angle of internal shearing resistance (commonly called the friction angle), as shown in Figure 2.10, with conjugate fracture sets dipping out of the cliff face. These failures often involve several tonnes of debris in every failure.

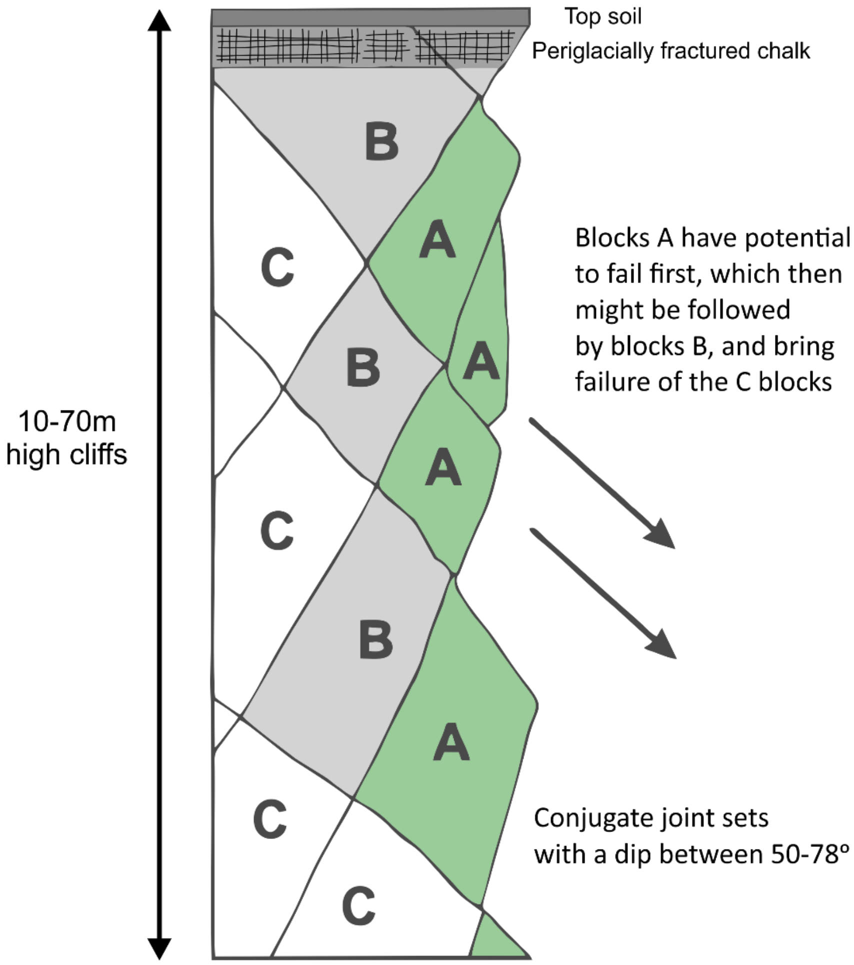

Figure 2.10. An example of a wedge collapse, adapted from Mortimore et al. (2004a)

2.3.2.1.3 Complex collapses

Complex failures are common and often occur when two or more formations are involved in the collapse. In this case the cliff can fail either as a whole, or parts of the cliff face fail on their own, with the failure mechanism dependent on the properties of chalk formation (Mortimore et al., 2004a). This kind of failure occurs at Beachy Head, the location of the tallest cliffs of East Sussex (Figure 2.11). The progressive erosion of the toe of the cliff leads to the chalk above it becoming unstable. It has been noted by Mortimore et al. (2004a) that the largest collapses tend to be focused close to the Beachy Head area, where New Pit, Lewes and Seaford Chalk formations are present within the cliffs, implying a strong lithological control on cliff failure, amplified by their great height.

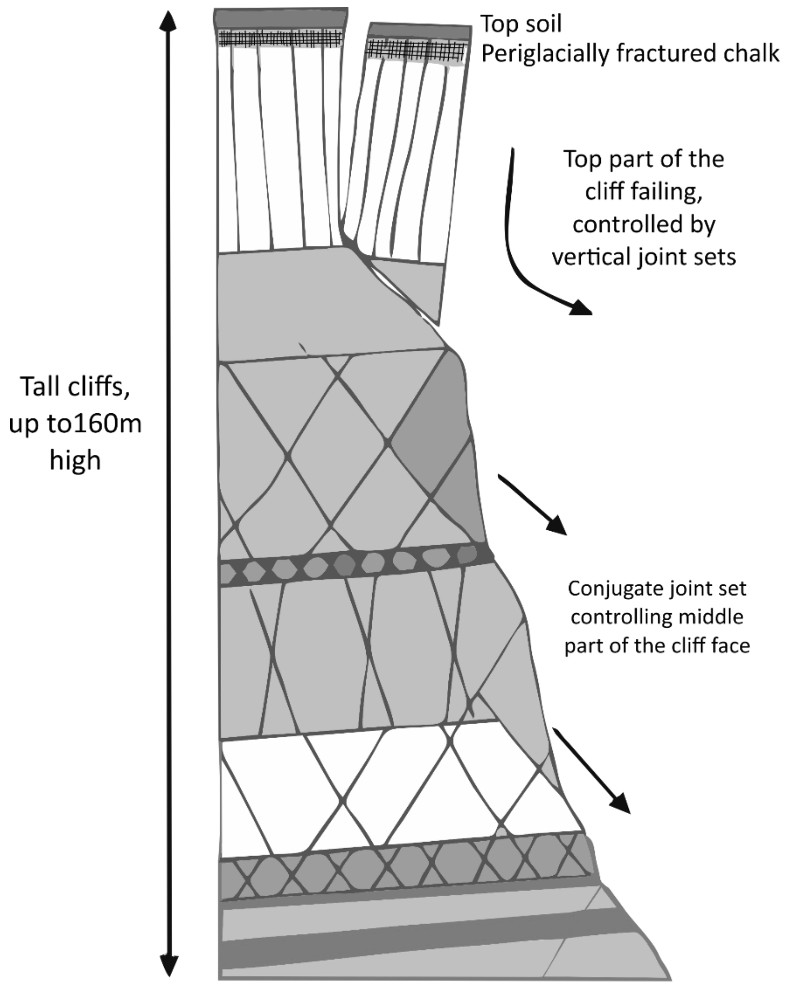

Figure 2.11. An example of a complex cliff collapse, modified from Mortimore et al. (2004a)

2.3.3 Landslides

Cruden (1991) defines a landslide as "a movement of a mass of rock, earth or debris down a slope". Varnes (1978) explains that landslides, or rather slope movements, can be categorised in multiple ways, based on factors including movement type, material type, speed of movement, development degree, geographic location, area geometry.

However, the main classification criteria should be based on the type of movement, and thus slope movement processes can be divided into five main types (Figure 2.12):

- Falls (or rockfalls);
- Topples;
- Slides;
- Spreads; and
- Flows.

A sixth group can be considered, comprising of a combination of two or more types of movements, and is called a complex slope movement.

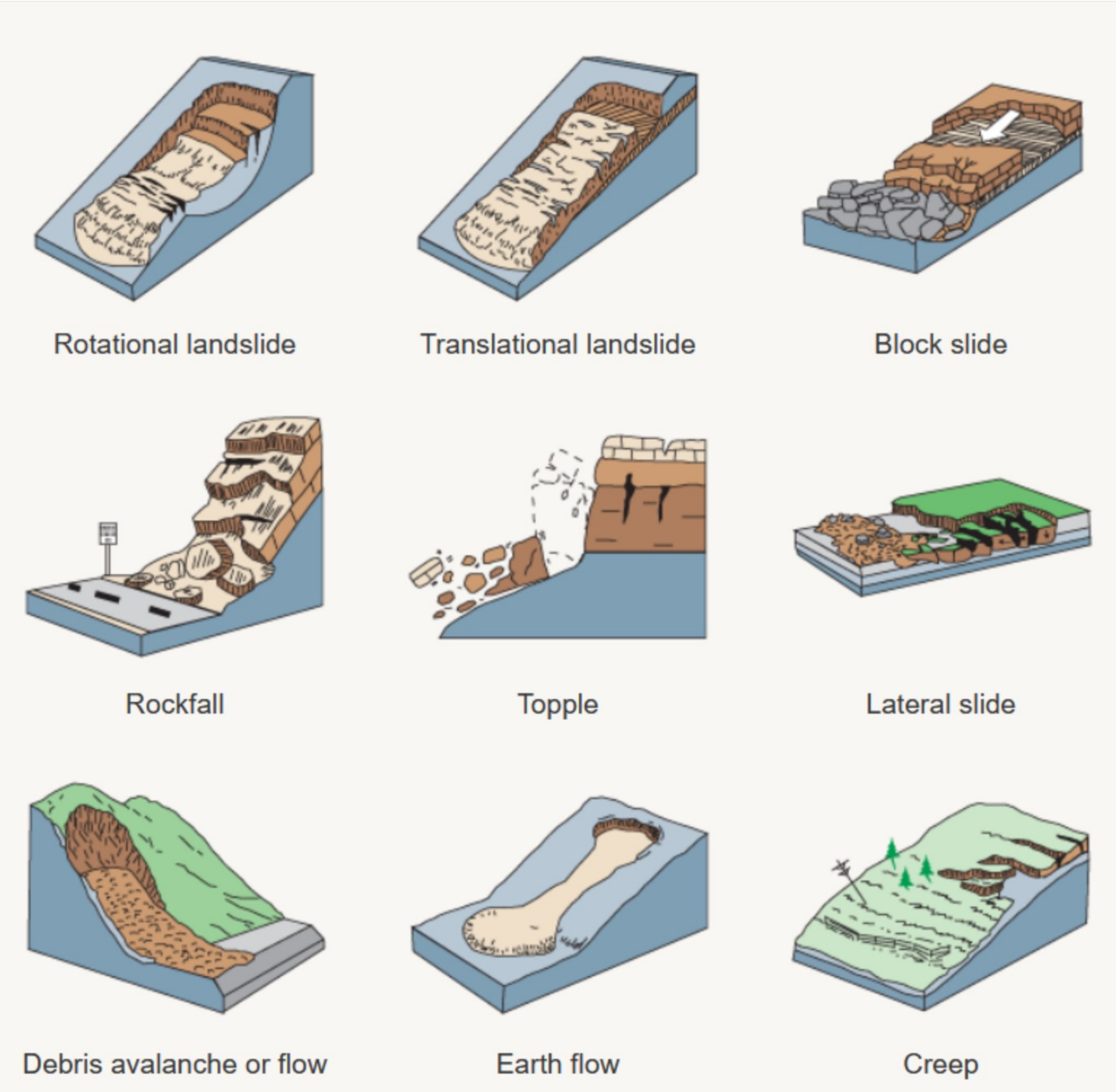

Figure 2.12. Types of landslides based on the type of movement (Crozier, 2006)

Falls happen quickly and are usually caused by the free-fall of a rock mass, as well as rolling or bouncing rock fragments (Resources Inventory Committee, 1998). The rock mass can be of any size and usually occurs along a surface on which no shear displacement is seen (Varnes, 1978).

Topples typically entail a rotation forward of a rock mass above a pivot point. They often occur in slopes that have a regular spacing of fractures that are parallel to the slope or more usually, dip slightly into the face of the slope (Wyllie (1980)).

Slides contain the movement along a surface, and can be divided into rotational and translational slides, based on the outline of the failure plane. The movement can be progressive, in terms of propagating from an initial area of failure further into a failure surface. Rotational slides (also called slumps) move along a failure plane that is curved, and commonly occur in mostly homogenous materials (Varnes, 1978).

Translational slides incur the movement of a rock mass along a plane, often involving movements of blocks of materials alone a failure plane. Frequently the failure plane is pre-existing (Resources Inventory Committee, 1998).

Spreads, or lateral spreads are primarily created by a lateral extension from tensile or shear fractures. They can be created as an inclusive extension from distributed movements, however without a well-defined plane of failure, or as movements that include fracture and extension of bedrock or soil due to liquefaction or plastic flow (Varnes, 1978).

Flows are a slope movement that are similar to a movement of a viscous fluid. Their velocity varies; however, it decreases laterally and with depth. One of the types of flow is creep, which occurs very slowly, with the rates of movement from cm a^{-1} to mm a^{-1} (Swanston and Howes, 1994).

Complex slope movements include a combination of several major types mentioned above. By definition, the complex failures can be considered compound, as compound landslides involve multiple failure surfaces of the same type or of different types.

This research will mainly focus on rotational slope movements (slumps), as they are very commonly present on the coast and easily accessible for field work. They are analysed in Chapter 5, and include a landslide at the Cow Gap location (grid reference TV 59599 95811), Ventnor landslide at Isle of Wight (grid reference SZ 56303 77552) and Folkestone Warren in Kent (grid reference TR 24907 38005).

2.3.4 Shore platforms

The shore platforms are rock surfaces, either horizontal or gently sloping (Masselink et al., 2014) and extend from the toe of the cliff to the seaward limit of the intertidal zone (Davidson-Arnott et al., 2019). They are considered to be erosional features (Masselink et al., 2014), created mainly by recession of the toe of the coastal cliff and are consequently modified by wave action that removes the eroded debris and weathering (Davidson-Arnott et al., 2019). Very often, the shore platform is associated with the cliff erosion, however the processes acting on it, are not always the same that cause the recession of the cliff (Masselink et al., 2014).

2.3.4.1 Shore platform morphology

According to Masselink et al. (2014), two major morphologies are generally being identified:

- Sloping platforms: with a slope angle between 0° and 5° that usually extend from cliff toe all the way to below low tide level. They tend to not have any major breaks within;
- Sub-horizontal platforms: these have a tendency to end in a low tide ramp or cliff. They can be supra-, inter- or subtidal.

There is some debate in the literature, in regards of the presence of different morphologies along the different environments. Trenhaile (1987) argues that the sub-horizontal platforms are most commonly present in micro- and meso-tidal regions, while sloping platforms are in macro-tidal environments. On the other hand, Sunamura (1992) explains that platform type development is more related to the rock resistance and wave action equilibrium. He clarifies that sloping platforms are more commonly found in weak rocks and under high energy wave environments, and sub-horizontal platforms tend to mature in stronger rocks and conditions that present lower wave energy (Davidson-Arnott et al., 2019). Other authors, like Davies and Clayton (1980) or Wright (1967) claim the platform morphology to be dependent on whether it has been developed in the northern or southern hemisphere. They explain that North American and British platforms seem to be wide and generally have a gentle slope to them, while Australian platforms are much narrower and often end rapidly with a small ramp. This, though can also be connected to the lower and higher tidal heights, which would support the discussion in Sunamura (1992). Trenhaile (1999) has discussed extensively the relationship between tidal range and the gradient of the platform, by comparing data from the UK, Canada, and Japan. He has found some confirmation to the connection between the sloping platforms and high tidal range (the UK), and sub-horizontal platforms that can be found around Australia's coasts, where tide height is usually low (Masselink et al., 2014).

When it comes to platform width, Moses (2014) explains that width is dependent on the amount of relative erosion between the edges of the platform at low and high tides, so the platform might widen or narrow throughout time depending on the erosion rate. If the so-called inner edge (where the high tide reaches) seem to retreat faster than outer edge (where low tide can reach), it may mean that the platform width will increase, at least until the waves can no longer reach the inner edge. A state of equilibrium can be achieved when the outer and inner edges are being eroded with the same speed, and the platform width stays constant over time.

The structure of the rock is another important feature that can determine the morphology of the platform. This includes the existence of joints, bedding planes and fractures within the rocks. The fracture patterns, as well as jointing can control the relief of blocks of rocks on the shore platform, and a spectrum of past and present wave sizes is responsible for the transport of those boulders along the platform's surface (Moses, 2014). Boulders produced this way are usually initially angular and become more rounded with weathering over time.

Moses (2014) discusses in "Shore Platforms of British Isles", the occurrence and role of the boulders on the shore platforms. She explains that the boulders that are present on shore platforms are mainly created either by cliff retreat or by platform erosion. The size of boulders that are created through cliff retreat processes is mainly associated with gravity, which seems to be the key driver for the rock falls. In the case of chalk cliffs, it is very common to see big boulders fracture on impact with the surface of the platform. This might not be the case for different lithologies, for example highly cohesive materials like till or clay will often have blocks released from the cliff that are bound by desiccation cracks forming while the face of the cliff dries. Most of the small to medium size boulders seem to cluster closer to the cliff face.

Some research shows that boulders and blocks that are created by platform erosion and downwearing commonly move in the landward direction, but steps on the platform may delay the movement (Henaff et al., 2006). In the British Isles there is very little research done on the dynamics of the boulder transport, be it platform or cliff derived. Moses and Robinson (2011) show that for the chalk coasts in the East Sussex, larger debris or boulders will stay on the platform for longer period of time, but it appears that the size of the debris is more important than the volume in controlling rates of removal. While some material will be washed out from the surface, much of it ends up filling the spaces between boulders that have been previously deposited on the platform surface.

Boulder removal, as well as the erosion of the beds that create steps in the platform, likely contributes to overall platform downwearing. The build-up of boulders on the surface can work similarly to rip-rap, by absorbing the wave energy and protecting the platform surface from the wave erosion (Moses, 2014). This process can lead to a concave shoreline, as beach sediments become trapped against steps and cause greater abrasion, coupled with the creation of a depression in front of the step (Henaff et al., 2006). The movement of the boulders on the platform's surface can cause its abrasion, however the contribution of this process to platform downwearing hasn't been investigated in detail (Moses (2014), Stephenson and Naylor (2011), Naylor and Stephenson (2010)).

2.3.4.2 Platform processes

Much of the discussion on shore platforms has focussed on mode of formation, debating whether platforms are created mainly by processes of weathering or wave erosion (Masselink et al., 2014). In the past, a shore platform was referred to as a "wave-cut platform", implying that wave energy is the only process responsible for the creation of shore platforms (Pethick, 1984). However, the majority of platforms will have both processes working on them, although it can be dependent on a location: sheltered platforms are less likely to be created by wave-cut motion, whereas high-energy wave environments will be expected to dominate their formation in those areas (Masselink et al., 2014).

Pethick (1984) considers the following processes acting on the shore platforms:

- Mechanical wave erosion, including abrasion;
- Weathering, including water-level weathering and sub-aerial weathering; and
- Solution.

2.3.4.2.1 Mechanical wave erosion

The surface of shore platforms are commonly abraded with the back-and-forth movement of sand grains (Blanco-Chao et al., 2007). Abrasion is often limited by the lack of the appropriate material, with sand grains often absent at low tide levels on the platforms (Pethick, 1984). However, wave action can work on these surfaces by creating wave shocks, air compression or wave hammers, processes that are often described as quarrying of the rocks. How effective they are depends on the lithology and rock structure. Trenhaile (1980) notes that the most commonly mechanically eroded platforms are those that exhibit gently sloping surfaces.

2.3.4.2.2 Weathering

Weathering can be divided into water-layer weathering and sub-aerial weathering. In the case of the former, alternate wetting and drying of the platform by tidal movements causes intricate weathering (Pethick, 1984) and is most effective in permeable and fine grained sediments (Trenhaile, 1980). This process requires low rates of mechanical erosion at rates similar to or lower than the weathering, otherwise the effects of water-layer weathering cannot develop. The sub-aerial weathering can potentially affect the rocks down to the level of permanent saturation and that material can then be easily removed by wave action (Bartrum, 1916).

2.3.4.2.3 Solution

This process is usually caused by the solution of the calcareous rock in the sea water. The platforms created by solution itself or solution and biological processes usually display smooth horizontal surfaces during the low tide (Pethick, 1984).

2.3.4.2.4 Platform erosion components and rates

Platform erosion can be separated into two components, vertical downwearing of its surface, which is usually measured in millimetres, and horizontal retreat of the steps, which may be measured in centimetres or metres (Moses, 2014). Some variation in the vertical erosion rates across platform surface has been identified by Moses (2014); she notes that the highest rates for downwearing are usually found at the top of the platform, close to the cliff toe, since that's where most abrasion of the surface with sediments usually occurs. Robinson (1977a) is one of a few, if not the only researcher who has studied the influence of the depth of the beach on erosion rates of the platforms. He has discovered that erosion rates are the highest in those areas where the depth of the beach is less than 5 cm, and in these cases the sediment is easily mobilised by waves to roughen the surface of the platform. For beach depths more than 5 cm, the sediment is too thick to be mobilised and so it protects the surface of the platform from erosion.

Seasonal variations in the erosion rates for platforms have also been noted, with rates usually being higher in the winter season (Robinson (1977b), Foote et al. (2006), Moses et al. (2010)). On top of this, Foote et al. (2006) suggested that chalk erosion is mainly caused by wave-driven erosion processes instead of subaerial weathering, since the observation that the platform downwearing is faster during stormy, cold winters than mild ones.

2.3.4.3 Shore platforms in the United Kingdom

According to Moses (2014), shore platforms in the UK are most commonly intertidal rock surfaces, gently sloping seawards and covered with water during high tide, but exposed to sub-aerial processes when the tide is low. Before the 1960s, there were not many research projects discussing the development of shore platforms in Great Britain, and they were mostly assumed to be created by wave-cut processes. Many British platforms end with cliffs that are above the high-tide sea levels, sometimes having a beach at their landward side or a man-made, engineering structure like a seawall. This is a case in East and West Sussex, where man-made coastal protections are very commonly surrounding the shore platforms. Most modern platforms in the British Isles show a sudden slope change at the landward end, often at cliff-platform connection, and they are commonly gently sloping, with a sub-horizontal surface (see examples on Figure 2.13), which is sometimes stepped. They can also have a beach on the upper platform and scattered boulders across the surface, occasionally gathered at the upper platform or on the beach (Moses, 2014).

Within the British Isles, particularly on the chalk coasts of the South-East England, flint contained within chalk becomes unconfined during erosion or cliff collapses to the beach surface. Due to the chalk being a weak rock, it is easily eroded which leaves flints, in angular shape, that are then rounded with time (Dornbusch et al., 2004). According to Dornbusch et al. (2006), in the coastal area of East Sussex, cliff erosion and its retreat, as well as platform downwearing contributes to adding close to 7700 m^3 of shingle per year.

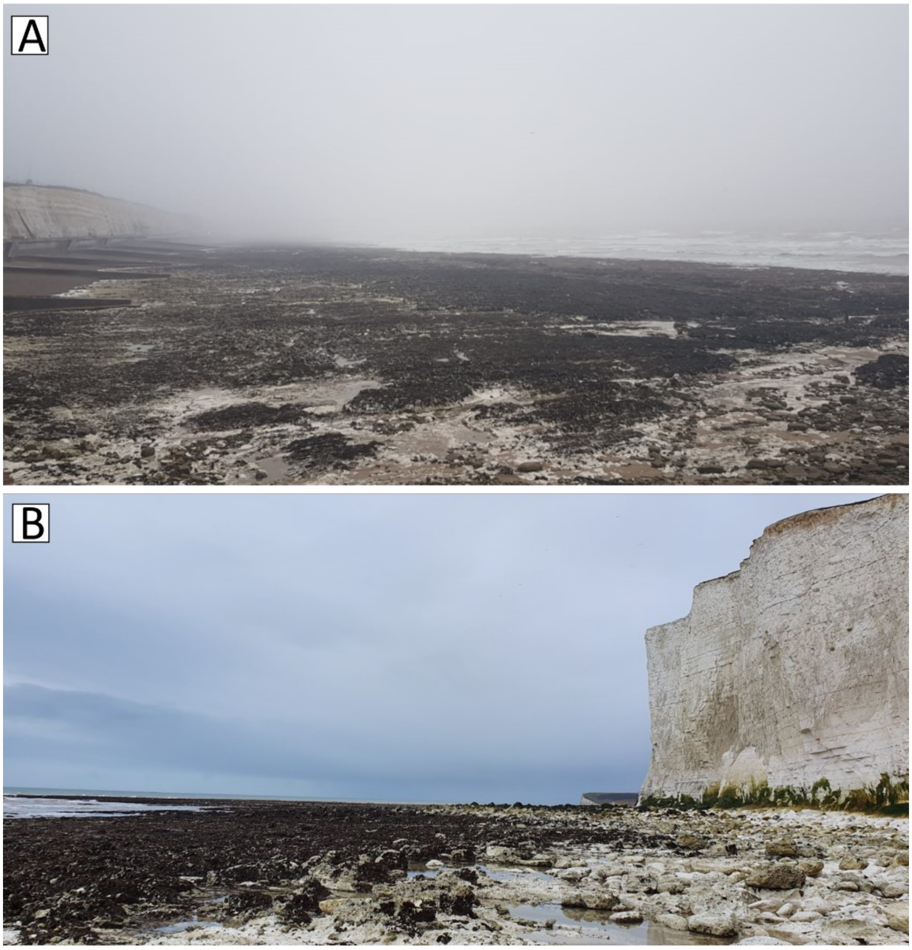

Figure 2.13. Examples of platform morphology from East Sussex. Figure A showing a platform in Brighton, close to the Marina (grid reference: TQ 34518 03029), with gentle slope and man-made coastal protection. FIgure B showing platform by Seven Sisters cliffs, near Birling Gap (grid reference: TV 53864 96678), with almost flat surface extending from the cliff face seawards, with no man-made protection.

2.4 Chapter summary

This chapter has discussed the coastal environments, in particular chalk coasts and the processes that are acting in the nearshore areas. It has provided an understanding of the chalk deposition and properties, as well as the main weathering processes that are encountered when analysing this rock formation. It has also focused on the coastal areas and their geomorphology, as well as processes and hazards that are active in these regions. The information included in this chapter is crucial for further understanding and successful analysis and interpretation of the InSAR data that are the main focus of this research.

The next chapter (Chapter 3) will discuss InSAR theory and PSI methodology, which have been used for the analysis of coastal and slope processes in this research.

3 InSAR methodology

3.1 Introduction

Chapter 3 focuses on the InSAR methodology that has been utilised for this research. It provides background on radar systems and Synthetic Aperture Radar theory, followed by a discussion on the PSI methodology and its applications in coastal environments and for monitoring of geomorphological processes, which are explored in Chapters 4, 5and 6.

3.2 Introduction to radar systems

Radar is a sensing system that uses electromagnetic waves for the detection and ranging of objects. Radar systems work by transmitting microwave energy from an antenna in short bursts over a period of time (Lillesand et al., 2015). Different radar sensors use different frequency bands, and the longer the wavelength, the further the sensor can penetrate through a dielectric material. Because of that, use of radar imaging is not limited by clouds, dust, or fog. Also, since it is an active system, it means that images are generated by illuminating an area with an electromagnetic pulse and what is recorded is an echo that is backscattered from natural, as well as man-made objects. The system can work independently of sun light and in any weather which makes the tool extremely valuable for Earth observation and remote sensing (Ferretti, 2014).

Radar is an active remote sensing system that collects information about terrain by sending microwave beams down to the surface and recording the strength of the signal reflected back to the sensor. Most radar systems acquire images in the X- and C- bands, but seven frequency bands are commonly used (Table 3.1).

Table 3.1. Most common frequency bands used in SAR systems, adapted from Moreira et al. (2013)

Frequency band	**Ka**	**Ku**	**X**	**C**	**S**	**L**	**P**
Frequency [GHz]	40 – 25	17.6 – 12	12 – 7.5	7.5 – 3.75	3.75 – 2	2 – 1	0.5 – 0.25
Wavelength [cm]	0.75 – 1.2	1.7 – 2.5	2.5 – 4	4 – 8	8 – 15	15 – 30	60– 120

A radar image is created in a continuous manner as a satellite (or an aircraft) moves along its flight path (Figure 3.1). While the radar system moves, microwave pulses are transmitted from the antenna to its footprint on the ground, which is illuminated by the radar beam pulse. Return signals from each pulse backscattered from surface targets are received back by the antenna, and are then processed and recorded (Liu and Mason, 2016).

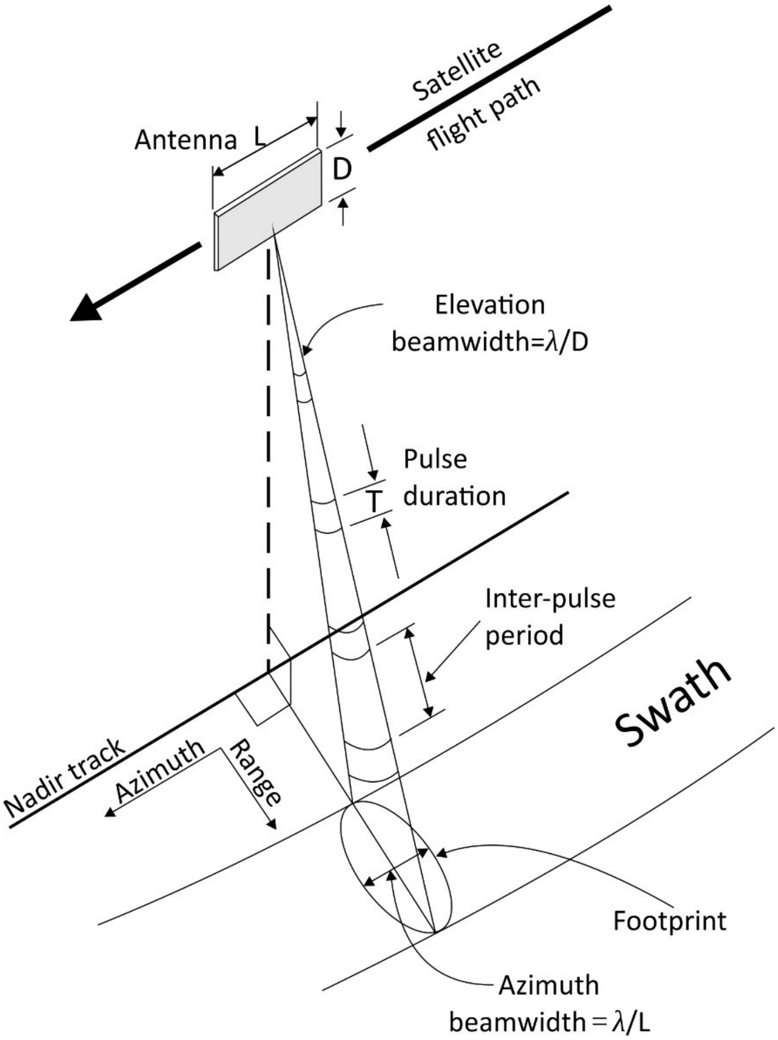

Figure 3.1. SAR imaging geometry, simplified from Sarmap (2009)

3.3 SAR definition and properties

Most imaging radar systems are configured to be side-looking because, being a ranging system, radar forms an image by recording the position of the return signal in time. Therefore, if the system was set up to see both sides of the platform symmetrically, it would cause the return signal from both sides at the same distance to be received at the same time, causing signal ambiguity. A radar image has two coordinates – in slant range and azimuth (see Figure 3.2).

The slant range perpendicular to the movement direction of the platform is equivalent to the two-way signal delay time, and azimuth is the direction of the image parallel to the movement direction. The delay time is measured between the pulse transmission and the reception of the backscattered echo from targets on the ground. From this delay, the distance between the radar and the ground can be established, as well as the target's location. The radar itself keeps moving along the flight path, transmitting microwave beam pulses, and scanning the one side of the path (usually to the right of the flight path). At the same time, backscattered signals are also being recorded. This way, the 2D radar image is created (Lillesand et al., 2015).

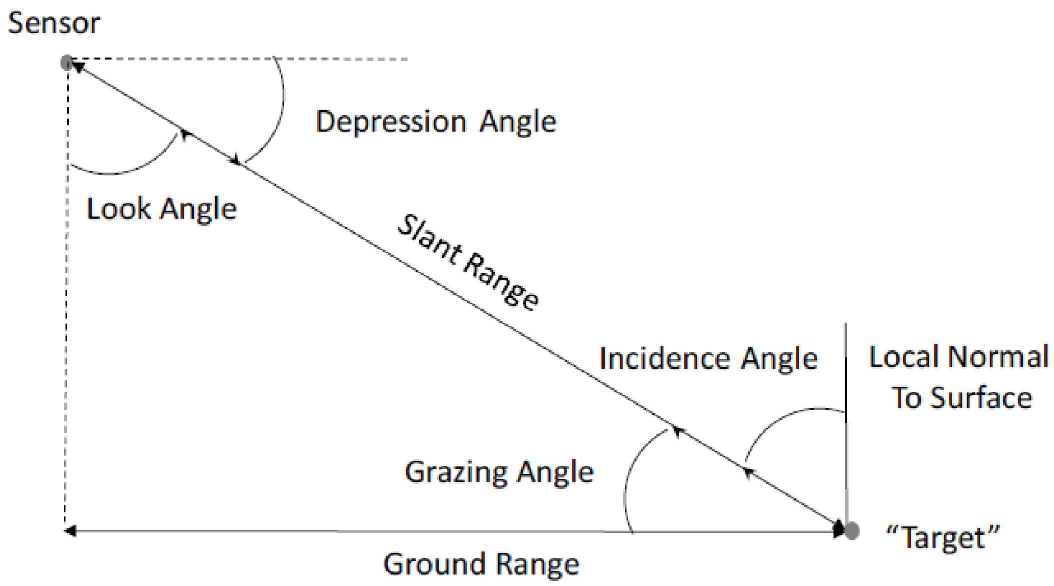

Figure 3.2 Radar imaging terms, from van Zyl (2011)

3.3.1 Geometry and resolution

3.3.1.1 Basic SAR imaging geometry

Radar images are acquired in strips, following the path of the satellite (or an aircraft), with the radar system mounted on them; referred to as swaths (or tracks). Two different directions can be recognised, the range direction also called across-track, and azimuth direction or along-track, as described in previous section. Range can also be divided into two different aspects – slant range and ground range (Figure 3.2). The ground range is the distance along the ground towards the scatterer. It's measured from the line that describes the position straight underneath the radar, also called the nadir track (van Zyl, 2011).

The look angle is another important term used when discussing radar imaging and is the angle between the vertical direction and the radar beam. If the curvature of the Earth's surface is ignored, the look angle will equal the incidence angle, which is the angle between vertical direction and the vector of the propagation of the radar wave at the surface. For spaceborne systems the Earth surface curvature must always be considered, since it causes the incidence angle to always be larger than the look angle for flat surfaces. By combining signals reflected from the target, objects on the ground can be illuminated multiple times by several radar pulses whenever the distance from the target is large enough (Ferretti, 2014). Once the signal is transmitted, the amplitude and phase of the surface backscatter are recorded by the radar. Rocky surfaces and man-made structures, like buildings and roads, have high amplitude and show as bright spots on the SAR images. The image is formed in the slant range and azimuth directions and must be transformed into ground coordinates.

There are several common scattering mechanisms that help in the characterisation of deterministic and random targets (Figure 3.3). They include as follows:

- Reflection and scattering from a surface. The main parameters of the radar backscatter are the relative permittivity (dielectric constant) of the target, the large-scale slope, and the roughness of the surface. When the surface is rough (in comparison to radar wavelength) the signal is then scattered, rather than reflected, meaning that the target is bright but a random scatterer, since the reflectivity is a random variable (as opposed to deterministic). Rough targets scatter energy in every direction, including back towards the radar. This means, the rougher the surface, the higher the scattering coefficient, although the larger the incidence angle, the smoother the surface appears to the radar.
- Dihedral reflection. When two flat surfaces are placed together at 90-degree angle, they form a dihedral. If both surfaces are smooth, they will create two specular reflections and will create a double bounce effect. This effect gives a strong backscattering coefficient for buildings with walls that are close to parallel to the satellite's trajectory (its azimuth direction), but the signal decays quickly when the signal is not reflected in a plane that's perpendicular to the dihedral axis. For a dihedral reflector, all the rays of a plane wave travel along the same path, hence they all reach the antenna in phase. This means that the phase value is dependant to the distance between the radar and the dihedral's axis. Double bounce scattering is also common in forested areas (when the radar signal can penetrate through the canopy), since trunks and terrain are often a very good double bounce reflector.
- Trihedral reflector. If a third plate is added to a dihedral reflector, orthogonal to the two other surfaces, it creates a trihedral (or corner) reflector. This most commonly occurs in urban environments, where man-made targets are present. Triple-bounce mechanism gives a broad Radar Cross Section (RCS, which is the equivalent to the area that's seen by a radar) for a wide range of azimuth and incidence angles, making it easily visible on SAR scenes. All rays of a plane wave that illuminate a trihedral reflector travel along the same optical path, meaning they reach the antenna in phase.
- Bragg scattering. When a set of scatterers is evenly spaced in the ground direction, where two-way travel path of the radar signal between any two of them is equivalent to an integer number of the wavelengths. These scatterers make a strong interference effect. This is a primary mechanism for backscattering over the ocean and non-smooth water bodies.
- Volume scattering: If the elementary scatterers are randomly distributed within a supporting layer, like for example tree branches in the canopy, radar waves will be scattered multiple times within that volume, e.g., within the tree canopy. It is quite common in vegetated areas, also where there is not enough of the wave penetration, such as loose snow. The targets that

can be characterised by volume scattering are generally not suitable for InSAR measurements (Ferretti, 2014).

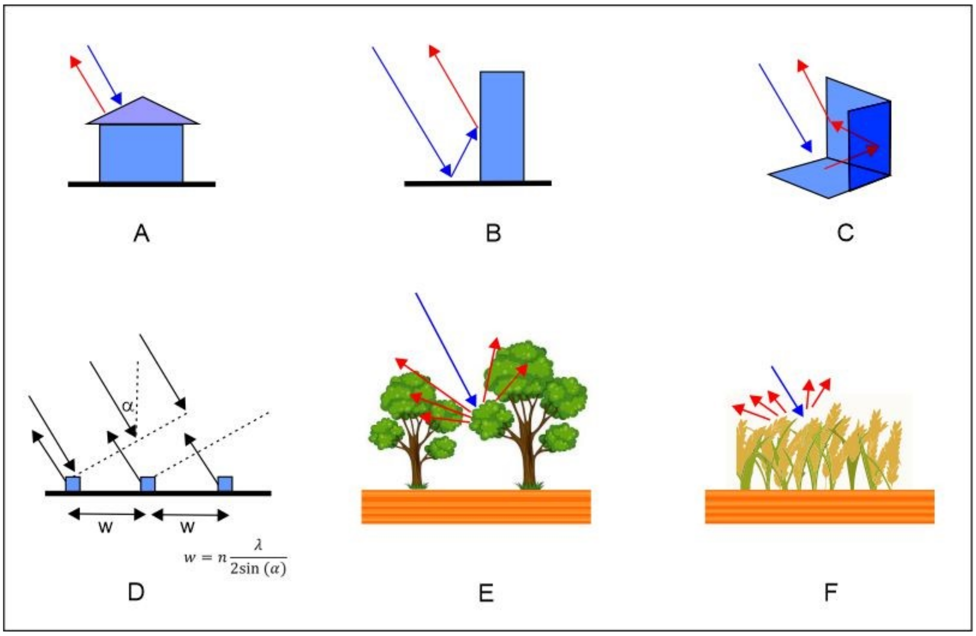

Figure 3.3. Scattering mechanisms, adapted from Ferretti (2014) showing as follows: A: reflection and scattering from a surface. B: dihedral reflection. C: trihedral reflection. D: Bragg scattering. E and F: volume scattering.

Since SAR satellites travel around the Earth in two directions, from South to North and then from North to South, and the SAR is side-looking, the orbit direction is an important feature of the radar. When the radar travels in the direction from South to the North, it is called an ascending orbit and it usually means that the sensor is looking to the East. The opposite satellite travelling from North to the South will have a descending orbit and the sensor will be west looking.

The resolution for the radar can be defined as the minimum distance between two adjacent scatterers of approximately equal strength at which the sensor distinguishes two discrete points; at smaller distances, only a single point is observed.

3.3.1.2 Resolution in the azimuth direction

The azimuth resolution, R_a, is a function of the wavelength of the radar (λ), the slant range (S) and the length of the antenna (D_r):

$$\boldsymbol{R_a} = \frac{S \times \lambda}{D_r} \qquad \text{Equation 3.1}$$

Based on this formula, azimuth resolution, R_a is inversely proportional to antenna's length (D_r). This means that for a given radar wavelength and slant range, high azimuth resolution requires a very long antenna which, for a spaceborne sensor, presents a problem of mass. For example, for a satellite operating above the Earth at a wavelength of 5 cm, a radar antenna would have to be 4250 m long to achieve a spatial resolution of 10 m, which makes it unreasonable to build. The Synthetic Aperture Radar (SAR) is a system that helps to solve this problem and to provide high spatial resolution in spaceborne radar systems. SAR uses a short physical antenna, to synthesise a virtual long antenna, and to improve spatial resolution (illustrated in Figure 3.4), by exploiting the coherent backscattered radar through signal processing, based on the Doppler frequency shift of the target signal (Lillesand et al., 2015). A surprising consequence of the synthetic aperture is that the SAR azimuth resolution depends only on the inverse of the antenna length and is independent of the slant range.

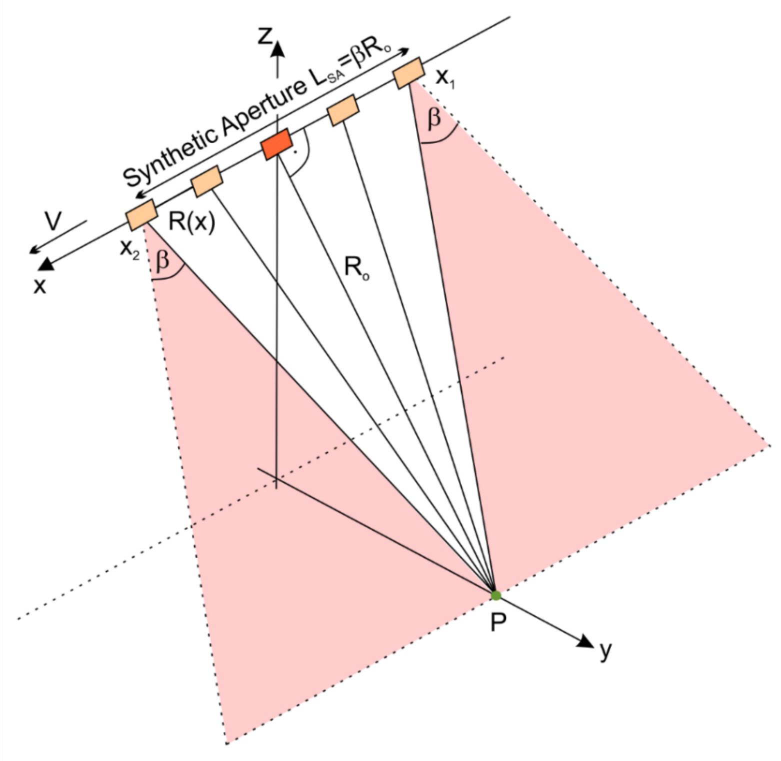

Figure 3.4. Geometry of a Synthetic Aperture for target P along track position x=0, adapted from Flores-Anderson et al. (2019)

3.3.1.3 Resolution in the range direction

Side-looking sensors have a resolution in the range direction specified by the radar pulse's length. It means that the pulse must be as short as possible to achieve high resolution. For a rectangular pulse, the range bandwidth (BW) of the pulse can be described as:

$$BW_r = \frac{1}{\tau}$$ Equation 3.2

Where τ is the pulse duration.

The pulse of the radar can't be made too short because of the limits on the peak transmitter power and the need to deliver sufficient electromagnetic energy to illuminate the object to reach the necessary Signal-to-Noise Ratio (SNR). This means that the SNR required and the power of the transmitter specify the length of the pulse (Engdahl, 2013). A shorter pulse needs a higher amplitude and peak power to achieve good return signals but there are practical limits to achieving this (Ferretti et al., 2001). To overcome this issue, the technique of range compression was developed. Instead of transmitting short, rectangular pulses, the radar system uses a chirp, which is a linear, frequency modulated pulse. Then, the radar returns are filtered with a matched filter, which means that the received signal is cross-correlated with a replica of the chirp used in transmission. This is called a range compression, and through the filtering, the effective duration of the signal shortens to a few nanoseconds (while the original chirp is a few microseconds). More information on range compression can be found in Ferretti et al., (2001); O'Donnell (2010); Cheney, (2001) or Curlander and McDonough, (1991). Range compression causes the received signal to be focused, using autocorrelation function of a chirp, into a narrow spike of much shorter than the actual chirp duration.

3.3.2 SAR image creation

Assuming the side-looking radar illuminates a point-wise scatterer that is isolated and surrounded by absorbing material, every range line (defined by time) is collected by the radar at a different azimuth coordinate (defined by the Doppler). However, because the image is synthesised by movement of the antenna in the azimuth direction, the Doppler for each scatterer varies during acquisition (there is a very small change in the range timing as well, but it is usually not measurable). To correct for this and focus the image in the azimuth direction, all the contributions from the scatterer are coherently added, allowing the computation of the complex signal value of the focused SAR image relative to the radar coordinates of the scatterer. For every image pixel that has radar coordinates r and a (range and azimuth respectively), every corresponding echo in the raw data matrix is identified first, assuming the acquisition geometry is known, and then the matched filter applied to integrate all the different contributions, once the Doppler is compensated (Ferretti, 2014).

When multiple elemental scatterers are present an effect called speckle can be noticed in the SAR images. These scatterers are characterised by a random distribution within a single resolution cell. The coherent sum of their phases and amplitudes creates strong variations of the backscatter from one resolution cell to another. This means that the intensity and phase of the image has uniform and exponential distribution. The speckle is considered to be a physical measurement of the resolution cell structure at a sub-resolution level. It cannot be reduced with the increase of the transmit signal power because its variance increases with intensity. Multi-look technique (Rosen et al. (2000)) is used to alleviate the speckle by averaging (non-coherent) the image intensity. Generally multi-look lowers the image resolution but it improves the interpretability of the SAR image (Moreira et al., 2013).

3.3.3 Geometric distortions

The area that is imaged within every resolution cell of a SAR image is dependent on the surrounding topography. It is commonly called the ground resolution cell and it depends on the slope of the terrain perpendicular to the orbit of the satellite in the ground range direction, as well as on the slope in the azimuth direction.

Geometric distortions can be mainly associated with regular sampling in range. This happens because the radar system measures a projection of a three-dimensional scene, with the coordinates slant-range and azimuth. Because of that, effects like shadows for areas that are hidden from the illumination of the radar, or foreshortening and layover are present as stretch and compression of sloped terrain (Moreira et al., 2013).

Figure 3.5 shows five slant range resolution cells that are identical. The first two cells represent flat terrain and include three triangles each. Cell number three includes seven triangles due to the change of topography and last two cells (fourth and fifth) only contain 2.5 triangles each, due to the terrain's slope being close to the off-nadir range that cause the cell dimensions to become larger and details being lost (Ferretti et al., 2007).

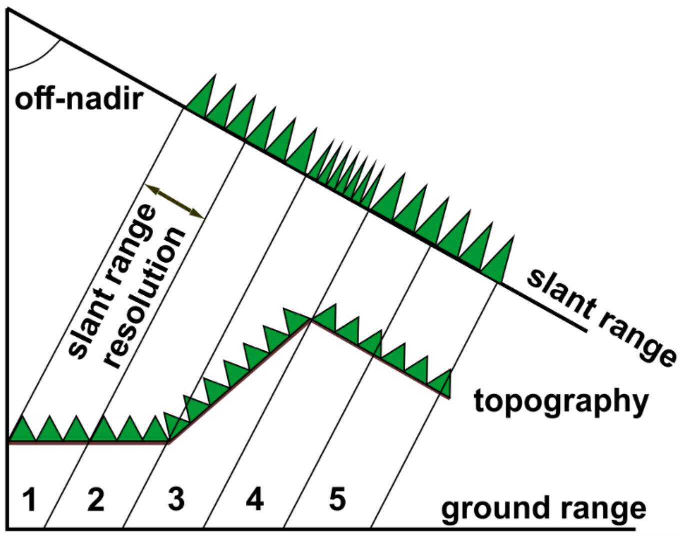

Figure 3.5. Terrain effect for the SAR image, adapted from Ferretti et al. (2007)

The terrain slope can cause issues like layover and shadow effects (Figure 3.6). Layover happens when the slope of the terrain is higher than the off-nadir angle of the radar – the scatterers are then imaged in the reversed order and overlaid on the other areas' contributions. The shadow effect is present when scatterers can't be illuminated by the satellite's radar, as they're in the shadow – this results in missing ground signal (dark gap) on the recorded image (Ferretti et al., 2007).

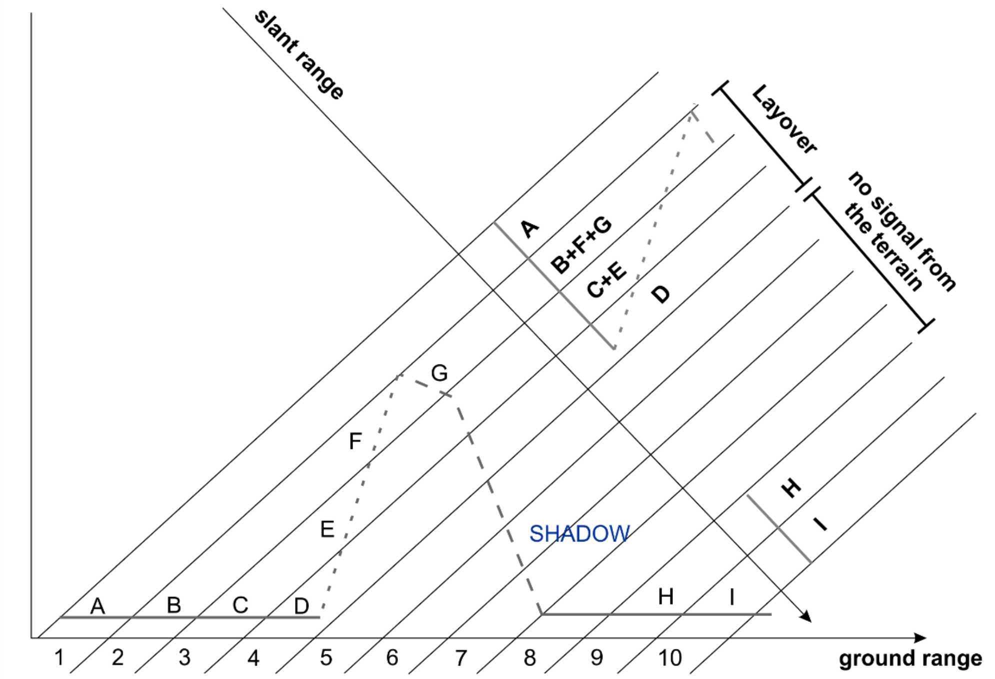

Figure 3.6. Layover and shadow effects, adapted from Ferretti et al. (2007)

3.4 SAR Interferometry

Space-borne Interferometric Synthetic Aperture Radar (InSAR) is increasingly used to monitor wide areas for local scale ground motions related to natural and anthropogenic geohazards with millimetre accuracy. InSAR has been used in this research for monitoring coastal zones because the existing conventional methods (see discussed in chapters 5, 6 and 7), are often expensive, weather dependent and can be easily affected by the harsh coastal environment.

InSAR uses the phase information derived from SAR Single Look Complex (SLC) images. SLC image, is made of real and complex pixel numbers, from which the intensity and phase of the signal can be derived. The intensity of the image is related to the backscattered energy returned from the ground. The phase is a function of the distance between the radar antenna and the target on the ground surface (Liu and Mason, 2016) together with other factors such as atmospheric humidity.

The phase φ of a pixel P can be described with an equation:

$$\boldsymbol{\varphi(P) = \varphi + \frac{4\pi}{\lambda} r + \alpha + v} \qquad \text{Equation 3.3}$$

Where following contributions can be distinguished:

- φ: Phase contribution. This is due to the location and nature of the elementary scatterers within the resolution cell that is related to the pixel (P) coherently adding to create radar return.

- $\frac{4\pi}{\lambda}r$: If a dominant scatterer exists in the resolution cell, *r* is the distance between the sensor and target.
- α: Atmospheric contribution. The propagation speed is affected by various atmospheric effects, like free particles in the clouds and ionosphere, water vapour, tropospheric fog etc.
- *v*: Noise source contribution, with the thermal noise being the key contribution (Ferretti, 2014).

The phase matrix of a single image is largely meaningless, but the difference in phase value for a pixel P in two SAR images can reveal subtle changes between the two images. These two images need to be properly re-samples (co-registered), so the pixels correspond to appropriate resolution cell. Based on this knowledge, from equation 1.4. below can be obtained:

$$\Delta\varphi(P) = \Delta\varphi + \frac{4\pi}{\lambda}\Delta r + \Delta\alpha + \Delta v \qquad \text{Equation 3.4.}$$

A map of the phase difference between two coherent SLC images (a fringe pair) is called a SAR interferogram (Figure 3.7). It is computed by multiplying the complex values of first SAR image (reference image) by the complex conjugate of the second image (secondary image):

$$I = Z_M \times Z_S^* = A_M \times A_S \times e^{j(\varphi_M - \varphi_S)} \qquad \text{Equation 3.5.}$$

If no change has occurred in between two image acquisitions, i.e., all of the scatterers within each resolution cell have neither moved nor changed their dielectric constant, and the atmosphere has been remained the same, then the interference fringes represent topography. Where changes have occurred then the residual, after removing the topographic fringes, is a measure of the ground deformation caused by natural and human made ground movements. The concept of the phase difference (phase shift) is presented on Figure 3.7 from Garthwaite et al. (2015), where two passes of the same satellite are shown, the second pass after a ground has occurred. If the pixels presented very high values of the SNR in both acquisitions, the equation 1.5. would become:

$$\Delta\boldsymbol{\varphi}(\boldsymbol{P}) = \frac{\boldsymbol{4\pi}}{\boldsymbol{\lambda}}\Delta\boldsymbol{r} \qquad \text{Equation 3.6.}$$

In this case, the phase value is still modulo-2π, however the term related to the reflectivity of the target and complex interaction with elementary scatterers is no longer present. By not measuring absolute range values, differential range measurements can be achieved (Ferretti, 2014).

The images must be co-registered, pixel by pixel and then the phase difference φ can be calculated from the phase angles, φ_1 and φ_2, of the pixels from their complex numbers.

$$\boldsymbol{\varphi} = \boldsymbol{\varphi_1} - \boldsymbol{\varphi_2} \qquad \text{Equation 3.7}$$

The distance between the radar signals for a round-trip equals 2δ and the interferogram (phase difference) can be described as:

$$\boldsymbol{\varphi} = \frac{\mathbf{4\pi}}{\boldsymbol{\lambda}}\boldsymbol{\delta} \qquad \text{Equation 3.8}$$

When looking at InSAR data, coherence is a very useful tool for recognising whether the processed data is of good quality. Coherence of an InSAR pair can be defined as a representation of complex correlation between two SAR images on a pixel-by-pixel basis, and it provides a quantitative measure of the amount of noise that exists in the interferogram (Chatterjee et al., 2010). Coherence's value ($|\bar{\gamma}|$) between two complex SAR images can be represented as follows:

$$\gamma = \frac{E[u_1 u_2^*]}{\sqrt{E[|u_1|^2]}\sqrt{E[|u_2|^2]}} = \frac{E[v]}{\bar{I}} \ ; \gamma < 1 \ ; \ \angle\gamma = \varphi_0 \qquad \text{Equation 3.9}$$

Where E is the expected value of the random variable x, and φ_0 is an expected value of the interferometric phase (Ferretti et al., 2007).

Coherence of an interferogram ($|\bar{\gamma}|$) is a measure of how well phase values correlate between interferograms. It is directly related to the Signal-To-Noise Ratio (SNR):

$$SNR = \frac{|\bar{\gamma}|}{1-|\bar{\gamma}|} \qquad \text{Equation 3.10}$$

If the scatterers have any random changes on the surface between the acquisitions of the two images, there will be some irregularities in phase which reduce the coherence of an image. It ranges from 0 to 1, where zero means that there is no useful information in the interferogram, and one means it is a perfect interferogram without phase shift. Any surface that is constantly subjected to random change, like growth of the vegetation or erosion, will have low coherence. Caution should be utilised during data collection and processing, with an emphasis on issues that might arise from using InSAR. Most common limitations are geometric distortions, atmospheric effects and issues arising with the temporal baseline.

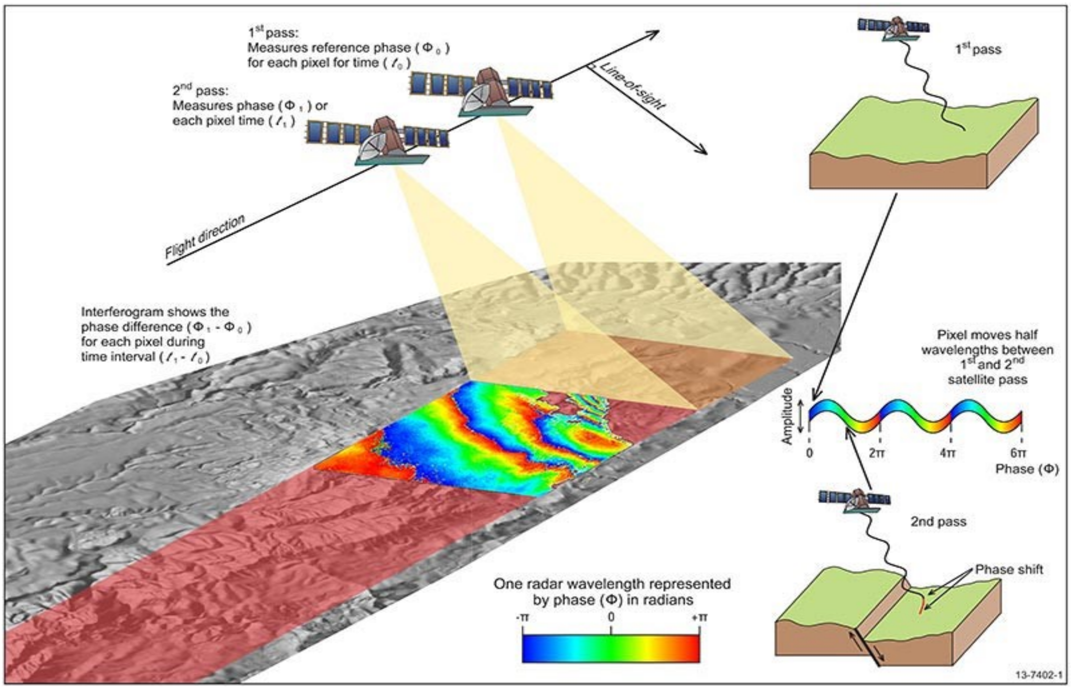

Figure 3.7. Phase difference between two passes of a satellite (Garthwaite et al., 2015)

Exploiting the ability to measure range variations, two main applications can be distinguished. Firstly, the same object can be observed from two different locations, so the third dimension can be estimated, and secondly, one area can be observed over time, using the same acquisition geometry and hence highlight any potential deformation (Ferretti, 2014).

Figure 3.8 (A-D) shows four interferometric configurations that are described below (based on Ferretti (2014)).

- A: Zero baseline and with no deformation occurring. This is a case when two SAR images acquired at different times over one area of interest have identical trajectory within fraction of a millimetre. This is a case, when the geometrical baseline equals to zero, meaning the geometries of both acquisitions are the same. In this case, the interferogram will be a matrix of zeroes, because $\Delta r = 0$ for every pixel of the image.
- B: Zero baseline, with non-zero deformation. This is a case, when a zero baseline interferogram is created, based on two SAR images acquired at different times over the same area, but there has been a deformation event that occurred between two acquisitions. In this case, phase variation would be measured for every pixel that has been affected by range changes. As it can be seen on the Figure X.(b), every interferometric fringe corresponds to a displacement along the Line-of-Sight of the satellite (of $\lambda/2$). If the displacement area is spatially correlated, the fringe pattern would resemble a set of contour lines, and phase unwrapping procedure would be performed to calculate the actual deformation of the area, by adding the proper number of cycles to each image, starting from the reference point.

- C: Non-zero baseline, with no surface deformation, and no topography. In case of a flat terrain, that is affected by changes in time, the geometrical baseline between two image acquisitions would create a set of fringes parallel to the azimuth direction. The larger the baseline, the higher frequency of the fringe is in range direction. This phase component is often called "flat Earth component". Because the distance between two satellite orbits tends to vary with azimuth, this phase ramp is slowly changing as a function of the azimuth coordinate.
- D: Non-zero baseline, with no surface deformation, and non-flat topography. For the interferograms over an area of interest that is not flat, and the normal baseline is not zero, the interferometric phase values are modulated by the local topography. Similarly, the larger the baseline, the larger the phase variation, based on the topographic profile. Once the flat Earth component is considered, the phase values are proportional to the topographic profile.

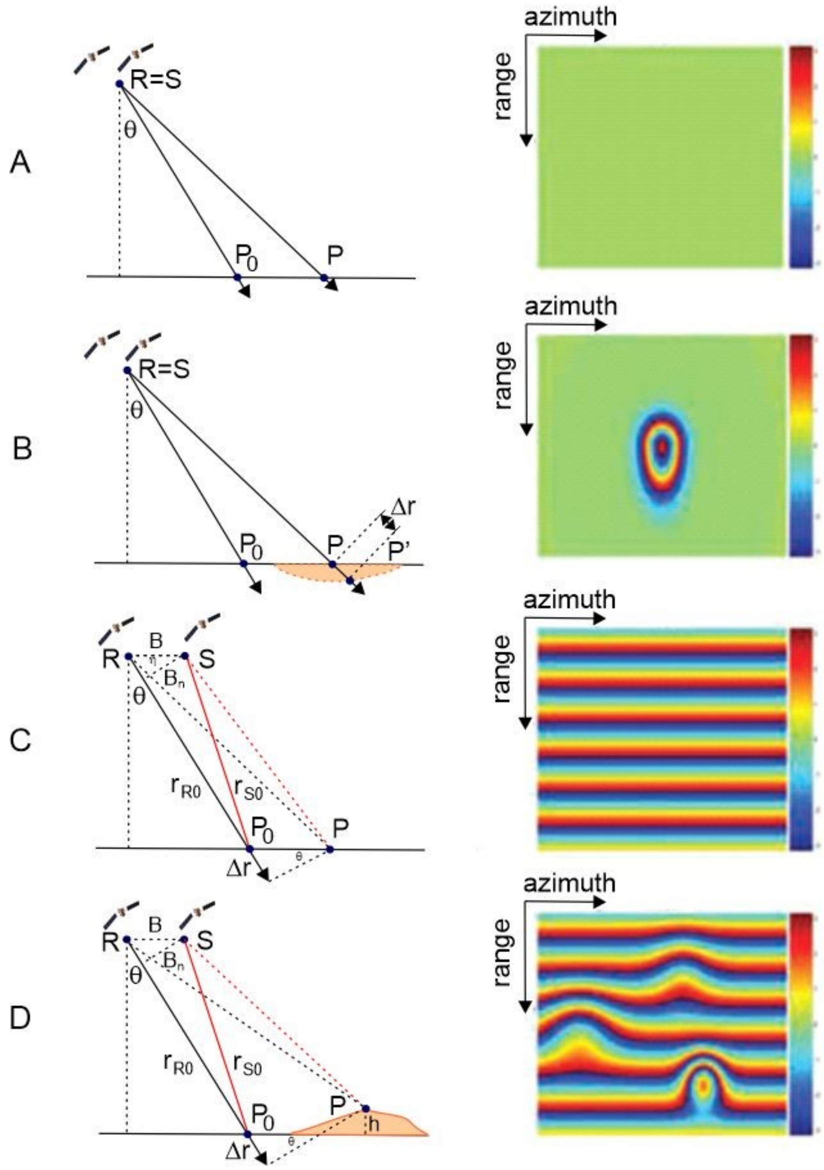

Figure 3.8. Four interferometric configurations, modified from Ferretti (2014)

3.5 Differential Interferometric Synthetic Aperture Radar (DInSAR)

Use of InSAR observations for surface monitoring can be challenging: often it is not possible to neglect the baseline-related phase contributions, and also the phase noise and atmospheric effects can hamper the approximations of the actual displacement field within the area of interest (Ferretti, 2014). A differential interferogram can be generated when a digital elevation model (DEM) is available. This helps to limit the impact of local topography on the interferometric phase.

Differential interferograms provide a way to detect changes to the ground surface, and they are created from repeat pass SAR images. Using two images, one before the event and one after, a differential interferogram can be created. By comparing two images, the phase shift caused by topography can be distinguished, but to show the geometric deformation of the ground a third image is needed to cancel out the effect of topography. An example of the phase shift is shown in Figure 3.9 (Liu and Mason, 2016). An external DEM (Digital Elevation Model) can also be used to extract the topographic information from the interferogram to create a differential SAR interferometric measurement where it is possible to detect the changes between two scenes acquired at different times.

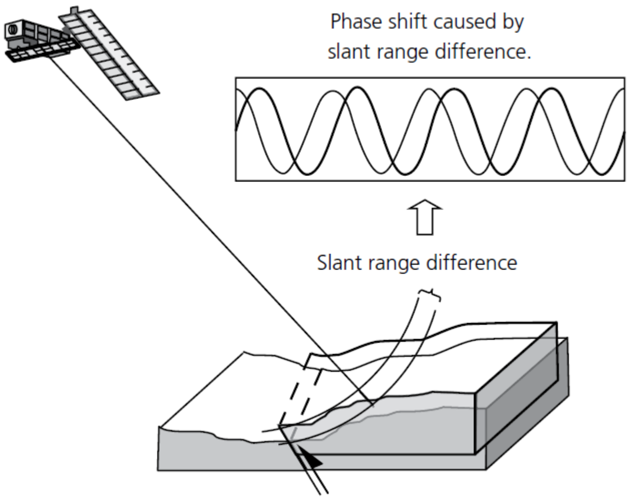

Figure 3.9: An example of the phase shift caused by the ground movement, from Liu and Mason, 2016

Once the topographic phase is removed, the interferogram can be described as:

$$\varphi_{disp} = \frac{4\pi}{\lambda}\Delta r_{disp} \qquad \text{Equation 3.11}$$

Where Δr_{disp} is the displacement in line-of-sight and λ is the length of the wavelength.

DInSAR can achieve accuracy on the subwavelength (cm) scale and so detect small-scale movements of the Earth's surface (Moreira et al., 2013). This method can show the ground behaviour before and after cliff failure, since the collapse of a cliff means the loss of the cliff face resulting in changes to the land surface which in turn should be visible on a differential interferogram. This method can be used to pin-point collapses on the radar and to show the changes in the ground before and after an event like an earthquake, subsidence, or glacial motion.

An interferogram's quality can be measured with an interferometric coherence ($|\bar{\gamma}|$), that has been briefly defined in Section 3.4, Equation 3.9. When looking at an image pixel, its coherence is based on the expected phase value for that pixel, found using a sliding estimator window, usually sized between 50 – 100 pixels. Because of that, the coherence map is always of lower spatial resolution than the interferogram, representing the trade-off between coherence resolution and accuracy. The bigger the window size, the better the coherence accuracy, but resolution is then lower (Eidener and Bamler, 2014).

The second important factor is temporal decorrelation, $|\bar{\gamma}|_{temp}$, which defines variations in scene microstructure and permittivity between two image acquisitions that are temporally separated. Other sources of decorrelation are geometric baseline and volume decorrelation ($|\bar{\gamma}|_{geo}$). Hence, the total coherence loss can be described as a product of the individual losses:

$$|\bar{\gamma}| = |\bar{\gamma}|_{SNR} \cdot |\bar{\gamma}|_{temp} \cdot |\bar{\gamma}|_{geo} \qquad \text{Equation 3.12.}$$

Coherence loss is an important factor and can cause large phase errors in interferograms. Phase noise can be mitigated by averaging locally the interferogram, before the phase values are extracted (Moreira et al., 2013).

For DInSAR to have good accuracy, the external DEM must be the same order of magnitude (or better) than the phase sensitivity of the interferometric baseline and the phase noise caused by temporal decorrelation needs to be considered, as well as variations in the propagation medium. These are usually a consequence of atmospheric delay, mainly caused by vapour content in the troposphere. Such delay is in the order of 2-4 metres, but the local scale gradient can be up to 1 cm/km or more. This limits the accuracy of conventional DInSAR. When a location is monitored over long time, these issues can become significant, hence the time series methodologies have been exploited as a solution to the limitations of conventional DInSAR methods. PSI is one of the methods that helps to avoid the Differential Interferogram issues, and it is described in the next section.

3.6 Persistent Scatterer Methods

3.6.1 PSI Methodology

The Persistent Scatterer Interferometry (PSI) method was first utilised by Usai and Klees (1999), who discussed how some of man-made structures show a coherent return signal even for baselines of many years. They discussed the possibility of looking at multi-temporal analysis rather than better interferogram filtering techniques as a way to identify good pixels from an incoherent background. When the SAR interferograms were analysed for the effects of the atmosphere, atmospheric disturbance is found to be uncorrelated in time but correlated spatially, which means that atmospheric noise can be averaged for multiple interferograms and create interferogram stacking (Sandwell and Price (1998); Lyons and

Sandwell (2003)). The data in an interferogram stack can be averaged and the signal-to-noise ratio (SNR) can be enhanced to extract data on displacement over long time periods easier than from a single interferogram (Ferretti, 2014).

PSI methodology was first developed in the late 1990s and early 2000s by the SAR group at the Milano Polytechnic (Ferretti et al. (2000); Ferretti et al. (2001); Colesanti et al. (2003)). This methodology consists of comparing 20 or more SAR images acquired at different times, comparing them all to each other and producing time series of ground deformation. Since atmospheric effects are uncorrelated in time but spatially correlated, the motion of the object of interest is usually correlated in time but shows variable levels of spatial correlation. To limit the number of the phase contributors, the method focuses on Permanent or Persistent Scatterers (PS) – objects that can be considered to be coherent and are only somewhat affected by the geometrical and temporal decorrelation, and with that showing constant reflectivity values (Ferretti, 2014).

A block diagram with steps describing the PS method is shown in Figure 3.10. The SAR images are co-registered with a Reference Image that is selected to reduce the temporal and geometrical baselines dispersion and maximise the average coherence. This follows with computing interferograms for every SAR image against the Reference Image using a DEM to remove topographic fringes. Once this is produced, differential interferograms are unwrapped on a grid of PS Candidates, atmospheric phase is estimated and removed and points with usable information are recognised, followed by generation of the final results. The detailed description of the technique can be found in multiple of publications, like Ferretti et al. (2001), Ferretti (2014), Crosetto et al. (2016), Moreira et al. (2013).

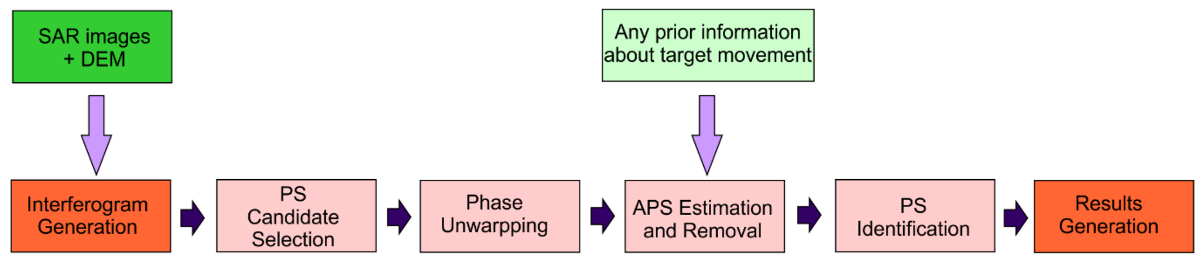

Figure 3.10. A block diagram with main steps for the PSI method, adapted from Ferretti (2014)

The PS are selected by analysing their coherence, using correlation thresholding approach, where objects with coherence higher than a threshold value are chosen as PS candidates. This can become problematic if an estimation window is too large, for example where data are averaged over a large area. It can then result in a lower resolution and many targets that are stable will be lost as they will be then surrounded by non-coherent points. As an alternative, amplitude can be analysed for every pixel in the AOI (area of interest) to search for stable scatterers – this allows to select PS candidates that show stable values of amplitude (Ferretti et al., 2001).

Once the candidates have been selected, they need to undergo phase unwrapping, as they all have time series of phase values wrapped:

$$\boldsymbol{\varphi^k} = \left[\boldsymbol{C_B} \times \boldsymbol{B_n^{(k)}} \times \boldsymbol{\varepsilon} + \frac{\boldsymbol{4\pi}}{\boldsymbol{\lambda}} \times \boldsymbol{d^{(k)}}\right] + \boldsymbol{\alpha^{(k)}} + \boldsymbol{n} \qquad \text{Equation 3.13}$$

Where:

$B_n^{(k)}$ – the phase component with normal baseline
ε – an elevation error in DEM
$d^{(k)}$ – the displacement
$\alpha^{(k)}$ – the atmospheric phase screen
n – noise.

This follows an estimation of the Atmospheric Phase Screen (APS), which removes any atmospheric elements that are superimposed on every SAR image. For every PS Candidate, a DEM error and polynomial coefficients are estimated. Once this is finished an interpolation of phase residues follows. The phase residues are also low-pass filtered and if there is a large enough number of images, also high-pass filtered in time. Following this, all the estimated atmospheric components are interpolated on a regular image grid, including their variograms, and are subtracted from interferograms. Once the interferograms are corrected for atmospheric disturbances, a pixel-by-pixel analysis is performed to search for additional PS (Ferretti, 2014). More detailed information on PS selection can be found in Colesanti et al. (2003).

As a result of this process, a set of PS points is identified in the coordinates of the SAR image, a movement for every PS is estimated as a movement in time, an average displacement for every PS is estimated, and each PS receives a set of parameters that depends on the model used in the processing and related standard deviation. Finally, meta-data about the geometry of the acquisition, the data set and the sensors of the radar are also provided (Ferretti, 2014).

The dimension of a PS can be smaller than the SAR resolution cell since small objects are very likely to act as PS, considering their radar reflectivity values would not be as sensitive to small acquisition geometry variations. The density of PS depends on cover of the terrain – for example areas heavily covered with vegetation will produce a lower density of potential objects that can act as permanent scatterers, while urban areas would be very efficient for PS selection with plentiful of targets that can act as PS (Ferretti et al. (2001) Ferretti (2014)).

This methodology works very well when analysing motion like urban subsidence or ground movements due to seismic faults, but not as successful when attempting to monitor seasonal effects of underground gas storage or an aquifer. Spatial filtering of the InSAR data before stacking reduces its resolution and potentially causes loss of useful data that might be isolated in pixels that have high SNR, and suppresses rapid changes in the displacement field (Ferretti, 2014).

3.6.2 DInSAR applications in coastal environments

The main use of InSAR long time series has been to monitor ground deformation and changes in projects like tunnelling in urban environments (for example, Gonzáles-Martí et al. (2017), Milillo et al. (2018), Giardina et al. (2019) and Scoular et al. (2020b)); monitoring building subsidence (Ciampalini et al., 2019); detection of surface deformation (Sousa et al., 2010); mapping interactions between geology and urban development (Pratesi et al., 2016) or monitoring CO_2 storage (Rohmer and Raucoules, 2012), as well as agricultural areas (Rohmer et al., 2014).

In contrast, only limited research has been published to date on InSAR and DInSAR monitoring of geomorphological changes in the coastal environments. The review below discusses applications of the InSAR methods in coastal environments and in monitoring geomorphological changes away from the coast.

Zhao et al. (2019) discusses a use of long-term InSAR ground displacement time series for a coastal area of Shanghai, using Small BAseline Subset (SBAS) methodology to create them. SBAS algorithm is a DInSAR algorithm, that uses a large number of SAR acquisitions and creates a combination of the multilook DInSAR interferograms to generate mean deformation velocity maps (Lanari et al., 2007). Detailed description of SBAS methodology can be found in Berardino et al. (2002). Their results show good comparison between different satellites and bands (ENVISAT in C-band, COSMO-SkyMed in X-band and Sentinel-1A in C-band) and explain how the use of statistical methods can help with estimation and corrections for systematic biases between the platforms. Several papers discuss the use of InSAR to monitor permafrost, (e.g. Short et al. (2011) or Rouyet et al. (2019)), where they focus on Herschel Island in Canada and Adventdalen in Svalbard respectively, using long time series to detect ground movements in areas that constantly freeze and thaw and therefore experience an ongoing heave and subsidence. Chen et al. (2020) have looked at marsh wetlands in the Great Lakes Basin in Canada to establish correlation between InSAR measurements and water level changes in the field. While mainly successful studies, they determined that the backscatter coefficient and coherence from plants and water varies between different sensor modes and more research is needed to help with the issues encountered. Frodella et al. (2016) compare the use of satellite and ground based remote sensing methods for monitoring rock cliffs in Northern Italy and developed remote sensing monitoring techniques. They used PSI to investigate ground movements before and after a large rock fall in the town of San Leo and discuss the use of a ground based InSAR system, which allows analysis of short term behaviour of the rock deposits from the fall. Rouyet et al. (2017) discuss monitoring of rock slopes 'breathing' with the use of ground based InSAR data, showing how the slope is inflating (moving upwards) during the months of May – June, due to high water inflation and saturation of the slope, and deflating from August until September, due to the water evacuating the slope and causing it to desaturate. Buckley et al. (2002) discuss the use of GPS photogrammetry and InSAR data for monitoring of coastal zones showing that incorporating GPR, photogrammetry and InSAR data together achieves a very efficient monitoring of the coastal zones. Normand and Heggy (2015) argue that InSAR can be used for assessing deformations in coastal terrains that are around urban environments. The study focuses on the city of Montreal in Canada, where large surface deformations are associated with groundwater movements, causing significant damage to the city's infrastructure. They are able to effectively monitor ground deformations of several millimetres a year. There are many publications on the monitoring of landslides with uses of InSAR, as well as ground based InSAR, including, but not limited to Bayer et al. (2018), Schlögel et al. (2015), Zhu et al. (2014), Squarzoni et al. (2020), Carlà et al. (2019). InSAR has also been used for sinkhole monitoring, as discussed in Intrieri et al. (2015) where they have successfully used ground based InSAR to attempt sinkhole creation prediction.

However, there has been limited use of PSI for monitoring and analysis of the geological processes that occur in coastal environments, which this research addresses.

3.6.3 PSI processing chain

All the InSAR data used in this research has been processed using the ENVI software, SARScape. ENVI is a software platform developed by L3Harris Geospatial and is commonly used for image processing and analysis. ENVI SARScape is a module within ENVI that allows processing and analysis of the SAR data, both of airborne and spaceborne origins. For this research the PSI method has been applied based on the Interferometric Stacking PS model in SARScape. This technique allows usage of large sets of multi-temporal scenes and creates results with up to few millimetres accuracy.

The processing workflow is presented on Figure 3.11 which mainly follows the general PSI technique steps.

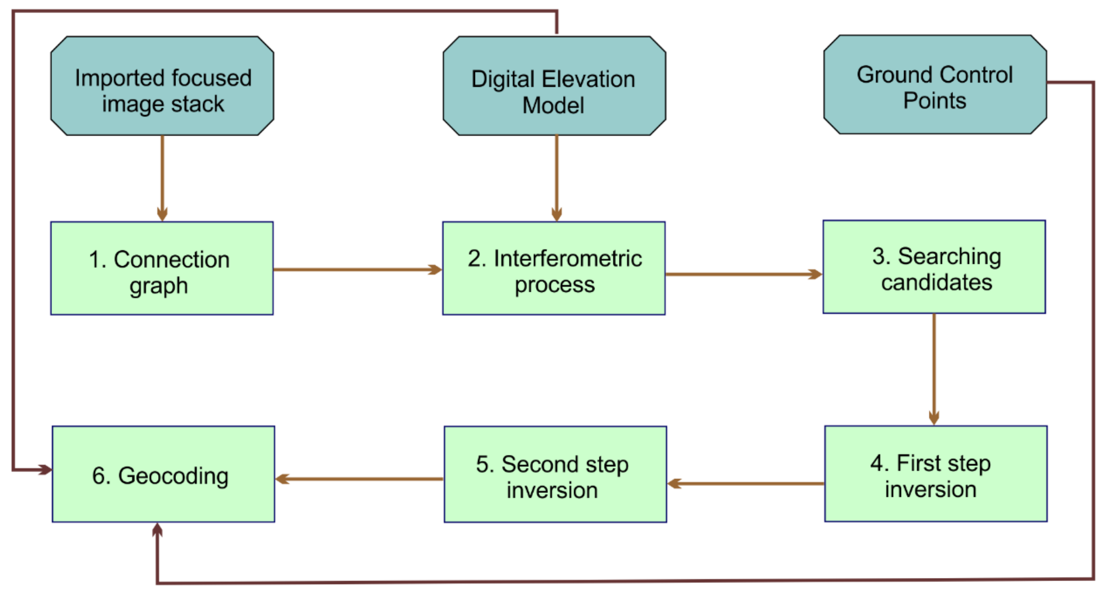

Figure 3.11. The processing sequence for PSI in the SARScape module of ENVI, adapted from ENVI (2010)

The PSI process has been described in detail in Section 3.6.1, however some specifics of the processing sequence in SARScape are discussed further here.

Once the SLC images are uploaded into the ENVI environment, a connection graph is created where all images create a network of Reference and Secondary image pairs and a connection network is generated. The data are then co-registered with the reference image, usually selected automatically. Interferometric stacking is then executed, which includes coregistration of the images and generation of interferograms and their flattening. First step inversion follows, involving identification of the PS; once selected their phase history is analysed (every coherent reflector is considered separately and represented as an image pixel) and an offset phase removed from the interferograms. Reference points are then selected automatically in the software so the phase offset can be calculated and removed. If the area of interest is large it is then split into smaller sub-areas (with small overlaps) which are then processed independently, and later mosaicked together into a merged area. This results in re-flattened interferograms that are used for approximation of the residual height and velocity (related to the ground displacement). These values are known as low pass components that are later removed from the interferograms so the atmosphere estimation can be performed on them. The next processing step, the second or final inversion, uses the linear models created in the previous step to estimate the atmospheric phase components. This step is applied to develop displacements date by date (after APC removal) and to create a displacement velocity model. The interferograms that are used in the step are the re-flattened interferograms, from which displacement information like velocity and displacement that are date specific and residual heights are calculated. Date by date ground displacement measurements, also called high pass components, are prepared so the software can then estimate the APC. This is run with two filtering procedures, atmosphere low pass and high pass. The low pass considers the atmospheric variations for the spatial distribution and is applied with a square window. The high pass considers the atmospheric variations for the temporal distribution and is applied using a temporal window. The final step in the processing, geocoding, follows. This includes geocoding the PS points and their displacements are then available for visualisation either as a shape or raster file (based on Harris Geospatial (2020)).

Information on the orbit number, the number of scenes and detailed information on the processing for every case study is provided in Chapters 4, 5 and 6 accordingly when the case studies are discussed in detail.

3.7 Sentinel satellites

The European Space Agency (ESA) has launched two SAR satellites, Sentinel-1A and Sentinel-1B in 2014 and 2016, respectively. The data from these two satellites is freely available from a European initiative called Copernicus, created by the European Commission (EC) through ESA. Sentinel-1 satellites provide C-band imaging data in four operating modes with varying resolution of up to 5 m and swaths up to 400 km wide. They are capable of collecting data in dual polarisation, have a short revisit time of 12 days for each satellite, but being in the same orbital plane, their revisit time is halved (European Space Agency, 2013). The primary aims for the Sentinel-1 imaging are monitoring ground movement of surfaces covered with forests, water, soil and agricultural areas, marine environments, sea-ice zones and polar areas. Sentinel's main operational modes are interferometric wide – swath mode (IW) and wave mode (WV), but it can also acquire data in strip map mode (SW) and extra wide – swath mode (EW) (Figure 3.12). All of these modes except the wave mode, can work in dual polarisation (HH + HV or VV + VH). The IW mode allows a high geometric resolution of 5 x 20 m on the ground with a large swath width of 250 km (Table 3.2). Interferometry is accomplished by having a sufficient overlap in the azimuth domain and the elevation domain (ESA, 2012). This research used the IW mode in VV polarisation for all the data processing.

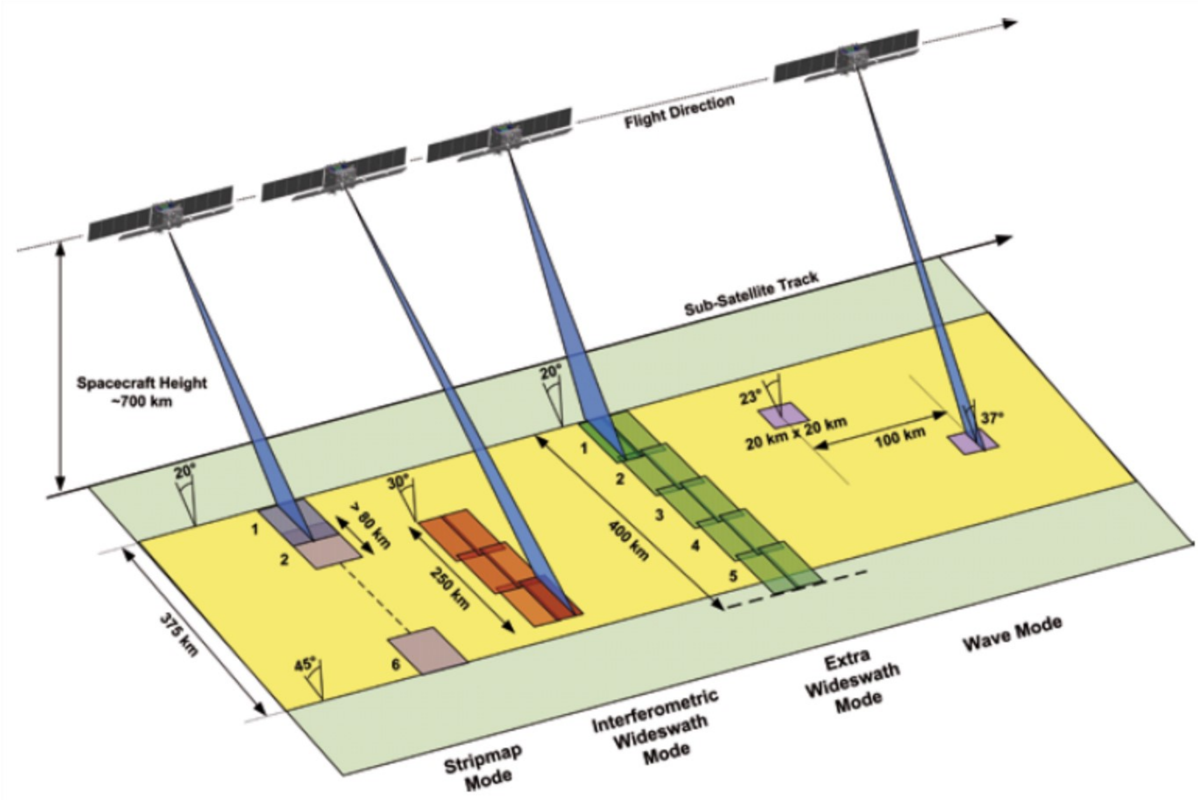

Figure 3.12. Interferometric modes for Sentinel-1A and 1B, from ESA (2012)

Table 3.2. Main characteristics of the Sentinel-1 nominal measurement modes, adapted from ESA (2012)

Parameter	*Interferometric wide-swath mode (IW)*	*Wave mode (WV)*	*Strip Map mode (SM)*	*Extra wide-swath mode (EW)*
Polarisation	Dual (HH+HV, VV+VH)	Single (HH, VV)	Dual (HH+HV, VV+VH)	Dual (HH+HV, VV+VH)
Access (Incidence angles)	31^o-46^0	23^o-37^0	20^o-47^0	20^o-47^0
Azimuth resolution	20 m	5 m	5 m	40 m
Ground range resolution	5 m	5 m	5 m	20 m
Azimuth and range looks	Single	Single	Single	Single
Swath	250 km	Vignette 20 x 20 km	80 km	410 km

3.8 Chapter summary

This chapter has discussed the theory behind the SAR technology, InSAR and Permanent Scatterer Interferometry methodologies, which have been the main processing methods used for this project. It has provided an insight on what kind of studies have been done so far on the topic of using InSAR to monitor coastal environments and processes that can be encountered within the coastal areas. It has discussed the general overview of the workflow that has been followed for the processing of the data in the project in Chapters 4 (Analysis and monitoring of cliff collapses), 5 (Analysis and monitoring of coastal landslides) and 6 (Analysis and monitoring of platform downwearing), as well as it has explained the software used.

The next Chapters (4, 5 and 6) will discuss the case studies that have been analysed during this research project, showing how the PSI methodology discussed in this chapter can be utilised for investigation and monitoring of processes that can be encountered within coastal areas.

4 Analysis and monitoring of cliff collapses

Chapter 4 discusses the attempt at monitoring cliff collapses near Birling Gap (Grid Reference: TV 55384 96110) in East Sussex, UK. It talks through the current monitoring techniques used at coastal cliffs and collapse events and explains how Persistent Scatterer Interferometry (PSI), a remote sensing methodology for monitoring of the cliff collapses. Study region is described in detail, specifying where and when analysed collapses have happened, followed by presentation of results and discussion based on them. It discusses methodology used for analysis for the case studies and achieved results.

4.1 Introduction

As it has been previously discussed in Chapter 2, coastal cliffs are considered a key feature of the shoreline, serving several functions, including provision of habitat to flora and fauna and sediment input to nearby beaches. They are, of course, prone to collapse which can pose significant hazards. Owing to their erosion they can create threats to the urban environment, infrastructure and natural protected areas (Young and Carilli, 2019).

Since chalk is a soft rock in comparison to many other lithologies, chalk cliffs are predisposed to relatively frequent erosion and collapse. Natural processes can therefore be observed to occur over relatively short time frames (such as within the length of a 4-year MPhil project) and thus chalk cliffs make the perfect analogue for similar processes occurring in other lithostratigraphic materials over longer time scales. Rapid erosion is a risk not only to houses located nearby quickly eroding coasts, but to all infrastructure, like roads, waste and water pipes, electricity lines, national parks, and the natural environment.

In a single collapse event, often up to 10 m of land surface perpendicularly to the coast (at the cliff top) may be lost. Collapses are very difficult to predict because of their stochastic nature. Multiple collapses occur each year in the UK, often in the long stretches of chalk cliff in the East Sussex, making them an obvious choice for the development of methods for prediction and monitoring of cliff collapses using InSAR techniques.

One of the best examples of a rapidly eroding coast in the UK is at Birling Gap cottages (Crangon Cottages, Figure 4.1, Grid reference: TV 55432 95978), East Dean. Looking at photographs taken over a 100-year period, the significant loss of land is apparent; just focusing on the farmhouse shown in Figure 4.1a (yellow ellipse), *ca* 20 m from the cliff face in 1906 and, in Figure 4.1b, less than 20 years later in 1920, the house is right on the edge of the cliff. Concentrating on the third chimney from the left (shown by the red arrow in Figure 4.1), it is clear that, 111 years later (Figure 4.1d), this house is very close to disappearing into the sea.

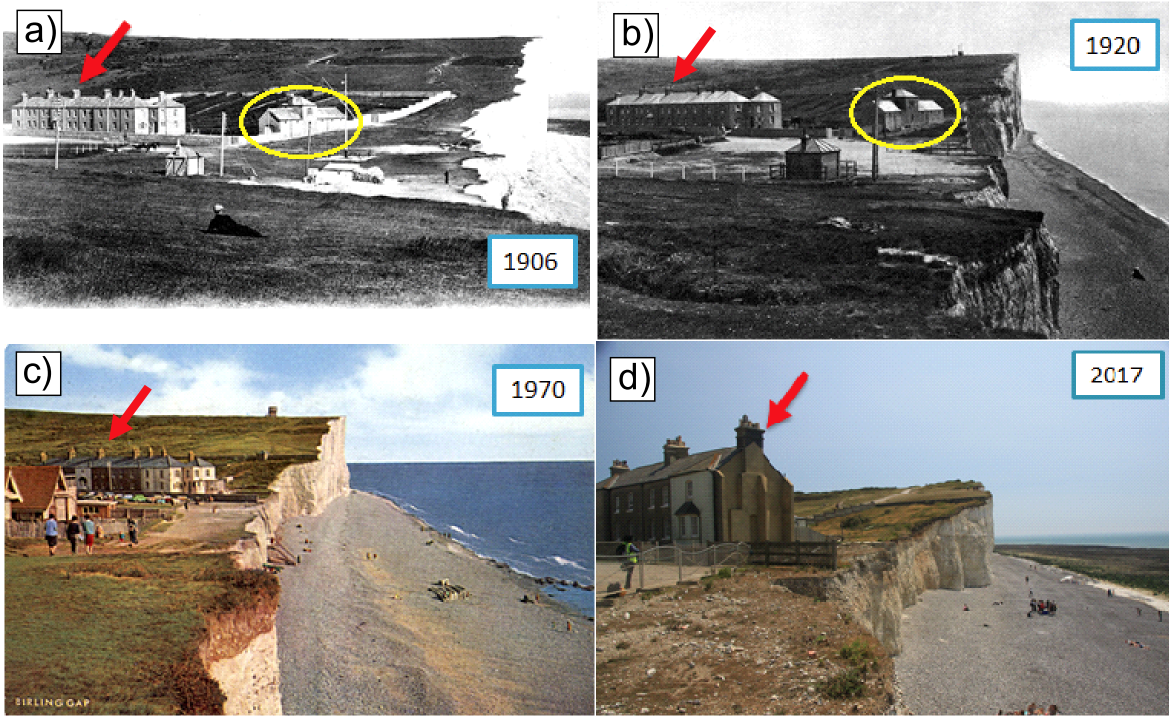

Figure 4.1. Birling Gap cottages, 70 m of erosion in 100 years (photographs accessed from http://www.sussex.ac.uk/geography/researchprojects/coastview/Rendels_postcards/birling_gap.htm, 2017 photo from personal archives)

Another example of coastal erosion risk comes from the Undercliff Walk in Brighton (Grid reference: TQ 33691 03343) where construction began in the first half of the 20th Century and has continued ever since, in an effort to protect the town of Brighton by preventing cliff erosion. Despite the efforts, including re-grading the angle of the cliff face, building rock groynes, and adding netting parapets, it is still unstable with small collapses occurring frequently and, although rare, larger collapses do occur in here. One of bigger collapses happened in 2001, where a failure occurred at close proximity to an ASDA supermarket at Brighton Marina, endangering staff and shoppers that were present near the event area.

Since it is not possible to prevent coastal erosion, even with coastal protection like groynes, shingle or regrading of the slope, multiple approaches to coastal cliff collapse monitoring have been undertaken. The area of East Sussex, being very prone to collapses given its soft chalk geology, has been the focus of many studies to understand coastal processes and assess whether prediction of cliff failures is possible, and how monitoring of coastal erosion can be performed. Some examples of studies are discussed in following paragraphs, focusing on cliff failure and the challenges that predicting such failures bring.

4.2 Current monitoring techniques for the area

The chalk cliffs in East Sussex have been subject to multiple studies, over many years, to assess the coastal zone erosion. This area, and many others across the globe, experience a variety of geological processes that endanger the coast (see Chapter 2.3). A wide range of methods are currently available for monitoring of the coastal cliff areas, including but not limited to, laser scanning surveys, Micro-Erosion Meters (MEM), walkover surveys and laboratory testing. All these methods require specialist equipment that is expensive and might not always be easily accessible. The cliffs are continually affected by storms and high tides, therefore the equipment that needs to be mounted permanently on the site will often end up damaged from the harsh environmental conditions. In addition, bad weather or high tides may restrict access and cause hazardous working conditions in the areas where measurements need to be taken.

Terrestrial Laser Scanning (TLS) gives a great outlook at the cliff face by creating digital surface models but presents limitations on the three-dimensional scope for capturing the data at coastal areas. Airborne LiDAR (Light Detection And Ranging) has hence been a preferred option, since it allows observations of the coastal areas from above, within the restrictions of the observation angle of the aircraft sensors (Barlow et al. (2017), Gilham et al. (2019)).

Stavrou et al. (2011) used GIS based methods, including geotechnical field mapping observation predictions of shoreline retreat, to appraise how much infrastructure is exposed to dangers of cliff collapse hazards and coastal retreat. The study included a walkover survey along the cliff tops to look for evidence of instability leading to the development of a hazard indication map. It also included analysis of historical shoreline retreat data to deliver evidence of the shoreline evolution and to present the effectiveness of existing coastal protection measures throughout the time. As a result, a risk zonation plan was created in the form of a map, illustrating how the risk scores vary between different areas of the coast and how probable it is for a particular area to have collapses and cliff falls.

Various research has been published on the factors that are causing the coastal chalk cliff erosion. An excellent example of such is a paper published by Brossard and Duperret (2004) which discusses how marine processes may be responsible for cliff failures. The authors performed several experiments in a wave flume tank, to analyse the pressures that are created from waves and their dissipation. Even though the pressure never exceeded the compressive strength of chalk, the fluctuations from periodic waves were sufficient to induce a fatigue process within the structure of the rock.

Dornbusch et al. (2008c) used data derived from maps between 1873 and 1925/28, as well as air photographs from 1973 and 2001 to analyse special and temporal changes within the coastal cliff retreat in East Sussex. The use of these photographs and maps allows inspection and analysis using almost the entire length of the study area (23 km), but the results cannot show a continuous change from 1873 onward, since they present only small snapshots in time, sampled only in the years when the air photographs were taken.

Busby et al. (2004) has undertaken a study under the project PROTECT (PRediction Of The Erosion of Cliffed Terrains), where two techniques have been used to assess whether they are suitable for prediction of coastal cliff failures. The first method used accelerometers to record high frequency seismic signals that should be generated by cracking of the rock mass before it collapses. The accelerometers have managed to record an increase in seismic energy 15 hours before cliff collapse, and the results have also been compared to laboratory measurements to help identifying collapse mechanisms that can be seen during various phases of the cliff fall. The second method used electrical resistance of the rock, assuming this changes with the azimuth, depending on the orientation of the major rock fractures. This method has shown that anisotropy changes when the cliff fails.

Gilham et al. (2018) published a paper discussing results of precision monitoring of chalk cliffs at Telscombe (UK) between August 2016 and July 2017. The authors used Monte-Carlo simulations to assess different erosion scenarios for 70 years (2020-2090), to analyse how they can affect the road that is in close proximity to the cliffs in the area. The study used UAV (Unmanned Aerial Vehicle) imaging and photogrammetry to evaluate mass movements on a monthly basis, to detect changes between 3D cliff models. The authors continued this work in Gilham et al. (2019), in presenting the successful detection of relatively small rockfalls, using 2.5D surface change detection. The research presents a comprehensive method of capturing the data that can help continuous coastal cliff monitoring.

All abovementioned methodologies bring potential for monitoring (not to mention failure prediction) of the cliff failures, but they are relatively costly to operate, and not always possible to operate in bad weather (i.e., UAV or TLS). Photogrammetry shows good potential, and can present great results, but it is highly dependent on the availability of historical photographs or maps. It also can be problematic to make precise comparison between surveys, as the data relies heavily on Ground Control Points and on photo quality. In practice, it cannot be used to achieve continuity of the monitoring over a chosen period of time, since the survey photographs are snapshots in time which would need to be acquired every few days to approach continuous monitoring.

Due to the limitations of the above methods, InSAR has been selected as a new approach, some of the advantages being: safety, since personnel do not need to be present at the chosen site of investigation; it can show results over a large area; and it can produce them over continuous period of time and often close to real time.

4.3 Methodology

The SAR data for cliff collapse analysis has been processed with the SARScape (ENVI software/Harris Geospatial) PS module that uses a PSI methodology, as discussed in chapter 3. One year of data from both satellites, Sentinel-1A and 1B, were processed, corresponding to the period when particular collapses were occurring.

Each of the events has been analysed separately, with the number of scenes and periods noted in Table 4.1. Each collapse was analysis based on a period (about a year each), since the cliff top is usually fully covered with vegetation and has very few buildings or other structures that can work as good reflectors, the concern was that longer periods of analysis would lead to a loss of coherence (explained in Chapter 3, InSAR methodology), mainly due to the vegetation growing and moving.

Table 4.1 Number of scenes and timeframes used for the processing and analysis of three collapses

Date of the event	Number of scenes analysed	Period of time
24/05/2016	39	12/2015 – 01/2017
21/06/2017	66	12/2016 – 01/2018
04/08/2018	62	01/2018 – 01/2019

The SAR data were processed such that only PS points above a minimum coherence threshold of 0.65 were selected in each case study. A higher coherence threshold e.g., 0.70 is preferable but, in this case, did not provide sufficient PS points across the vegetated study areas. The processed PS data for each collapse identified in Table 4.2 were exported into Excel to calculate a moving average of displacement values, with a step-size of seven scenes, to reduce noise and allow broader trends to become visible: thereby facilitating visual analysis. The PS point data are coloured by displacement value and are overlain on image maps, and selected PS are further displayed as time-series plots in the areas where collapses have occurred.

4.4 Study region and analysed collapses

East Sussex and its white chalk cliffs are very prone to collapsing. Starting in 2016, the area from Seaford (grid reference: TV 48254) to Birling Gap (grid reference: TV 55384 96110) was monitored, in ways of following media reports and any information that might be published on cliff collapses. In the years 2016 – 2018, five collapses were reported in the media, of which three are presented in this Chapter. Whilst large collapses are often reported throughout the year, multiple smaller collapses occur unobserved and unreported – often because they happen in unprotected areas, where no continuous monitoring is available. The Sentinels 1A and 1B data have been used to process and analyse the areas of the abovementioned collapses, for specific periods that will be discussed in subsequent sections.

Figure 4.2. Map with locations of the reported in media collapses in East Sussex in years 2016 – 2018

Table 4.2. List of analysed collapses in East Sussex in years 2016-2018

Collapse date	Collapse area	Grid reference
24/05/2016	Brass Point, Seven Sisters	TV 53335 96984
21/06/2017	Seaford Head	TV 49663 97656
04/08/2018	Birling Gap	TV 55424 95910

4.4.1 Collapse at Brass Point, 24 May 2016

The first major collapse recorded during this research programme happened on 24 May 2016 at Brass Point (TV 53335 96984), which is the fourth hill along the Seven Sisters section. The Brass Point area (Figure 4.3) is a coastal cliff section where the top of the cliff is covered by short vegetation; the hill is situated within the South Downs National Park. The collapse produced between 5 to 10 m of cliff loss, with length of about 170 m, and its total volume has been estimated at 105 000 m^3, assuming 20% bulking factor, following the methodology of Duperret et al. (2004). During the site investigation in June 2017, debris from the collapse was still present at the cliff base and was visible from Hope Gap. The most likely collapse mechanism is simple vertical fall that would have started from joint sets in Seaford Chalk formation. These joint sets form sub-parallel to the cliff face, progressively opening and leading to failure. The photographs of the collapse in Figure 4.3 were reported in the Eastbourne Herald in 2016 (https://www.eastbourneherald.co.uk/news/dramatic-pictures-show-cliff-fall-1-7401798).

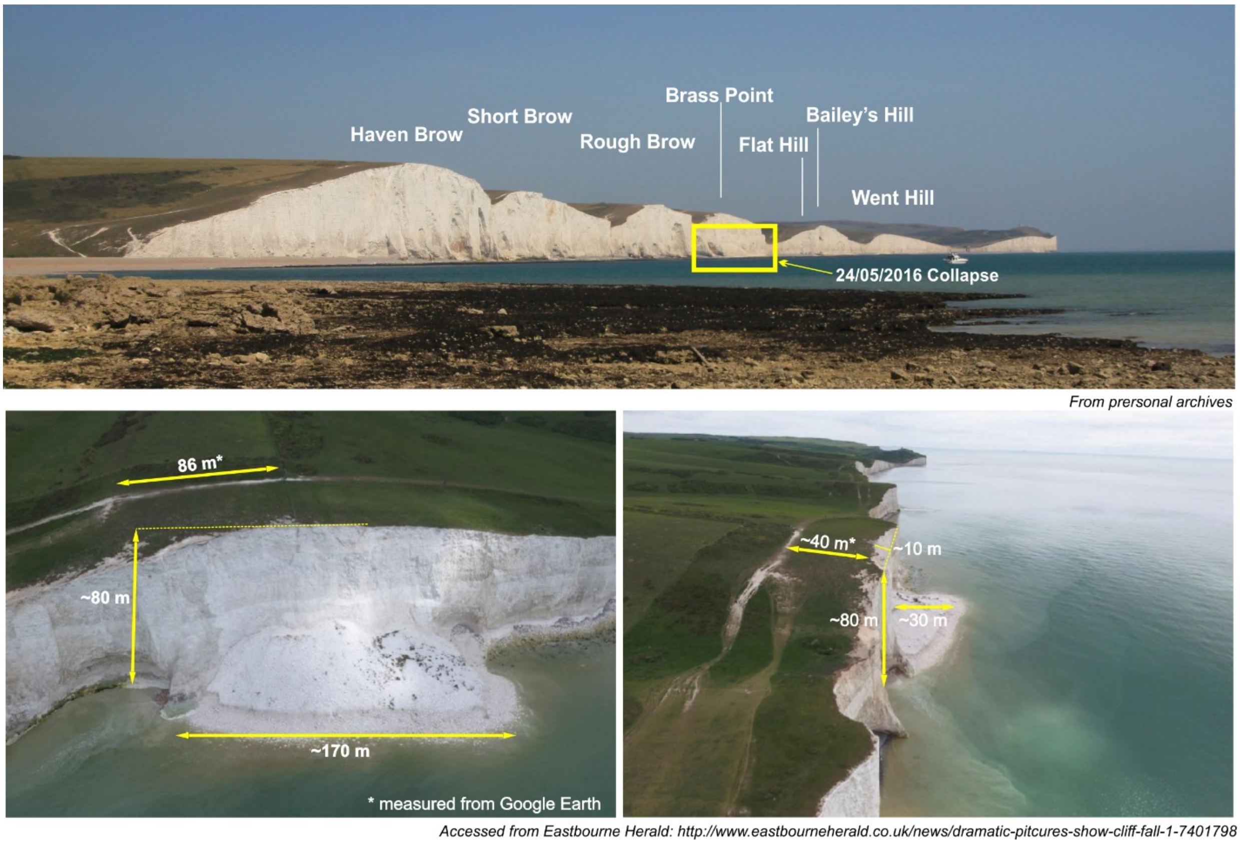

Figure 4.3. Photographs from the collapse on Brass Point, on 24 May 2016

4.4.2 Collapse at Seaford Head, 21 June 2017

This collapse occurred during the hottest period of summer 2017. It consisted of three consecutive collapses, first on 21st July 2017, followed by a second and a third on 22nd July 2017. Cliff loss was estimated to be up to 10 m, and total collapse volume of about 68 000 m^3. The photographs (Figure 4.4) of the first of the three events were reported in the media. The suggested collapse mechanism is a complex collapse, since two formations, Lewes Nodular and Seaford Chalk outcrop within the cliffs.

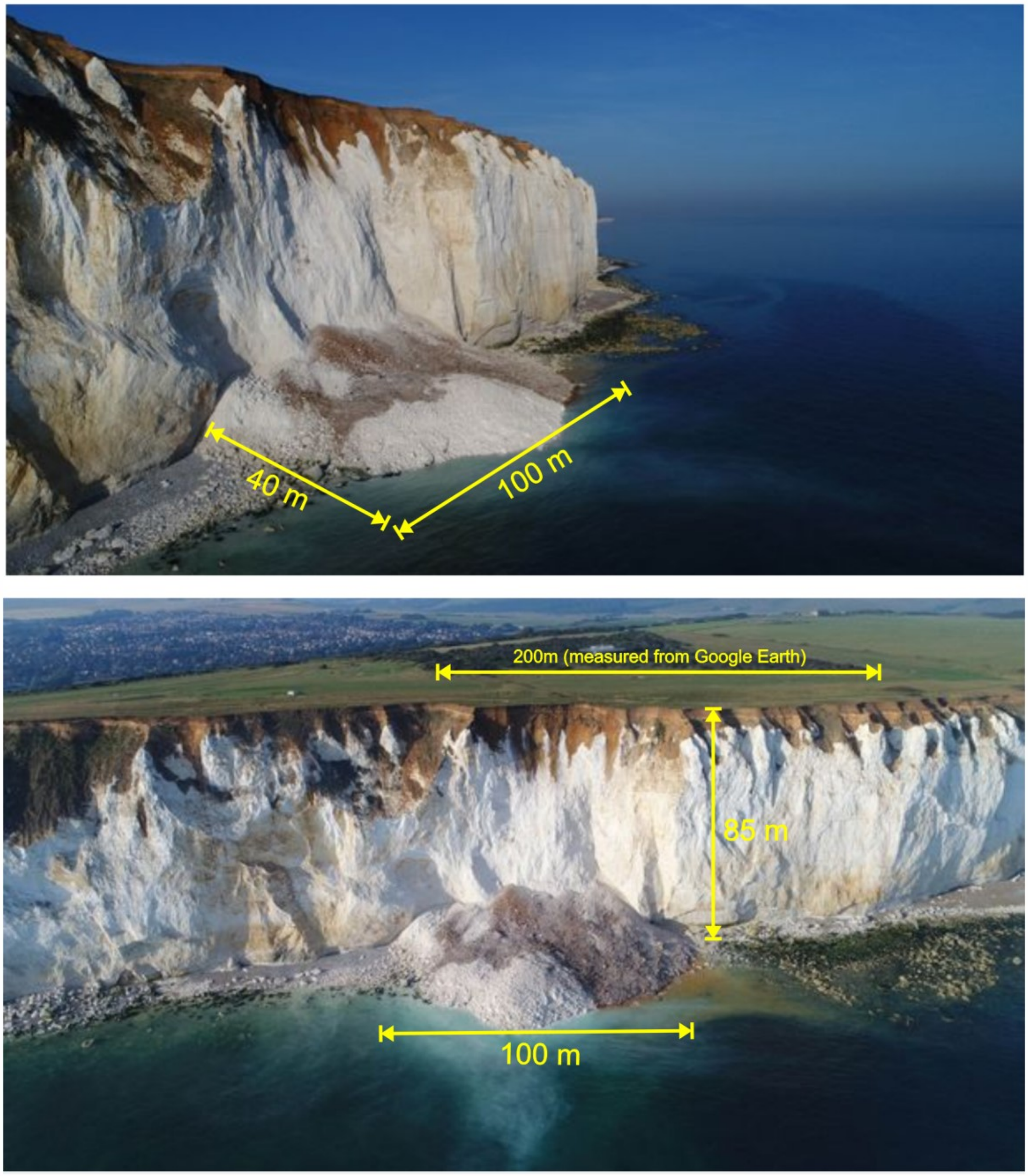

Figure 4.4. Photographs of the collapse from 21st June 2017, near Seaford Head, accessed from http://www.mirror.co.uk/news/uk-news/cliff-collapses-50000-tonnes-chalk-10662930#ICID=sharebar_twitter

4.4.3 Collapse near Birling Gap, 4 August 2018

This collapse occurred on 4th August 2018 and also happened after a very hot summer (similar to the collapse from 21st June 2017). This collapse was in close proximity to a fault running through the site, which is visible on the photographs (Figure 4.5). Compared to previously described collapses, this was a relatively small event, taking between 2 - 3 m of the cliff, and showing only about 15 m of debris in front of the cliff face and estimated volume of 1080 m^3.

Figure 4.5. Photographs of the cliff collapse near Birling Gap on 4th August 2018, accessed from bbc.co.uk, taken by Eddie Mitchell

4.5 Results and discussion

Three cliff collapses between 2016 and 2018 that has been analysed within this study is presented in this section. The PS points have been examined to monitor ground level change with time, with a focus on the 3-4 month period before and after the cliff failure has occurred. The aim of evaluating the time-series before the event was to assess whether there are any visible precursors prior to the cliff failure. The expectations were that due to the fracture dilatation and/or water saturation of the rock mass before the collapse, there should be some noticeable or detectable ground movement that might appear on the time-series. The analysis of the data after the collapse aimed to investigate if any post failure movement or rebound occurred after a significant amount of the rock fails is recorded.

4.5.1 Brass Point collapse, 25 May 2016

The Brass Point Collapse time-series was analysed between December 2015 and December 2016 and based on 39 SAR scenes. Two plots have been created, one including PS points located on the top of the cliff, up to 100 m inland and a second one including PS pointed located on the cliff edge and in front of the cliff face. The rationale for considering data points on top of the cliff, up to 100+ m away from the cliff edge, is that research published by Busby and Jackson (2006) involved an azimuthal resistivity approach and potentially identified movement of the rock mass up to 50 m from the collapses. Busby and Jackson (2006) considered that these observations where the result of the continuous fracture network within the chalk rock mass, so that events occurring at the cliff edge, were detectable further away.

The plots for every collapse have been analysed to discuss three main elements: pre-collapse movement, post-collapse movement, and post-collapse stabilisation. Additional explanations for the processes and limitations are also discussed.

The data on Figure 4.6A shows points on the top of the cliff and up to 100+ m away from the cliff edge. These PS points have been chosen to test whether a movement can be detected further inland, due to the connected fracture network within the rock mass. Prior to the collapse, until about April 2016, very little ground movement can be observed, showing that the area is relatively stable. Just within a month prior to the collapse, the data shows slight upwards (towards the satellite) motion, however it is only 1-2 mm, close to detection limits. Looking at the movement post-collapse, a small upwards trend can still be seen up to 3 months after the failure (until about September 2016). This might be related to post-collapse stress release within the rock; however, the movement is below 3 mm within 3-4 months' time, which makes this interpretation inconclusive. The ground movement 4+ months after collapse (after September 2016) shows relatively little ground movement, similar to the time interval before the collapse event has occurred.

Figure 4.6B shows results based on the PS collated in front of the cliff face and extending on the platform up to 100 m towards the sea. Similar to the previous plot, the time prior to the collapse, during the first 2+ months, show very little movements, the average oscillating around zero value. A month before the collapse, small, but visible movement upwards, towards the satellite of approximately 2 mm can be observed, which is close to the limit of the accuracy of used technique. By the time of the collapse, the ground movements stabilise for about 4 months, showing very little movement. Remembering this data show cliff edge and the platform in front of the cliff face, the lack of movement after the event can be interpreted by possibly having the cliff face stable after a major amount of rock mass has fallen from it. The lack of movement in front of the cliff is less clear, this can be potentially associated with several dry months and very little vegetation being present on the shingle/rocks. Logically however, it would be expected to have small ground movement in front of the cliff, especially while the fallen rocks are being removed by the wave motion. The lack of the ground movement on the data can be explained firstly by the low number of PS points, and secondly by recalling that the data are averaged for the platform, so while some ground movement might still occur, the averaging might be taking the variation between PS points out of the trend. This would be especially true if the data values were varying rapidly between points, such as wave motion moving rocks away from the platform.

Overall, only small changes are visible in the data analysed. These may be connected with cliff collapse, but given their magnitude is similar to the detection limits of the technique, they may be associated with an actual collapse event or simply representative of a more generic constant ground movement.

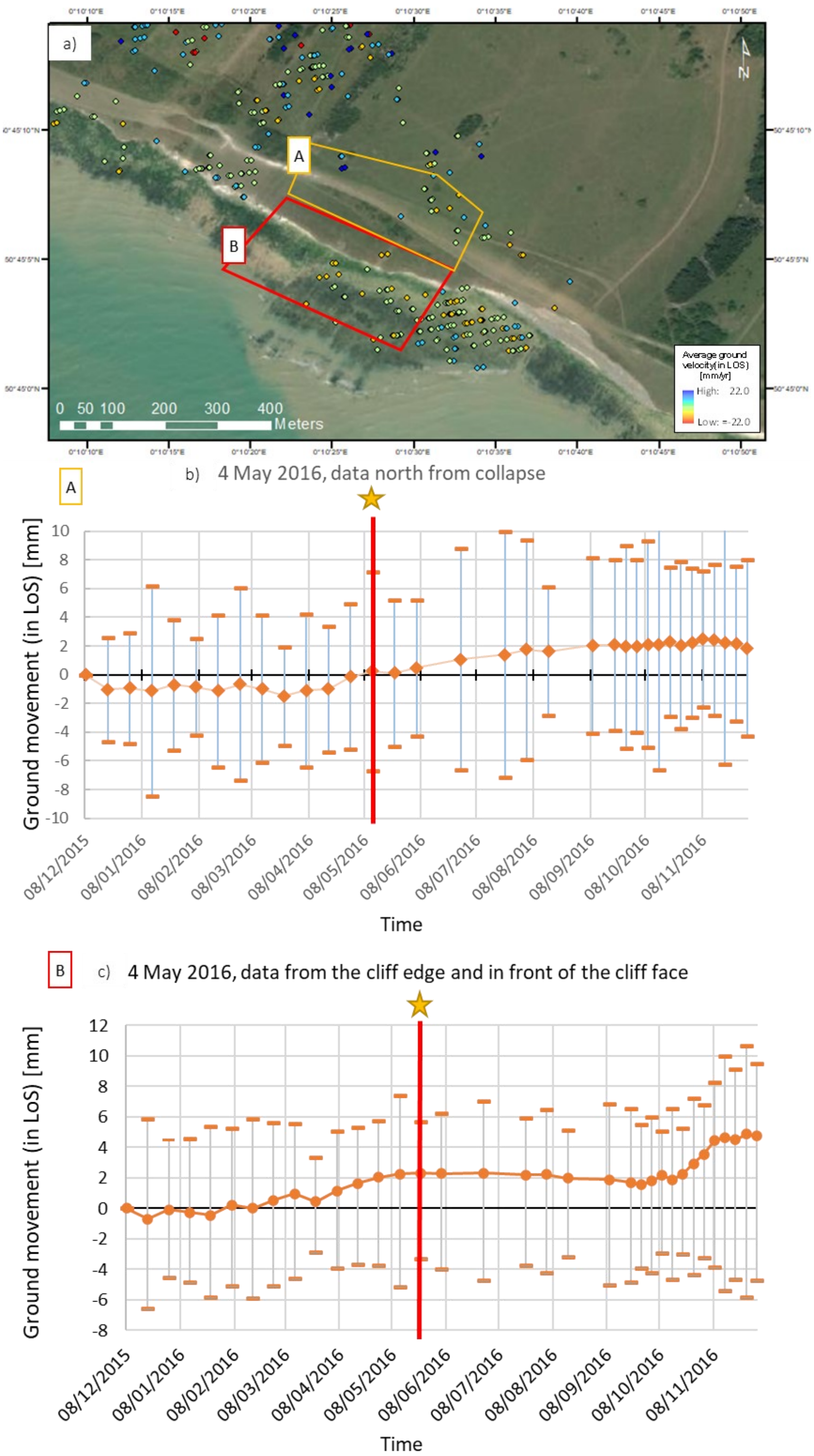

Figure 4.6. Results for the Brass Point collapse from 25 May 2016: a) aerial view of the collapse site, with the main area of the collapse marked with red polygon (B). Orange polygon (A) marks the data collected "north from collapse" that include PS points up to 90 m away from the cliff edge. Points on the aerial view are the average velocity of the PS data in mm a^{-1}: red colours represent movement away from the satellite (downward), and blue colours mean movement towards the satellite (upwards); plots of average ground movement between Dec 2015 until Dec 2016, in b) area A and c) area B. Yellow star indicated the date of cliff collapse.

4.5.2 Seaford Head collapse, 21 June 2017

The Seaford Head collapse on 4th June 2017 has been analysed using the same PS methodology as previous collapse. The analysis was based on 66 SAR scenes, collected between December 2016 and December 2017. The data plotted on Figure 4.7 represents an averaged movement of all PS points in the closest vicinity of the collapse, mainly close to the edge of the cliff and directly in front of it. Only 16 PS were identified within the area of the collapse, largely because of vegetation growth, leading to a loss of signal coherence. This area is a part of South Downs National Park and is a home to various birds, insects, and rare plants, hence it is kept as natural as possible. Due to the scarcity of the PS points in the area, all have been averaged and smoothed (with moving average) to remove noise and help to visualise the ground movement in time.

The available data show little variability with time; it is mainly consistent around zero value with very small changes that can be seen throughout the analysed period of time. There is a small upward movement (towards the satellite) of < 2 mm a^{-1}, beginning mid-May 2016, about a month before the collapse; its small magnitude suggests it is unlikely to be related to the actual failure event. After the collapse, a small downward movement (away from the satellite) is visible but, again it is within 2 mm, hence it is unlikely to be related to the actual collapse or is within the margin of error and could be related vegetation growth, seasonal changes, or atmospheric variations. Slightly more variability directly after the collapse can be observed in Figure 4.7, which could be inferred as rock mass stress relief but relating this to rock mass stress relief or any other processes related to cliff collapse is very challenging.

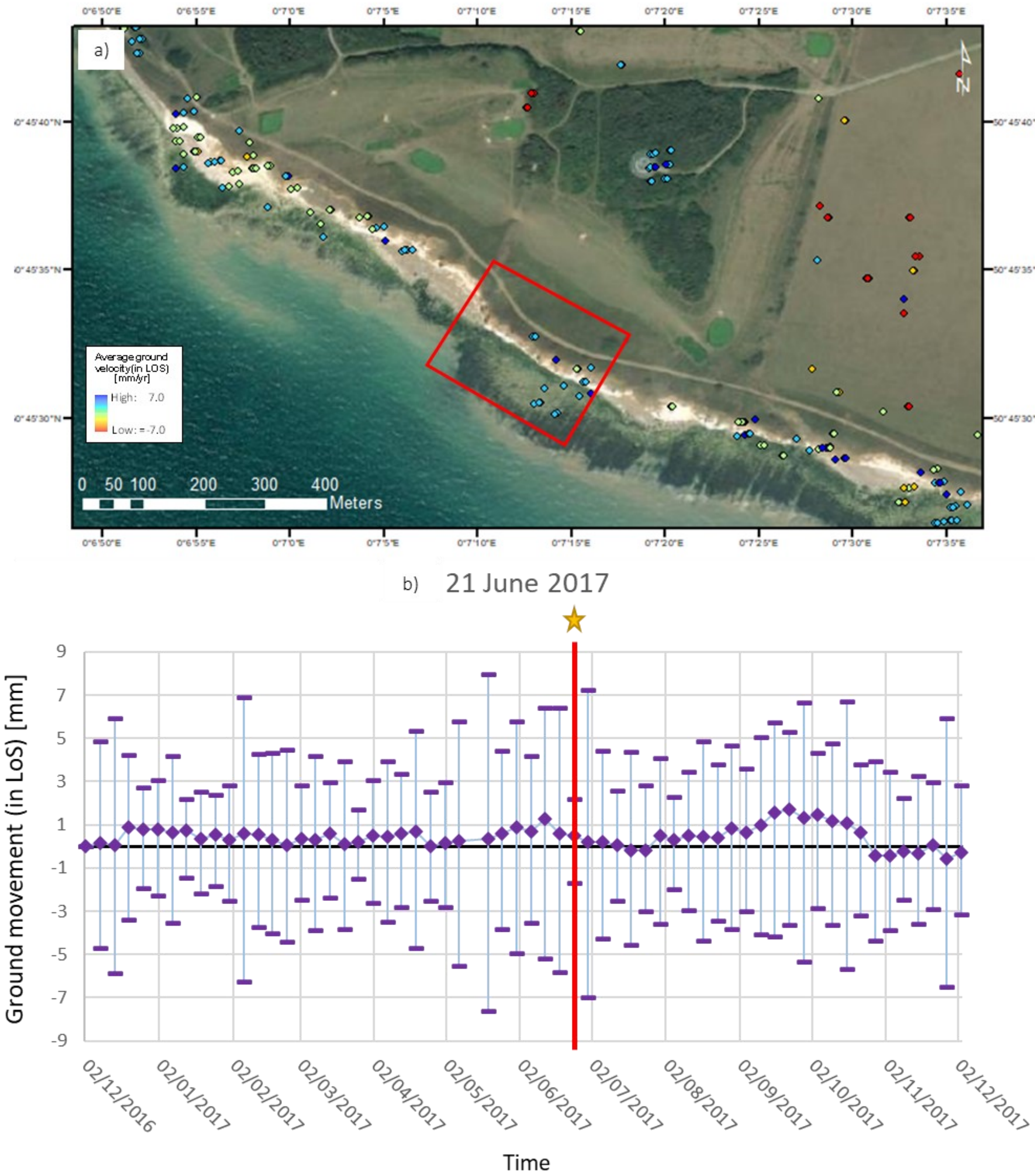

Figure 4.7. Results for the Seaford Head collapse from 21 June 2017: a) image shows an aerial view of the research site, with average velocity of the PS points on the ground in mm a^{-1}: red colours represent movement away from the satellite (downward), and blue colours mean movement towards the satellite (upwards); and b) Plot of average ground movement of the area within the red box, from Dec 2016 to Dec 2017. Error bars show the standard deviation to visualise the variability. Yellow star indicates the date of cliff collapse.

4.5.3 Birling Gap collapse, 4 August 2018

The collapse near Birling Gap on 4th August 2018 has also been analysed. The analysis was based on 62 scenes acquired between January 2018 and December 2018. Figure 4.8 shows the averaged movement of all PS that have been recorded within the area of the collapse.

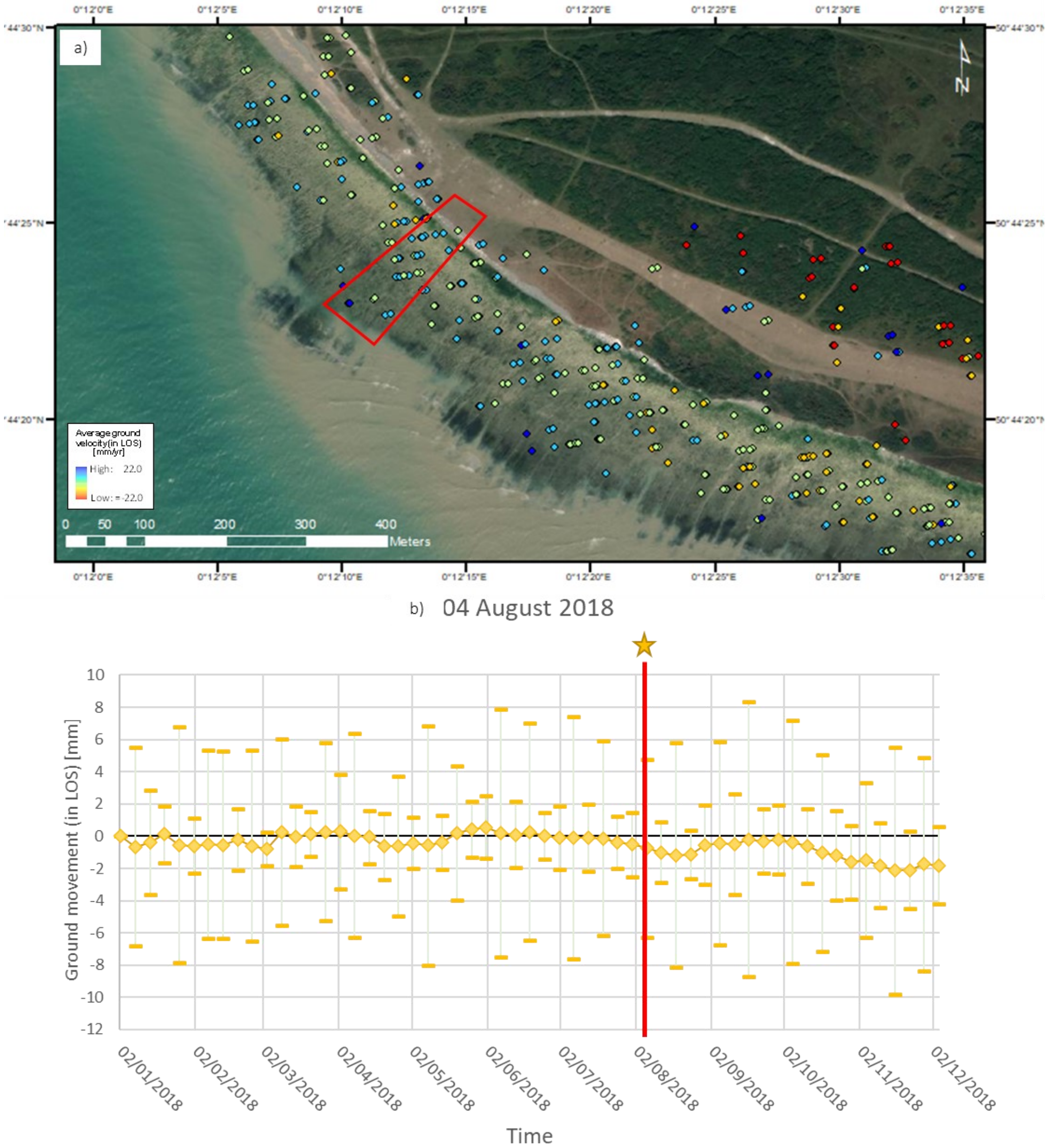

Figure 4.8 Results for Birling Gap collapse from 4th August 2018: a) image shows an aerial view of the research site, with average velocity of the PS points on the ground in mm a^{-1}: red colours represent movement away from the satellite (downward), and blue colours mean movement towards the satellite (upwards). Image b) shows an average ground movement of the area within the red box, vertical axis displaying the ground movement in mm, and horizontal axis showing the time frame during which the analysis was done (January 2018 until December 2018). Yellow star indicates the date of cliff collapse.

From the processed data, the area of the collapse is reasonably stable throughout the eight months period before the cliff collapse, oscillating around zero millimetres of the ground movement, with only small variations of less than 1.0 mm a^{-1}. There is small downward movement directly after the collapse, but it is below 2 mm, and this recovers less than a month after the collapse. This could potentially be linked with rock removal from the toe of the cliff after the failure event, but it is unlikely to be the reason for such small movement, especially seeing the upward movement in early September following it.

4.6 Discussion of the analysis of the collapse results

Analysis of the three cliff collapses in section 4.5 shows he used methodology is not optimal for achieving the expected results. While results have potential for the collapse monitoring, they are inconclusive for each collapse that has been processed and analysed. Although small movements were observed near to the collapses, the scale of the movements means it could be considered within a margin of error and it was challenging to definitively link any changes to coastal cliff collapse processes. For future work, a test site with reliable independent in-situ instrumentation to measure the collapse movement, vibration, and corner reflectors along the cliff top would be a good supplement to PSI methodology, to corroborate the results and to enable more confident interpretation of them.

In two out of three collapses (Brass Point from May 2016 and Seaford Head from June 2017) show very small, yet consistent uplift movement within about a month prior to collapse. This could be an indication that ground movement is detectable but, as mentioned previously, it is on the lower limit of this method's accuracy. The difficulty in tracking the collapses relates to processing PS data from vegetated, rural areas, where most PS have loss coherence and therefore can't be distinguished, in addition to Sentinel-1 satellites being a C-band, therefore not being able to penetrate through the vegetation. The vegetation that covers the top of these cliffs continuously grows and moves in response to climatic conditions so very few stable PS are found using this method, so reducing the value of the analysis. Several small foot paths can be seen on Google Earth maps, and it is thought these are returning good PS, but they are not sufficient to produce enough data points for the analysis.

Since the cliff faces in the East Sussex are of bare rock, mainly made of chalk, with little vegetation growing on close to steep faces, they should reflect provide plentiful scatterers, but they are firstly too steep and secondly South-facing (most orbiting SAR sensors are right-looking and therefore insensitive to North- or South-facing slopes and movements). They provide the best results for the West- or East- facing slopes. This analysis has been performed specifically on short periods of time between 6-9 months, to ensure that the vegetation does not disrupt PS creation, but despite these efforts, the results shown here do not show significant variation before and after each collapse.

Although the ambition was that this PS approach would reveal ground movement related to cliff collapse processes and in particular due to the rock mass relaxation further in land, it is unclear how far inland such movement could extend. Even though the fracture network within chalk is extensive, it is unlikely, especially for smaller collapses, that their effects would be seen more than 50-60 m inland from the cliff face.

Based on the results from case studies presented in this chapter, it can be concluded, that PS approach is not the most suitable for coastal collapse monitoring. This study used C-band Sentinel-1 satellites data, which can only penetrate down to *ca.* 5 cm from the backscatter surface, which does not provide sufficient enough depth of penetration to pass through the vegetation. An L-band satellite might be able to penetrate deeper through the vegetation and present more data – this would improve interpretation of the results. Different techniques like SBAS or SqueeSAR might be able to distinguish more PS within the area, allowing for better ground movement monitoring.

4.7 Chapter summary

This chapter has discussed an attempt to use the PSI analysis for cliff collapse prediction and monitoring. The current techniques that exist for coastal cliff collapse monitoring have been discussed in detail, followed by an introduction to the methodology that has been used in this study. The study regions were described, and three cliff collapses examined, including photographs and size description of each. Results have been presented for each case study, presenting them in a form of time series to see whether movement of the ground can be distinguished prior and post collapses and whether it can be associated with the geological processes. The results achieved show only very small ground movements, with unclear causes of them. However, the variations that is visible on the data, are consistent, therefore can be considered signal, not noise. Thus, this methodology needs more development before it can be used for prediction of the coastal cliff collapses.

Next Chapter (5) will discuss results of analysis done for monitoring coastal landslides, one of which have been published in Remote Sensing Journal.

5 Analysis and monitoring of coastal landslides

5.1 Introduction

Chapter 5 discusses three landslides and their surroundings in detail, presenting the use of PSI methodology for monitoring them, and how can this methodology be utilised to present ground movements that occur within each landslide. This chapter includes landslides which occur in both rural and urban environments: Cow Gap, Sussex (rural), Ventnor Landslide on Isle of Wight (urban) and Folkestone Warren, Kent (urban and rural) (Figure 5.1). All three of them can be classified as rotational/complex types of landslides, and they all have majority of strata within Chalk formations, with base layer of Gault Clay, which acts as a slip surface. This chapter explains the approach used in the analysis of these landslides and explains the results achieved, followed by a short discussion based on the results achieved.

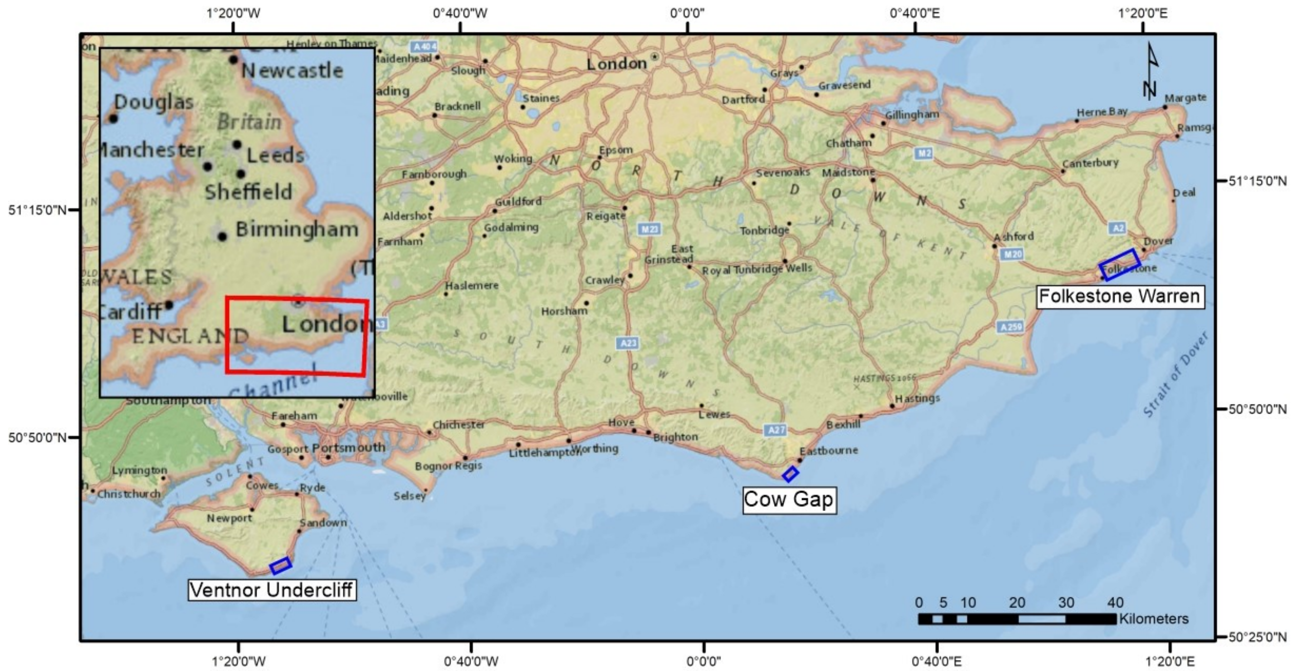

Figure 5.1. Map presenting study area. Location of three landslides marked with small, blue rectangular shapes.

As it has been described in Chapter 2, Section 2.3.3, rotational slope movements are very common within the coastal areas, and since they are usually easily accessible for site investigation, these three landslides have been chosen to represent this geological process. Since they all have similar failure mechanism, but they represent different environments (rural and urban), they have been presented as case studies, providing robust evidence for use of PSI methodology in monitoring and analysis of landslide movements.

The Cow Gap case was, in part, included in an article published in the Geoscientist, vol. 31, no. 02 (Scoular et al., 2021). Analysis of Ventnor Undercliff landslide has been published in the journal *Remote Sensing*, in Sept 2021 (doi: https://doi.org/10.3390/rs13183711).

All three case studies have been processed with SARScape PS module (ENVI, Harris Geospatial), which uses PSI methodology described in detail in Chapter 3, Section 3.6.1. Every study is different in that the number and dates of SAR scenes used varies, depending on location and timeframe for the analysis, with the details specified in Table 5.1.

Table 5.1. Initial parameters for each of the case studies presented in this chapter

Case Study	*Folkestone Warren*	*Cow Gap*	*Ventnor Undercliff*
Orbit	*81*	*132*	*132 and 81*
Period of analysis	*Dec 2017 – Aug 2019*	*Mar 2015 – Feb 2019*	*Mar 2015 – Dec 2019*
Total number of scenes	*102*	*184*	*104*
Filtered number of scenes	*37*	*93*	*80*
Coherence threshold	*0.65*	*0.65*	*0.65*

5.1.1 Past coastal landslides monitoring

Coastal instability has been an ongoing issue all around the world for many years, and new and improved monitoring methods are continuously developed with the aim of refining their quality and accuracy. Local authorities have been investing heavily in remedial works and ground monitoring techniques for coastal areas. These techniques include TLS, LiDAR, creating LSMs (Landslide Susceptibility Maps) or performing in-situ surveys. Hutchinson (1969) presented an analysis of a coastal landslide at Folkestone Warren, Kent (grid reference: TR 24988 38114), but the study focuses on stability analysis of past failures and predates current methods of monitoring the ground movement there. Bromhead (1978) presented similar retrospective analysis for slope failures in Herne Bay, Kent (grid reference: TR 17695 68217), but he also compared them to other data from field and laboratory studies. At Folkestone Warren, Network Rail has invested significantly in remedial works like sea walls or rock revetments, as well as ground monitoring with instruments like TLS to provide near-real time monitoring (Birch and Warren, 2007). At Folkestone Warren this is especially crucial, given the mainline railway line running across the landslide. In this case the availability of ground deformation measurements can reduce hazards and risks for the railway line (Birch and Anderson, 2011). Use of TLS requires an onsite specialist to run the measurements. It is limited by the dense vegetation at Folkestone Warren and the health and safety implications of the low tide window for working on the coastal (foreshore) area also needs to be considered (Birch and Anderson, 2011). Francioni et al. (2018) used LiDAR (both terrestrial and aerial) and photogrammetry data for analysis of a landslide located in Cornwall, UK between Hell's Mouth (grid reference: HY 22420 16819) and Portreath (SW 65453 45444), to highlight different kinematic failure mechanisms occurring in the area, and to help distinguish areas that are more prone to instabilities. The authors discuss the benefits of combining field surveys with data like aerial LiDAR and photogrammetry, especially in cases that are difficult to access in person, like area of this landslide in Cornwall.

Studies beyond the UK have also been performed, for example Dickson and Perry (2016), who explored machine-learning methods on coastal cliff landslides around Auckland, in New Zealand to establish their use for coastal management applications. The authors used data from LiDAR and geological surveys to create Machine Learning (ML) models to appraise and predict spatial patterns of coastal landslides. By utilising ML methods, they can avoid starting their study with an assumed structural model, as ML uses algorithms to learn relationship between response and predictors. The main outcome of this study was providing ML based results with high predictive accuracy, as well as reliably identifying variables important for landslide patterns. All of the statistical methods used in the study have shown the same predictors – unfailed cliff slopes and the distance to faults to be leading the reasoning for the landslide patterns.

Young (2015) analysed LiDAR data and GPS surveys collected for a deep-seated coastal landslide in San Diego County, California (USA). GPS surveys data for years 2008 – 2012 have been used for this study, along with LiDAR collected between 1998 and 2010. Results show LiDAR presenting good spatial coverage, but only vertical changes in elevation. While GPS data provides good estimates for 3D changes, it is limited spatially to the locations. However, using both datasets together can give a more comprehensive view of the landslide motion. For this study it was possible to distinguish the complex motion of the landslide, mark out the periods of landslide activity and when it was triggered by ground conditions being elevated. Additionally, secondary processes that could be distinguished were identified.

5.1.2 InSAR in monitoring landslides

The majority of the current published literature focuses on land–locked, rather than coastal, landslides, e.g. Yin et al. (2010) discuss the incorporation of GPS and InSAR observations for monitoring of the Jiaju landslide in China. By integrating both tools the authors were able to provide horizontal measurements from GPS data and vertical motion measurements from InSAR. Corner reflectors were installed to improve the RADARSAT monitoring in the dense vegetation cover of the landslide. This satellite only acquires scenes once per month, which limits the accuracy of the results, but the GPS observations were recorded continuously. Overall, the data collected with both methods were comparable. The authors acknowledge that more frequent InSAR data and a denser GPS positioning would improve the accuracy of the results.

Ciampalini et al. (2016) used InSAR to improve LSMs (Landslide Susceptibility Maps); the authors discuss how the LSMs are commonly affected by errors (both false negative and false positive), and how these errors can reduce the reliability of such maps. The LSM are created using GIS, with statistical and landslide inventory-based probabilistic techniques. In this study the landslide susceptibility map of the

Messina province in the region in north-eastern Sicily (Italy) has been created using MATLAB algorithms. The authors have used both PS and SqueeSAR™ (Ferretti et al., 2011), the latter using both PS and Distributed Scatterers (DS) in homogenous areas spread over groups of pixels on a SAR image. SqueeSAR increases the density of points in comparison with traditional PSI techniques, especially over highly vegetated areas. Ciampalini et al. (2016) used COSMO-SkyMed data and combined the processed results with LSM data to classify susceptibility of a landslide. Results show that adding information from InSAR can improve the area classification, but it is limited by dense vegetation. The authors recommend using L-band data instead of short wavelength data like COSMO-SkyMed (X-band), since it is better able to penetrate areas covered in vegetation.

Aslan et al. (2020) discuss using PSI techniques for monitoring and mapping of landslides in the French Alps using Sentinel-1A and 1B acquired over the period of 4 years to automatically detect and assess how active a slow-moving landslides are within the study area. The study proved that small (regional) scale InSAR can improve the classification of active landslides, and when paired with in – situ measurements and modelling it can also aid for the characterisation of the mechanical processes of such landslides.

Sajinkumar et al. (2020) use PSI as a tool for assessing changes of the beach morphology. They analyse Sentinel-1A images acquired over 15 months to monitor erosional and depositional processes along the south-west coast of India. The results show the consistency and efficacy of using the InSAR data on coastal areas, particularly since the monsoon causes annual erosion and deposition of beaches. Their results based on InSAR data complement lab testing and studies performed with SEM (scanning electron microscope).

5.2 Folkestone Warren

5.2.1 Study region

The Folkestone Warren (grid reference: TR 24988 38114) landslide is a 2.7 km long and 340 m wide active, deep seated compound coastal slope failure (Figure 5.2) that has been studied since early 1800s, mainly because of the busy railway line running across it (Figure 5.3). Published literature record landslips and chalk falls from the early 1800s to the present day (Environment Agency (2010)). Trenter and Warren (1996) describe the largest and most destructive landslip to date, "The Great Fall" of 1915. This landslip caused a reactivation of the major backscarp slip surface, moving the railway line and the land around it approximately 50 m in the seaward direction. The failure was apparently triggered by extensive rainfall and erosion of the toe, which led to three chalk falls and more damage to the railway tracks. These events forced the council to close the railway tracks for four years to repair damage (Hutchinson et al., (1980a)) but area of Folkestone Warren has been subject to extensive remedial works and continuous management ever since. These include 20 drainage headings, installation of a 3 km long seawall, beach replenishment and toe weighting. These ongoing remedial works have slowed the movement of the landslide and moderated toe erosion (Birch and Anderson (2011)).

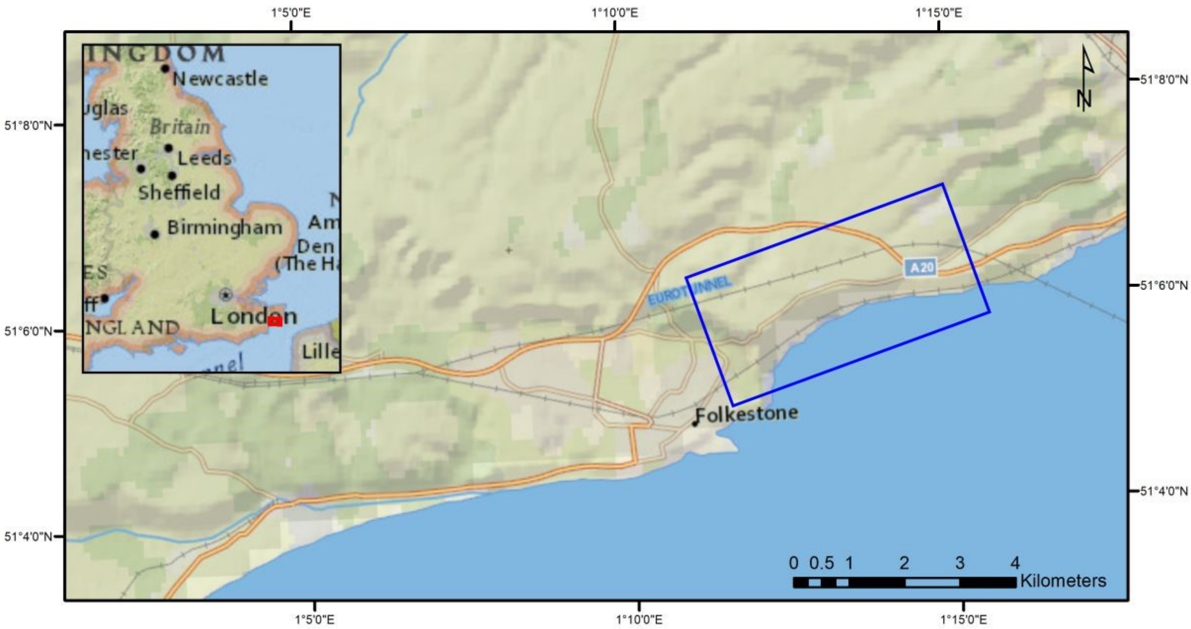

Figure 5.2. Location of the Folkestone Warren.

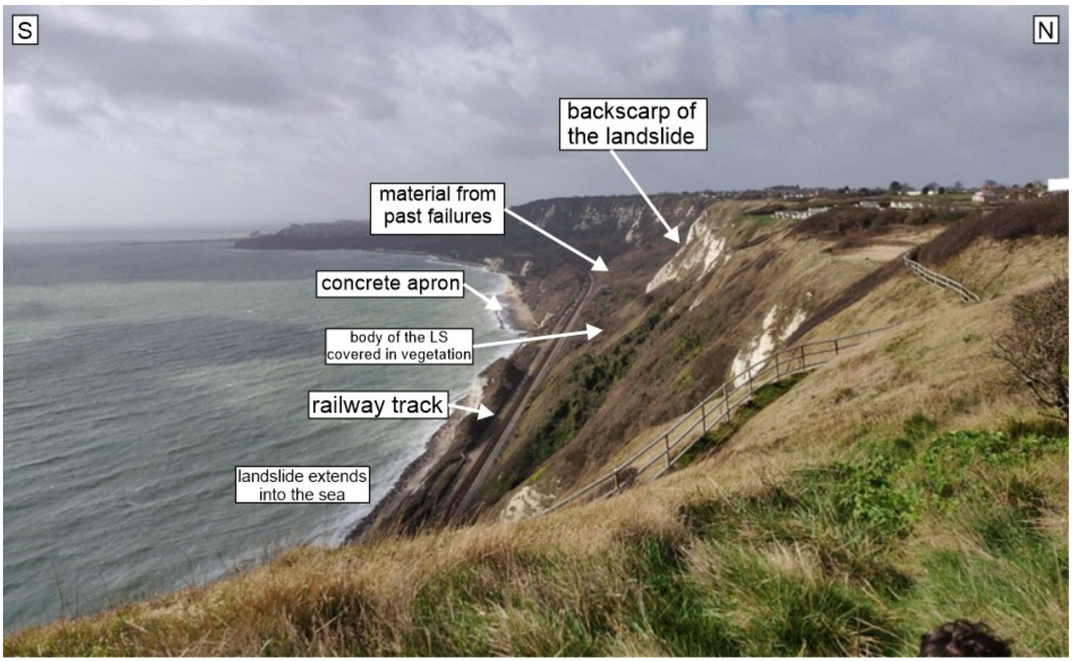

Figure 5.3. Folkestone Warren landslide (viewed from the eastern end) with chalk backscarp and railway track visible, linking Folkestone and Dover.

The body of the Folkestone Warren landslide can be split into two sections: the High Cliff and the Under Cliff (Hutchinson et al., 1980a). The landslide is mainly composed of Chalk (Figure 5.4) with the main slip surface within the Gault Clay formation.

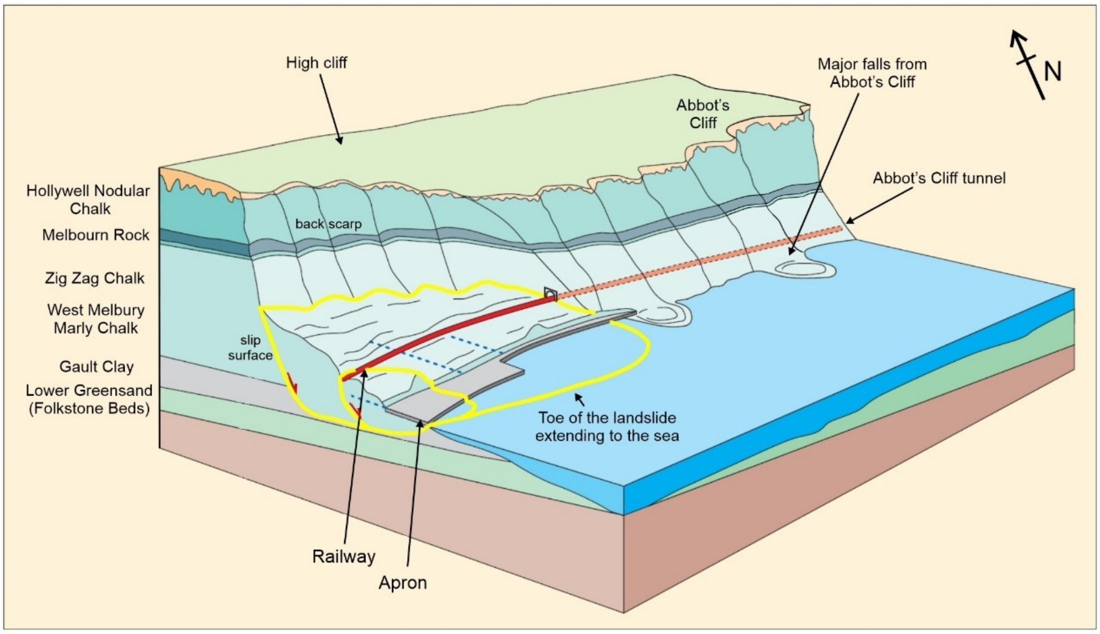

Figure 5.4. A simplified 3D model of the Folkestone Warren landslide, with a detailed geological sequence and the rotational slip mechanism. Modified after Birch and Anderson (2011).

The landslide is complex (multiple failure types) and compound (multiple failure surfaces) but the primary mechanism is rotational, with a concave slip surface and upward pointing toe. Multiple slip surfaces can be recognised within the landslide mass (Figure 5.5): slip 1 creates the main back scarp of the landslide mass, with the smaller slip 2 located 150 m to the south. Both slip zones have smaller rotational and translational mass displacements within them, which are mainly composed from chalk and clay debris. Further rotational slip is caused by toe erosion, and an increase in the mass of the Under Cliff section. It should also be mentioned that increased rainfall is a common trigger for more ground movement, since it increases ground water pressure and reduces rock strength, cohesion and increases bulk density, causing landslide failure events (Birch and Warren, 2007)).

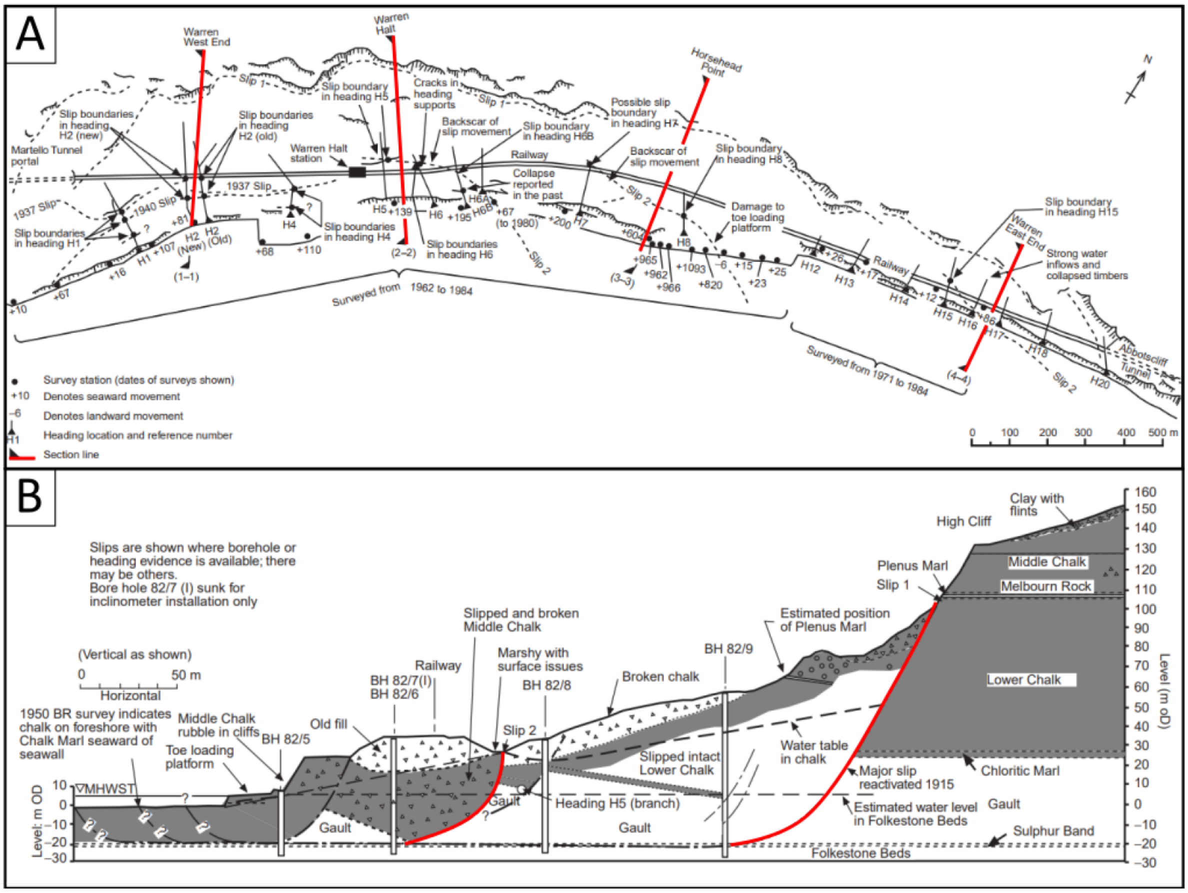

Figure 5.5. Geotechnical map of the Folkestone Warren landslide, showing the seaward movement and slip surfaces that have been explored during site investigations and geological mapping of the area; and B: Warren Halt cross section showing the complexity of the landslide and its geology. Major slip surfaces 1 and 2 are marked in red, and positioning of the toe weighting is also shown. Modified after Trenter and Warren (1996).

The area of the High Cliff is predisposed to chalk falls caused by physical weathering of the rock mass, creating major hazards, blocking the railway tracks and causing ground movements and track displacements (Bromhead and Ibsen, 2007). The precursors for rock falls are usually more apparent than slips since cracks often appear within the rock mass that can be closely monitored for further falls. Construction of Folkestone harbour to the west of Folkestone area increased the activity of the landslide, with erosion and landslips more common, due to the decrease in littoral drift of sediments eastwards to Folkestone Warren, increasing beach erosion and decreasing beach replenishment (Hutchinson et al., 1980b).

Network Rail has invested significant funds in remedial works, including rock revetments to provide sea wall support, and ground monitoring using TLS (Terrestrial Laser Scanning). While accurate, TLS measurements are relatively expensive since they require in-situ mobilisation and are limited by the dense vegetation. Borehole sampling, piezometer monitoring, site investigation surveys and hazard assessments are also regularly completed throughout the area of the landslide. These methods usually require a person present on site to take measurements, descriptions, and photographs, which is not always practical or safe. The weather may be prohibitive, with storms, and there may be a risk of new or fresh slips making the ground unstable. These can cause damage to in-situ monitoring equipment or pose health and safety risks, such as uneven ground and falls from height. PSI monitoring would therefore be useful alternative, providing not only continuous monitoring but also an inexpensive alternative method to acquire information about the site of interest.

5.2.2 Analytical approach

All scenes used in this study were acquired on descending orbit 81. The dataset covers 2 years from December 2017 until August 2019 and the processing and analysis was supported by an MSci independent project study by Bethany Grant in 2020 (Grant, 2020).

The coastal location and presence of high tides means that only scenes acquired within a two-hour window of a low tide can be used for processing, so that the platform in wave-cut front of the landslide is visible in every scene; a custom python script was written for this purpose (and was also used for the analyse of platform downwearing in Chapter 6, full script can be found in Appendix 1). The tidal information for Dover were downloaded from publicly available Tide Gauge Network data provided by the British Oceanographic Data Centre (BODC). The data for this case study were processed in the SARScape module of ENVI Geospatial with a coherence threshold of 0.65 to provide sufficient PS coverage in the highly vegetated areas.

5.2.3 Results

Much of Folkestone Warren is heavily vegetated, such that the central portion of the railway tracks produce very few PS data, and data of high coherence cannot be achieved, as illustrated in Figure 5.6; in contrast, the shore and infrastructure that surrounds it generate high density PS points. The areas on the figure marked from A-H are discussed within this section. This has allowed the ground deformation measurements to represent a good estimate of the landslide movement within the landslide mass. The Inverse Distance Weighted average (IDW) method has been used to produce average displacement maps for the area. The relatively regular distribution of PS points means that IDW produces an excellent interpolation of displacement; IDW (within ArcGIS) was used with power of 2 and search radius of 50 m. The map in Figure 5.7

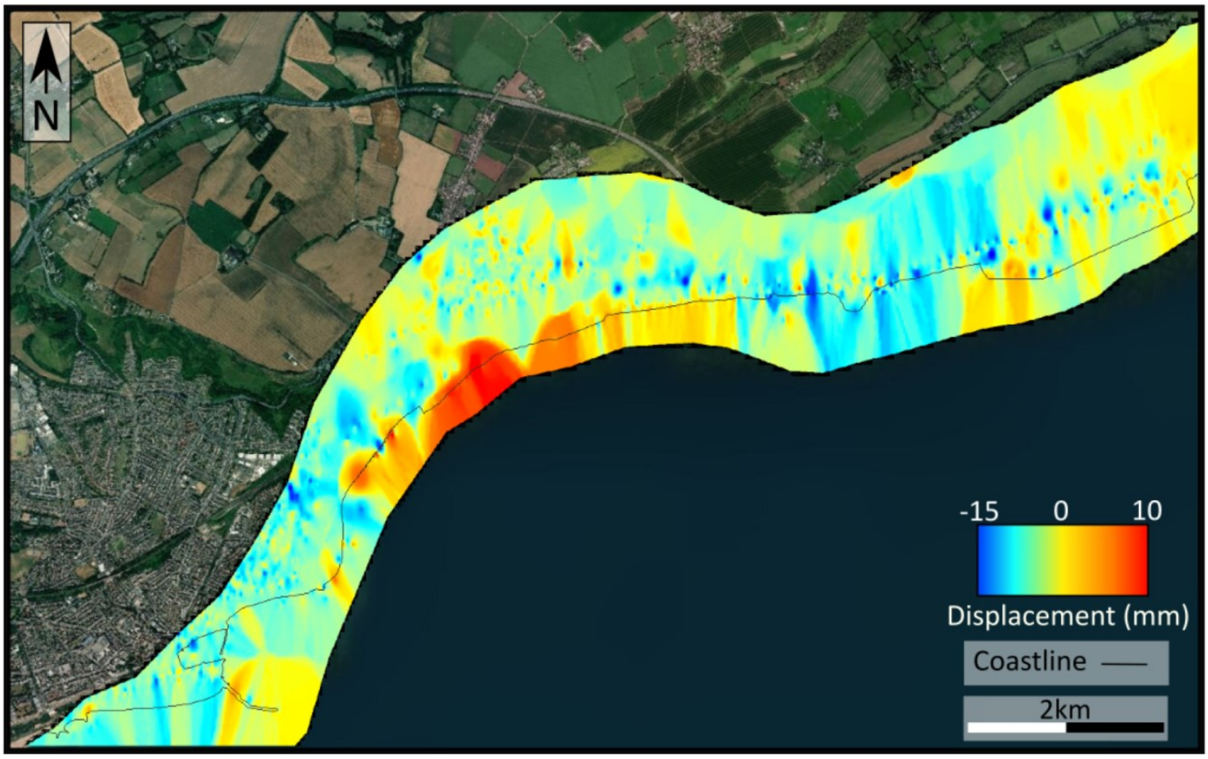

, presents results based on 2 years' worth of data. The backscarp of the landslide and railway tracks are relatively stable, with displacements of less than ± 5 mm a^{-1}, and magnitude of ground displacement decreasing to the east.

Figure 5.6. Measured LoS displacement PS point data over the Folkestone Warren Landslide, in mm a^{-1}, with some investigated areas marked on the maps. A: Western foreshore, B: Western railway tracks, C: Western High Cliff and backscarp, D: Central railway track, E: Central foreshore, F: Eastern High Cliff and backscarp, G: Eastern railway line and H: Eastern Foreshore.

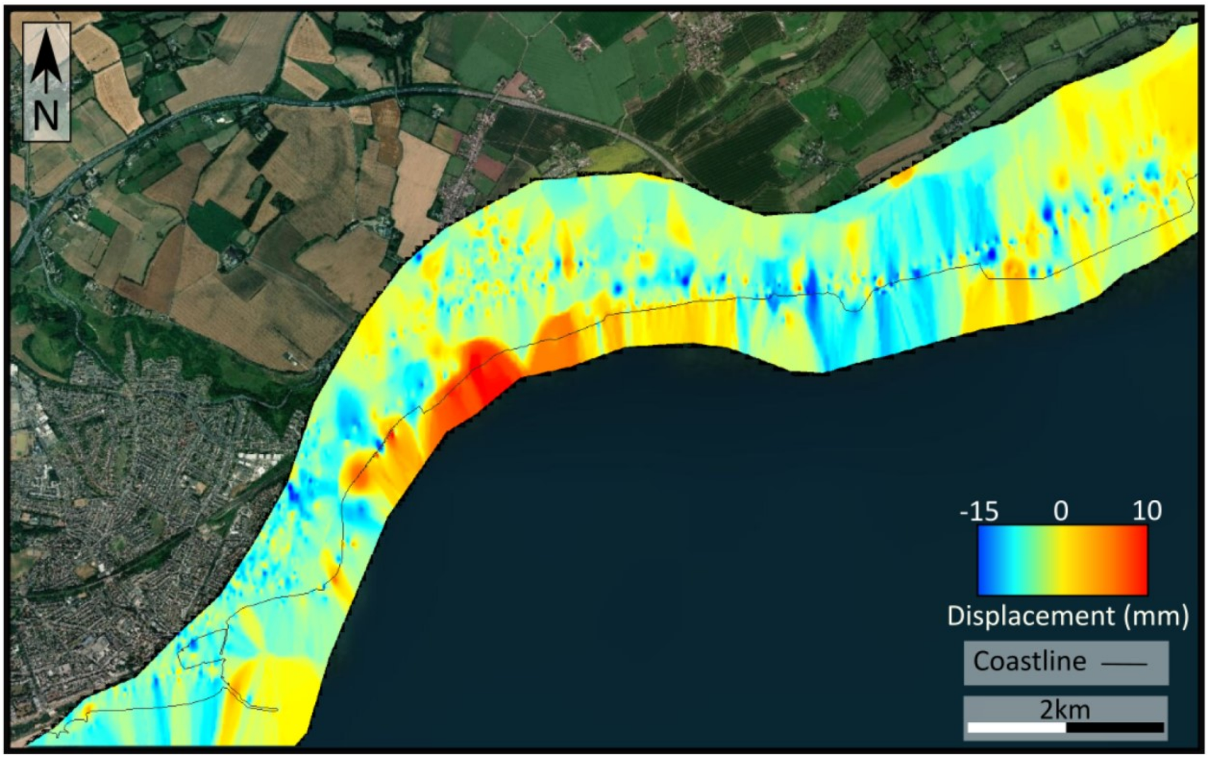

Figure 5.7. Interpolated displacement (velocity) map (produced using IDW) for the entire length of the landslide, based on processing of data between 2017 – 2019. Areas of uplift of around 10 mm a^{-1} are shown in red along the shore, green and yellow colours represent areas relatively stable.

Looking at the data from the western part of the foreshore (Figure 5.8), the greatest displacements are observed between the period of December 2017 and August 2019, with values between 5 and 15 mm of ground movement. The data show the most significant ground movement patterns between June 2018 and February 2019, with the ground relatively stable before and after this time period. The calculated total ground movement between 2015 and 2019 shows more than 100 mm of the ground displacement.

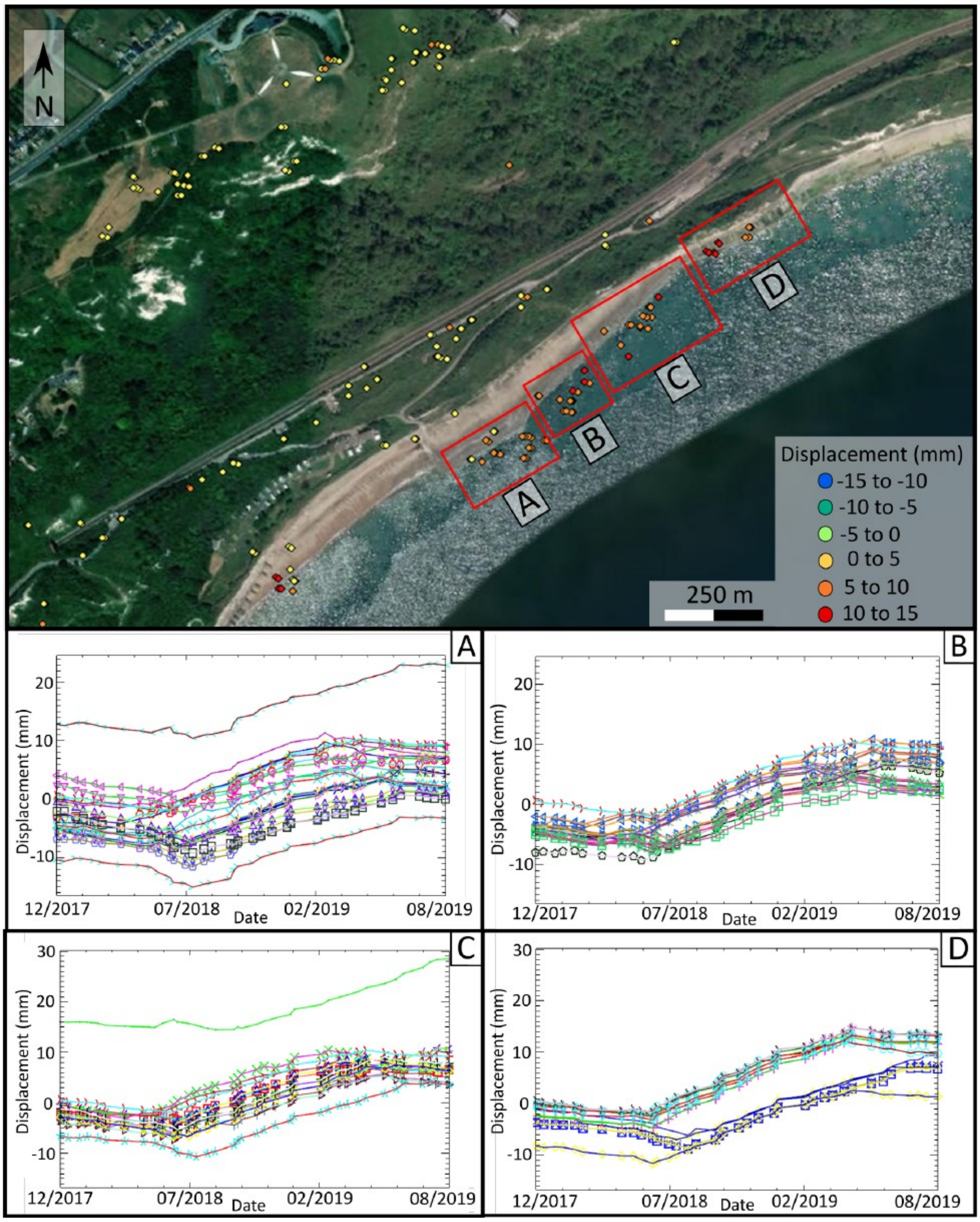

Figure 5.8. Measured LoS displacement PS point data across the western shore, with the annual ground displacement PS plotted, based on processing of scenes from 2 years period. Time series below (A, B, C and D) show the ground movement over time with upward trend, splitting the coastal area into four sections.

Figure 5.9 shows a cross-section plot for the area of the Folkestone Warren foreshore, visualising three main trends within the data. Part A shows subsidence of approximately 20 mm and part B displays heave of 22.5 mm. Overall the general trend of the ground displacement throughout the foreshore can be classified as an upward (heave) motion. The ongoing engineering works can be a potential cause of the subsidence within part A, or possibly a detached failure plane that has not been distinguished before. Considering the proximity of A and B, the latter is however not very likely. Parts B and C show similar upwards trends, with the area within part C showing initial subsidence followed by heave. The whole part C time series reveals some cyclicity within itself, which could be explained with rainfall events, which were greater during the winter of 2018-2019. Rainfall fluctuations cause changes in groundwater levels, which in turn can cause a slight increase in ground displacement and accelerated weathering of exposed chalk outcrops.

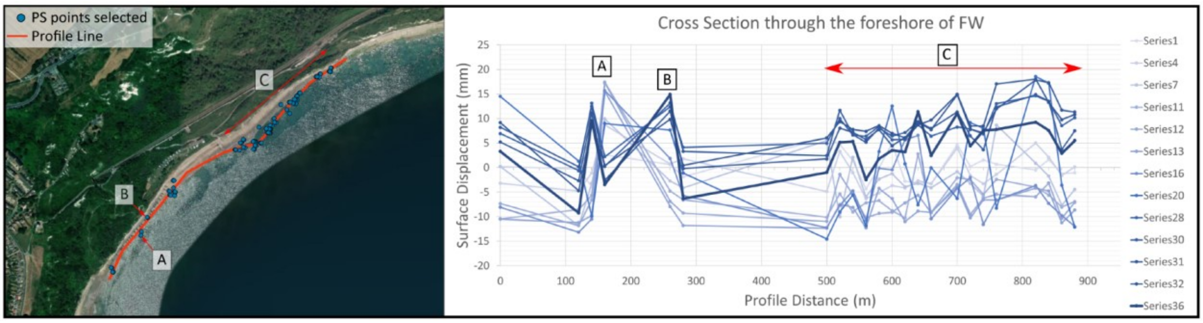

Figure 5.9. Profile of PS along the Folkestone Warren foreshore based on two-year SARScape data. The light to dark blue colours represent profiles in time to present, with the darkest blue being most recent.

Figure 5.10 shows further analysis of the foreshore area, with a cross-sectional profile running through the part of the landslide closest to the sea, roughly perpendicular to the slip direction (in the NW-SE direction). The landslide has a rotational slip surface, which explains the upwards movement that is seen along the foreshore. The geological cross-section from Trenter and Warren (1996), in Figure 5.10B shows the weighted platform located at the toe of the landslide. Their cross-section shows two rotational slip surfaces that produce the foreshore movement. When compared with PSI measurements it appears that the movement upwards (toward the satellite) is caused by the upward movement of the landslide toe, but it is unclear which of the multiple slip surfaces is responsible for the measured movement, since there are no PS data on the backscarp and very few on railway section to constrain the details of this process. Thus, the PSI data do not show exactly where the toe movement begins within the landslide. The toe movement may be facilitated by insufficient toe weight leading to rotational slip, which suggests that further remedial works (e.g., increased toe loading) should be carried out to prevent larger movements in the future.

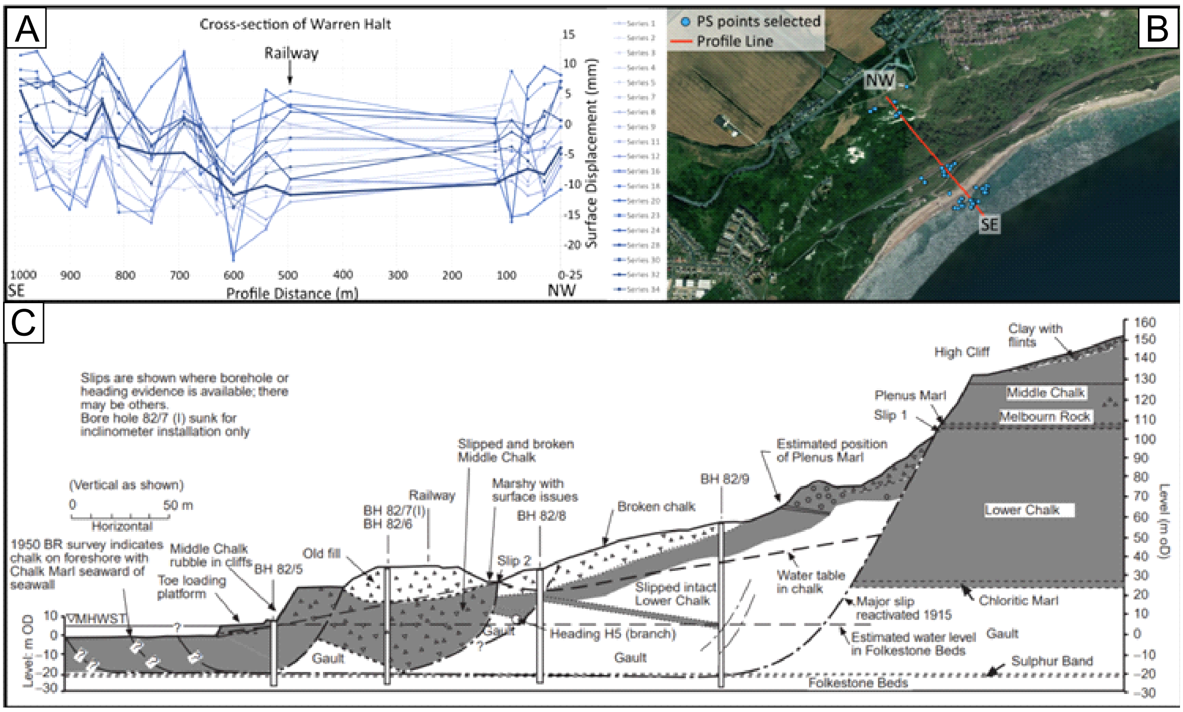

Figure 5.10. A: Profile of ground movement with distance over time, based on the two-year SARScape data processing (PS shown in B), represented by series 1 to 34. Light to dark blue colours of the lines show different profiles with time, with the darkest blue being the most recent profile; C: Geological cross-section through the neighbouring area of Warren Halt from Trenter and Warren (1996).

Figure 5.10 A, B and C reveal average ground movement along the Warren Halt cross section. The profile on Figure 5.10A has a range of movement between -25 to +15 mm of surface displacement, however displacement of each point is not easy to determine, since there is no simple directional trend. The location of the railway track can be approximated on the profile, and based on that information downwards cyclical movement can be noted within a range of 20 mm. The railway tracks are located South of slip 2, on top of the Chalk and Gault clay debris. Further from that, the velocity of the PS data shows extreme variability when looking toward the foreshore (between 800 and 900 m along the profile), and no strong trend in either direction can be determined. Additionally, the area between High Cliff and the railway tracks has no coherent PS data, so that the displacement of that area cannot be determined.

Analysis of the foreshore (Figure 5.11 (a-d)) over two years period reveals differences in magnitude of the ground displacement at different locations along the shore. The majority of the ground displacement on the landslide is within the western area (Figure 5.11b, area marked as 1), with an average movement of 6 mm a^{-1}, a similar magnitude and pattern is present within time-series in Figure 5.11c. Conversely, in Figure 5.11d the ground movement oscillates throughout the time, however by the end of monitoring period it slows down and shows little change. Even with the change in magnitude within the landslide movement from West to the East the pattern is very similar. Within a period of six months on Figure 5.11 parts 1 and 2 move about -5 mm, and then start moving upwards (towards the satellite) from July 2018. This is then followed by no significant movement from February 2019, suggesting that the foreshore becomes more stable thereafter.

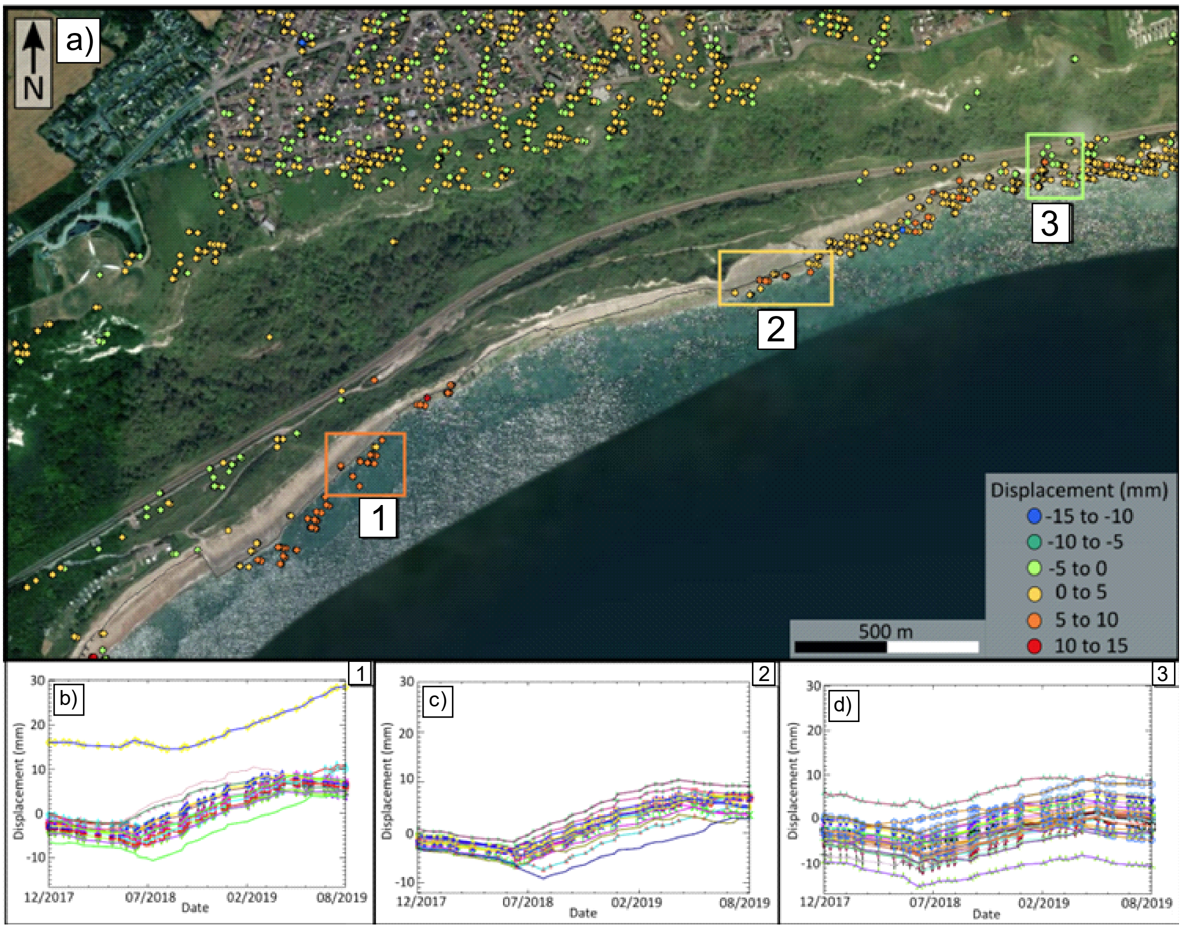

Figure 5.11. a) Map of PS distribution and displacement value from a 2-year time-series of the foreshore area, with focus areas 1, 2 and 3 marked in orange boxes. Time-series plots (b – d) are shown for focus areas 1, 2 and 3, to show the ground movement, where x-axis shows time and y-axis shows ground displacement in LoS in mm. In general, these reveal a decrease of the magnitude of the ground movement from SW to NE along the landslide.

The area of the High Cliff presents hazards of chalk falls, which in turn causes an exposure of the chalk outcrops along the back scarp, which creates potential coherent PS targets. However, due to the heavy vegetation in the area as well as rainfall, there is still only a handful of PS on the backscarp. Figure 5.12 shows a selection of PS from the High Cliff's backscarp for the 2-year long data analysis. A small cyclical pattern of ±5 mm that can be seen on the plot. Downward movement of the backscarp is expected due to the movement of the landslide along the rotational slip surface.

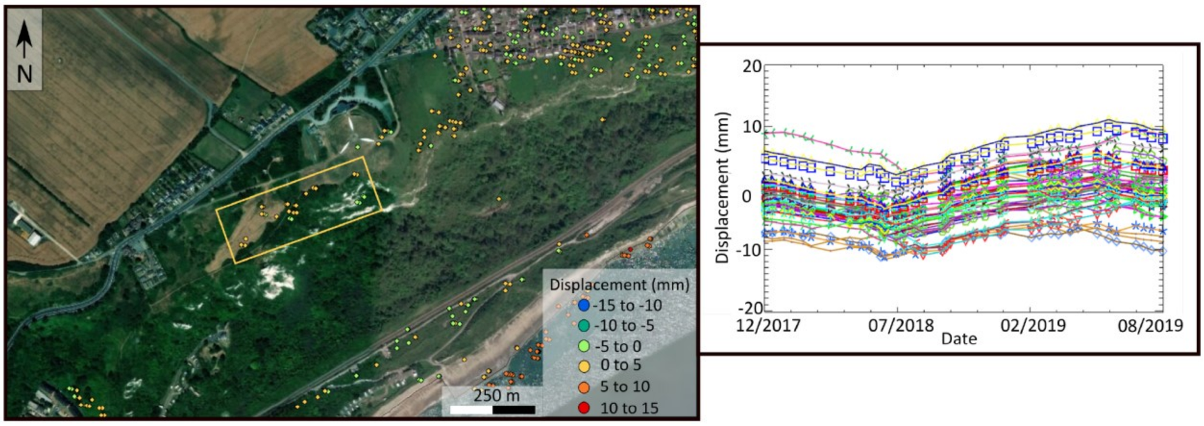

Figure 5.12. Average ground velocity per annum is plotted on the left image, based on the two-year analysis, and the time series plots showing the ground movement in mm over 2 years-time on the right. The stability of the backscarp can be seen, with small cyclical displacement.

Due to the continuous maintenance and remedial works of the railway line the coherence of PS data across the landslide is low. Even though the railway is in constant use and has very little vegetation the central part of the railway has almost no coherence (low coherence). This can be explained by up-track and down-track movement of the trains, and by the continuous remedial works that are carried out by Network Rail. The south-west part of the foreshore also has a very low number of PS data, most likely caused by the factors like constant movement of the foreshore sediments in the area and the lack of well-reflecting heavy toe weight. It is also worth noting that the longer temporal baseline between images would cause lower coherence.

In summary, analysis of the Folkestone Warren rotational landslide provides information on the ground movement of the toe of the landslide, showing the anticipated slight upward motion, indicating that the landslide is still active, and the toe is most likely being pushed by the mass of the landslide body, which has also been detected. These movements confirm the rotational character of the Folkestone Warren landslide. Even with some areas not presenting a high density of points, the ground movement is very consistent and can be used for monitoring and assessment of the stability of the area, which can be supported by in-situ measurements and site surveys.

5.3 Cow Gap

5.3.1 Study region

Cow Gap (grid reference: TV 5959 9581) is a rural site located south-west from Eastbourne in East Sussex, UK (Figure 5.13). It is a cliff section containing an active rotational landslide *ca* 1000 m long and 200 m wide. This area has no coastal defences in place meaning that the platform and cliffs are continually exposed to geomorphological processes. The landslide consists of several small slips, all of which comprise Chalk Formations overlying the Upper Greensand Formation, which BGS describes as “an unconsolidated, non-calcareous sands, chert and cherty sandstone with thin clay seams and shell beds" (British Geological Survey, 2020). These units have been deposited on top of the Gault Clay, which is a dark grey marine clay or mudstone, glauconitic in part, with a sandy base (British Geological Survey, 2020). At the top of the cliff the landslide's back scarp can be seen at the surface, and at low tide the toe of the landslide is visible on the shore platform as shown in Figure 5.14.

Figure 5.13. Location of the Cow Gap landslide, with marked cliff line in black continuous line, as well as marked main body and the toe of the landslide

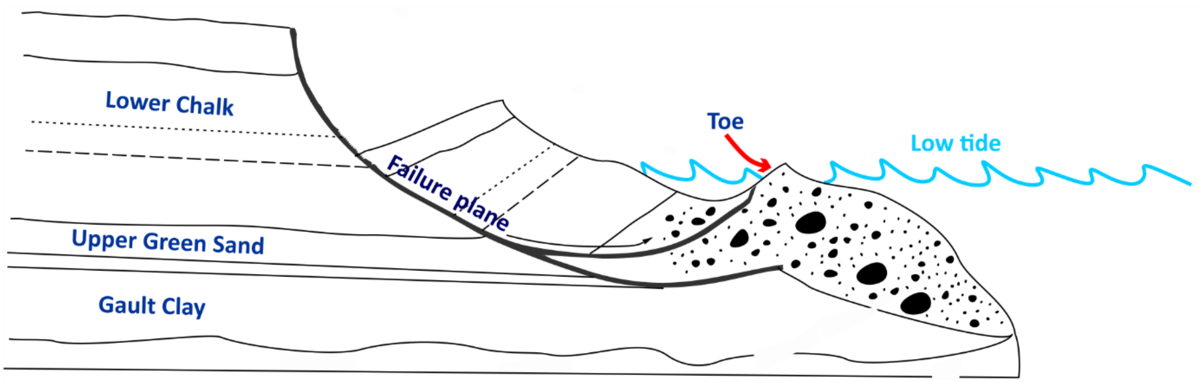

Figure 5.14. Sketch of the landslide at Cow Gap, with formations and failure plane indicated, as well as the toe of the landslide which is visible at low tide (modified after Potter (2007).

5.3.2 Analytical approach

The study is based on Sentinel-1 SAR data covering *ca* 3.5 years, from 7th Mar 2015 until 2nd Feb 2019, from orbit 132, on the ascending track. The coherence threshold has been set to 0.65.

Similarly to Folkestone Warren landslide study in Section 5.2.2, this case study benefitted from using a low-tide python script so that the wave-cut platform in front of the landslide would be visible in every scene. This approach means that 93 scenes were (out of a possible 184) were used for analysis and interpretation, but with significantly improved coherence because scenes where the platform was covered with water were removed, leading to much improved quality of results.

5.3.3 Results

The area of investigation shows a good density of measurement points (*ca* 720 points), both on the platform and at the base of the cliff. Importantly, the area of PS measurement points also includes the toe of the landslide which is visible only at low tide. The locations and motion sense of the PS points are displayed on Figure 5.15, with the red colours showing movement away from the satellite (downwards) and blue show movements toward the satellite (upwards). The main body of the landslide is moving at −8.84 mm a^{-1} on average (in Line of Sight in downward direction), while the toe moves +0.65 mm a^{-1}.

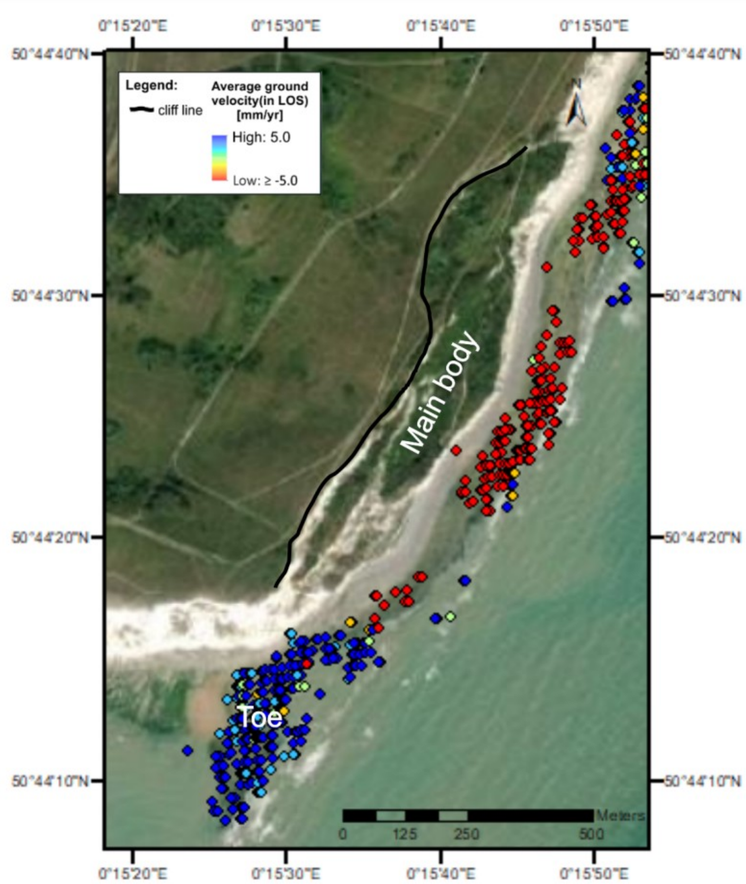

Figure 5.15. PS points across the landslide at Cow Gap, displayed in mm a^{-1}, with colour scale showing general direction of the movement; in red showing movement away from the satellite (downwards) and in blue movement towards the satellite (upwards).

The time series are shown on Figure 5.16 A and B and are presented separately for the main body of the landslide and the toe respectively. Both plots show time on the horizontal axis, from May 2015 until Feb 2019, and LoS ground movement in mm on vertical axis. In Figure 5.16A, the downward trend is prominently visible, showing the platform moving away from the satellite (down) at a higher rate. In contrast the toe of the landslide, as shown in Figure 5.16B, shows less movement (just a few mm in 3.5 years) towards the satellite. Both time series data have been averaged with a moving average of 7 scenes to remove the noise from the data and focus on the trends present within the Cow Gap area.

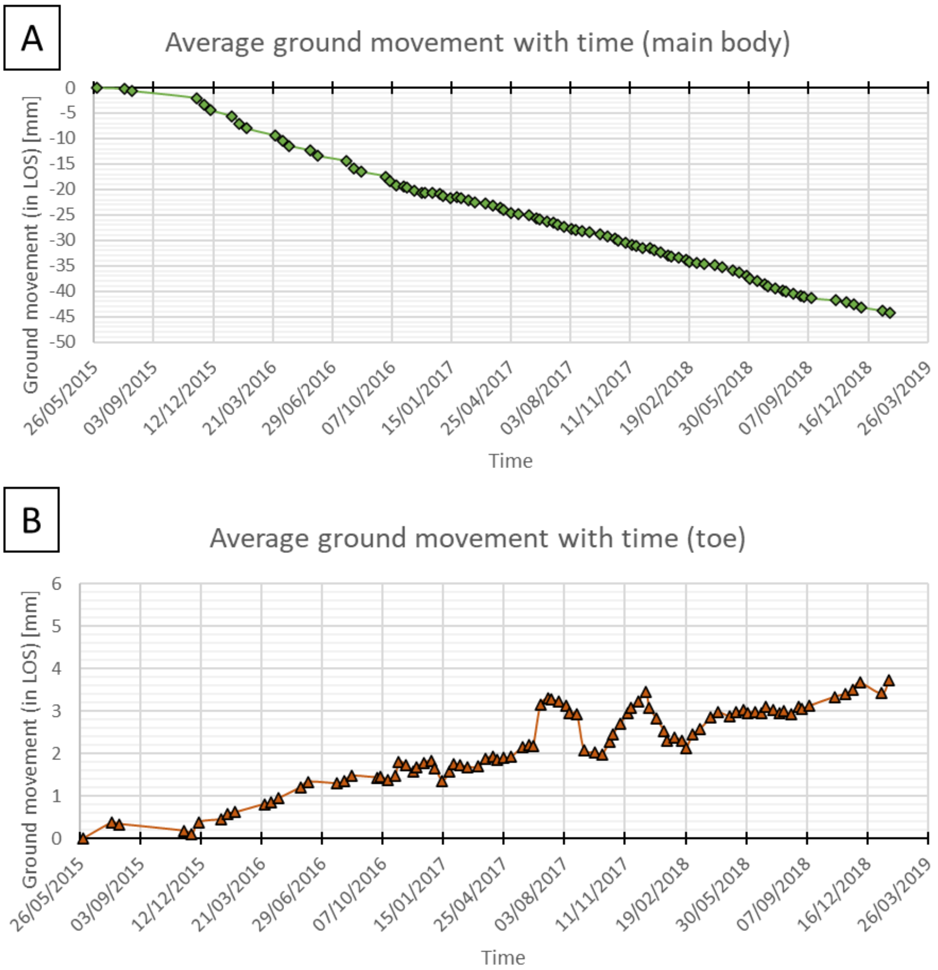

Figure 5.16. Time-series showing subsidence across the main body (A) and heave on the toe (B) of the landslide. Vertical axis showing ground movement in mm, and the horizontal axis showing time (from March 2015 until January 2019).

The ground movements in Figure 5.16A can be interpreted as a movement of the landslide mass moving downwards. Some of the movement may be associated with platform downwearing, but this would not produce more than a few millimetres of erosion over the 3.5 years of the study (see chapter x on platform downwearing for reference). The toe of the landslide seen on Figure 5.16B shows upwards (in LoS) movement of the ground, which is expected to be present in a rotational type of landslide. The movement is significantly smaller than the movement of the main body of the landslide (0.65 mm a^{-1} vs 8.84 mm a^{-1}), which is what would typically be expected from the toe of a rotational landslide. Since the main body of the landslide is where the movement usually originates, it will have higher velocity, as well as higher elevation to build the speed and distance of the movement, while the toe, located at the very bottom, will have less distance and less energy, as it will be mostly dispersed within the main mass of the rock mass.

5.4 Ventnor

5.4.1 Study region

The town of Ventnor is located on Isle of Wight, UK (grid reference: SZ 55944 77388, Figure 5.17) and has been built on a landslide complex, known as the Undercliff. The town was constructed and developed rapidly during the Victorian period to fulfil a newly expanding tourist industry for good pulmonary health in the favourable microclimate. The main town was developed on a sequence of terraces with a steep gradient. This area is known to be undergoing constant but slow ground movements which have been recorded since the early 1800's and are still ongoing in present day.

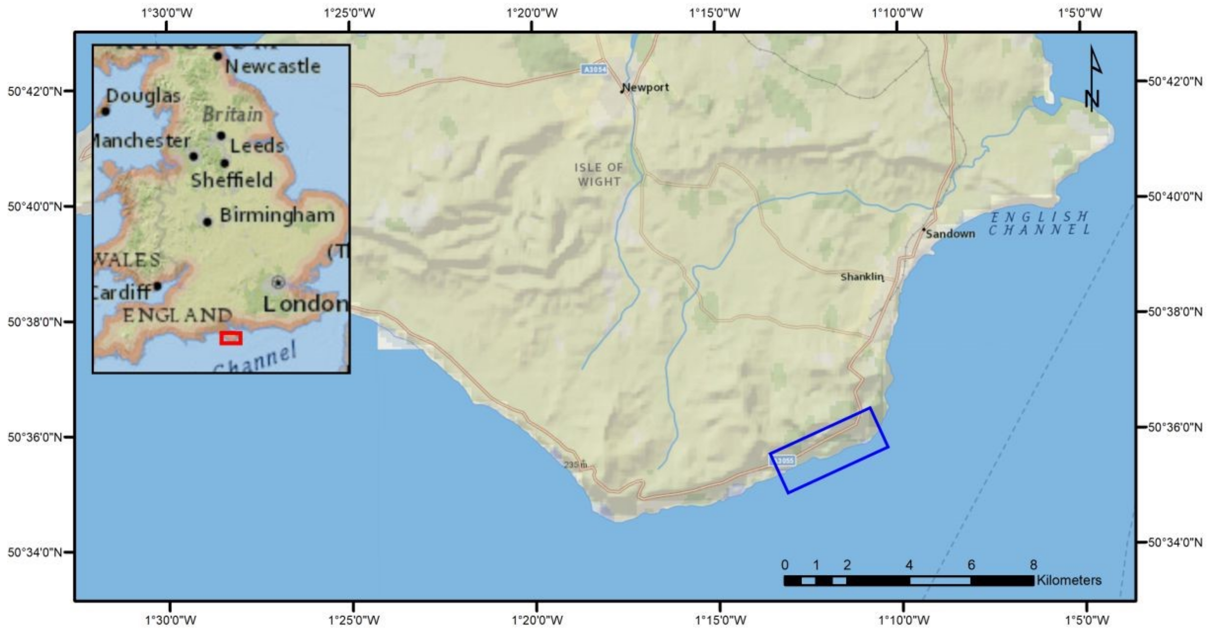

Figure 5.17. Location of Ventnor within the UK, with Ventnor town area marked with blue rectangular shape.

The Ventnor Undercliff is one of the largest urbanised landslides in Europe, and the largest in England and Wales. It is approximately 8 km in length, covering the area from St Catherine in the west to Ventnor town in the east. Several areas within the Undercliff landslide are known to be at higher risk of ground movements, meaning that any developments in the area must consider the conditions of the ground (Environment Agency, 2010). It is a complex, deep-seated landslide, which is moving at a slow but continuous rate (of 5-10 mm a^{-1} ((Carey et al., 2015)). The landslide has a rotational component at the rear scarp and main translational component, on which all failures are seated, and the whole landslide mass is moving seawards. This ongoing movement damages infrastructure, including retaining walls, roads, and underground services. The landslide requires constant management and repair, which is estimated to exceed a cost of £3 million per year (McInnes, 2007).

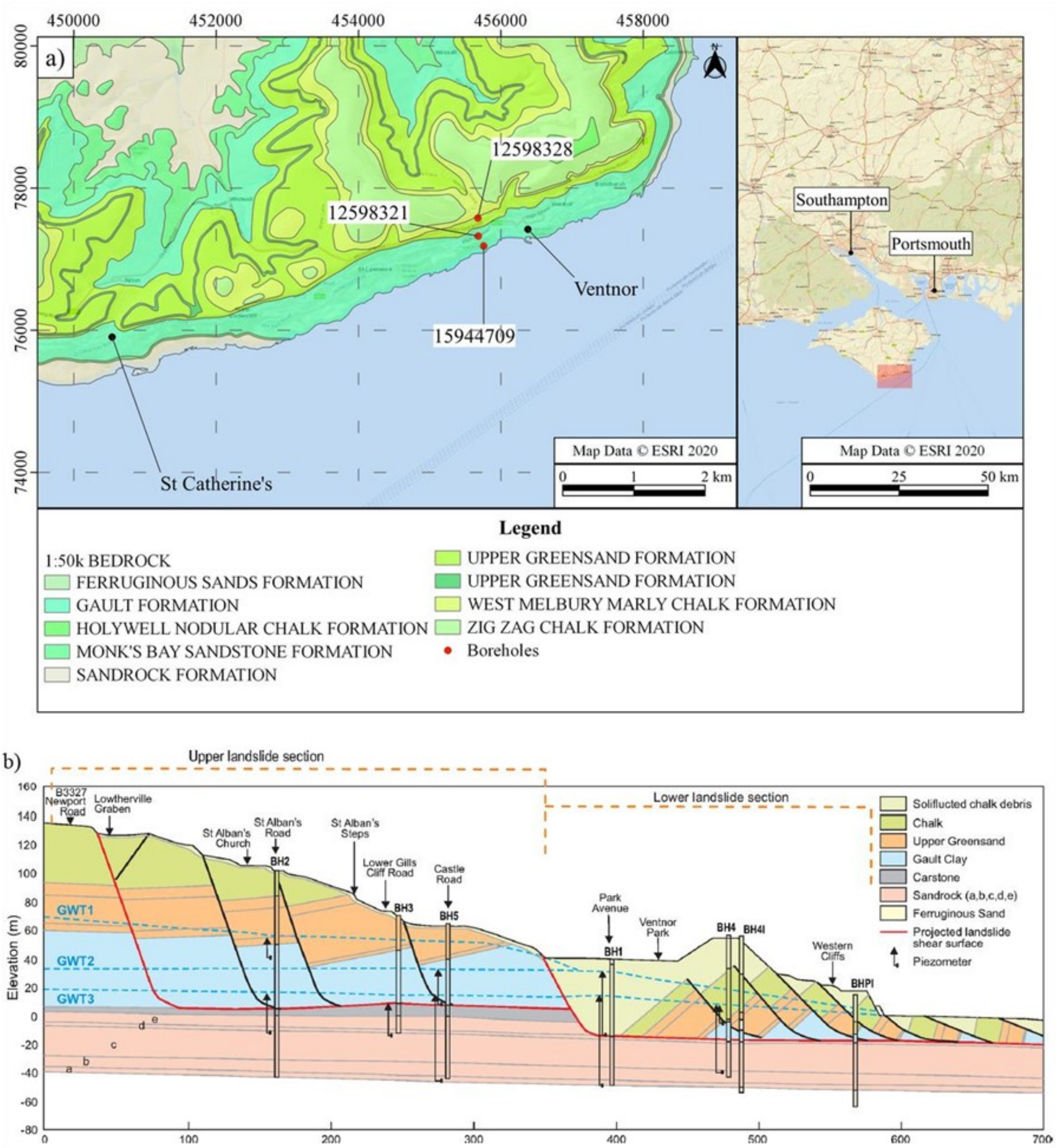

Figure 5.18. a) The bedrock geology of the Ventnor area; and b) A ground model of the landslide developed by Halcrow (2006), with boreholes from (a) aligned approximately. The ground model also shows the potential failure surface in red. The Upper landslide section covering area from Newport Road to Park Avenue, and Lower landslide section from Park Avenue all the way to the foreshore. Bedrock geology map is based on the data from BGS (last updated 2013), plotted in QGIS.

The instability of the Undercliff landslide is mainly controlled by the underlying geology (shown in Figure 5.18). The sedimentary rocks deposited during the Cretaceous period covers the majority of the southern part of the Isle of Wight, and mainly consist of alternating layers of sandstone and clay. These layers are overlain with Chalk strata. The strata in the Undercliff dip very gently seawards at about 1.5°, which further contributes to the overall instability. The landslide itself has two distinct sections, an upper section – from Newport Road to Park Avenue, and a lower section – from Park Avenue all the way to the coast. The failure plane of the landslide in the upper section lies between the Gault Clay and the Monk's Bay Sandstone. This section has a very clearly defined graben, called the Lowtherville Graben (Figure 5.19A) and historically has the largest ground movements. The lower section is less distinguishable (the landslide toe is shown in Figure 5.19 B), consisting of back-tilting blocks of Chalk debris, the Upper Greensand and the Gault Clay. The most probable trigger for the landslide movements here are increases in groundwater pressure, which are directly related to rainfall, and marine erosion of the toe of the landslide (McInnes, 2007).

Figure 5.19. Photographs of the Lowtherville Graben (A) and toe of the Undercliff landslide (B).

One of the main geological processes affecting the landslide is coastal erosion. Costal erosion has been continuously reducing the stability of the slopes of the Undercliff landslide and is especially visible when encountered in conjunction with heavy rain periods. The larger and faster ground movements tend to be seen more commonly during winter months, since rainfall is heavier and evapotranspiration rates are low, causing the groundwater levels to rise and pore-water-pressures to be higher.

The location of Ventnor town on the Undercliff landslide presents a series of hazards for the town's community. While slow, the ground movement is almost continuous and persistently causes damage to the town. The local council has developed a landslide management strategy and a systematic review of ground movement damage has also been carried out. McInnes (2007) indicated that majority of the town has been affected by negligible damage due to the ground movement (79%), while about 6% of the area has been affected by moderate damage and 15% of the town by severe damage.

The earliest mentions about ground movements in Ventnor were by writers in 1806 (Bullar, 1806) and 1818 (Albin, 1818), describing it as "the subsidence of a landslip" (Chandler, (1984)). Chandler also reports significant movements between 1960 and 1961 (totalling 0.63 m) and slower intermittent movements from 1963 – 1981, all of which were associated with high rainfall events. They were monitored by field surveys, using rod extensometers (developed at Imperial College London) in the early 1980s, vibrating wire piezometers, crackmeters, settlement cells and a weather station installed at Ventnor Park in 1990s. In early 2000, further inclinometers and piezometers were installed. Recent ground movements have been recorded and these resulted in closures and repairs to Newport Road (2013), and of Belgrave Road (2020) when a section of a wall has collapsed. Summarised results in selected areas of Ventnor are presented in

Table 5.2 5.2.

Table 5.2. A compilation of historical monitoring surveys at Ventnor, after Chandler (1984), Geomorphological Services Limited (1991), Moore et al., (2007).

Survey Method	*Location*	*Monitoring Period*	*Estimated Annual Rate of Vertical Movement (mm a^{-1})*
Benchmark Survey	Steephill Down Rd	1960–1982	29
	Newport Rd	1960–1982	28
	Albert St	1939–1960	27
	Gills Cliff Rd	1939–1982	19
	Ocean View Rd	1939–1982	12
	Bath Rd	1907–1982	11
Extensometer Survey	Newport Rd	1981–1982	20 to 39
	Havenbush	1981–1982	27 to 30
	Gills Cliff Rd	1981–1982	16
Ground Survey	Newport Rd	1988	12 to 125
	Winter Gardens	1988	30
Photogrammetry	Ocean View Rd	1949–1988	67
	Bath Rd	1949–1988	65
	Esplanade	1949–1988	20
	Belle Vue Rd	1949–1988	15
Council Records	Bath Rd	1995–2005	33
	Newport Rd	1995–2005	22

Various coastal defences have been implemented along Ventnor town to stabilise the toe of the landslide and slow down the coastal erosion (Figure 5.20). These defences include a seawall within the

Ventnor Bay area, with gravel (shingle) beach and timber groynes west of Ventnor Bay. In the west part of Ventnor town, rock armour revetments extend all the way to Castle Cove to protect steeper sections of cliffs, which consist of weak chalk debris and marls and are quite prone to the erosion. Rock armour groynes are also located within this area (Environment Agency, 2010).

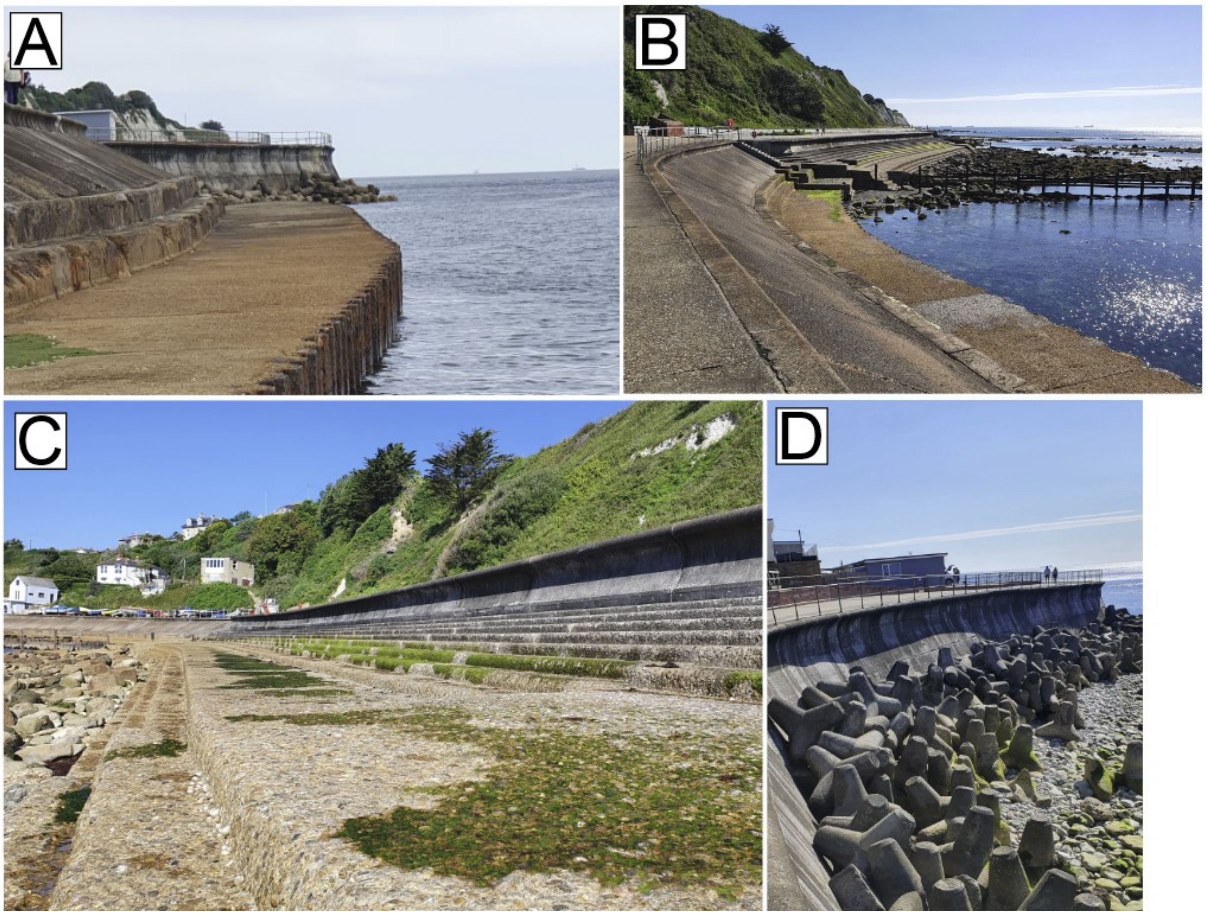

Figure 5.20. Photographs of examples of the coastal defences around Ventnor town. A: Exposed sheet piles along the sea wall, B: seawall section with old wooden groynes and small amount of shingle, C: close- up view of the seawall with steps, D: rock armour along the seawall near the marina.

Existing monitoring methods require in-situ technicians or expensive equipment and do not provide continuous spatial and temporal monitoring. PSI – based methodology has been used as an additional monitoring option since it shows great potential for future coastal management planning around the Undercliff, especially within the urbanised area of the Ventnor town.

The methodology described in next section examines the details and limitations of InSAR based monitoring and is followed with results achieved from processing of InSAR data for the area of Ventnor.

5.4.2 Analytical approach

Processing and analysis was supported by an MSc independent project study by William O'Connor in 2020 (O'Connor, 2020). It has later been published the journal *Remote Sensing*, in Sept 2021 (doi: https://doi.org/10.3390/rs13183711). This case study utilises two sets of data to calculate actual vertical and horizontal ground movements. The first set from ascending and the second set from descending orbits, rather than pure Line of Sight results.

Data from orbit number 132 for ascending track and number 81 for descending track have been chosen for analysis. Once again, only scenes acquired within two hours of low tide were used. Some 80 scenes were used in the processing for the descending orbit, and 104 scenes for ascending orbit. Both sets of data were processed with coherence threshold of 0.65. As previous in-situ works in the area of Ventnor have proved that rainfall is one of the main causes of landslide movement, rainfall data has been downloaded from the Environment Agency website for the local rain gauges at Afton and Ventnor Park. The data was kept in daily format to show any prolonged events and spikes.

InSAR data are usually processed in Line of Sight (LoS) direction only. While this method provides a good indicator of ground movement, it can be beneficial to look at true vertical and horizontal displacements. This case study therefore uses datasets from two orbits, ascending and descending which allows the true vertical and horizontal values of ground movements to be obtained. Fuhrmann and Garthwaite (2019) describe the process of decomposition of LoS values using different satellite views and geometry (Figure 5.21). Assuming the N component is running parallel to the N-S direction (follows azimuth direction), it can be neglected:

$$\begin{matrix} \boldsymbol{V_{asc}} \\ \boldsymbol{V_{desc}} \end{matrix} = \begin{pmatrix} -\boldsymbol{sin\theta_a cos\alpha_a} & \boldsymbol{cos\theta_a} \\ -\boldsymbol{sin\theta_d cos\alpha_d} & \boldsymbol{cos\theta_d} \end{pmatrix} \begin{pmatrix} \boldsymbol{V_E} \\ \boldsymbol{V_U} \end{pmatrix} \qquad \text{Equation 5.1.}$$

Where:

V is velocity, α is the orbit azimuth angle and θ is the incidence angle. V_E represents horizontal and V_U vertical velocities. For the purpose of the study, average values for orbit azimuth angle and the incidence angle were used, since the variation for those numbers wasn't significant enough to affect the results. MATLAB software was used to solve the system of equations to find the coefficients to be used later.

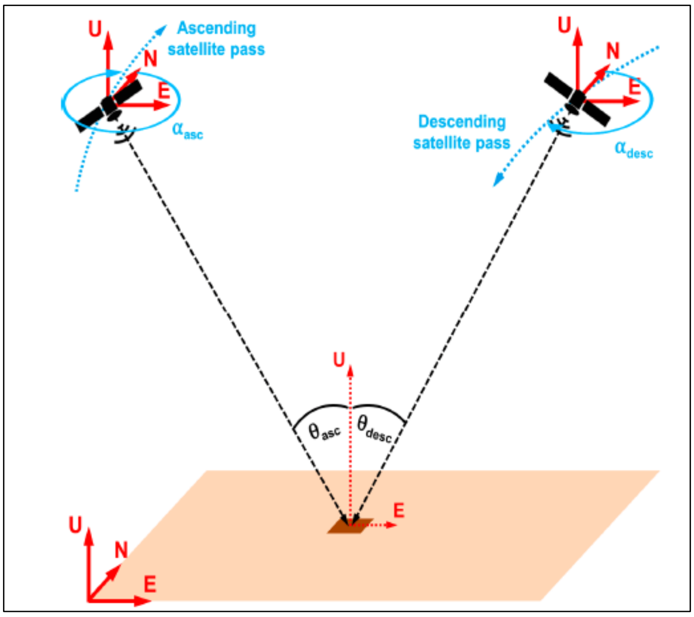

Figure 5.21. 3D InSAR geometry, based on Fuhrman and Garthwaite (2019)

Equations for horizontal and vertical velocities can be found below (Equation 5.2 and 5.3):

$$\alpha_a = 344.9° \qquad \theta_a = 32° \qquad V_E = -0.8016V_{asc} + 0.9042V_{desc}$$ Equation 5.2.

$$\alpha_d = 188.3° \qquad \theta_d = 41.2° \qquad V_U = 0.6956V_{asc} + 0.5453V_{desc}$$ Equation 5.3.

The raster calculator in QGIS has been used for calculations, with two inputs V_{asc} and V_{desc}. Wherever the rasters were not sufficiently overlapping spatially and temporally, the calculations generate errors in results. The resultant horizontal component is measured in east – west plane and not projected along local axes of the geometry of the landslide.

5.4.3 Results

Chandler (1984) carried out a one year-long monitoring study during their research. For a direct comparison between their investigation and this study, a sample of results for year 2016 has been conducted. Year 2016 has been chosen because it has the greatest number of ascending and descending scenes after running the low tide script on the dataset. Figure 5.22 shows the 2016 results, with PS plotted on the map. Only the maxima and minima of the ground movements have been plotted, $V_{LoS} > 20$ mm a^{-1} and $V_{LoS} < 20$ mm a^{-1}. The obtained results are consistent with the historical findings for the site, showing subsidence around the Lowtherville Graben and heave at Ventnor Park as expected.

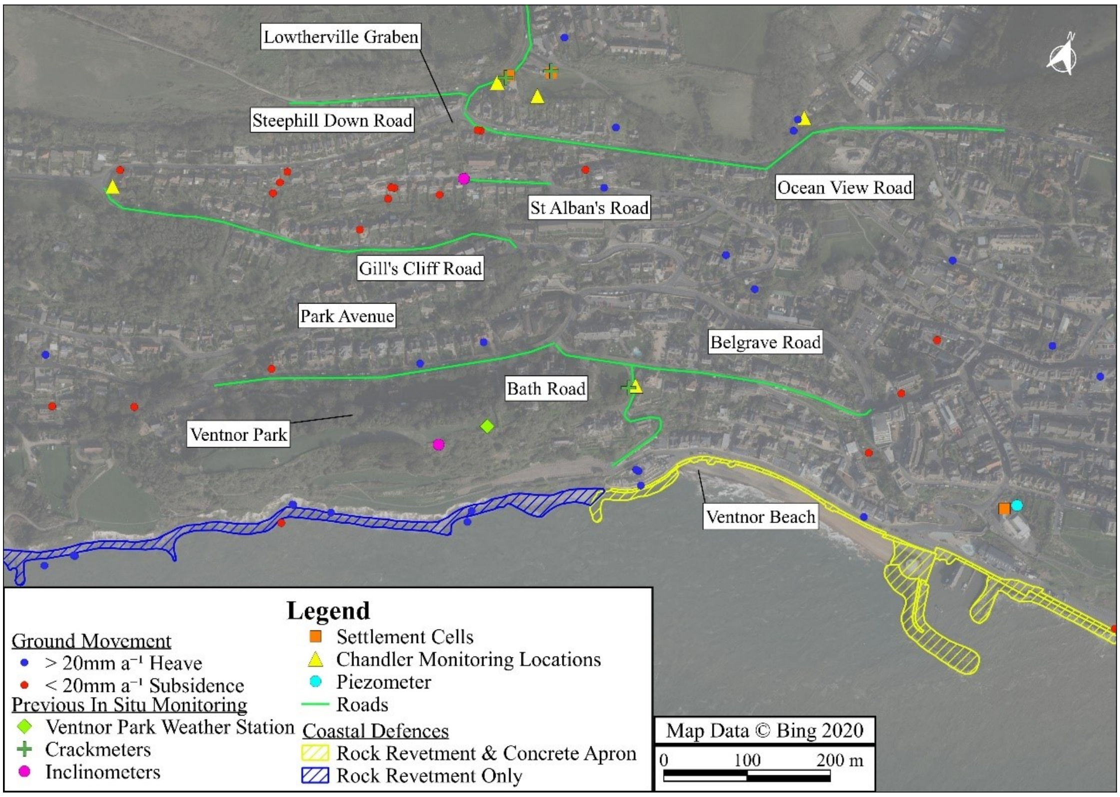

Figure 5.22. PS point displacements in LoS, based on year 2016, with only largest (>20 mm a^{-1}) and smallest (<20 mm a^{-1}) ground movements (heave and subsidence) shown (in blue and red accordingly).

The data on Figure 5.22 show the information of the ground movement in Line of Sight, which is not directly comparable to measurements commonly acquired during the field surveys. With the use of the methodology described in Section 5.4.2 (by Garthwaite et al. (2015)), the actual vertical and horizontal ground movements have been calculated for this study to provide a more accurate comparison with historical monitoring results estimated using the methodology and equations described in the previous section. The horizontal and vertical velocity is plotted on Figure 5.23 (a) and (b) respectively. These results are presented for the same year 2016 as above, so they are comparable with Chandler (1984) study.

Looking at the Figure 5.23b, a significant East – West ground movement on the landslide can be seen. This complex movement was not previously captured in the ground model by Halcrow (2006) (presented on Figure 5.18b). To aid the investigation of the nature of the ground movement, a 2D ground model was created from publicly available borehole records from the BGS. These show a failure surface at approximately 3° incline, dipping to the east at the depth of 0 m OD. The failure surface is encountered within the Gault Clay and Chalk debris. Figure 5.24 presents the 2D model with the failure surface added, illustrating how the overlying block of sediment slides eastwards along the surface, with the block of material below the failure surface being stable. Throughout the town of Ventnor, a similar East – West movement can be observed. This is not considered to be significant due to more robust coastal defences present in the eastern part of the area. It is possible that these movements are second order movements triggered by more significant sliding mechanism in the North – South direction that would produce lateral spread. These are however not picked up by the SAR satellites due to the near-polar orbital geometry and east/west viewing geometry of Sentinel-1. By analysing the 2D model and comparing with the PSI results it can be concluded that the results are reasonably well aligned, proving that PSI models can distinguish potential surface failures when paired with in-situ investigations. The range of true vertical and horizontal movements are presented in Table 5.3. The vertical movement being within a range of -16.9 to 14.5 mm a^{-1}, and horizontal movements within slightly wider range from -18.7 to 30 mm a^{-1}.

Table 5.3. A summary of minimum and maximum results for vertical and horizontal ground movements during year 2016

Time Series	*Value*	*V_U (mm a^{-1})*	*V_E (mm a^{-1})*
2016	Min (Subsidence/West)	-16.9	-18.7
	Max (Heave/East)	14.5	30

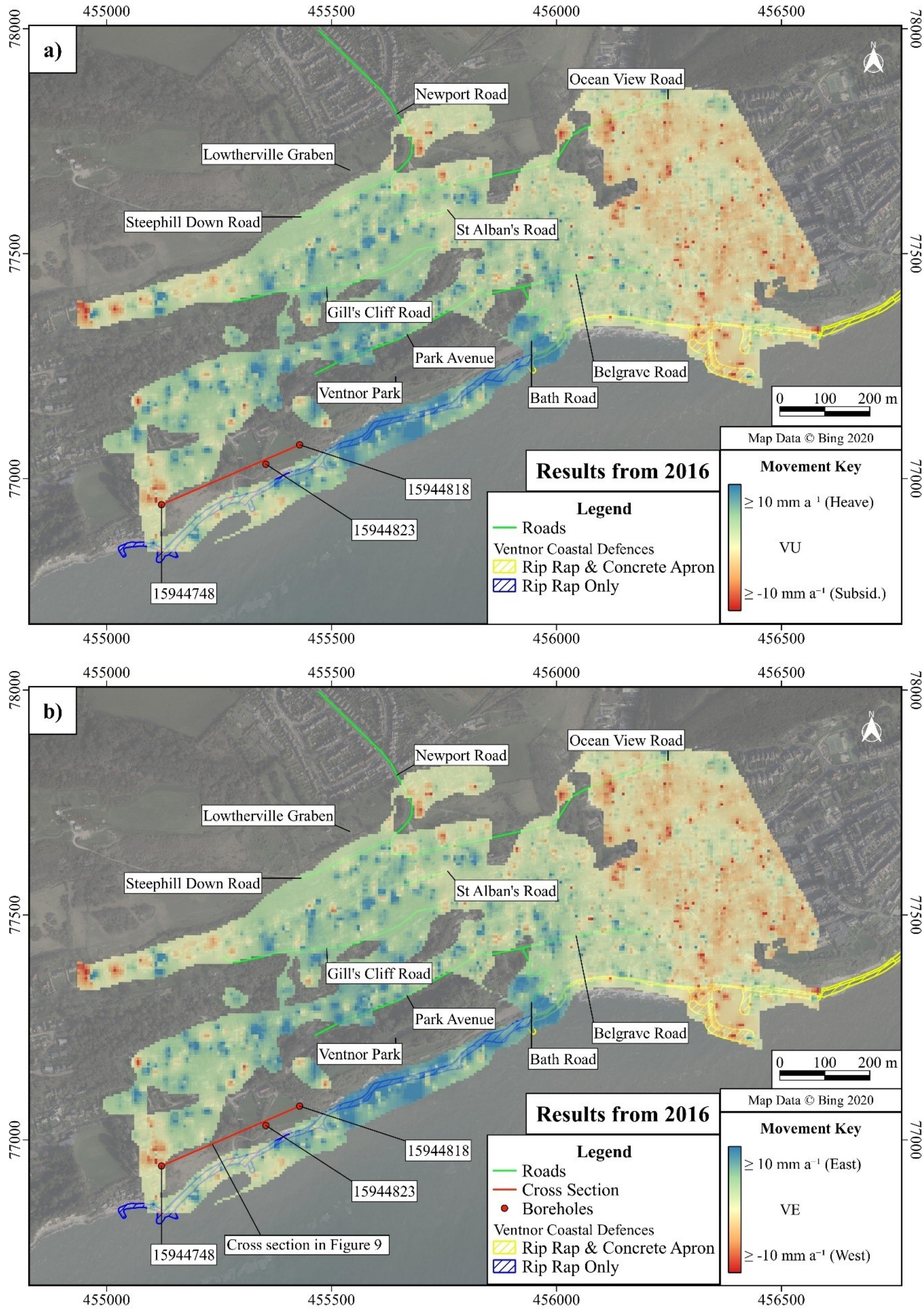

Figure 5.23. (a) Vertical (Vu) and b) horizontal (V_e) velocity components, based on the scenes from year 2016 only. Approximate location of the cross-section from Figure 1.12 marked in red with boreholes used for the cross-section generation.

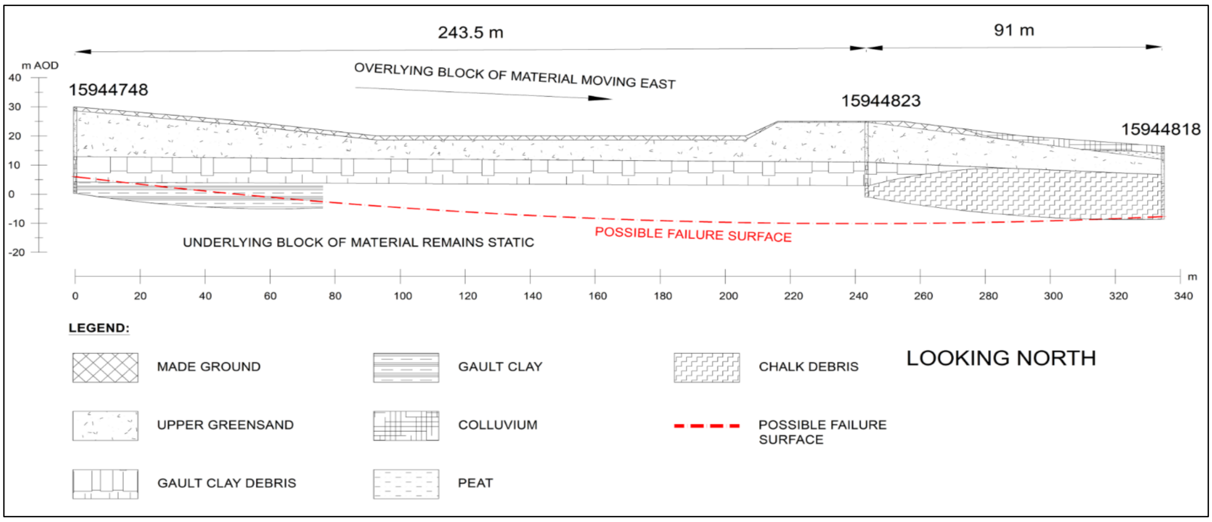

Figure 5.24. The 2D ground model in the East-West direction, based on the boreholes available from BGS marked on Figure 1.11, west of Ventnor Park. Approximate failure surface marked in red, dipping close to parallel to the ground level. The movement being most likely to be caused by the overlying blocks of the landslide sliding east along the slip surface within the Gault Clay formation, with the underlying block being motionless. (Borehole data accessed from Borehole Scans (2020))

Time series analysis has also been undertaken for a period of ~3.5 years from March 2015 to December 2019 for the ascending series and May 2015 – December 2019 for the descending series. Similar to the data in chapter X where platform downwearing has been analysed, the results have been plotted as IDW maps and as plots of time series. Additionally, the time series have been plotted with minimum and maximum ground movement in time, with rainfall data from Ventnor Park rain gauge included. As in previous cases, the data for PS points on Figure 5.25 and Figure 5.26 have been averaged with a moving average to remove noise from the data and highlight the trend of the time series.

Figure 5.25 presents results from processing the ascending data, showing the calculated IDW map for the area of interest as well as the time series for two chosen locations of Ventnor Park and Lowtherville Graben. Close inspection of the time series plots reveals that while the ground movements are nearly constant, there is some variability in the rates, which show several cycles of increased displacement, followed by much slower movements. This is especially visible in the case of Lowtherville Graben. Periods of increased subsidence in the areas of interest usually follow a period of increased rainfall, for example, the period between mid-December 2016 and early March 2017, where a cumulative 244 mm of rainfall was recorded, which in turn triggered a movement of -1.5 mm of the ground at the Lowtherville Graben. The actual subsidence happened approximately 20 days after the excessive rainfall event, an expected delay. Another example occurred between mid-May 2017 until late September 2017 after a recorded rainfall of 317 mm. This precipitation event was followed by 2 mm of ground subsidence at Ventnor Park registered around October 2017, occurring 13 days after the rainfall. Following these two examples, it can be concluded that higher total rainfall will create a shorter delay in the larger ground movement displacement after the rain event.

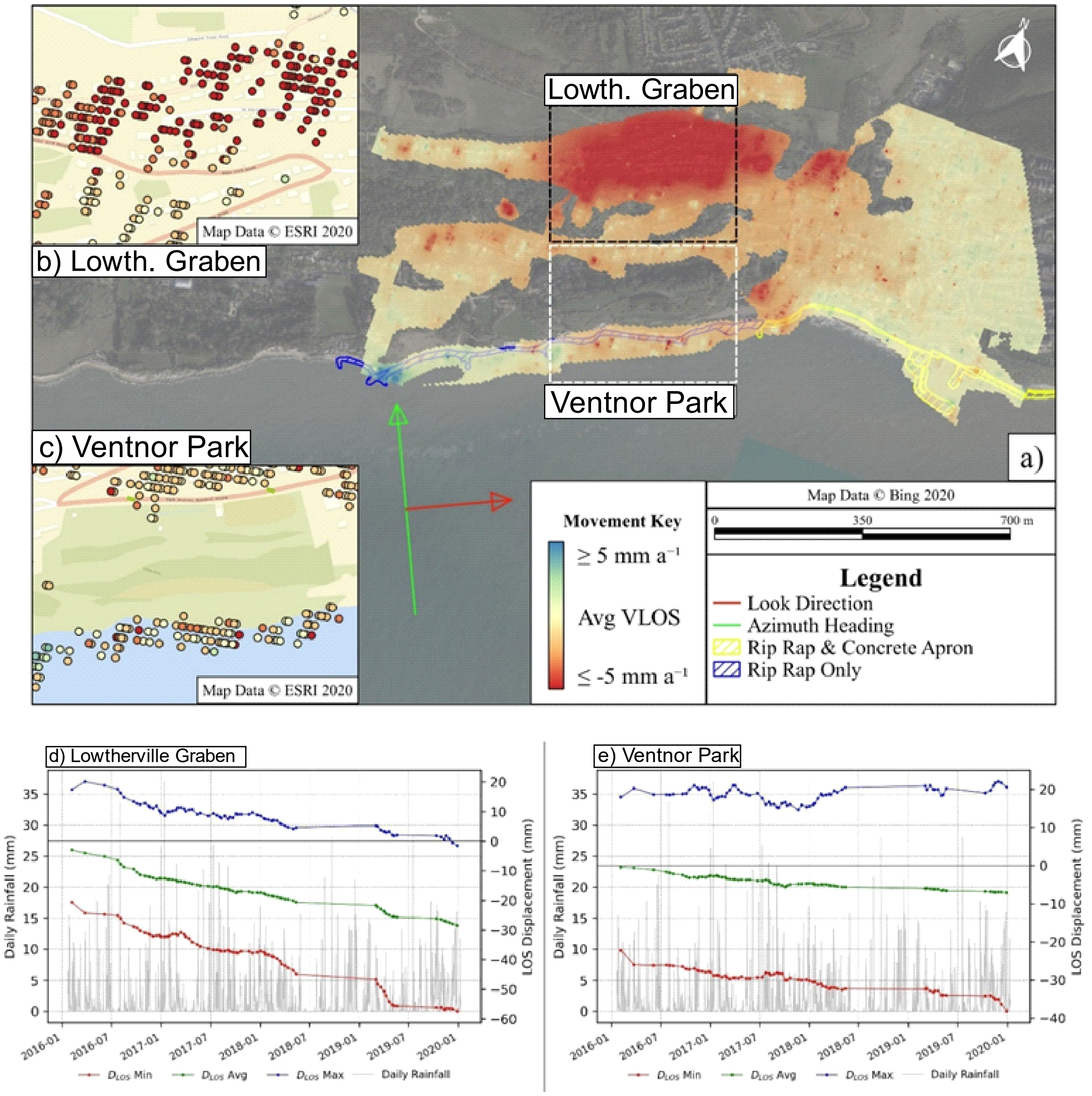

Figure 5.25. a) Aerial view of interpolated average LoS velocity across the Ventnor area (ascending data only), with colourised PS point displayed for b) Lowtherville Graben and b) Ventnor Park. Figures d) and e) present time series for the areas in b and c, with an average in green, minimum values of ground movements in red and maximum in blue. The grey vertical lines (in d and e) show daily incident rainfall totals as recorded by the Ventnor Park rain gauge.

Figure 5.26 shows the results from processing descending data, and the calculated IDW map, as well as the time series with Ventnor Park and Lowtherville Graben locations that have been analysed closely. It appears that the ground movement is slower when observing the descending data at Lowtherville Graben area. The rainfall total was 253 mm between mid-October 2016 and late January 2017. This was then followed by subsidence of about -4 mm over the next 100 days, potentially prolonged due to the rainfall events over that time period. In the case of Ventnor Park, short periods of stability can be observed, however the area is mainly moving upwards towards the satellite (i.e. heaving). Being the toe of the Undercliff landslide, the ground is expected to be moving upwards due to rotational movement of the ground. Again, days with higher rainfall values correlate to longer periods of ground movements, which can be explained with higher pore pressure being generated within the landslide complex.

The Lowtherville Graben ground movements seen on the processed data from both orbits are consistent with the ground movement expected based on the previously discussed 2D ground model (Figure 5.24). In the case of the Ventnor Park, the ground movement shown on the data processed from ascending orbit has the downward trend, while the descending orbit data presents trends towards the satellite (upwards). These movements follow the East – West components of the landslide, from the fig Figure 5.23. The different ground movement trends for the same area can be mainly related to the direction of travel of the satellite and the direction the satellite sensors that observe the ground. The satellites always look to the right, which means that Sentinel-1 looks East on ascending orbits, and West on descending orbits. This allows the signal to be reflected off slightly different features and structures, and some features may be occluded in images of one or other orbital tracks. Using both orbits to decompose the 2D components of motion is therefore absolutely necessary to get a complete picture from the data.

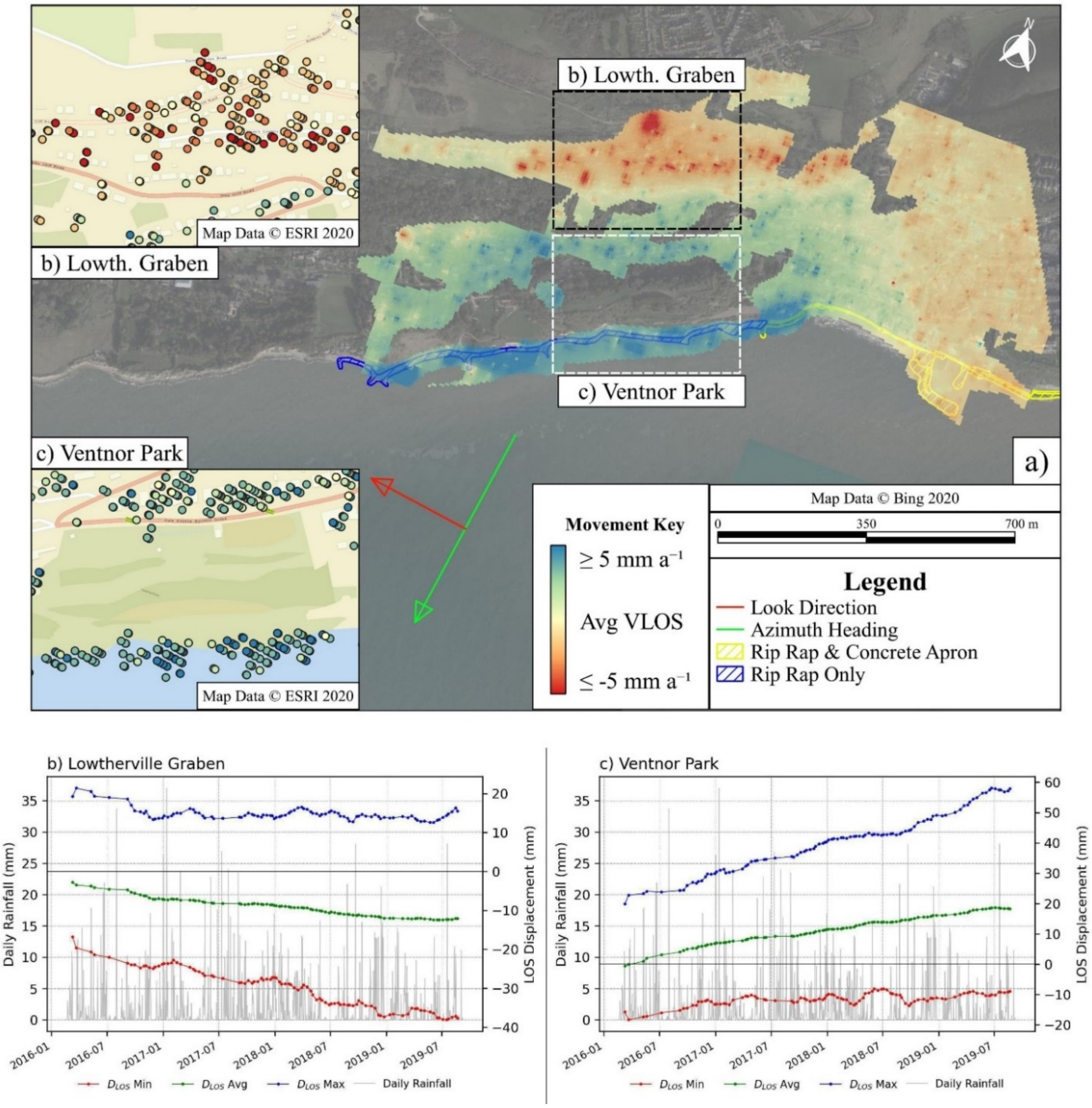

Figure 5.26. a): An aerial view of the Ventnor area with IDW map, presenting an average velocity per annum, based on descending data, with PS data displayed for Lowtherville Graben (top) and Ventnor Park (bottom). Figures b) and c) present time series for the areas of interest, with an average in green, minimum values of the ground movements in red and maximum in blue. The grey lines show the rainfall information that has been collected from Ventnor Park rain gauge. The figure is based on the MSc thesis by O'Connor W., 2020.

The IDW map (Figure 5.26) shows that the coastal defences located between Ventnor Beach and Wheeler's Bay provide reasonable ground stabilisation. The movement in the coastal area is negligible, which compares well with observations made by Chandler (1984), proving that coastal defences are sufficiently protecting the shore from the erosion. The minimum and maximum of the vertical and horizontal ground movements based on the time series data from the 3.5 years are shown in Table 5.4.

Table 5.4. A summary of minimum and maximum vertical and horizontal ground movement for the full time series.

Time Series	*Value*	*V_U (mm a^{-1})*	*V_E (mm a^{-1})*
Full	Min (Subsidence/West)	-9.8	-3.7
	Max (Heave/East)	8.5	12.4

5.5 Summary of results

This section presents a short summary of the results, while the more detailed discussion is presented in Chapter 7, Section 7.4.

Three case studies have been presented in this chapter, showing Cow Gap landslide within a rural environment; Folkestone Warren, a landslide in both rural and urban environments; and Ventnor Undercliff Landslide, located within urban environment.

The Folkestone Warren case study presents analysis of two data sets, with a shorter and longer time-series of 2 and 5 years respectively, showing a variety of areas investigated and interpreted. Although there is very little information coming from the vegetated section of the landslide mass, the results are still informative, showing the ground movement of the landslide, both on the toe, as well as on the main body of the landslide. Results of the analysis, presented on both the IDW map and on the time series, display ground movements within the landslide, showing areas of uplift that could be connected to the movement of the toe of the landslide, and generally smaller movements of the main body of the landslide, which could be associated with the remedial works stabilising the rock mass. Interpretation of the movements show an effective way for retrospective and ongoing monitoring of the geological processes occurring within the area. The PSI methodology provides a comprehensive evidence for the ground motion, which can be used in the future in conjunction with conventional (both direct and remote) methods for coastal landslide monitoring.

Cow Gap presents good data density, with clear and continuous ground movement over the five years analysed. By using the script for filtering low tide data only, the visualisation of the landslide's toe has been made possible, by improving the PS density on the platform in front of the landslide and on the toe section of it. The results provide a clear distinction between the movement of the main mas of the landslide, showing the rock mass moving down in LoS at 8 mm a^{-1}, and the landslide's toe moving upwards, at slightly less than 1 mm a^{-1}.

The Undercliff Landslide in Ventnor discusses analysis of two datasets, in ascending and descending orbit, showing true vertical and horizontal ground movements. This analysis is compared with conventional in-situ methods previously used in the area, showing good correlation. Thanks to the PSI processing and interpretation, a new 2D ground model has been produced, with interpreted slip surface, also indicating good correlation with past interpretation based on in-situ surveys, pointing to the slip surface being located within the Gault Clay formation.

Although the PSI method still presents limitations (like low PS density in highly vegetated areas), it also offers great potential for future investigations, and highlights limitations of conventional geological surveys, that might not be able to fully describe the continuity of the motion, or the full assessment of the geological hazards. All three landslides are within chalk strata, with Gault Clay acting as a slip surface, showing a very similar slip mechanism. That mechanism produces very specific ground movements, with the main body of the landslide moving downwards (towards the sea) and the toe moving upwards, but with a smaller magnitude of movement. PSI analysis performed for these three locations has shown the movements expected, proving that it is possible to visualise them on time series plots, showing the ground movement in time. This, confirmed with field work where available, demonstrates how PSI can be utilised for monitoring landslide movements, as well as helping to understand the mechanisms of the processes encountered. This is especially useful within highly populated areas like Ventnor, where monitoring of a continuous landslide movement is crucial for safety of the citizens.

5.6 Chapter summary

Landslides, being one of the geological processes that occur within coastal zones (see Chapter 2, Section 2.3.3), have been here studied within this chapter and show the value of using PSI, described in Chapter 3, for monitoring landslide movements.

This chapter discusses three case studies, encompassing urban and rural areas, where coastal landslides are active. It shows the great potential for PSI in the retrospective monitoring of ground movement related to landslides located close to the foreshore. These studies can be used as an analogue for any area around the world. The processing chains, as well as the scripts involved, can be used with ease on any satellite data, showing unique solutions as well as potential for analysis and monitoring of complex landslides in pivotal areas.

Chapter 6 presents a study on platform downwearing, providing a robust study on the monitoring of coastal erosion with remote sensing technique such as PSI.

6 Analysis and monitoring of platform downwearing

6.1 Introduction

The content covered within this chapter has been published in Remote Sensing Journal under the title "Monitoring Littoral Platform Downwearing Using Differential SAR Interferometry" on 6th October 2020 (doi: 10.3390/rs12193243). The chapter discusses a methodology that has been developed for the monitoring, measurement, and quantification of littoral platform downwearing. This chapter will illustrate the effectiveness of the methodology through the detailed description of three case studies that have been presented in Mider et al. (2020). It provides an assessment of compatibility with conventional methods of platform downwearing monitoring, presenting an effective solution that can be utilised on daily basis for coastal engineers in their maintenance and monitoring work.

Shore platform morphology, and the processes encountered there, have been described in Chapter 2, Section 2.3.4. Climate change models currently predict that global sea levels may rise between 0.29 and 0.67 m by year 2100, and between 0.6 and 1.7 m by year 2300 (Howard et al., 2019), which will increase risks in coastal areas. As a result, identifying suitable methods for monitoring, that are reliable and repeatable, is of utmost importance to the progress of understanding and predicting the influence of climate change on coastal environments and communities within them.

This analysis of platform downwearing has been provided to help with better understanding of the processes that cause it, and of the development of the dynamic coastal platforms. It also provides information on the coastal erosion origins and shows how effective coastal defences are within the urban environments. Owing to the existence of a wide range of previous conventional studies for platform downwearing, this has allowed a comparison with PSI results, showing good compatibility.

6.2 Current measuring methods for platform downwearing

Platform monitoring has been researched widely for many years now, with much focus on the area of East Sussex, UK on which multiple studies have been focused. This section reviews a handful of the monitoring methods that have been published in last 40+ years. Current methods for monitoring and measurement of the platform erosion utilise techniques which are both direct and indirect. Direct methods are predominantly focused on collecting information that is of a point scale and collected over a set period of time.

One example of a direct method is Micro-Erosion Metre (MEM), developed by Robinson (1976). An MEM (Figure 6.1 A) is a small triangular instrument which is permanently fixed to the surface of a platform. The height from the top of the MEM to the rock platform surface is measured by lowering a probe onto the rock surface (Swantesson et al., 2006). Multiple measurements are performed over a period of time and the downwearing rate is calculated from the difference between two consecutive measurements. The accuracy of the MEM is quite high, with dial gauge resolution of 0.001 mm, however it only records the data at a single point position. The instrument must always remain in situ, which means it can be damaged. Additionally, the measurements are time consuming, and must be performed by a trained individual, making them costly.

One of the most common noncontact methods is a portable Terrestrial Laser Scanner (TLS) (Swantesson, 1992) (see Figure 6.1 B). This method has been used by (Swantesson et al.) to measure small platform areas of 40 x 40 cm, with a height resolution of 0.025 mm. The laser probe scans in two directions, x- and y-, between 10-15 cm above the rock surface. This tool can generate micromaps, based on multiple measurement points and can also quantify surface roughness. It is however not fixed to the surface of the rock, which can lead to measurement accuracy errors up to 2 mm (Stephenson and Finlayson, 2009b). The TLS tools are portable but can be heavy (up to 30 kg) and often require two people to carry and set them up. The instrument also only measures a limited area each time.

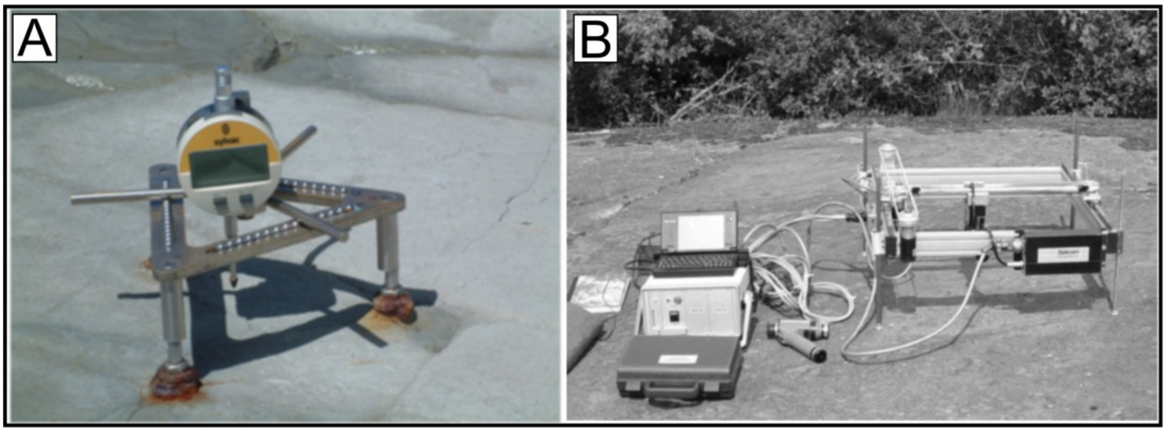

Figure 6.1. The existing tools for platform downwearing monitoring. Photograph A: MEM tool fixed to the rock platform (image from Stephenson and Finlayson (2009a)). Photograph B: TLS equipment, from Swantesson (2006)

Neither the TLS nor MEM instrument can monitor surfaces continuously and both require a trained operator to be on-site, which makes the surveys time consuming and expensive. They are also weather dependent, as they cannot monitor the sites in bad weather conditions.

The laser scanning (LS) instruments are also commonly mounted on drones and aircrafts, in the form of Light Detection and Ranging (LiDAR) surveys. This can provide information about platform erosion over large areas and can be repeated regularly. They are, however, less accurate than TLS or MEM measurements. The LiDAR's accuracy is mainly dependant on the flight speed and height. The data that are produced require calibration prior to surveying (Moses et al., 2014).

Dornbusch et al. (2008a) who focused on the East Sussex coast in the UK, calculated platform downwearing rates using 1:5000 scale aerial photography and photogrammetry. This was achieved by comparing two aerial surveys from 1973 and 2001. Both series of photographs were taken as a part of an Annual Beach Monitoring survey. The 1973 photographs were taken with a ground resolution of ca. 7 cm, and the 2001 photographs taken with a resolution of 11 cm. This study used Ground Control Points (GCP) that were collected with a differential GPS, with a horizontal and vertical accuracy of +/- 0.2 m. Unfortunately, some of the areas had experienced significant cliff erosion, which made feature comparison difficult. Also new coastal defences were built and some of the groynes had deteriorated between the two survey times. A Digital Elevation Model (DEM) was extracted based on the comparison of the high-resolution stereo photographs of the study area. The DEM was produced with horizontal ground resolution of 0.1 m, so small-scale topographic variations were possible to distinguish. The vertical accuracy was +/- 0.2 m, based on a set of elevation points (provided by Environmental Agency). While this method has proved to be cost-effective, it did require an archived set of photographs, a high-accuracy GCPs, and regular repeated surveys. It is not common to have archival photographs easily available for the retrospective comparison, which means that monitoring of downwearing rates can really be only done on current data. Furthermore, taking the photographs from low altitude with high accuracy is very costly.

However, as mentioned before, the coast of East Sussex has been a very fruitful area for multiple studies. The section of coast between Brighton and Hove has had MEM measurements taken since 1980s. These were taken to calculate the rates of platform downwearing there, especially near the groynes. Based on research from 1981 – 1983, Ellis (1986) calculated erosion rates of 3.5 mm a^{-1}. Dornbusch et al. (2007) used photographic surveys to calculate overall erosion rates for the platforms near Roedean and Hope Gap, with the rates of 0.1 – 0.9 mm a^{-1} near Roedean and 3.0 – 25.4 mm a^{-1} around Hope Gap. The authors have also recognised a substantial variation and stochastic nature in the downwearing between the sites (Table 6.1). Swantesson et al. (2006) also worked on the area of East Sussex, where they compared downwearing rates based on measurements from MEM and TLS instruments. They concluded that the downwearing rates were irregular all around the platform, but also that greatest rates were found next to the cliffs. The authors reported that even when analysing small survey areas, like 200 x 200 mm or 240 x 240 mm, downwearing rates vary significantly. Differences in erosion rates over time were also discussed in their work, showing only small variations between summers of 1999 and 2000 at Peacehaven (TQ 41207 01477), followed by an almost ten times greater erosion in 2001, as measured by a TLS survey.

Table 6.1. Surface erosion based on various measurement methods. Data in the table has been collated in Dornbusch and Robinson (2011)

Location	Grid reference	Photogrammetry [mm a^{-1}]	MEM measurements [mm a^{-1}]	Laser Scanning [mm a^{-1}]
Roedean	TQ 34667 03136	-0.9 to -0.1	-3.5	
Peacehaven	TQ 41207 01477	-4.9 to -1.0	-1.5	-0.3
Hope Gap	TV 51041 97373	-20 to -6		

6.3 Study region

The research described in this chapter focuses on the30 km stretch of the littoral zone between Brighton (TQ 31272 0418) and Eastbourne (TV 60749 98791) in East Sussex (see Figure 6.2). This area is mainly formed of chalk cliffs, which dominate the coastline. The East Sussex coast has a tidal range of more than 6 m, which in turn leads to the development of an exposed intertidal zone.

Three research sites have been chosen to show the changes in the ground movement that can be interpreted as platform downwearing. The sites include: Roedean (TQ 34731 02984), Saltdean (TQ 37758 01964) and Flagstaff Point (TV 53844 96674). The Roedean and Saltdean sites are considered urban environments with coastal defences. Flagstaff Point represents an unprotected rural coastal area, where natural erosional processes occur.

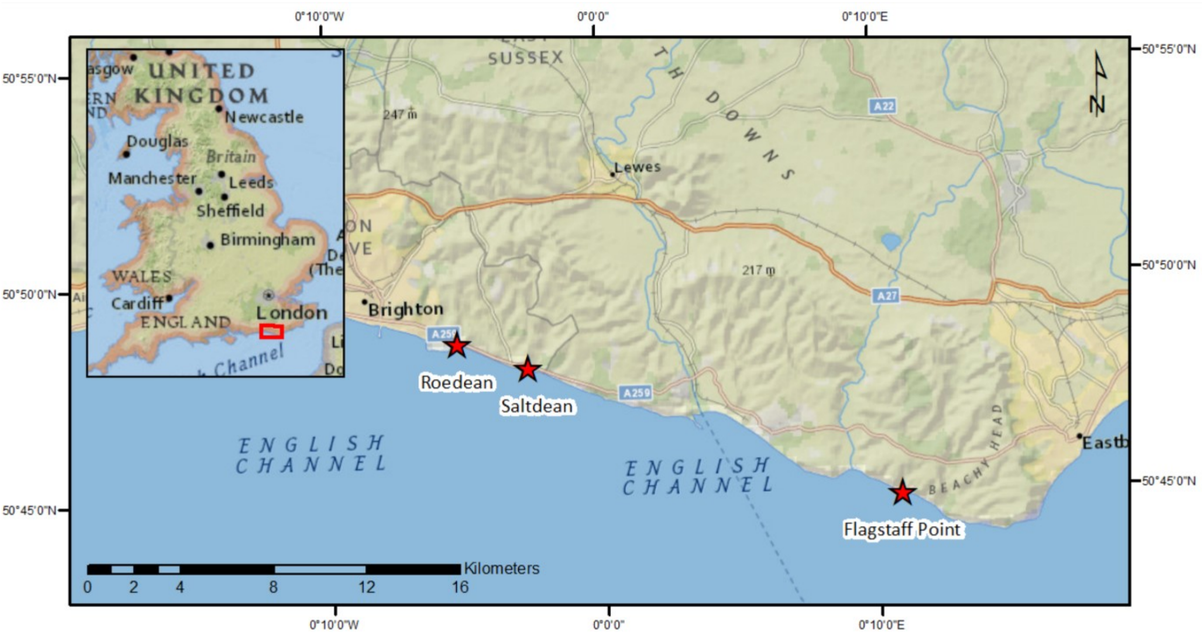

Figure 6.2.Study area map. Research sites are marked with red stars.

6.3.1 Roedean site

This site extends over an area of 140 x 520 m and is adjacent to the Brighton Marina (Figure 6.3). There are several types of coastal defences installed either along the whole section or at specific points, including a seawall, six groynes, “rip-rap” protection, and a concrete undercliff walkway. The platform between the groynes is only uncovered during the low tide. The undercliff walkway is frequently used for recreational purposes, especially during the summertime.

Figure 6.3. Roedean site, seen at low tide. Photograph A looking East with groynes visible in the distance and sediment being accumulated between them, with chalk platform located in front of the sediment. Photograph B showing view looking South-West, showing the rip-rap protection in front of the Brighton Marina.

6.3.2 Saltdean site

The Saltdean site (Figure 6.4) is an area that measures 35 x 335 m and, similarly to the Roedean area, has an undercliff walkway, seawall, splash wall and four groynes. This area is also subjected to frequent usage by residents and tourists. As it can be seen on Figure 6.4 A and B, the erosion at the seawall has exposed its foundations, as well as the chalk that lies under it. On the Figure 6.4 B, a slight concave shape is visible in the bottom step, that has been caused by a non-stop erosion of this area.

Figure 6.4. The Saltdean location. Photograph A: splash wall, undercliff walk, seawall with steps and shingle beach in front of them. Photograph B showing a part of the seawall directly on the shingle beach. The erosion at the seawall has exposed the seawall foundations and the chalk that underlies it. The bottom step has slight concave shape from nonstop wave erosion.

6.3.3 Flagstaff Point

Flagstaff Point is an area of is 250 x 320 m in size and is a rural and hence an unprotected area of the littoral zone (Figure 6.5). It lies on the coastal stretch known as Seven Sisters, which is a series of chalk cliffs located within the South Downs National Park. The platform in front of the cliffs is covered in rocks and a small amount of shingle, but only fully exposed at the lowest point of the tidal cycle.

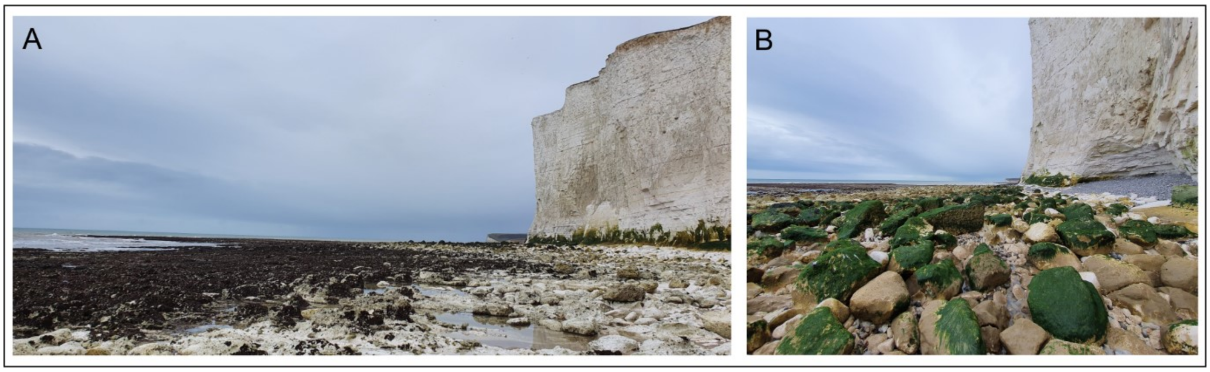

Figure 6.5. The area of Flagstaff Point at the low tide. Photograph A: platform in front of the cliff face, spreading 200 m into the sea. Photograph B: large chalk boulders that are distributed on the platform and provide stable response to the 1 radar waves.

6.4 Methodology

The study uses SAR data processed with the SARScape PS module and the PSI methodology explained in Chapter 3 Section 3.6.1. The data used come from track 132, an ascending orbit, and were processed with a minimum coherence threshold of 0.65, providing good point density for the purpose of this study.

The Sentinel-1A and -1B satellites obtain images at similar time of the day each day – once in the morning and once in the evening. Unfortunately, this means that the time of the image acquisition does not always coincide with the same tide conditions. The coastal area of East Sussex has tidal ranges of about 6 m per day and at high tide the platform is fully submerged, therefore only selecting SAR images acquired at low tide is essential. To achieve this, a python script has been used (script's syntax attached in Appendix 1) to filter for scenes acquired within a two-hour window of the low tide were selected for the processing. The entire stack of 183 SAR scenes acquired over 3.5 years (07/03/2015 – 02/02/2019), has been filtered to select only low tide scenes; reducing the number of scenes used to 93. The difference between two stacks of data is presented on the research site at Flagstaff Point, showing an increase of the PS points for the area of the study. A fourfold increase from 233 to 935 PS points is shown on the Figure 6.6, where a difference between low- and high- tide data is displayed. The data have been generated with the same coherence threshold and data quality. This has enabled higher quality of results and easier interpretation of the ground level changes across the whole platform.

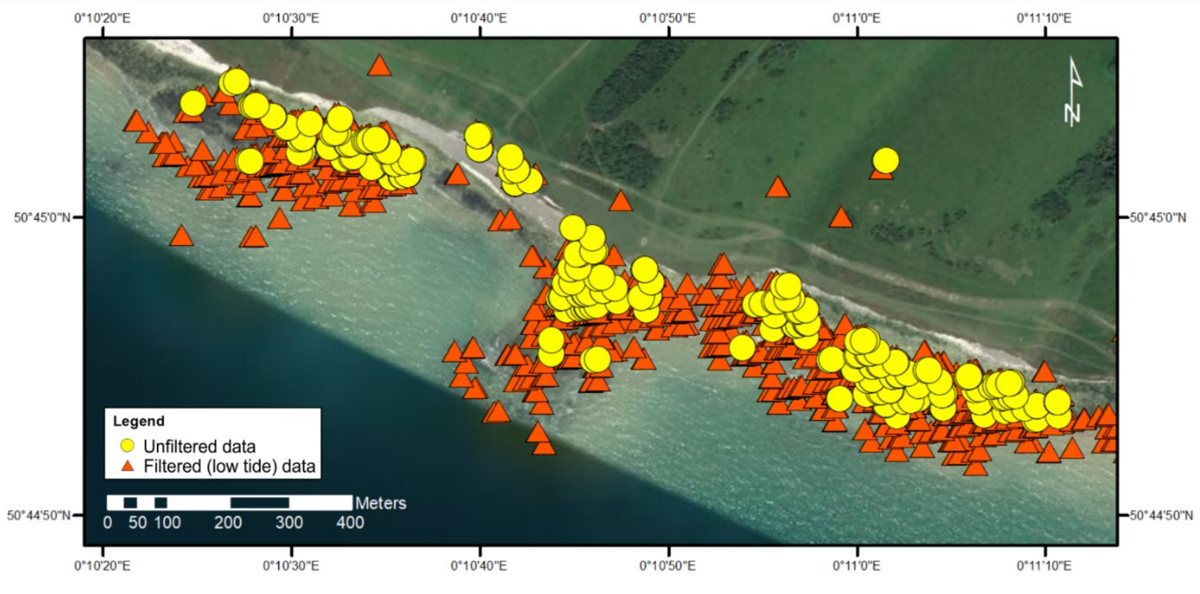

Figure 6.6. Point density difference between data based on every scene recorded during the investigation time period (yellow circles) and data that has been filtered to include only low-tide scenes (orange triangles). Data from every scene processing has produced 233 PS points, in comparison with the low tide data that has produced 935 PS points.

From the SARScape and ENVI software (Harris Geospatial), the data were exported into Excel. A seven scenes step moving average was used to smooth the data and represent the trends, as well as improve the visual breakdown. It has also allowed the removal of noise contribution to the results and aide in the clarity of the presentation. Average velocity maps were created in ArcGIS software with an Inverse Distance Weight (IDW) average interpolation, where a fixed search radius of 200 m and a power of 2 were used to generate continuous surfaces of velocity. The processing results presented in the discussion on case studies (Section 6.5) have been displayed on ArcGIS images with time series for PS data points created in Excel for every study area.

In the analysis it is immediately visible that there are fewer scenes for the year 2015, which is due to having only one satellite orbiting the Earth at the time. This creates longer gaps between scene acquisition dates, and in turn even fewer data are available when only scenes within low tide were used; meaning that the results for 2015 are slightly less informative for the monitoring of platform erosion.

This study covers areas of urban and rural environments. The urban areas have multiple coastal defences in place, like seawalls, splash walls and groynes, while the rural areas have none of these features. This separation helps to provide understanding as to the variations of the ground level changes, as well as highlighting how effective the coastal defences are for the urban environments.

6.5 Results and discussion

6.5.1 Regional overview

An interpolated map of average ground velocities per annum (in LoS) with the region of investigation shows the results of the PSI ground level changes for the littoral zone within the research area between Brighton and Eastbourne (Figure 6.7). Local site-level detail for three research areas is presented on the Figure 6.7**Error! Reference source not found.**, A, B, C and D. These maps display PS data that have b een interpolated, as the PS points are irregularly distributed along the coastal area. By interpolating them, it is possible to see the spatial patterns for the littoral zone.

Average movements per annum are shown on Figure 6.7, where yellow to red colours represent ground movement in the downward direction (in the LoS movement away from the satellite's sensor) in mm a^{-1}, while blue colours are upward direction of the movement of the ground (LoS movement, towards the satellite's sensor) also in mm a^{-1}. The changes that can be seen on the maps occur in spatially clustered patterns and are not random – several areas have pronounced upward movement, while others show similarly noticeable movement downwards.

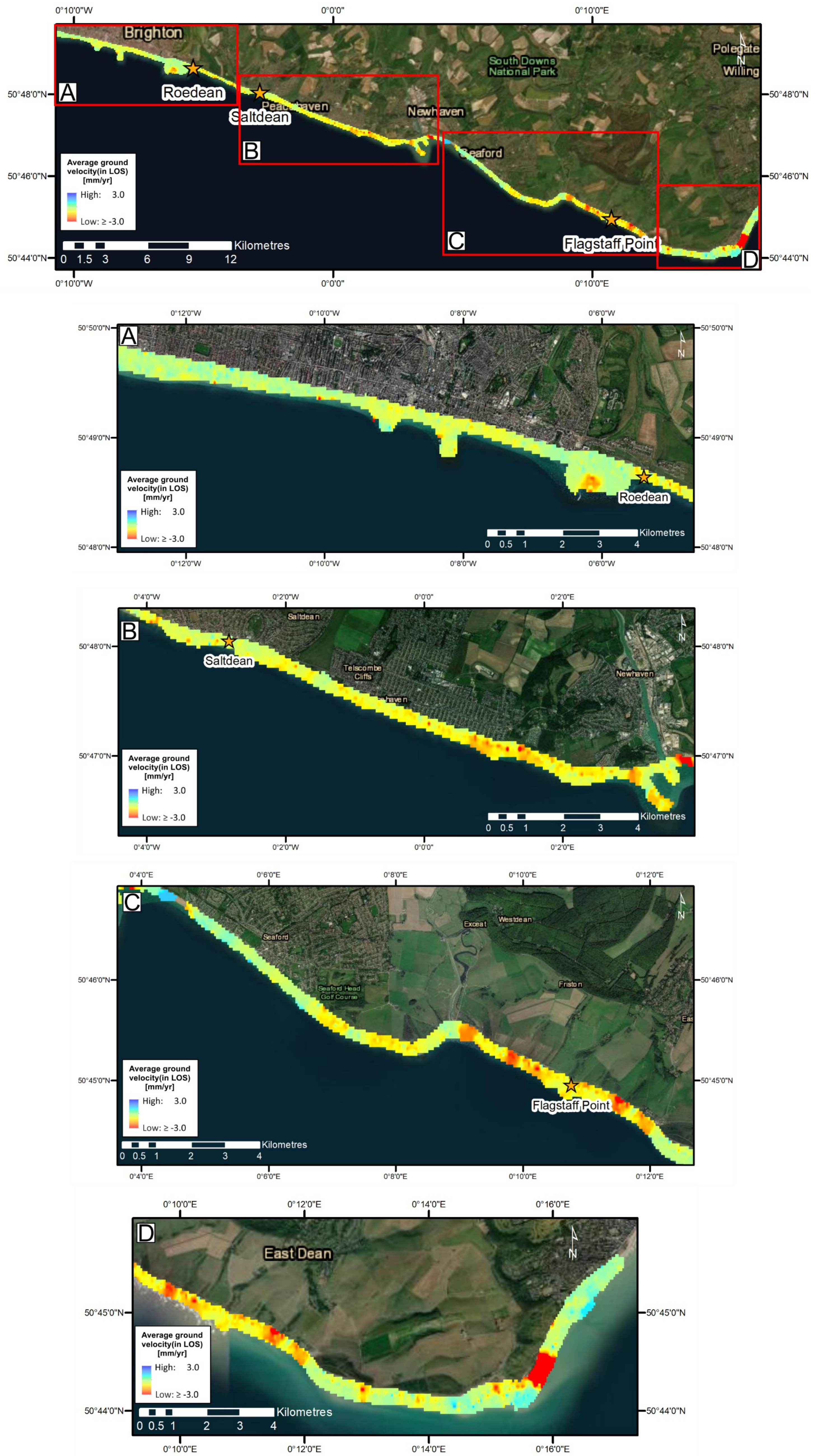

Figure 6.7. Map presenting regional overview of the results, with average velocity overlain for the area from Brighton in the West, to Eastbourne in the East. Movement downwards (away from the satellite) is marked with red colour, while the upward motion (towards the satellite) is coloured in blue. Figures A, B and C display areas surrounding the research sites.

An average downward trend of -0.36 mm a^{-1} for the whole region is observed. This movement is slower in urban areas (-0.33 mm a^{-1}), while unprotected areas are moving faster, with an average of -1.10 mm a^{-1}. This trend is interpreted as a platform downwearing. In the urban areas the slower rates can be explained by the existence of man-made coastal protections. However, some areas have substantially higher rates of downwearing in comparison to others, especially locations near Brighton, Peacehaven and Saltdean. Based on the PSI ground movement maps, these areas are recommended to be investigated further by coastal engineers to see whether maintenance work is required. In contrast, areas near Saltdean and Newhaven are quite stable with ground level changes oscillating near zero. This suggests the coastal defences there are more effective in comparison to the aforementioned areas or potentially these areas are less prone to downwearing.

The lithostratigraphy of the coastal platform was also considered as a cause for the platform erosion (Figure 6.8). The average ground movements have been calculated for formations that are exposed on the platform (Table 6.2). Lewes Nodular Chalk is considered to be the most resistant of the three formations, it erodes at a relatively slower rate (-0.53 mm a^{-1}), when compared to softer Seaford Chalk (-0.66 mm a^{-1}). The Newhaven Chalk is downwearing slower (-0.40 mm a^{-1}), even though it has similar properties to Seaford Chalk, and also erodes 0.13 mm a^{-1} slower than Lewes Nodular Chalk Formation. This can attribute to the fact that Newhaven Chalk only crops out along urban sections of the coast, while Lewes Nodular Chalk and Seaford Chalk are predominantly in rural, unprotected areas. This suggests that coastal engineering has greater erosional influence than the rock formation does. It is important to mention that even though these results are close to the accuracy limits for the PSI methods, they are founded on a long time series of 3.5 years of data and on continuous ground movement with a downward trend that is consistent over time, hence they are considered to be reliable.

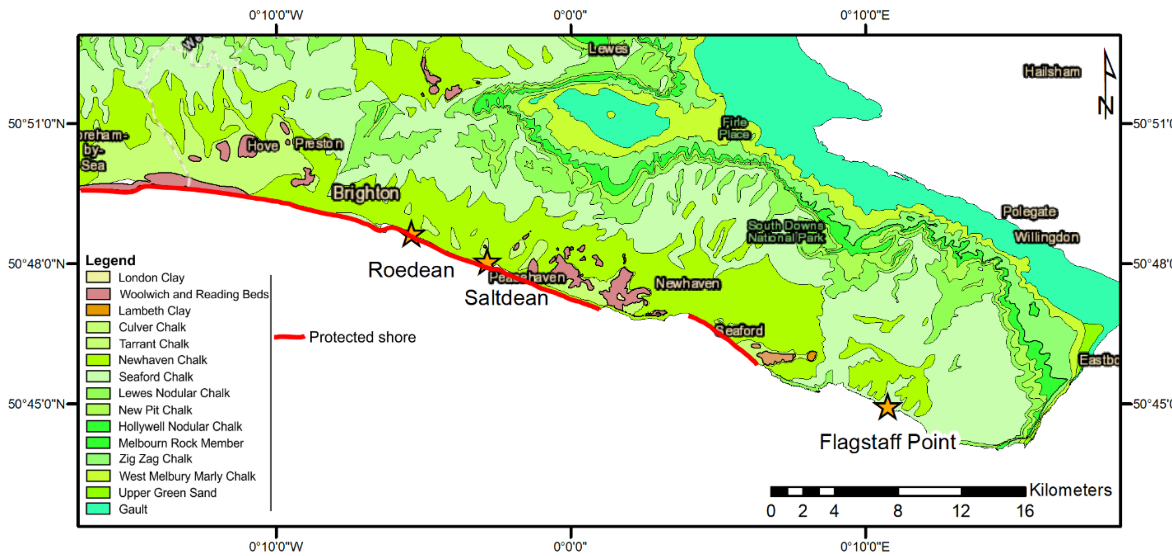

Figure 6.8. East Sussex bedrock geology, with area that are protected by man-made coastal defences marked in red.

Table 6.2. Average velocity per annum for different chalk formations that outcrop within the littoral zone

Formation name	Average velocity [mm a^{-1}]	Number of points analysed	Type of area
Newhaven Chalk	-0.40	36824	Protected
Seaford Chalk	-0.66	3788	Unprotected
Lewes Nodular Chalk	-0.53	1811	Unprotected

6.5.1.1 Comparison with previous studies

Table 6.3 shows results from other established methods of monitoring platform erosion in comparison with PSI results. The results from PSI method are comparable with the other monitoring studies around East Sussex, UK. Roedean research area shows a velocity of -0.1 mm a^{-1}. Peacehaven has an average of -1.27 mm a^{-1}, and Hope Gap of -0.61 mm a^{-1}. The results are within the range of previous studies and confirm the validity of the PSI method.

Roedean results are lower than MEM data and at the high end of the photogrammetry methods. Peacehaven results based on the PSI are comparable with MEM measurements and within the lower end of the photogrammetry, but higher than laser scanning. In the case of the Hope Gap location, the results from PSI are at the lower range of photogrammetry results that Dornbusch and Robinson (2011) have published in their study. However, their photogrammetry measurements discuss three areas near Hope Gap, with erosion rates significantly varying between each other.

Table 6.3. The comparison of the surface downwearing based on various measurement methods, updated with the results based on InSAR data. Previous data collated in Dornbusch and Robinson (2011). Exact position of the measurements from the terrestrial tools aren't known.

Location	Grid reference	Photogrammetry [mm a^{-1}]	MEM measurements [mm a^{-1}]	Laser Scanning [mm a^{-1}]	InSAR [mm a^{-1}]
Roedean	TQ 34667 03136	-0.9 to -0.1	-3.5		-1.0
Peacehaven	TQ 41207 01477	-4.9 to -1.0	-1.5	-0.3	-1.27
Hope Gap	TV 51041 97373	-20 to -6			-0.61

6.5.2 Ground level change at the research sites

The point-based PSI dataset can produce not only information about average ground motion changes for large areas but can also display changes in the ground level for every PS point. This way, a point-specific pattern of the ground level change can be produced as time series for different research sites.

6.5.2.1 Roedean site

Figure 6.9 shows the research site of Roedean, which has a good PS density and coverage of about 450 points. The entire platform's average ground level change (in LoS) for this site is -1.0 mm a^{-1}, which is just at the accuracy limit for the PSI method. However, the time series plot shows consistent downward trend over the time of analysis (2015 – 2019) of overall ~4 mm of erosion (movement away from the satellite) over the 3.5 years which is above the data uncertainty. The consistency of the trend proves that the averages are reliable and realistic. The PS point-based data on Figure 6.9 have been averaged with a moving average to remove noise and present the trend of the time series clearly. Standard deviation has been calculated for the data and is displayed on the plot to demonstrate variability of the data. The research site of Roedean presents a continuous downward movement over time (away from the satellite), that starts in March 2015 until the end of the analysed period in January 2019. Some variation throughout time on the time series plots is visible, but to be expected. They are due to the heterogeneity of the platform itself, given that some limited vegetation grows over the rocks, as well as sediment can be brought in and out from the platform.

This area's results show an average of 0.98 mm a^{-1} (at R^2=0.89), and they are comparable with previous studies (see Table 6.1), where ground movements for Roedean based on photogrammetry results were between 0.1 and 0.9 mm a^{-1}, and MEM were 3.5 mm a^{-1}.

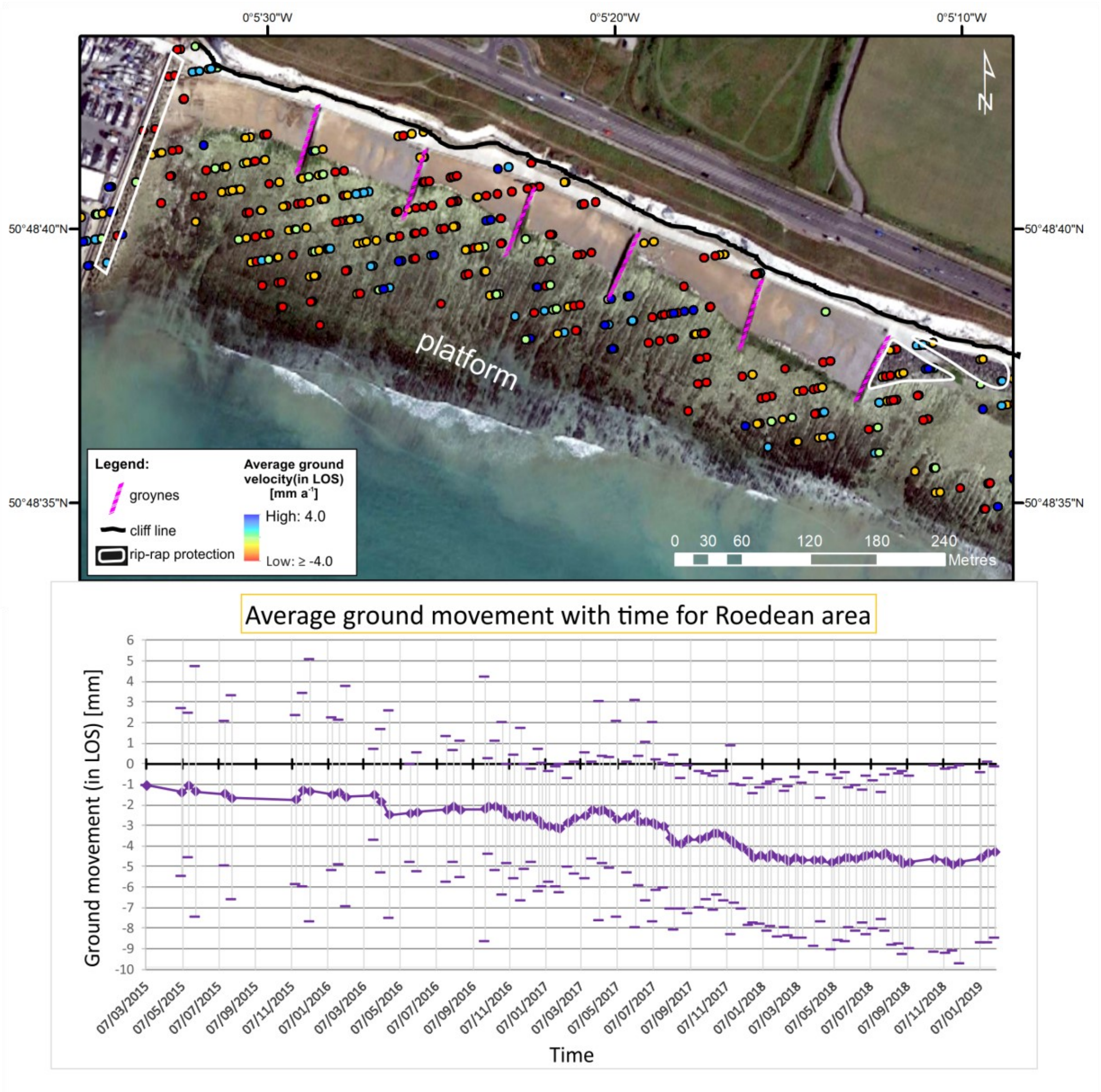

Figure 6.9. Roedean research site with aerial view of the results. The top image shows man-made coastal defences (groynes, rip-rap protection) and the cliff line. Average ground velocity per annum is also displayed (in mm a^{-1}), where red colours indicate downward ground movement (away from the satellite) and blue upward ground movement (towards the satellite). The bottom image displays the average ground movement of the whole area with y-axis showing ground movement in mm, and x-axis showing time, from March 2015 until January 2016. Standard deviation is shown as error bars on the plot to visualise the variability.

6.5.2.2 Saltdean

The platform by Saltdean is fully covered with medium to coarse sized gravel shingle, which is constantly shifting in random directions and causes loss of coherence between SAR scenes. Because of this, only few PS points can be extracted straight from the platform. Only a handful of PS points with high coherence can be distinguished from the area of undercliff walkway, against the seawall and on the exposed chalk at the seawall base. The average ground level change across the platform is -0.86 mm a^{-1} (at

R^2=0.59). The undercliff walk structure has 3 m high seawall that is located right in front of it, followed with cemented steps and platform in front that is covered in gravel (see Figure 6.4).

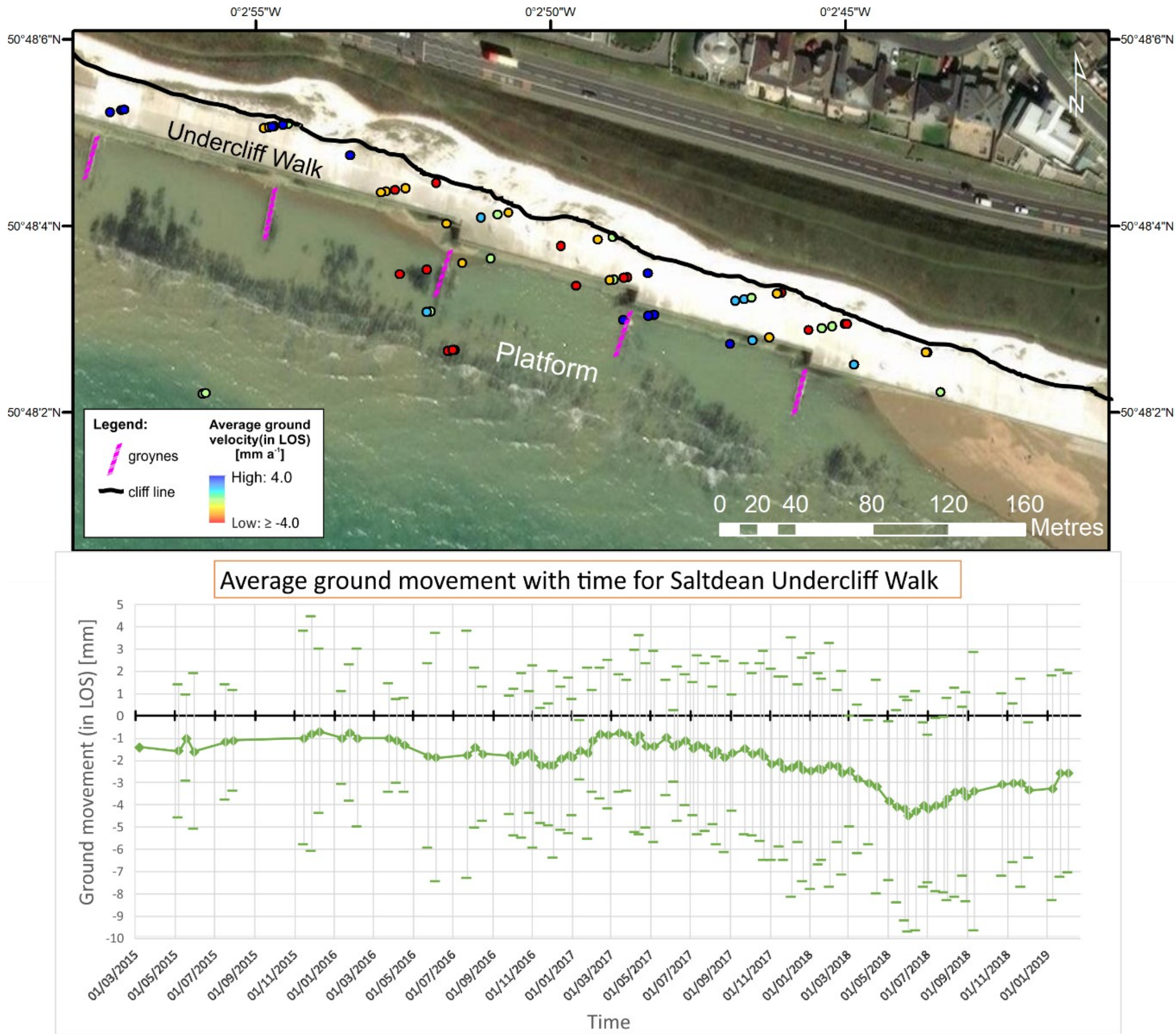

Figure 6.10. Saltdean Undercliff Walk research site. The top image shows an aerial view of the site, with groynes marked in pink and cliff line displayed in thick black line. On top of the map the average velocity of the PS points is shown in mm a^{-1}, with red colours representing movement away from the satellite (downwards) and blue colours being movement towards the satellite (upwards). The bottom image presents the average ground movement with time for the whole area, where y-axis is the ground movement in mm, and x-axis shows time (March 2015 – January 2019). The standard deviation is shown as error bars to represent the variability of the data.

The time series plot for Saltdean research site (Figure 6.10), shows a significant variation, however the most prevailing trend is showing the movement downward. Due to the shingle present on the surface of the platform, the 30 m of spatial resolution of SAR data, the direction of SAR illumination (in terms of the bearing of the shoreline), and the vertical angle of the shore (in terms of the seawall location), the PS points are likely to be situated on the seawall. This can be substantiated as it is the brightest scatterer in the SAR imagery (see Figure 6.4). This research area shows only small changes in the ground movement, while the fastest movement can be observed between 2017 until mid-2018. The downward movement on the SAR data at this site can be connected to the undercutting and downwearing of the chalk against the seawall. This is visible on the Figure 6.4, where a concave notch is seen to be developing. Considering the aging infrastructure, and continuous erosion of its foundations, the chalk under the foundations has been exposed. Because chalk is softer than the foundations of the defences, it erodes much faster, causing faster than expected degradation of the coastal protection. This is a very clear example of the platform downwearing impact on the aging coastal defences, and monitoring such is crucial, which can be easily provided with use of the PSI results.

6.5.2.3 Flagstaff Point area

The third research area is located within the Seven Sisters cliffs, it's the fifth of the 'Sisters' (counting from west to east), called Flagstaff Point, with the following Flagstaff Bottom (Figure 6.5). This area is remarkable due to having an extensive platform that is visible at the low tide, meaning it will have the highest PS point density in the unprotected (rural) area. The average velocity of the ground level change here is -1.03 mm a^{-1}. This area has also had a moving average applied to the data presented as time series, so the noise level has been reduced. Standard deviation has been calculated as well and presented on the plot (Figure 6.11) to reveal data variation. Figure 6.11 shows the area separated into two zones, A and B, zone A displaying the data in front of the hill, and zone B being in front of the valley. It can be seen on the Figure 6.11 that zone A is moving downwards (away from the satellite) slightly faster (-1.21 mm a^{-1}) than zone B (-0.94 mm a^{-1}). This is also visible on the time series plot, where zone A has slightly higher ground movements than zone B. This may be explained by hydrodynamic regime variation between the areas, and with the existence of the longshore drift from west to east. For zone A, which is in front of the pronounced hill, the platform is extended, which may be shielding zone B (in front of the valley) from the platform erosion. This case will change with time, as the platform in zone A and cliff line erode, which will in turn expose zone B to more erosion.

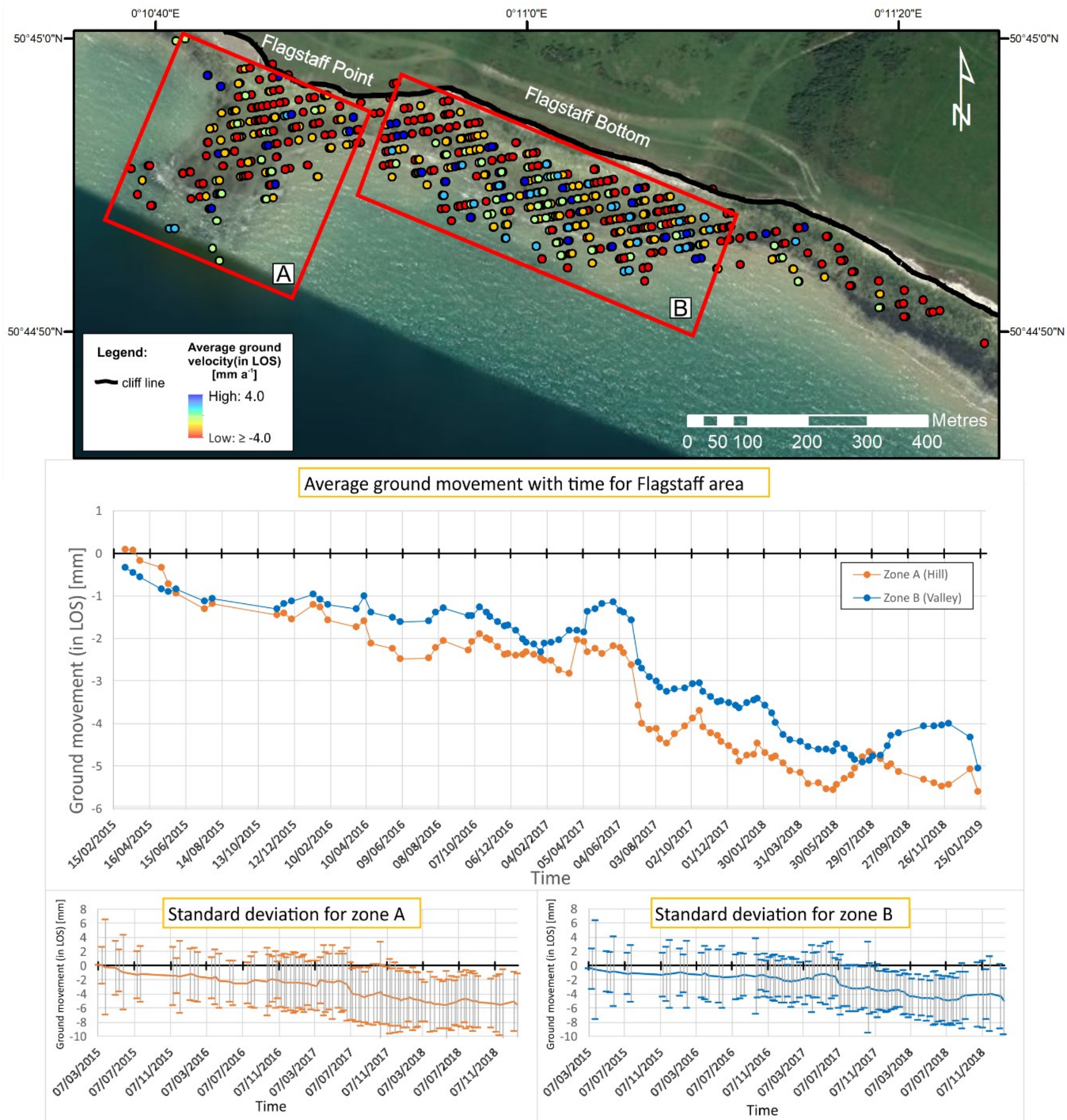

Figure 6.11. Flagstaff research site. The top image shows the top-down view of the area with cliff line displayed in thick black line. Velocity of the PS points is overlain on the aerial view, with red colours showing movement away from the satellite (downward), and blue colours showing movement towards the satellite (upwards). The middle image shows the average ground movement for the whole area, where y-axis represents the ground movement in mm, and x-axis is the time (March 2015 – January 2019). The standard deviation has been calculated for both zones A and B and displayed on the two bottom images to present the variability of the data.

6.5.3 Overview of the results

An average ground movement of -0.36 mm a^{-1} has been calculated for the whole area, and it can be interpreted as caused by platform erosion and its downwearing. Some variations in the downwearing rate are seen, however they can be associated with the engineered coastal defences or the lack of thereof in urban and rural areas respectively. Rural sections are eroding faster, with an average rate of -1.10 mm a^{-1}, while the urban areas are downwearing with an average velocity of -0.33 mm a^{-1}. When considering the material properties of the different chalk formations that are exposed on the platform, the areas with weaker chalk, like Seaford Chalk Formation, erode more rapidly with the rates of -0.66 mm a^{-1}, compared to the more resistant Lewes Nodular Chalk Formation that is downwearing with an average of -0.53 mm a^{-1}.

Intuitively it would be expected that the platform closest to the cliff face would erode faster than that further from the cliffs, but no sign of this pattern is detected in these data, which means that if erosion is happening there, it must be below the limits of detection by this method (~1 mm a^{-1}).

Considering the local scale, results based on three research sites that represent various environments show small but consistent downward trends for the ground level changes. These are also consistent with point-based studies that have been published in the past. They show that despite man-made defences in urban sections of the coast, all the areas experience steady and measurable platform erosion, of which the impact is clear in Figure 6.4 where the foundations of the defences have been undermined.

Using the PSI methodology represents a new, cost-effective and safe way of monitoring of the coastal platform downwearing that is complementary to the conventional in situ methods, as well as offering a different perspective, and can disclose both spatial and temporal patterns that happen along the littoral zone.

6.6 Chapter summary

This chapter has discussed the use of the PSI methodology for platform downwearing monitoring. The study was created based on 3.5 years of Sentinel-1 SAR data between years 2015 – 2019. By using only scenes that were acquired at low tide times, the number of PS points of high coherence has been increased four-fold, despite reducing the number of scenes available for processing. The results presented in this chapter validate that accurate and quantitative information can be created not only on local, but also on wide regional scale, as well as they can be produced in retrospection. The information about the ground movements can also be presented in continuous manner and over extended periods, which helps revealing patterns and helps with calculating average rate of the ground movement over time.

Using PSI methods, platform downwearing can be not only monitored semi-continuously over a prolonged period of time but can also be quantified as an erosion rate per annum. This methodology has also been successful in revealing spatial patterns in average platform downwearing, which can be easily used in future by coastal engineers and local councils for coastal defences maintenance and planning, helping with focus on the areas that need to be assessed as priority (i.e. when they're being eroded faster in comparison to others).

Results show how erosion rates differ between the urban and rural areas, showing urban areas, where coastal defences are present are being eroded *ca.* 0.77 mm a^{-1} slower than rural areas, where no manmade defences are present. Differences in platform downwearing rates based on lithostratigraphic variations have also been demonstrated, showing that softer Seaford Chalk erodes more rapidly than stronger, more resistant formation like Lewes Nodular Chalk. While Swantesson et al. (2006) have seen some differences in erosion rates with variable distance from the cliff edge, this has not been noticed within the analysed data in this project, so it could not be confirmed.

Although the results are just within the limit of precision of the PSI methodology, the downward trends that are seen, are consistent over 3.5 years of data and continuous, making them reliable and trustworthy. The results achieved with PSI method have also been compared to previous studies and they are within previously achieved ranges.

Overall, this platform downwearing monitoring study has been successful and shows great potential for future use by local councils of seaside towns, as well as by coastal engineers that require ground movement information to assess and plan current and future maintenance, and upgrades to coastal defences. With climate change likely to raise future sea levels, which in turn will force further rapid coastal erosion, remote sensing monitoring tools can be of great help, providing a continuously sampled (from orbit), cost-effective solution, which after processing can be presented in an easy-to-read manner. Studies like this, are immensely beneficial in demonstrating the practicality of the methodology and results presented show a successful, novel approach to monitoring of downwearing of coastal platforms, that has not been yet demonstrated in past research.

7 Summary of results and discussion

7.1 Introduction

Chapter 7 summarises and critically evaluates the outcomes of this research and pin-points the key findings from the various cases analysed. It also draws out the benefits of this approach that are relevant to local councils and civilian users. In addition, the limitations and challenges overcome during the development this research are discussed, highlighting where further work is still required.

7.2 Main research outcome

This research focuses on three main areas, where coupled natural and geological processes lead to cliff collapses, coastal landslides, and platform downwearing. The principal objective was to investigate whether analysis, monitoring and prediction of these processes are achievable by the use of PSI methodology. While working with different geological processes that occur in the coastal areas, the optimum methodology for their analysis has been developed and defined.

The positive results lead to a successful outcome, demonstrating that coastal areas can be precisely monitored, and processes can be characterised in detail, using spaceborne Earth Observation technology, specifically InSAR. While some limitations have been come upon, the results achieved within the study show robust interpretation and analysis and provide good foundation for further research in this area.

The successful application of the techniques developed in this research necessitated the use of a relatively weak rock in which failures were likely to occur in the few years available in a MPhil. Chalk proved ideal for this purpose, but the understanding gained from its study is equally applicable to stronger rocks prone to less frequent failures.

In terms of the methodology and software, improvements have been made to make the processing more efficient and productive. Python scripts have been created to help with scene selection and with data display specifically in coastal environments. The low tide script used in case studies related to coastal landslides and platform downwearing (Chapter 5 and 6) has been a major enhancement to the PSI methodology within the coastal areas as it has allowed the littoral platform in front of the cliffs and landslides to be included in the processing, following with much better PS coverage.

The Ventnor landslide analysis, described in Chapter 5, Section 5.4, has had data processed from both orbits, ascending and descending, allowing for the deconvolution and for calculating the actual vertical and horizontal velocities. While this methodology has been used with great success, it is a time-consuming exercise, due to the processing times of each of the sets which was the main reason for not having it performed on every research site.

7.3 Cliff collapse analysis and monitoring

The analysis of cliff collapse data in Chapter 4 has given inconclusive results, showing that the current PSI methodology is not yet suitable for predicting or monitoring this kind of geological processes. From analysis of three cliff collapse events, it can be concluded that while small ground movements can be observed, the scale of them is within a margin of the error associated with the PSI technique (i.e., of the order of 1 mm $^{a-1}$) and a direct relation to actual collapses is disputable. The main difficulty with the cliff collapse monitoring is caused by coherence loss through vegetation growth and change, and this is a common problem for PSI in rural areas. Cliff tops in East Sussex are heavily covered in vegetation that grows and changes throughout the year, causing very few stable PS to be distinguished. Additionally, the collapse events, being quite rapid, are likely occurring more rapidly than the return period of every six days for the Sentinel 1 satellites. Amitrano et al. (2005) monitored a cliff collapse using acoustic emissions recorded a build-up of signals only 15 hours prior to the cliff collapse. Processing results in rural cliff top environments tends to produce very few PS points as coherence is frequently lost. Some foot paths can be spotted on Google Earth maps, although often they are hard to distinguish, and based on the information from field visits, they can be seen to be covered with vegetation, especially during the summer seasons. Thus, even though chalk cliff faces should be good reflectors, they tend to have low coherence and produce few PS.

Cliff faces, mainly consisting of bare chalk, are also too steep to provide good signal reflectors. The PSI measurements usually provide best results for East-West facing cliffs (while East Sussex cliff are South facing), since this way no layover or shadow effects are created, which in turn would lead to higher PS density and more accurate data.

The analysed period of time was chosen to be relatively short, *c.a.* 12 months, because it was expected that the constantly changing vegetation cover causes coherence loss over time, however this has still not enabled the interpretation to give conclusive results. It was expected that some ground movement would be seen up to several months before the collapse event, but as the movements were so small, it is not clear whether the movement was due to the actual event or just due to the noise that was registered within the data acquired and processed.

With a handful of PS located quite far away from the cliff face inland (closest of them being 70-100 m away from cliff), the ground movements recorded were small (within 1-2 mm), with the scale of movements within a margin of error of the PSI method, challenging to make a definite link of the changes with coastal cliff collapse processes. It was not possible to conclude whether the recorded movement would have been related to the actual cliff failure or just described general ground movement.

7.4 Landslide analysis and monitoring

The landslide analysis in Chapter 5 has provided a positive outcome and case studies have shown good results in terms of monitoring of the coastal landslides. Three landslides have been investigated, including Cow Gap in a rural environment and Folkestone Warren and Ventnor town, both urban locations.

All three rotational landslides prove the PSI methodology can be successfully used in such areas and can be a helpful tool to distinguish different types of ground movements within such type of a landslide. This has been shown with presenting the downward movement of every main body of every discussed landslide, as well as the upward movement of their toes, which were also usually moving slower on average in comparison to the main body. Additionally, by analysing IDW maps, an average velocity for different blocks within landslides can be distinguished, which can help determining different sections of a landslide, like in the case of Ventnor Undercliff, where the Lowtherville Graben, while still being a part of the landslide, was clearly highlighted as a semi-independently moving block. The three case studies presenting landslides in Chapter 5 are within chalk strata, with Gault Clay underlying it, acting as slip surface. Because of this, the ground movements are relatively fast. This also makes them a good analogue that can be used for other environments, where the rock formations are stronger and therefore move slower. Thanks to the use of PSI method, a continuous monitoring of such processes is possible over long time period, which is also supported by the ESA Sentinel-1A and 1B satellites being in orbit since 2015 onward, providing a continuous source of good quality of SAR scenes that can be used for long term monitoring of coastal locations. Using the PSI methodology for determining the landslide movements, especially when combined with conventional in-situ methods, provides a comprehensive outcome that can reveal temporal patterns of change. These results can be easily used by coastal engineers when planning landslide maintenance, by showing areas that might need more attention than others – for example when ground movement velocity has increased over a period of time. By carefully analysing PSI results, the cost of maintenance could be lowered, as the site visits could be focused on the zones with highest rates of ground movements, instead of necessity of frequent visits to assess the stability of sites.

7.4.1 Folkestone Warren

Folkestone Warren landslide (Chapter 5, Section 5.2) has been investigated with a dataset of 2 years (December 2017 – August 2019). The dataset was filtered to include only low-tide scenes to improve the PS density on the foreshore. The processed data has been used to analyse several areas, including the foreshore and the toe of the landslide, the central area where the railway lies, and the backscarp of the landslide. Due to the majority of the landslide being heavily vegetated, the PS point density was low and sparsely distributed, especially around the backscarp section. The foreshore showed better more PS points in the area, which can be associated with using low tide scenes, increasing the coherence of the platform. An IDW map (Chapter 5, Figure 5.7) has been created for the whole landslide, based on a 2-year dataset, showing areas of uplift that can be connected to the movement of the toe and indicating that the majority of the landslide body is relatively stable with displacements less than ±5 mm a^{-1}. The western area of the foreshore (Chapter 5, Figure 5.8) presents the most significant ground movements between June 2018 and February 2019, followed by a relatively stable period. The ground movement seen within this area can be related to the movement of the toe of the landslide which would be expected due to the rotational movement of the landslide mass. Looking at the section along the foreshore, an overall upward motion (heave) can still be distinguished, confirming the upward movement of the toe of the landslide. The PS data presents more regular movement towards the north-east of the analysed area, with a minor element of rainfall related cyclicity can be observed in the data. A cross-section of the landslide (Chapter 5, Figure 5.9) has also been created and PS along that cross-section have been analysed. The upward movement (towards the satellite) is distinguishable and again confirms movement of the toe. This movement is most likely happening as there is not enough toe weight located in this area and it is causing rotational slip movement to continue along in the base of the Gault Clay. This also suggests additional engineering works like increasing toe loading might be beneficial to minimise the movement along this section. The area where the railway track (Chapter 5, Figure 5.10) is located has also been analysed, it shows movements in the region of 0- 5 mm a^{-1} along the central portion of the track. Looking at the scarp of the landslide (Chapter 5, Figure 5.13) a very few PS points are produced over the area, as it is heavily vegetated, causing the loss of coherence. Results over 2-years show small cyclical trend within the data of ±5 mm.

7.4.2 Cow Gap

Results from Cow Gap (Chapter 5, Section 5.3) show very clear and continuous ground movement over time and a five-year period was processed and analysed in the project. Time series show the main body of the rotational slide moving down (in LoS) -8.84 mm a^{-1} on average, and the toe of the landslide moving upwards +0.65 mm a^{-1}. By using python script to select only scenes acquired at low tide, investigation of the toe movement has been made possible. This script has reduced the number of scenes available for processing, however it has improved overall coverage of the platform in front of the landslide and the beforementioned landslide toe.

7.4.3 Ventnor Undercliff

In the Ventnor town area (Chapter 5, Section 5.4), two data sets have been processed, in ascending and descending orbit, with the aim to produce a true vertical and horizontal ground movements. This data has also been filtered to include low-tide scenes only. Results from this processing have been compared with previous, conventional studies (published in Chandler M. P. (1984), Geomorphological Services Limited (1991) and Moore et al. (2007)) and show good correlation between them, showing subsidence around Lowtherville Graben and heave at Ventnor Park. Vertical and horizontal movements for the landslide have been calculated and are between -9.8 to +8.5 mm a^{-1} for vertical movements, and between -3.7 and +12.4 mm a^{-1} for west – east movements. Based on the results from this processing, it was possible to support and update the existing 2D model (Chapter 5.4, Figure 5.24) highlighting the potential slip (failure) surface. It has also been shown that this matches previous interpretations of the failure plane being located within the Gault Clay. Time series have been created for two key areas, Lowtherville Graben and Ventnor Park and IDW maps (Chapter 5, Figure 5.25 and Figure 5.26) have been also generated for the Ventnor town area to show the hot spots of ground movements and display results spatially. IDW maps show very clear downward movement within the Lowtherville Graben area and small heave at the foreshore of the town (with an average ground movement below 5 mm a^{-1}) – which can be correlated with the toe of the landslide moving slowly upwards. Some correlation with rainfall has also been possible, showing prolonged rainfall can be causing faster ground movements that occur after rainfall (20-30 days later). This can be related to higher pore pressure generation within the landslide due to increased amount of water within the rock mass.

7.5 Platform downwearing analysis and monitoring

Platform downwearing (Chapter 6) has been analysed in East Sussex based on 3.5-year long dataset, results of which have been also published in Remote Sensing journal in October 2020. PSI methodology for monitoring and analysis of platform downwearing has not been previously used anywhere in the world, making this a pioneering approach for such coastal processes.

These results show a robust methodology that has been developed for platform downwearing, that provides results of high degree of precision at both regional and local scale. With the use of PSI method, platform downwearing can be not only monitored over time, but also quantified in terms of the speed of erosion per annum, which has not been achieved before. The results provide not only temporal, but also spatial extend, for the information on the ground erosion, covering a continuous 30 km stretch of the coast from Brighton all the way to Eastbourne, UK. Such information can be easily used by coastal engineers and local councils, for coastal defences maintenance and planning, and it also provides indication on the areas of high priority, where platform downwearing is happening faster in comparison to others.

Outcome of this study shows that PSI technique is a very effective monitoring tool, not only able to analyse platform erosion, highlighting areas where it is the most intense (such as seen on the interpolated map in Chapter 6, Figure 6.7), which in turn can show potential areas where coastal defences might be failing. When used as a long-term monitoring tool, PSI has a great potential to observe the deterioration or the lack of it of the man-made coastal protection, helping the coastal town councils to assess them in person and then plan repairs accordingly.

An interpolated map (Chapter 6, Figure 6.7) has been created showing average ground velocity per annum between Brighton and Eastbourne. Based on that map, an average ground movement for the whole region of -0.36 mm a^{-1} has been calculated showing the platform is gradually downwearing, as would be expected. However, for the first time it was possible to accurately quantify the rate on a regional scale and at a local scale allowing for interpretation of the natural processes and the impact of coastal defences. Difference in the velocity of the movements between protected (where man-made coastal defences are present), and unprotected (without such defences) areas have been identified, in protected areas the average velocity is -0.33 mm a^{-1}, while unprotected areas are downwearing more rapidly with movements away from the satellite of -1.10 mm a^{-1} and those trends have been interpreted as downwearing of the platform as this is a known process and consistent with previous investigations ((Dornbusch et al. (2008b), Ellis (1986), Dornbusch et al. (2007), Dornbusch and Robinson (2011)).

The protected areas, being within urban zones, are moving slower due to the presence of man-made coastal defences. As the coastal defences protect the areas through a number of methods, such as increasing the retention of sediment supply, helping to reduce the platform exposure; absorbing and dissipating some of the wave energy, thus reducing the impact of it on the direct downwearing of the platform; both especially important during storm seasons, when the effects of weather increase the erosion of the platform. The impact of the defences can be seen in the results achieved with PSI, on the IDW map mentioned above, with quantified details shown in Chapter 6, Table 6.2, where average velocities per different formation are presented, as well as pointed out whether the investigated area lies within a protected or unprotected zone.

Lithostratigraphy has also been taken into consideration in Section 6.5.1., and averages have been calculated per platform outcropping formation within the study area. Results indicate the downwearing of the Lewes Nodular Chalk is the slowest at a rate of -0.53 mm a^{-1} compared to Seaford Chalk with an average downwearing of -0.66 mm a^{-1}. This is most likely because the Lewes Nodular Chalk is generally stronger than the Seaford Chalk especially the nodular beds (Mortimore et al., 2004a). Surprisingly the Newhaven Chalk platform downwearing is slower than the other formations at -0.40 mm a^{-1} even though it has similar properties to the Seaford Chalk (Lord et al., 2002). This can be explained by the location of Newhaven Chalk outcrops as it is only shown on the surface along the urban sections of the foreshore, while Lewes Nodular and Seaford Chalk outcrop along unprotected areas within rural sections of the coast (See Chapter 6, figure 6.8). These results are just within the limit of accuracy of the methodology; however, they are based on 3.5 years of data, and the downward trend is continuous and consistent over the analysed period of time, providing confidence in the results. The PSI results have also been compared with previous studies, and they are within ranges previously achieved, summary of which can be found in Table 6.3.

Three smaller focused research sites have been chosen to look into in more detail to show point – specific ground changes in time. Two urban based locations have been chosen (Roedean and Saltdean, Sections 6.5.2.1 and 6.5.2.2) and one rural location (Seven Sisters platform, Section 6.5.2.3). Average platform downwearing for Roedean site is -1.0 mm a^{-1}, which is at the accuracy limit for the PS method.

Based on the time series plot (Chapter 6, Figure 6.9), a consistent downward trend can be seen over the 3.5 years of analysis with an overall 4 mm of erosion confirming the reliability of the results. While some variation can be seen on the time series, it is expected to be present due to the heterogeneity of the platform and some small amounts of vegetation over the rocks, as well as the sediment transport to and from the area.

The Saltdean research site shows a ground velocity of -0.86 mm a^{-1}, however this area has only a small number of PS across the site, mainly on the undercliff walkway on the exposed chalk at the base of the seawall. The time series (Chapter 6, Figure 6.10) show a significant variation with the prevalent movement being downward (away from the satellite). The downward movement that is seen on the time series can be associated with the action of chalk downwearing against the seawall, as has been discussed in Chapter 6, Section 6.5.2.2.

The third local research site was within Seven Sisters cliff, more specifically Flagstaff Point and Flagstaff Bottom, which show an average downwearing velocity of -1.03 mm a^{-1}. For this specific location, two separate zones have been analysed, one in front of Flagstaff Point cliff line and one in front of Flagstaff Bottom cliff line (Chapter 6, Figure 6.11). They show with slightly different average velocities – Flagstaff Point is downwearing slightly faster - at 1.21 mm a^{-1} compared to Flagstaff Bottom which is down wearing at a rate of -0.94 mm a^{-1}. These results can be explained with different hydrodynamic regimes for the areas, as well as by the presence of longshore drift from west to east. The platform in front of Flagstaff Point is extends further out into the sea, especially at low tide, which causes a shielding of the platform in front of the Flagstaff Bottom, potentially cause the lower erosion.

7.6 Methodology limitations

While the research has been largely successful, some difficulties have been encountered and several areas have been identified where InSAR has limitations or with further work future improvements could be made.

In terms of the software and preparation, a fast internet connection and large storage capacity is required to manage the data downloads, since a single scene is about 7 Gb in size, and most of the studies have to be performed on 80+ scenes. The data preparation needed to be carefully planned, with correct areas of investigation being chosen and cut to an appropriate size, so the processing could be done within a manageable time frame. For all of the studies presented in this thesis, the areas of investigation have been chosen based on the spatial extend of the coastal processes that were anticipated to be encountered within. The number of scenes selected for each of the case studies has been chosen to suit the type of the process, for example shorter time frame for cliff collapses, and longest available time for platform downwearing, where the ground movement (erosion) was small and within the limits of the tool's accuracy, meaning that long time-series were necessary to provide enough information for it to be robust and accurate.

The majority of results produced are presented in LoS, as achieving true vertical and horizontal movements requires the processing of two data sets from both orbits (ascending and descending), making processing times longer and requiring more data storage space for the scenes to be processed. Since it is common practice to present InSAR results in LoS rather than vertical, since the differences are usually minor, only the Ventnor Landslide was processed to include both directions, to provide the highest accuracy of the results.

Data have been processed with ENVI, a SARScape software program, that has proven to work efficiently, having well established procedures, however it is not a freely available software. For future works, software like StaMPS (Stanford Method for Persistent Scatterers) could be used having less costly licenses and also providing PSI processing tools; as well as an internal, newly developed processing tool from Imperial College London, ICSAR is now available for future students.

It has been shown that in coastal areas different environments require different timescales of processing to achieve the best results. When processing data for cliff collapse monitoring, the longer the time period, the less information it would have provided due to the vegetation coverage changing throughout the seasons and causing loss of coherence. On the other hand, a short time period would not be suitable for platform downwearing study, as even the 3.5 years of data analysed proved to be just within the margins of the PSI accuracy.

To allow for ease of use and interpretation by the end user moving averages were found to be the most effective way of communicating the results and have been calculated for every research area.

Due to the fact that majority of the sites were located within highly vegetated areas, the coherence threshold had to be set quite low at 0.65, otherwise the PS density would have been too low to provide enough information about the specific AOI. Such threshold is however still within acceptable limits and results show reasonable coverage for the purpose of the research.

7.7 Summary

This chapter provides a summary and discussion for the research outcome, with detailed results from all case studies. It also presents the positive outcomes of the PSI methodology, as well as some downfalls that have been encountered during the time of this MPhil project.

The main aim of this research has been successfully achieved, proving that coastal processes can be analysed and monitored with PSI methodology. While, not fully conclusive in every case investigated, this methodology provides robust information on the movement of rotational landslides, as well as the speed of platform downwearing. Investigation results achieved have not only been discussed with local councils, but have also been published in journal of Remote Sensing (Mider et al. (2020) for platform downwearing and O'Connor et al. (2021) for Ventnor Undercliff analysis), demonstrating novel take on use of remote sensing analysis for monitoring of coastal processes. By analysis of cliff collapses, landslides, and platform downwearing processes within the coastal areas, the methodology has been developed and improved to deliver more robust results. For cliff collapse monitoring, it has been exposed that the methodology is not yet fully effective, however small ground changes could be seen on the data, showing potential for further development. Landslide analysis and monitoring has been very successful, providing robust results that can be confirmed based on walkover surveys and in-situ measurements where available. Platform downwearing monitoring is a pioneering use of the methodology, that has not been done before and shows very positive results, proving the PSI is a great solution for working on such coastal processes, not only presenting results based on ground movements, but identifying differences in erosion between different rock formations, speed of deterioration of coastal defences, as well as for first time providing results for a wide spatial extent. Both landslide and platform monitoring techniques have been significantly improved with using python script to include only data acquired during low tide times, showing higher PS density, and therefore higher coherence for the AOIs.

In terms of cliff collapses, the results only show small ground movements, with uncertain cause. Some ground movement variation can be seen, and it is consistent, thus can be considered as signal not noise. This process, however, cannot be conclusively predicted, nor monitored with PSI methodology, thus it needs more development before it can be confidently used for the coastal collapse prediction. Coastal landslide analysis proves that rotational landslides within coastal areas can be monitored with PSI, and their movements can be quantified with this methodology. Not only general direction of the toe and main body of the landslide can be distinguished, but also small semi-independent blocks within a landslide can be identified, and their average ground motion can be calculated based on the data analysis. In the case of Ventnor Undercliff, the results have been presented to the Isle of Wight council and it has been met with great interest, considering the monitoring information such as presented within this thesis (Chapter 5, Section 5.4.3) can be used for future coastal planning that is very cost effective and can provide a continuous spatial and temporal information about the ground movement. Platform downwearing has shown that the small-scale erosion can also be seen based on the PSI method, as it provides consistent downward movement within the areas of interest, that is still within the accuracy of the method. These results have been presented to Brighton and Hove City Council and have also been met with a positive feedback. Since the coastal defences within towns are often ageing, continuous maintenance of them is often required, which can be costly, if long stretched of a coast need to be considered. By using tools like IDW map created for the platform downwearing study in Chapter 6, potential "hot spots" of where defences are wearing down quicker than in others can be recognised. Information based on PSI results can, and should be, joined with in-situ measurements and site visits, but thanks to the maps and time-series information, the site investigation can be focused on smaller areas, saving time and cost for visual monitoring and assessment of the man-made coastal defences.

The outcome of this MPhil project has a potential to be developed into an automated, close to real-time and retrospective coastal monitoring. The methodology has been tested on three different coastal events, showing capability of the method to be used for highlighting areas that need attention due to possible coastal protection deterioration, or faster than usual ground movements. While this would require a retrospective analysis, so a ground movement baseline can be determined, it would be a logical next step for a potential project continuation in the future.

Final Chapter 8 provides conclusions for this project, as well as discusses recommendations for future work.

8 Conclusions

8.1 Introduction

This chapter highlights the main conclusions from this research project and outlines recommendations for future work. Following the results discussed in Chapter 7, it can be concluded that this research has been able to identify coastal processes with use of PSI and has shown how InSAR can be used effectively in a range of coastal environments.

The main aim of this research was to provide better understanding of the geological evolution of chalk cliffs and coastal processes by analysis of Persistent Scatterer InSAR data. This has been achieved by examining three main processes that are ubiquitous in coastal zones:

- Cliff collapses;
- Coastal landslides; and
- Platform erosion.

These processes have been thoroughly investigated at a series of sites, in both urban and rural environments, analysing the rates and patterns as well as the impact of coastal processes, and to establish how effective are any manmade coastal defences, and the effects of rock formation heterogeneities on the magnitude of coastal erosion.

8.2 Main findings of the research

This research has made use of freely available Sentinel-1A and 1B SAR data and PSI methodology for data processing to evaluate whether a spaceborne remote sensing method is capable of monitoring the above processes to sufficient accuracies and precisions. All data have been processed in ENVI SARScape software and further analysed in ArcGIS and Excel.

Findings include:

- Coastal cliff collapse analysis (Chapter 4) proved inconclusive in the following respects:
    - Very small ground movements can be distinguished in each of the case studies. The magnitudes of these movements are approximately equal to the measurement error of the PSI method but, importantly, they show consistent trends and are detectable over considerable spatial extent. These data and this method together cannot be used to confidently determine their cause;
    - The cliff tops, within the rural area of East Sussex, are typically covered in vegetation and provided insufficient PS points near the cliff edge to successfully correlate ground movements with collapse events.
- Coastal landslide analysis (Chapter 5) has been highly successful in the following respects:

- Ground movements are clearly distinguished in both rural and urban areas;
- Three rotational landslides have been analysed; the movement of the main body of the landslide been detected in time series plots, as well as the upward movement of the toe,
- The filtering of Sentinel-1A and 1B scenes to exclude those acquired at high tide resulted in improved density on coastal platforms, enabling confident analysis of toe movement;
- Dense vegetation causes low coherence, and low PS density in vegetated areas. This is observed in the main body of each landslide, where only a handful of PS are present;
- Comparison of PSI results with in-situ data has been useful in validating the remotely sensed results and demonstrating that spaceborne measurements can be a useful tool in areas that are difficult or be hazardous to access and monitor in person;
- Use of the ascending and descending orbital data allows the vertical and horizontal velocity components of motion to be derived, giving more accurate information of the actual ground movement. This effectively doubled the processing time, since two datasets needed to be processed and then decorrelated to generate 2D motion results and improves the understanding of ground movements;
- In general, these analyses demonstrate that near-real-time monitoring is achievable, with low-cost and high accuracy, and provides detailed spatiotemporal information of the landslide movements.

- Platform downwearing monitoring (Chapter 6) has enabled the following conclusions to be drawn:
  - While the results are at the limit of current PSI accuracy, use of a sufficiently long time series demonstrates that movements have consistent temporal trends and show continuous ground movements over the 3.5 years of data analysis;
  - Filtering the data to exclude scenes acquired at high tide resulted in a reduced dataset but the PS point density generated from it increased four-fold;
  - Conventional monitoring techniques can only be used in areas of limited extent, while the PSI technique allows the monitoring of platform downwearing at a regional scale, across the whole 30 km section of coast between Brighton and Eastbourne in a single batch of processing and analysis;
  - At regional scale, interpolated velocity maps were produced to show variations in the average rate of platform erosion. These maps illustrate the areas that are downwearing fastest and that may need further attention from local councils and coastal engineers;
  - At a local scale, these analyses show that this methodology can be utilised successfully in urban and rural environments; providing useful information on current coastal erosion presented as time-series plots;

- Downwearing rates have been compared for several different rock formations, confirming softer and weaker formations to be wearing down faster than more resistant formations;
- By comparing results on coastal platforms from areas where man-made coastal protection is in place with those that are left to nature, variations in downwearing speed have been demonstrated. As expected, areas with coastal protection show slower erosion, demonstrating the effectiveness of protection within the foreshore platform;
- Comparison of PSI with conventional monitoring methodologies shows good agreement with previous studies performed in these areas.

The sites that have been analysed there, supported by field work, have enabled coastal processes to be identified and confirmed the InSAR analysis. While InSAR provides objective data about ground motion in these coastal areas, cross-checking of the results with either in-situ measurements or site investigation, is essential to fully understand the interaction with natural processes.

Results have been presented to Brighton and Hove City Council (in East Sussex) and to the Isle of Wight Council in a clear and concise fashion, explaining the fundamentals of the methodology, processing steps and results of the case studies. The final results proved to be easily understood and show the great potential for the use of PSI in the future by councils in maintenance planning. They provide a cost-effective solution to characterisation and quantification of the coastal zone changes over large areas. They can be used in both rural and urban areas and are especially effective when combined with conventional direct (in-situ) methodologies of ground monitoring. The results have been highly appreciated by the councils, with discussions underway as to how they can be implemented in future maintenance and coastal defences planning.

8.3 Future work recommendations

This thesis presents a study based on use of PSI methodology to analyse geological processes within coastal areas and while as thorough as possible, the following future work recommendations should be considered.

- Use of a method which exploits Distributed Scatterers as well as point PS, such as SBAS or SqueeSAR™ to derive more information in vegetated areas. The rural locations have proven to be difficult to achieve high coherence due to dense vegetation constantly growing and changing, causing loss of coherence and lack of PS within the area. Distributed scatterer methodologies may provide better measurement coverage and density. The SBAS uses smaller baseline subsets and theoretically achieve higher coherence for the areas in question, which could be highly beneficial, especially for cliff collapse analysis, however it might suppress small ground movements, therefore data validation with in-situ results should be performed.

- Use of both ascending and descending datasets for every research site. This would provide true vertical and horizontal ground movements, instead of only Line of Sight. This is resource-intensive and needs to be scheduled ahead of time so that analysis of multiple case studies fits within future projects timelines.
- Automation of the data downloading, achieved through scripting, allowing data to be downloaded onto sufficiently large storage from the servers as they become available.
- Automation of data preparation and processing. SARScape could be utilised to create processing chains, or in-house software could be developed to do so. This could help with processing data more efficiently.
- Use of older satellite data, like ENVISAT or RADARSAT to provide longer monitoring periods, since Sentinel satellites have only been in orbit since 2015. The data from the majority of satellites is usually not freely available so there would be budget considerations in using their data.
- Use of different band sensors might be beneficial. X-band sensors provide higher resolution and increased data density in urban area, while L-band sensors can improve results in vegetated areas by penetrating vegetation better than the C-band Sentinel-1 satellites.

8.4 Final remarks

This research presents a novel methodology using Earth Observation data to monitor, measure and quantify the geological processes in coastal areas. The research on monitoring platform downwearing with the use of PSI has not been achieved before and is a successful advancement in monitoring and analysis of such coastal areas. The recognition of the 2D landslide patterns in coastal zones is a pioneering approach to the interpretation of the landslide movements.

The majority of results demonstrate that accurate, detailed, and quantitative results can be produced on local and regional scales and over very extensive areas when needed. They present continuous, retrospective information over long periods of time for coastal processes, revealing patterns and rates of ground level changes. The improved PSI methodology used during this MPhil can be easily used in any coastal environment and provide results for any rock formations present on the coast anywhere around the world. In addition, PSI and conventional methods are complementary to each other, and used in tandem can provide robust information on temporal and spatial patterns of change.

9 References

ALBIN, J. 1818. *A companion to the Isle of Wight*, Longman.

ALLEN, D. J., BREWERTON, L. J., COLEBY, L. M., GIBBS, B. R., LEWIS, M. A., MACDONALD, A. M., WAGSTAFF, S. J. & WILLIAMS, A. T. 1997. The physical properties of major aquifers in England and Wales. Keyworth, Nottingham: ENVIRONMENT AGENCY R&D PUBLICATION 8.

AMITRANO, D., GRASSO, J. R. & SENFAUTE, G. 2005. Seismic precursory patterns before a cliff collapse and critical point phenomena. *Geophysical Research Letters,* 32.

ASLAN, G., FOUMELIS, M., RAUCOULES, D., DE MICHELE, M., BERNARDIE, S. & CAKIR, Z. 2020. Landslide Mapping and Monitoring Using Persistent Scatterer Interferometry (PSI) Technique in the French Alps. *Remote Sensing,* 12.

BARLOW, J., GILHAM, J. & IBARRA COFRÃ, I. 2017. Kinematic analysis of sea cliff stability using UAV photogrammetry. *International Journal of Remote Sensing,* 38**,** 2464-2479.

BARTRUM, J. A. High-water rock platforms: a phase of shoreline erosion. Trans. Proc. New Zealand Inst., 1916. 132-134.

BAYER, B., SIMONI, A., MULAS, M., CORSINI, A. & SCHMIDT, D. 2018. Deformation responses of slow moving landslides to seasonal rainfall in the Northern Apennines, measured by InSAR. *Geomorphology,* 308**,** 293-306.

BELL, F., CULSHAW, M. & CRIPPS, J. 1999. A review of selected engineering geological characteristics of English Chalk. *Engineering geology,* 54**,** 237-269.

BERARDINO, P., FORNARO, G., LANARI, R. & SANSOSTI, E. 2002. A new algorithm for surface deformation monitoring based on small baseline differential SAR interferograms. *IEEE Transactions on Geoscience and Remote Sensing,* 40**,** 2375-2383.

BIRCH, G. & ANDERSON, I. 2011. LiDAR monitoring for the Folkestone Warren landslide. *Ground Engineering, May*.

BIRCH, G. & WARREN, C. 2007. Landslide and chalk fall management on the Folkestone to Dover railway line, Kent. *Landslides & climate change. Taylor & Francis Group, London***,** 295-304.

BLANCO-CHAO, R., PÉREZ-ALBERTI, A., TRENHAILE, A. S., COSTA-CASAIS, M. & VALCÁRCEL-DÍAZ, M. 2007. Shore platform abrasion in a para-periglacial environment, Galicia, northwestern Spain. *Geomorphology,* 83**,** 136-151.

BOREHOLE SCANS. 2020. Available: https://www.bgs.ac.uk/data/boreholescans/home.html [Accessed].

BOWDEN, A. J., SPINK, T. W. & MORTIMORE, R. N. 2002. The engineering description of chalk: its strength, hardness and density. *Quarterly Journal of Engineering Geology and Hydrogeology,* 35**,** 355-361.

BRISTOW, R., MORTIMORE, R. & WOOD, C. 1997. Lithostratigraphy for mapping the Chalk of southern England.

BRITISH GEOLOGICAL SURVEY. 2020. *The BGS Lexicon of Named Rock Units [online]* [Online]. Keyworth, Nottingham, UK. Available: https://www.bgs.ac.uk/technologies/the-bgs-lexicon-of-named-rock-units/. [Accessed 2020].

BROMHEAD, E. 1978. Large landslides in London Clay at Herne Bay, Kent. *Quarterly Journal of Engineering Geology and Hydrogeology,* 11**,** 291 - 304.

BROMHEAD, E. & IBSEN, M.-L. 2007. Folkestone Warren landslides and the impact of the past rainfall record. *Landslides and Climate Change, Taylor & Francis Group, London***,** 17-24.

BROSSARD, J. & DUPERRET, A. 2004. Coastal chalk cliff erosion: experimental investigation on the role of marine factors. *Geological Society, London, Engineering Geology Special Publications,* 20**,** 109-120.

BRYDONE, R. M. 1912. The Stratigraphy of the Chalk of Hants. *Geological Magazine,* 10**,** 122-123.

BRYDONE, R. M. 1914. The Zone of Offaster pilula in the South English Chalk. *Geological Magazine,* 1**,** 405-411.

BRYDONE, R. M. 1915. The Marsupites Chalk of Brighton. *Geological Magazine,* 2**,** 12-15.

BUCKLEY, R. 2018. The axial behaviour of displacement piles in chalk.

BUCKLEY, S. J., MILLS, J. P., CLARKE, P. J., EDWARDS, S. J., PETHICK, J. & MITCHELL, H. L. 2002. Synergy of GPS photogrammetry and InSAR for coastal zone monitoring. *Symposium on Geospatial Theory, Processing and Applications.* Ottawa, Canada.

BULLAR, J. 1806. *A historical and picturesque guide to the Isle of Wight.[Another]*, Baker and son.

BURLAND, J. B. & LORD, J. A. 1970. The load-deformation behaviour of Middle Chalk at Mundford, Norfolk. Building Research Station Garston.

BUSBY, J. P. & JACKSON, P. 2006. The application of time-lapse azimuthal apparent resistivity measurements for the prediction of coastal cliff failure. *Journal of Applied Geophysics,* 59**,** 261-272.

BUSBY, J. P., SENFAUTE, G., GOURRY, J.-C., LAWRENCE, J., PEDERSEN, S. & MORTIMORE, R. 2004. Developing tools for the prediction of catastrophic coastal cliff collapse. *Littoral 2004 : proceedings of the 7th International symposium***,** 596-601.

CAREY, J., MOORE, R. & PETLEY, D. N. 2015. Patterns of movement in the Ventnor landslide complex, Isle of Wight, southern England. *Landslides,* 12**,** 1107-1118.

CARLÀ, T., TOFANI, V., LOMBARDI, L., RASPINI, F., BIANCHINI, S., BERTOLO, D., THUEGAZ, P. & CASAGLI, N. 2019. Combination of GNSS, satellite InSAR, and GBInSAR remote sensing monitoring to improve the understanding of a large landslide in high alpine environment. *Geomorphology,* 335**,** 62-75.

CARPENTER, N., DICKSON, M., WALKDEN, M., NICHOLLS, R. & POWRIE, W. 2014. Effects of varied lithology on soft-cliff recession rates. *Marine Geology,* 354**,** 40-52.

CASTEDO, R., MURPHY, W., LAWRENCE, J. & PAREDES, C. 2012. A new process–response coastal recession model of soft rock cliffs. *Geomorphology,* 177-178**,** 128-143.

CHANDLER M. P. 1984. *The coastal landslides forming the undercliff of the Isle of Wight.* PhD, Imperial College of Science and Technology London.

CHATTERJEE, R., LAKHERA, R. & DADHWAL, V. 2010. InSAR coherence and phase information for mapping environmental indicators of opencast coal mining: a case study in Jharia Coalfield, Jharkhand, India. *Canadian journal of remote sensing,* 36**,** 361-373.

CHEN, Z., WHITE, L., BANKS, S., BEHNAMIAN, A., MONTPETIT, B., PASHER, J., DUFFE, J. & BERNARD, D. 2020. Characterizing marsh wetlands in the Great Lakes Basin with C-band InSAR observations. *Remote Sensing of Environment,* 242**,** 111750.

CHENEY, M. 2001. A mathematical tutorial on synthetic aperture radar. *SIAM review,* 43**,** 301-312.

CIAMPALINI, A., RASPINI, F., LAGOMARSINO, D., CATANI, F. & CASAGLI, N. 2016. Landslide susceptibility map refinement using PSInSAR data. *Remote Sensing of Environment,* 184**,** 302-315.

CIAMPALINI, A., SOLARI, L., GIANNECCHINI, R., GALANTI, Y. & MORETTI, S. 2019. Evaluation of subsidence induced by long-lasting buildings load using InSAR technique and geotechnical data: The case study of a Freight Terminal (Tuscany, Italy). *International Journal of Applied Earth Observation and Geoinformation,* 82.

CLARK, M. 1979. Marine processes. *Processes in Geomorphology*.

CLAYTON, C. 1983. The influence of diagenesis on some index properties of chalk in England. *Geotechnique,* 33**,** 225-241.

CLAYTON, C. & MATTHEWS, M. 1987. Deformation, diagenesis and the mechanical behaviour of chalk. *Geological Society, London, Special Publications,* 29**,** 55-62.

CLAYTON, C. J. The chemical environment of flint formation in Upper Cretaceous chalks. International flint symposium. 4, 1986. 43-54.

COLESANTI, C., FERRETTI, A., NOVALI, F., PRATI, C. & ROCCA, F. 2003. SAR monitoring of progressive and seasonal ground deformation using the permanent scatterers technique. *IEEE Transactions on Geoscience and Remote Sensing,* 41**,** 1685-1701.

COOMBES, M. A. 2014. Chapter 5 The rock coast of the British Isles: weathering and biogenic processes. *Geological Society, London, Memoirs,* 40**,** 57-76.

CROSETTO, M., MONSERRAT, O., CUEVAS-GONZÁLEZ, M., DEVANTHÉRY, N. & CRIPPA, B. 2016. Persistent scatterer interferometry: A review. *ISPRS Journal of Photogrammetry and Remote Sensing,* 115**,** 78-89.

CROZIER, M. J. 2006. *Landslides - Gravity always wins, Te Ara - the Encyclopedia of New Zealand* [Online]. Available: http://www.TeAra.govt.nz/en/diagram/8782/landslide-types [Accessed 26 January 2021].

CRUDEN, D. M. 1991. A simple definition of a landslide. *Bulletin of the International Association of Engineering Geology-Bulletin de l'Association Internationale de Géologie de l'Ingénieur,* 43**,** 27-29.

CURLANDER, J. C. & MCDONOUGH, R. N. 1991. *Synthetic aperture radar*, Wiley, New York.

DAVIDSON-ARNOTT, R., BAUER, B. & HOUSER, C. 2019. *Introduction to coastal processes and geomorphology*, Cambridge University Press.

DAVIES, J. L. & CLAYTON, K. M. 1980. *Geographical variation in coastal development*, Longman London.

DICKSON, M. E. & PERRY, G. L. W. 2016. Identifying the controls on coastal cliff landslides using machine-learning approaches. *Environmental Modelling & Software,* 76**,** 117-127.

DORNBUSCH, U., MOSES, C., ROBINSON, D. & WILLIAMS, R. 2004. Laboratory abrasion tests on beach flint shingle. *Geological Society, London, Engineering Geology Special Publications,* 20**,** 131-138.

DORNBUSCH, U., MOSES, C., ROBINSON, D. A. & WILLIAMS, R. 2008a. Soft copy photogrammetry to measure shore platform erosion on decadal timescales. *Journal of Coastal Conservation,* 11**,** 193-200.

DORNBUSCH, U. & ROBINSON, D. A. 2011. Block removal and step backwearing as erosion processes on rock shore platforms: a preliminary case study of the chalk shore platforms of south-east England. *Earth Surface Processes and Landforms,* 36**,** 661-671.

DORNBUSCH, U., ROBINSON, D. A., MOSES, C. A. & WILLIAMS, R. B. 2008b. Temporal and spatial variations of chalk cliff retreat in East Sussex, 1873 to 2001. *Marine Geology,* 249**,** 271-282.

DORNBUSCH, U., ROBINSON, D. A., MOSES, C. A. & WILLIAMS, R. B. G. 2006. Chalk coast erosion and its contribution to the shingle budget in East Sussex. *Annals of Geomorphology,* 144**,** 215-2330.

DORNBUSCH, U., ROBINSON, D. A., MOSES, C. A. & WILLIAMS, R. B. G. 2008c. Temporal and spatial variations of chalk cliff retreat in East Sussex, 1873 to 2001. *Marine Geology,* 249**,** 271-282.

DORNBUSCH, U., ROBINSON, D. A., WILLIAMS, R. B. G. & MOSES, C. A. 2007. Chalk shore platform erosion in the vicinity of sea defence structures and the impact of construction methods. *Coastal Engineering,* 54**,** 801-810.

DRUMMOND, P. V. O. 1967. *Cenomanian palaeogeography of Dorset and adjacent counties.* University of London.

DUPERRET, A., GENTER, A., MARTINEZ, A. & MORTIMORE , R. N. 2004. Coastal chalk cliff instability in NW France: role of lithology, fracture pattern and rainfall. *Geological Society, London, Engineering Geology Special Publications,* 20**,** 33-55.

EIDENER, M. & BAMLER, R. 2014. InSAR Error Sources. *SAR EDU Remote Sensing Education Initiative* [Online]. Available: https://eo-college.org/resources/insar_errors/.

ELLIS, N. 1986. *Morphology, process and rates of denudation on the chalk shore platform of East Sussex.* Brighton Polytechnic.

EMERY, K. O. & KUHN, G. G. 1982. Sea cliffs: their processes, profiles, and classification. *Geological Society of America Bulletin,* 93**,** 644-654.

ENGDAHL, M. 2013. Multitemporal InSAR in land-cover and vegetation mapping.

ENVI 2010. Exploring the SARscape Modules for ENVI.

ENVIRONMENT AGENCY 2010. Isle of Wight Shore Management Plan 2. Policy Development Zone 4 - Ventnor and the Undercliff. *In:* ISLE OF WIGHT COUNCIL, C. M. (ed.).

ESA 2012. *Sentinel-1 ESA publication*, ESA Communications.

EUROPEAN SPACE AGENCY 2013. Sentinel-1 user handbook.

EVANS, E. 2004. Foresight: future flooding: scientific summary: volume I: future risks and their drivers.

FERRETTI, A. 2014. *Satellite InSAR Data: Reservoir Monitoring from Space*.

FERRETTI, A., FUMAGALLI, A., NOVALI, F., PRATI, C., ROCCA, F. & RUCCI, A. 2011. A New Algorithm for Processing Interferometric Data-Stacks: SqueeSAR. *IEEE Transactions on Geoscience and Remote Sensing,* 49**,** 3460-3470.

FERRETTI, A., MONTI-GUARNIERI, A., PRATI, C., ROCCA, F. & MASSONNET, D. 2007. *InSAR Principles: Guidelines for SAR Interferometry Processing and Interpretation,* The Netherlands, ESA Publications.

FERRETTI, A., PRATI, C. & ROCCA, F. 2000. Nonlinear subsidence rate estimation using permanent scatterers in differential SAR interferometry. *IEEE Transactions on geoscience and remote sensing,* 38**,** 2202-2212.

FERRETTI, A., PRATI, C. & ROCCA, F. 2001. Permanent Scatterers in SAR Interferometry. *IEEE TRANSACTIONS ON GEOSCIENCE AND REMOTE SENSING,* 31**,** 8-20.

FLORES-ANDERSON, A. I., HERNDON, K. E., THAPA, R. B. & CHERRINGTON, E. 2019. The SAR Handbook: Comprehensive Methodologies for Forest Monitoring and Biomass Estimation.

FOOTE, Y., PLESSIS, E., ROBINSON, D. A., HENAFF, A. & COSTA, S. 2006. Rates and patterns of downwearing of chalk shore platforms of the Channel: comparison between France and England. *Annals of Geomorphology,* 144**,** 93-115.

FRANCIONI, M., COGGAN, J., EYRE, M. & STEAD, D. 2018. A combined field/remote sensing approach for characterizing landslide risk in coastal areas. *International Journal of Applied Earth Observation and Geoinformation,* 67**,** 79-95.

FRODELLA, W., CIAMPALINI, A., GIGLI, G., LOMBARDI, L., RASPINI, F., NOCENTINI, M., SCARDIGLI, C. & CASAGLI, N. 2016. Synergic use of satellite and ground based remote sensing methods for monitoring the San Leo rock cliff (Northern Italy). *Geomorphology,* 264**,** 80-94.

FUHRMANN, T. & GARTHWAITE, M. C. 2019. Resolving Three-Dimensional Surface Motion with InSAR: Constraints from Multi-Geometry Data Fusion. *Remote Sensing,* 11.

GABRIEL, A. K., GOLDSTEIN, R. M. & ZEBKER, H. A. 1989. Mapping small elevation changes over large areas: Differential radar interferometry. *Journal of Geophysical Research,* 94.

GARTHWAITE, M. C., NANCARROW, S., HISLOP, A., THANKAPPAN, M., DAWSON, J. H. & LAWRIE, S. 2015. The Design of Radar Corner Re ectors for the Australian Geophysical Observing System. *Geoscience Australia*.

GASTER, C. T. A. 1932. The zones of the Chalk of the Arun Gap, Sussex: With description of new species of Bicavea. *Proceedings of the Geologists' Association,* 43**,** 212-IN1.

GEOMORPHOLOGICAL SERVICES LIMITED 1991. Coastal Landslip Potential Assessment: Isle of Wight Undercliff. Ventnor, UK.

GIARDINA, G., MILILLO, P., DEJONG, M. J., PERISSIN, D. & MILILLO, G. 2019. Evaluation of InSAR monitoring data for post - tunnelling settlement damage assessment. *Structural Control and Health Monitoring,* 26**,** e2285.

GILHAM, J., BARLOW, J. & MOORE, R. 2018. Marine control over negative power law scaling of mass wasting events in chalk sea cliffs with implications for future recession under the UKCP09 medium emission scenario. *Earth Surface Processes and Landforms,* 43**,** 2136-2146.

GILHAM, J., BARLOW, J. & MOORE, R. 2019. Detection and analysis of mass wasting events in chalk sea cliffs using UAV photogrammetry. *Engineering geology,* 250**,** 101-112.

GONZÁLES-MARTÍ, J., NEVARD, S. & SÁNCHEZ, J. 2017. The use of InSAR (Interferometric Synthetic Aperture Radar) to complement control of construction and protect third party assets. *Crossrail Learning Legacy Report, London, UK, Crossrail Ltd*.

GRANT, B. 2020. *Cliff and Landslide Monitoring with PSInSAR in Folkestone Warren, Kent, UK.* MSci, Imperial College London.

HALCROW 2006. Ventnor Undercliff, Isle of Wight coatsal instability risk: interpretative report and quantitative risk analysis. . *Technical report to the Isle of Wight Council*.

HALL, K. & THORN, C. E. 2014. Thermal fatigue and thermal shock in bedrock: An attempt to unravel the geomorphic processes and products. *Geomorphology,* 206**,** 1-13.

HANCOCK, J. M. 1975. The petrology of the Chalk. *Proceedings of the Geologists' Association,* 86**,** 499-535.

HARRIS GEOSPATIAL 2020. SARScape Help *In:* SARMAP SA 2020 (ed.).

HART, M. 1987. Orbitally induced cycles in the Chalk facies of the United Kingdom. *Cretaceous Research,* 8**,** 335-348.

HEMMINGSEN, S. A., EIKAAS, H. S. & HEMMINGSEN, M. A. 2007. The influence of seasonal and local weather conditions on rock surface changes on the shore platform at Kaikoura Peninsula, South Island, New Zealand. *Geomorphology,* 87**,** 239-249.

HENAFF, A., LAGEAT, Y. & COSTA, S. 2006. Geomorphology and shaping processes of chalk shore platforms of the Channel coasts. *Annals of Geomorphology,* 144**,** 61-91.

HOWARD, T., PALMER, M., GUENTCHEV, G. & KRIJNEN, J. 2019. Exploratory sea level projections for the UK to 2300. Bristol, UK: Environment Agency.

HUTCHINSON, J., BROMHEAD, E. & LUPINI, J. 1980a. Additional observations on the Folkestone Warren landslides. *Quarterly Journal of Engineering Geology and Hydrogeology,* 13**,** 1-31.

HUTCHINSON, J. & DE GRAFF, J. 2002. Chalk flows from the coastal cliffs of northwest Europe. *Catastrophic Landslides: Effects, Occurrence, and Mechanisms. Boulder, Colorado: The Geological Society of America***,** 257-302.

HUTCHINSON, J. N. 1969. A reconsideration of the coastal landslides at Folkestone Warren, Kent. *Geotechnique,* 19**,** 6-38.

HUTCHINSON, J. N., BROMHEAD, E. N. & LUPINI, J. F. 1980b. Additional observations on the Folkestone Warren landslides. *Quarterly Journal of Engineering Geology and Hydrogeology,* 13**,** 1-31.

INTRIERI, E., GIGLI, G., NOCENTINI, M., LOMBARDI, L., MUGNAI, F., FIDOLINI, F. & CASAGLI, N. 2015. Sinkhole monitoring and early warning: An experimental and successful GB-InSAR application. *Geomorphology,* 241**,** 304-314.

KENDON, M., MCCARTHY, M., JEVREJEVA, S., MATTHEWS, A. & LEGG, T. 2019. State of the UK climate 2018. *International Journal of Climatology,* 39**,** 1-55.

KING, C. A. M. 1972. *Beaches and coasts*, Arnold.

LAMONT-BLACK, J. & MORTIMORE, R. N. 1996. Determination of the intact dry density of irregular chalk lumps: a new method. *Quarterly Journal of Engineering Geology and Hydrogeology,* 29**,** 241-248.

LANARI, R., CASU, F., MANZO, M., ZENI, G., BERARDINO, P., MANUNTA, M. & PEPE, A. 2007. An overview of the small baseline subset algorithm: A DInSAR technique for surface deformation analysis. *Deformation and Gravity Change: Indicators of Isostasy, Tectonics, Volcanism, and Climate Change***,** 637-661.

LAWRENCE, J. A., MORTIMORE, R. N., STONE, K. J. & BUSBY, J. P. 2013. Sea saltwater weakening of chalk and the impact on cliff instability. *Geomorphology,* 191**,** 14-22.

LILLESAND, T., KIEFER, R. W. & CHIPMAN, J. 2015. *Remote sensing and image interpretation*, John Wiley & Sons.

LIM, M. 2014. Chapter 3 The rock coast of the British Isles: cliffs. *Geological Society, London, Memoirs,* 40**,** 19-38.

LIU, J. G. & MASON, P. J. 2016. *Image processing and GIS for remote sensing: Techniques and applications*, John Wiley & Sons.

LORD, J. A., CLAYTON, C. R. I., MORTIMORE, R. N., ASSOCIATION, C. I. R. & INFORMATION 2002. *Engineering in Chalk*, CIRIA.

LORD, J. A., TWINE, D. & YEOW, H. 1994. *Foundations in chalk*, Construction Industry Research and Information Association London.

LYONS, S. & SANDWELL, D. 2003. Fault creep along the southern San Andreas from interferometric synthetic aperture radar, permanent scatterers, and stacking. *Journal of Geophysical Research: Solid Earth,* 108.

MASSELINK, G., HUGHES, M. & KNIGHT, J. 2014. *Introduction to coastal processes and geomorphology*, Routledge.

MASSONNET, D., ROSSI, M., CARMONA, C., ADRAGNA, F., PELTZER, G., FEIGL, K. & RABAUTE, T. 1993. The displacement field of the Landers earthquake mapped by radar interferometry. *Nature,* 364**,** 138-142.

MCINNES, R. 2007. The Undercliff of the Isle of Wight. A guide to managing ground stability. *In:* CENTRE FOR THE COASTAL ENVIRONMENT, I. O. W. C. (ed.). Isle of Wight.

MIDER, G., LAWRENCE, J., MASON, P. & GHAIL, R. 2020. Monitoring Littoral Platform Downwearing Using Differential SAR Interferometry. *Remote Sensing,* 12.

MILILLO, P., GIARDINA, G., DEJONG, M. J., PERISSIN, D. & MILILLO, G. 2018. Multi-temporal InSAR structural damage assessment: The London crossrail case study. *Remote Sensing,* 10**,** 287.

MOORE, R., CAREY, J., MCINNES, R. & HOUGHTON, J. Climate change, so what. Implications for ground movement and landslide event frequency in the Ventnor Undercliff, Isle of Wight. This Conference, 2007.

MOREIRA, A., PRATS-IRAOLA, P., YOUNIS, M., KRIEGER, G., HAJNSEK, I. & PAPATHANASSIOU, K. P. 2013. A tutorial on synthetic aperture radar. *IEEE Geoscience and Remote Sensing Magazine,* 1**,** 6-43.

MORTIMORE, R. 2011. A chalk revolution: what have we done to the Chalk of England? *Proceedings of the Geologists' Association,* 122**,** 232-297.

MORTIMORE R. N, D. A. 2004. Coastal Chalk Cliff Instability.

MORTIMORE, R. N. 1986. Stratigraphy of the upper cretaceous white chalk of Sussex.

MORTIMORE, R. N. 2014. Logging the Chalk. Whittles Publishing.

MORTIMORE, R. N., LAWRENCE, J., POPE, D., DUPERRET, A. & GENTER, A. 2004a. Coastal cliff geohazards in weak rock: the UK Chalk cliffs of Sussex. *Coastal Chalk Cliff Instability***,** 3-31.

MORTIMORE, R. N., STONE, K. J., LAWRENCE, J. & DUPERRET , A. 2004b. Chalk physical properties and cliff instability. *Geological Society, London, Engineering Geology Special Publications,* 20**,** 75-88.

MORTIMORE, R. N., WOOD, C. J. & GALLOIS, R. W. 2001. British upper Cretaceous stratigraphy.

MOSES, C., CHARMAN, R. & WILLIAMS, R. 2010. Downwearing rates and patterns on a cohesive shore platform, Isle of Sheppey, UK. *EGUGA***,** 5393.

MOSES, C. & ROBINSON, D. 2011. Chalk coast dynamics: Implications for understanding rock coast evolution. *Earth-Science Reviews,* 109**,** 63-73.

MOSES, C., ROBINSON, D. & BARLOW, J. 2014. Methods for measuring rock surface weathering and erosion: A critical review. *Earth-Science Reviews,* 135**,** 141-161.

MOSES, C. A. 2014. Chapter 4 The rock coast of the British Isles: shore platforms. *Geological Society, London, Memoirs,* 40**,** 39-56.

NAYLOR, L. & STEPHENSON, W. 2010. On the role of discontinuities in mediating shore platform erosion. *Geomorphology,* 114**,** 89-100.

NORMAND, J. C. L. & HEGGY, E. 2015. InSAR Assessment of Surface Deformations in Urban Coastal Terrains Associated With Groundwater Dynamics. *IEEE Transactions on Geoscience and Remote Sensing,* 53**,** 6356-6371.

O'CONNOR, W. 2020. *An investigation into coastal erosion along the Isle of Wight coast using InSAR.* MSc, Imperial College London.

O'DONNELL, R. M. 2010. Radar Systems Engineering Lecture 11 Waveforms and Pulse Compression. *IEE New Hampshire Section*, 1-58.

O'CONNOR, W., MIDER, G., LAWRENCE, J. A., AGAR, S., MASON, P. J., GHAIL, R. & SCOULAR, J. 2021. An Investigation into Ground Movement on the Ventnor Landslide Complex, UK Using Persistent Scatterer Interferometry. *Remote Sensing,* 13**,** 3711.

PETHICK, J. S. 1984. *An introduction to coastal geomorphology,* London, United Kingdom, Arnold, Member of Hodder Headline Group.

POTTER, P. E. 2007. *Exploring the geology of the Cincinnati/northern Kentucky region*, Kentucky Geological Survey, University of Kentucky.

PRATESI, F., TAPETE, D., DEL VENTISETTE, C. & MORETTI, S. 2016. Mapping interactions between geology, subsurface resource exploitation and urban development in transforming cities using InSAR Persistent Scatterers: Two decades of change in Florence, Italy. *Applied Geography,* 77**,** 20-37.

PRICE, M. 1987. Fluid flow in the Chalk of England. *Geological Society, London, Special Publications,* 34**,** 141-156.

RESOURCES INVENTORY COMMITTEE 1998. Terrain stability mapping in British Columbia: a review and suggested methods for landslide hazard and risk mapping. *Victoria, BC. Resources Inventory Committee 1996b. Guidelines and Standards for Terrain Mapping in British Columbia. Victoria, BC. Resources Inventory Committee*.

ROBINSON, L. 1977a. Erosive processes on the shore platform of northeast Yorkshire, England. *Marine Geology,* 23**,** 339-361.

ROBINSON, L. 1977b. Marine erosive processes at the cliff foot. *Marine Geology,* 23**,** 257-271.

ROBINSON, L. A. 1976. The micro-erosion meter technique in a littoral environment. *Marine Geology,* 22**,** 51-58.

ROHMER, J., LOSCHETTER, A., RAUCOULES, D., DE MICHELE, M., LE GALLO, Y. & RAFFARD, D. 2014. Improving Persistent Scatterers Interferometry (PSI) analysis in highly vegetal / agricultural areas for long term CO2 storage monitoring. *Energy Procedia,* 63**,** 4019-4026.

ROHMER, J. & RAUCOULES, D. 2012. On the applicability of Persistent Scatterers Interferometry (PSI) analysis for long term CO2 storage monitoring. *Engineering Geology,* 147-148**,** 137-148.

ROSEN, P. A., HENSLEY, S., JOUGHIN, I. R., LI, F. K., MADSEN, S. N., RODRIGUEZ, E. & GOLDSTEIN, R. 2000. Synthetic Aperture Radar Interferometry. *IEEE Geoscience and Remote Sensing Magazine,* 88**,** 50.

ROUYET, L., KRISTENSEN, L., DERRON, M.-H., MICHOUD, C., BLIKRA, L. H., JABOYEDOFF, M. & LAUKNES, T. R. 2017. Evidence of rock slope breathing using ground-based InSAR. *Geomorphology,* 289**,** 152-169.

ROUYET, L., LAUKNES, T. R., CHRISTIANSEN, H. H., STRAND, S. M. & LARSEN, Y. 2019. Seasonal dynamics of a permafrost landscape, Adventdalen, Svalbard, investigated by InSAR. *Remote Sensing of Environment,* 231**,** 111236.

ROWE, A. W. 1900. *The Zones of the White Chalk of the English Coast*, Geologists' Assoc.

SAJINKUMAR, K. S., BINCY, H. S., BOUALI, E. H., OOMMEN, T., VISHNU, C. L., ANILKUMAR, Y., THRIVIKRAMJI, K. P. & KEERTHY, S. 2020. Picturing beach erosion and deposition trends using PSInSAR: an example from the non-barred southern west coast of India. *Wetlands Ecology and Management*.

SANDWELL, D. T. & PRICE, E. J. 1998. Phase gradient approach to stacking interferograms. *Journal of Geophysical Research: Solid Earth,* 103**,** 30183-30204.

SARMAP, S. 2009. Synthetic Aperture Radar and SARscape: SAR Guidebook. *Sarmap SA: Purasca, Switzerland***,** 274.

SCHLÖGEL, R., DOUBRE, C., MALET, J.-P. & MASSON, F. 2015. Landslide deformation monitoring with ALOS/PALSAR imagery: A D-InSAR geomorphological interpretation method. *Geomorphology,* 231**,** 314-330.

SCHOLLE, P. A. 1977. Chalk diagenesis and its relation to petroleum exploration: oil from chalks, a modern miracle? *AAPG Bulletin,* 61**,** 982-1009.

SCOULAR, J., AGAR, S., MIDER, G., MORGAN, T., CARPENTER, A., LAWRENCE, J. A., MASON, P. & GHAIL, R. C. 2021. Expanding Horizons *Geoscientist* 24-31.

SCOULAR, J., CROFT, J., GHAIL, R., MASON, P., LAWRENCE, J. & STOIANOV, I. 2020a. Limitations of Persistent Scatterer Interferometry to measure small seasonal ground movements in an urban environment. *Quarterly Journal of Engineering Geology and Hydrogeology,* 53**,** 39-48.

SCOULAR, J., GHAIL, R., MASON, P., LAWRENCE, J., BELLHOUSE, M., HOLLEY, R. & MORGAN, T. 2020b. Retrospective InSAR Analysis of East London during the Construction of the Lee Tunnel. *Remote Sensing,* 12.

SHEPARD, F. P. & GRANT, U. S. 1947. Wave erosion along the southern California coast. *Geological Society of America Bulletin,* 58**,** 919-926.

SHORT, N., BRISCO, B., COUTURE, N., POLLARD, W., MURNAGHAN, K. & BUDKEWITSCH, P. 2011. A comparison of TerraSAR-X, RADARSAT-2 and ALOS-PALSAR interferometry for monitoring permafrost environments, case study from Herschel Island, Canada. *Remote Sensing of Environment,* 115**,** 3491-3506.

SOUSA, J. J., RUIZ, A. M., HANSSEN, R. F., BASTOS, L., GIL, A. J., GALINDO-ZALDÍVAR, J. & SANZ DE GALDEANO, C. 2010. PS-InSAR processing methodologies in the detection of field surface deformation—Study of the Granada basin (Central Betic Cordilleras, southern Spain). *Journal of Geodynamics,* 49**,** 181-189.

SQUARZONI, G., BAYER, B., FRANCESCHINI, S. & SIMONI, A. 2020. Pre-and post-failure dynamics of landslides in the Northern Apennines revealed by space-borne synthetic aperture radar interferometry (InSAR). *Geomorphology,* 369**,** 107353.

STAVROU, A., LAWRENCE, J., MORTIMORE, R., MURPHY, W. & GÜNTHER, A. 2011. A geotechnical and GIS based method for evaluating risk exposition along coastal cliff environments: a case study of the chalk cliffs of southern England. *Natural Hazards & Earth System Sciences,* 11.

STEPHENSON, W. & FINLAYSON, B. 2009a. Measuring erosion with the micro-erosion meter—contributions to understanding landform evolution. *Earth-Science Reviews,* 95**,** 53-62.

STEPHENSON, W. & NAYLOR, L. 2011. Geological controls on boulder production in a rock coast setting: insights from South Wales, UK. *Marine Geology,* 283**,** 12-24.

STEPHENSON, W. J. & FINLAYSON, B. L. 2009b. Measuring erosion with the micro-erosion meter—Contributions to understanding landform evolution. *Earth-Science Reviews,* 95**,** 53-62.

SUNAMURA, T. 1976. Feedback relationship in wave erosion of laboratory rocky coast. *The Journal of Geology,* 84**,** 427-437.

SUNAMURA, T. 1992. *Geomorphology of rocky coasts*, John Wiley & Son Ltd.

SWANSTON, D. & HOWES, D. 1994. Slope movement processes and characteristics. *A Guide for Management of Landslide Prone Terrain in the Pacific Northwest, edited by Chatwin, S. C., Howes, DE, Schwab, JW, and Swanston, DN, British Columbia Ministry of Forests, Land Management Handbook,* 18**,** 1-17.

SWANTESSON, J. O. H. 1992. Recent microweathering phenomena in southern and central Sweden. *Permafrost and periglacial processes,* 3**,** 275-292.

SWANTESSON, J. O. H., MOSES, C., BERG, G. E. & JANSSON, K. 2006. Methods for measuring shore platform micro erosion: A comparison of the micro-erosion meter and laser scanner. *Zeitschrift fur Geomorphologie, Supplementband,* 144**,** 1-17.

TRENHAILE, A. 1980. Shore platforms: a neglected coastal feature. *Progress in physical geography,* 4**,** 1-23.

TRENHAILE, A. 2005. Modelling the effect of waves, weathering and beach development on shore platform development. *Earth Surface Processes and Landforms: The Journal of the British Geomorphological Research Group,* 30**,** 613-634.

TRENHAILE, A. 2016. Rocky coasts—their role as depositional environments. *Earth-science reviews,* 159**,** 1-13.

TRENHAILE, A. S. 1987. *The geomorphology of rock coasts*, Oxford University Press, USA.

TRENHAILE, A. S. 1999. The width of shore platforms in Britain, Canada, and Japan. *Journal of Coastal Research***,** 355-364.

TRENTER, N. & WARREN, C. 1996. Further investigations at the Folkestone Warren landslide. *Geotechnique,* 46**,** 589-620.

USAI, S. & KLEES, R. 1999. SAR interferometry on a very long time scale: a study of the interferometric characteristics of man-made features. *IEEE Transactions on Geoscience and Remote Sensing,* 37**,** 2118-2123.

VAN ZYL, J. J. 2011. *Synthetic aperture radar polarimetry*, John Wiley & Sons.

VARNES, D. J. 1978. Slope movement types and processes. *Special report,* 176**,** 11-33.

WAKELING, T. R. 1970. A comparison of the results of standard site investigations methods against the results of a detailed geotechnical investigation in middle chalk at Mundford, Norfolk.

WALKDEN, M. & HALL, J. 2005. A predictive mesoscale model of the erosion and profile development of soft rock shores. *Coastal Engineering,* 52**,** 535-563.

WARD, W. H., BURLAND, J. B. & GALLOIS, R. W. 1968. Geotechnical Assessment of a Site at Mundford, Norfolk, for a large Proton Accelerator. *Géotechnique,* 18**,** 399-431.

WOOD, C. & SMITH, E. 1978. Lithostratigraphical classification of the chalk in North Yorkshire, Humberside and Lincolnshire. *Proceedings of the Yorkshire Geological Society,* 42**,** 263-287.

WRIGHT, L. 1967. Some characteristics of the shore platforms of the English Channel coast and the northern part of the North Island, New Zealand. *Zeitschrift für Geomorphologie NF,* 11**,** 36-46.

WYLLIE, D. C. 1980. Toppling rock slope failures examples of analysis and stabilization. *Rock mechanics,* 13**,** 89-98.

YIN, Y., ZHENG, W., LIU, Y., ZHANG, J. & LI, X. 2010. Integration of GPS with InSAR to monitoring of the Jiaju landslide in Sichuan, China. *Landslides,* 7**,** 359-365.

YOUNG, A. P. 2015. Recent deep-seated coastal landsliding at San Onofre State Beach, California. *Geomorphology,* 228**,** 200-212.

YOUNG, A. P. & CARILLI, J. E. 2019. Global distribution of coastal cliffs. *Earth Surface Processes and Landforms,* 44**,** 1309-1316.

ZHAO, Q., MA, G., WANG, Q., YANG, T., LIU, M., GAO, W., FALABELLA, F., MASTRO, P. & PEPE, A. 2019. Generation of long-term InSAR ground displacement time-series through a novel multi-sensor data merging technique: The case study of the Shanghai coastal area. *ISPRS Journal of Photogrammetry and Remote Sensing,* 154**,** 10-27.

ZHU, W., ZHANG, Q., DING, X., ZHAO, C., YANG, C., QU, F. & QU, W. 2014. Landslide monitoring by combining of CR-InSAR and GPS techniques. *Advances in space research,* 53**,** 430-439.

10 Appendix 1

10.1 Python script syntax for filtering out the Sentinel-1A and -1B scenes to provide a list of scenes acquired within +/- 2 hours of the lowest daily tide

```
import pandas

import matplotlib.pyplot as plt

import numpy as np

from datetime import datetime, timedelta

from scipy.signal import argrelextrema


def tides(tidedata, startdate, enddate, buffer, waterheight, filelist):

#   colnames = ['number', 'datetime', 'waterlevel', 'residual'] # assigns column names for imported csv
data

   colnames = ['datetime', 'waterlevel'] # assigns column names for imported csv data

   data = pandas.read_csv(tidedata, names=colnames) # imports csv data using pandas and assigns
column names

   datetimes = data.datetime.tolist() # puts imported csv data into lists

   waterlevels = data.waterlevel.tolist()

   tides = np.array(waterlevels) # converts lists into numpy arrays for use with argrelextrema

   times = np.array(datetimes)


   if waterheight == 0: # process if lowtide input is given (waterheight = 0)

      lowtidesindex = argrelextrema(tides, np.less) # provides indexes of all local minima

      lowtidesindexlist = list(lowtidesindex) # converts lowtidesindex array into a list, in order to sort it

      usabletimes = times[lowtidesindexlist] # creates an array of times, based on the indexes found in
lowtidesindexlist

      usabletimeslist = list(usabletimes) # converts usabletimes, an array, into a list

      firstindices = []  # finds first instance of the startdate and records the index of this as firstindex

      for i, elem in enumerate(usabletimeslist):

         if startdate in elem:

            firstindices.append(i)

      firstindex = min(firstindices)

      lastindices = [] # finds last instance of the enddate and records the index of this as lastindex

      for i, elem in enumerate(usabletimeslist):

         if enddate in elem:

            lastindices.append(i)
```

```
    lastindex = max(lastindices)
    usabletimeslist = usabletimeslist[firstindex:lastindex+1] # slices usabletimeslist to the startdate and enddate
    with open('usabletimes.csv', mode="w+") as outfile:  # writes usabletimeslist to a .csv file
      for s in usabletimeslist:
        outfile.write("%s\n" % s)
    colnames2 = ['date', 'time'] # assigns column names for imported csv data
    data = pandas.read_csv('usabletimes.csv', names=colnames2, delimiter = ' ') # reads in data from newly created .csv file
    dates = data.date.tolist() # puts imported csv data into lists of dates and times
    times = data.time.tolist()
    newdates = [] # reformats dates into the desired YYYY-MM-DD format
    for x in dates:
      olddateformat = datetime.strptime(x,'%d/%m/%Y')
      newdateformat = olddateformat.strftime('%Y-%m-%d')
      newdates.append(newdateformat)
    Ttimes = ["T" + t + ":00.000000Z" for t in times] # formats times as Ttime:00.000Z
    dateTtime = [i + j for i, j in zip(newdates, Ttimes)] # combines newdates and Ttimes into dateTtime
    datetimedt = [] # assigns datetime formatting to all values in dateTtime, storing in datetimedt
    for dt in dateTtime:
      dateTtimeformat = datetime.strptime(dt, "%Y-%m-%dT%H:%M:%S.%fZ")
      datetimedt.append(dateTtimeformat)
    alltimes = [] # creates a list of all possible hour values within the defined buffer either side of the low tide
    counter = 0
    for x in datetimedt:
      earlytime = x - timedelta(hours = buffer)
      latetime = x + timedelta(hours = buffer)
      alltimes.append(earlytime)
      while earlytime < latetime:
        earlytime += timedelta(hours=1)
        alltimes.append(earlytime)
    alltimesf = []
    for x in alltimes: # creates a list from all possible hour values in the format YYYYMMDDTHH
      ftime = datetime.strftime(x, "%Y%m%dT%H")
```

```
        alltimesf.append(ftime)
      with open('comparabletimes.csv', mode="w+") as outfile:  # writes the possble hour values to csv file
        for s in alltimesf:
          outfile.write("%s\n" % s)


  if waterheight == -1: # process if hightide input is given (waterheight = 0)
      hightidesindex = argrelextrema(tides, np.greater) # provides indexes of all local maxima
      hightidesindexlist = list(hightidesindex) # converts hightidesindex array into a list, in order to sort it
      usabletimes = times[hightidesindexlist] # creates an array of times, based on the indexes found in
hightidesindexlist
      usabletimeslist = list(usabletimes) # converts usabletimes, an array, into a list
      firstindices = []  # finds first instance of the startdate and records the index of this as firstindex
      for i, elem in enumerate(usabletimeslist):
        if startdate in elem:
          firstindices.append(i)
      firstindex = min(firstindices)
      lastindices = [] # finds last instance of the enddate and records the index of this as lastindex
      for i, elem in enumerate(usabletimeslist):
        if enddate in elem:
          lastindices.append(i)
      lastindex = max(lastindices)
      usabletimeslist = usabletimeslist[firstindex:lastindex+1] # slices usabletimeslist to the startdate and
enddate
      with open('usabletimes.csv', mode="w+") as outfile:  # writes usabletimeslist to a .csv file
        for s in usabletimeslist:
          outfile.write("%s\n" % s)
      colnames2 = ['date', 'time'] # assigns column names for imported csv data
      data = pandas.read_csv('usabletimes.csv', names=colnames2, delimiter = ' ') # reads in data from
newly created .csv file
      dates = data.date.tolist() # puts imported csv data into lists of dates and times
      times = data.time.tolist()
      newdates = [] # reformats dates into the desired YYYY-MM-DD format
      for x in dates:
        olddateformat = datetime.strptime(x,'%d/%m/%Y')
        newdateformat = olddateformat.strftime('%Y-%m-%d')
```

```
            newdates.append(newdateformat)
        Ttimes = ["T" + t + ":00.000000Z" for t in times] # formats times as Ttime:00.000Z
        dateTtime = [i + j for i, j in zip(newdates, Ttimes)] # combines newdates and Ttimes into dateTtime
        datetimedt = [] # assigns datetime formatting to all values in dateTtime, storing in datetimedt
        for dt in dateTtime:
            dateTtimeformat = datetime.strptime(dt, "%Y-%m-%dT%H:%M:%S.%fZ")
            datetimedt.append(dateTtimeformat)
        alltimes = [] # creates a list of all possible hour values within the defined buffer either side of the high
tide
        counter = 0
        for x in datetimedt:
            earlytime = x - timedelta(hours = buffer)
            latetime = x + timedelta(hours = buffer)
            alltimes.append(earlytime)
            while earlytime < latetime:
                earlytime += timedelta(hours=1)
                alltimes.append(earlytime)
        alltimesf = []
        for x in alltimes: # creates a list from all possible hour values in the format YYYYMMDDTHH
            ftime = datetime.strftime(x, "%Y%m%dT%H")
            alltimesf.append(ftime)
        with open('comparabletimes.csv', mode="w+") as outfile:  # writes the possble hour values to csv file
            for s in alltimesf:
                outfile.write("%s\n" % s)


    if waterheight > 0:
        tidesl = tides.tolist() # converts tides array to a list
        tidesl2 = [str(i) for i in tidesl]
        for item in tidesl:
            int(item)
        wh_val = str(waterheight) # converts waterheight float into a string
        indices1 = []
        for i, elem in enumerate(tidesl2): # creates a list of the index of each value containing the given
waterheight value
            if wh_val in elem:
```

```
            indices1.append(i)
        indices2 = []
        for i in indices1: # creates a list (indices2) of indices in a given range of each index in indices1. range
defined by 'buffer' input
            earlyindex = i - buffer
            lateindex = i + buffer
            idxrange = list(range(earlyindex, lateindex+1))
            indices2 = indices2 + idxrange
        indices2.sort() # sorts indices
        indices2 = list(dict.fromkeys(indices2)) # removes duplicates by converting the list to a dictionary and
back to a list - dictionaries cannot contain duplicate entries
        usabletimes = times[indices2] # creates an array of times, based on the indexes found in
lowtidesindexlist
        usabletimeslist = list(usabletimes) # converts usabletimes, an array, into a list
        firstindices = []  # finds first instance of the startdate and records the index of this as firstindex
        for i, elem in enumerate(usabletimeslist):
            if startdate in elem:
                firstindices.append(i)
        if firstindices:
            firstindex = min(firstindices)
        else:
            firstindex = 0
        lastindices = [] # finds last instance of the enddate and records the index of this as lastindex
        for i, elem in enumerate(usabletimeslist):
            if enddate in elem:
                lastindices.append(i)
        if lastindices:
            lastindex = max(lastindices)
        else:
            lastindex = -2
        usabletimeslist = usabletimeslist[firstindex:lastindex+1]
        with open('usabletimes.csv', mode="w+") as outfile:  # writes usabletimeslist to a .csv file
            for s in usabletimeslist:
                outfile.write("%s\n" % s)
        colnames2 = ['date', 'time'] # assigns column names for imported csv data
```

```
    data = pandas.read_csv('usabletimes.csv', names=colnames2, delimiter = ' ') # reads in data from newly created .csv file
    dates = data.date.tolist() # puts imported csv data into lists of dates and times
    times = data.time.tolist()
    newdates = [] # reformats dates into the desired YYYY-MM-DD format
    for x in dates:
        olddateformat = datetime.strptime(x,'%d/%m/%Y')
        newdateformat = olddateformat.strftime('%Y-%m-%d')
        newdates.append(newdateformat)
    Ttimes = ["T" + t + ":00.000000Z" for t in times] # formats times as Ttime:00.000Z
    dateTtime = [i + j for i, j in zip(newdates, Ttimes)] # combines newdates and Ttimes into dateTtime
    datetimedt = [] # assigns datetime formatting to all values in dateTtime, storing in datetimedt
    for dt in dateTtime:
        dateTtimeformat = datetime.strptime(dt, "%Y-%m-%dT%H:%M:%S.%fZ")
        datetimedt.append(dateTtimeformat)
    alltimes = [] # creates a list of all possible hour values within the defined buffer either side of the high tide
    counter = 0
    for x in datetimedt:
        earlytime = x - timedelta(hours = buffer)
        latetime = x + timedelta(hours = buffer)
        alltimes.append(earlytime)
        while earlytime < latetime:
            earlytime += timedelta(hours=1)
            alltimes.append(earlytime)
    alltimesf = []
    for x in alltimes: # creates a list from all possible hour values in the format YYYYMMDDTHH
        ftime = datetime.strftime(x, "%Y%m%dT%H")
        alltimesf.append(ftime)
    with open('comparabletimes.csv', mode="w+") as outfile:  # writes the possble hour values to csv file
        for s in alltimesf:
            outfile.write("%s\n" % s)


  colname2 = ['granulename'] # assigns column names for imported csv data
```

```
    filedata = pandas.read_csv(filelist, names=colname2) # imports csv data using pandas and assigns column names
    granules = filedata.granulename.tolist() # puts imported csv data into lists
    usablegranules = [] # creates empty list called usablegranules
    for x in alltimesf: # adds name of each granule that contains one of the usable times to the list usablegranules
        matching = [s for s in granules if x in s]
        usablegranules.append(matching) # usablegranules is a list of lists, with every non-matching granule forming an empty list i.e. [[],[],[S1A...],[]]
    usablegranules = [e for e in usablegranules if e] # removes empty lists from list of lists
    result = sum(usablegranules, []) # combines all lists in list to form one, uninterrupted list
    result = list(dict.fromkeys(result)) # removes any duplicates by converting to dictionary and back again

    with open('2016_usablegranules.txt', mode="w+") as outfile: # writes all usable granules to a .txt file, with a preamble showing the used parameters
        outfile.write("Generated at: ")
        outfile.write(str(datetime.now()))
        outfile.write(" UTC\nStart date: ")
        outfile.write(startdate)
        outfile.write("\nEnd date: ")
        outfile.write(enddate)
        outfile.write("\nBuffer: ")
        outfile.write(str(buffer))
        outfile.write(" hours\nWater height [where 0 = low tide, -1 = high tide]: ")
        outfile.write(str(waterheight))
        outfile.write(" metres \nTide data input: ")
        outfile.write(tidedata)
        outfile.write("\nGranule metadata input: ")
        outfile.write(filelist)
        outfile.write("\nUsable granules (")
        outfile.write(str(len(result)))
        outfile.write(" usable / ")
        outfile.write(str(len(granules)))
        outfile.write(" inputted): \n")
        for s in result:
            outfile.write("%s\n" % s)
```

```
    return usablegranules

tides('2016DOV-edited.csv', '01/01/2016', '31/12/2016', 2, 0, 'granules.csv')
```